UNIVERSITÉ
DE LORRAINE

AVERTISSEMENT

Ce document est le fruit d'un long travail approuvé par le jury de soutenance et mis à disposition de l'ensemble de la communauté universitaire élargie.

Il est soumis à la propriété intellectuelle de l'auteur. Ceci implique une obligation de citation et de référencement lors de l’utilisation de ce document.

D'autre part, toute contrefaçon, plagiat, reproduction illicite encourt une poursuite pénale.

Contact : ddoc-theses-contact@univ-lorraine.fr

LIENS

Code de la Propriété Intellectuelle. articles L 122. 4
Code de la Propriété Intellectuelle. articles L 335.2- L 335.10
http://www.cfcopies.com/V2/leg/leg_droi.php
http://www.culture.gouv.fr/culture/infos-pratiques/droits/protection.htm

N°d'ordre : XXXX-XX-TH

**Université de Lorraine**

**École doctorale EMMA**
**« Énergie, Mécanique et Matériaux »**
LMOPS, « Laboratoire Matériaux Optiques, Photonique et Systèmes »

**Thèse de doctorat**
Domaine : SPI
Spécialité : Photonique

Soutenance prévue le 20 Octobre 2016 par
**Noémi Wiersma**
à CentraleSupélec, Metz, France.

# PHOTOREFRACTIVE SELF-FOCUSING OF AIRY BEAMS: NONLINEAR INTERACTIONS AND ALL-OPTICAL WAVEGUIDING

Composition du jury :

| | | |
|---|---|---|
| Directeur de thèse : | Pr. Delphine Wolfersberger | CentraleSupélec |
| Co-directrice de thèse : | Dr. Nicolas Marsal | CentraleSupélec |
| Co-encadrant de thèse : | Pr. Marc Sciamanna | CentraleSupélec |
| Rapporteurs : | Pr. Cornelia Denz | Universität Münster |
| | Dr. Eric Louvergneaux | Université Lille 1 |
| Examinateurs : | Pr. Eugenio Del Re | Université de Rome La Sapienza |
| | Pr. Jean-Paul Salvestrini | Université de Lorraine |
| | Dr. Mustafa Tlidi | Université Libre de Bruxelles |

# DEDICATION

---

This thesis has been an eye-opening experience as well from the scientific as from the human point of view.

First of all it has been a enriching experience to deepen my experience in the photonic field which I have discovered through my engineering studies and in particular the photonic teaching team of CentraleSupélec and the University of Lorraine. First I would like to thank my close research team at the LMOPS-laboratory being Pr. Dr. Delphine WOLFERSBERGER and Dr. Nicolas MARSAL, my two thesis-directors who guided me all along my research. Without their close help, their counsels, their large support (from the experimental and theoretical work to the communication skills), this thesis would by far not be as successful as I am proud to present here. As backbone of my research work, Pr. Dr. Marc SCIAMANNA has played a key role in the broadening of this research work and these communication opportunities. In addition to this core team, I would like to thank the larger cooperation team where I have as well enjoyed the welcoming joyful atmosphere as the diverse expertise. Among all I would like to express my deep gratitude in particular to Dr. Damien RONTANI, Mario FERNANDES and Gilles BERLIN for their countless support.

During these three years I have been fully integrated and it has been an honor to working within a growing and steadily changing environment at the LMOPS-laboratory of the University of Lorraine and the Graduate School of Engineering CentraleSupélec in Metz. In particular I would like to thank Pr. Dr. Jean-Paul SALVESTRINI, director of the LMOPS-laboratory, and Dr. Konrad SZAFNICKI, director of CentraleSupélec Metz, and his predecessor Dr. Serge PERRINE for their warm welcome in their institutions. During this thesis I had the opportunity to meet many new colleagues, who have shared with me their experience and given me administrative and personal help and support all along. Within the PhD-community I have found a very positive atmosphere and I have experienced various events and scientific popularization contests. In particular I am thinking of my office mates Matthieu LAUFFER, Chi-Hak UY, Dr. Lionel WEICKER and those who are pursuing the research projects within the team.

As a transition to my personal circle, I would like to thank Dr. Emeric MERCIER and Elodie MIRISOLA for their scientific support, their kindness and wish them all the best for the future. Also a key person to convince me to enter the research was Dr. Andreas KARSAKLIAN DAL BOSCO who shared his passion for photonics with the students and opened the research world for many engineering students such as myself. In general the CentraleSupélec student life has helped me to merge my research project with the community spirit that enriched my daily life. Without naming all individually, those who have shared with me the different events will recognize themselves and I will be always grateful for their motivation, curiosity and positive spirit they have shared with me.

During these thesis I have been surrounded by many friends who I am deeply grateful for: my dear Marie, Julie, Muriel, the Adrénaline team, the Mettensis Orchestra... and foremost my family. Without them I would not have experienced such a rich and colorful photonic thesis. So I would like to finish this dedication page with naming those who I could not be grateful enough for and who, for over twenty years, help me develop my strengths and become a fulfilled scientific woman: Michelle, Marylène, Wopke, Eugénie and my dear sister Nathalie.

Thank you to you all and I wish you all the best for the future.

# ABSTRACT

In this thesis we study the propagation and the self-focusing of Airy beams in a photorefractive crystal.

The Airy beam is a so-called accelerating beam which propagates in free space along a curved trajectory and with a shape-preserving and self-healing nature. The self-focusing of conventional beams, such as Gaussian beams, has been studied in nonlinear media in particular for all-optical routing solutions. By propagating optical beams in such photosensitive media, one can induce waveguides with the shape of the optical beams' trajectories. The unique shape and trajectory of the Airy beam however suggest innovative waveguide possibilities.

In this manuscript we theoretically and experimentally study the self-focusing mechanisms of the Airy beam. In particular during the transient self-focusing effect, we enlighten peculiar spatiotemporal dynamics suggesting an analogy with the gravitational interactions between a mass and a wave propagating in a curved spacetime. In a second step we add an Airy beam propagating in the opposite direction to analyze their cross-coupling interactions. The guiding structures induced by one or two counterpropagating Airy beams are then tested and show peculiar guiding possibilities that are not achievable using two conventional beams: optical beams can be guided along curved trajectories and eventually split into multiple beams. Furthermore the limits of the waveguiding strength are studied by increasing the self-focusing nonlinearity of the system. The resulting spatiotemporal dynamics present a peculiar behavior and evolution with possible applications in static and dynamical all-optical routing as well as optical computing such as random number generation.

Finally with this thesis we demonstrate that the Airy beam offers promising alternatives in general physics and more specifically in photonics for all-optical routing.

# RÉSUMÉ

La thèse présente l'étude de la propagation et de l'auto-focalisation de faisceaux d'Airy dans un milieu photoréfractif.
Le faisceau d'Airy est un faisceau dit accélérant qui, dans l'espace libre, présente une trajectoire curviligne, ne se déforme pas et est capable de se régénérer après un obstacle. L'auto-focalisation de faisceaux conventionnels, tels les faisceaux gaussiens, a été étudiée dans des milieux nonlinéaires en particulier pour des applications de routage tout-optique. En propageant des faisceaux optiques à travers de tels milieux photosensibles, il est possible de graver optiquement des guides d'onde retraçant la trajectoire de ces faisceaux. C'est dans ce contexte que le faisceau d'Airy suscite beaucoup d'intérêt, grâce à sa forme et sa trajectoire uniques.
Dans ce mémoire nous étudions expérimentalement comme théoriquement les mécanismes d'auto-focalisation du faisceau d'Airy. Durant le régime transitoire de l'effet d'auto-focalisation, nous montrons des dynamiques spatiotemporelles singulières qui suggèrent une analogie avec les interactions gravitationnelles entre un objet massique et une onde se propageant dans l'espace-temps courbe. Dans un second temps, nous ajoutons un faisceau d'Airy se propageant dans la direction opposée au premier afin d'analyser leurs interactions. Ensuite, nous testons ces structures guidantes photoinduites par un ou deux faisceaux d'Airy, qui révèlent des possibilités de guidage uniques, non accessibles avec deux faisceaux conventionnels. Ces faisceaux optiques peuvent permettre de réaliser des fonctions de couplage, routage et multiplexage optique. Par ailleurs, nous étudions les limites de la force de guidage en augmentant la nonlinéarité d'auto-focalisation du système. Les dynamiques spatiotemporelles qui en dérivent présentent des comportements et une évolution particuliers suggérant des applications dans le routage tout-optique stationnaire tout comme dynamique.
Pour conclure, cette thèse nous permet de démontrer les alternatives prometteuses que nous offre le faisceau d'Airy dans la physique générale et plus particulièrement dans la photonique pour le routage tout-optique.

# SCIENTIFIC COMMUNICATIONS

---

## PUBLICATIONS IN PEER-REVIEWED JOURNALS

- N. Wiersma, N. Marsal, M. Sciamanna, D. Wolfersberger, "All-optical interconnects using Airy beams". In: *Opt. Lett.* 39.20 (2014), pp.5997-6000. DOI: 10.1364/OL.39.005997.

- N. Wiersma, N. Marsal, M. Sciamanna, D. Wolfersberger, "Spatiotemporal dynamics of counterpropagating Airy beams". In: *Sci. Rep.* 5.2011 (2015), pp.13463. DOI: 10.1038/srep13463.

- N. Wiersma, N. Marsal, M. Sciamanna, D. Wolfersberger, "Optical gravitational lensing from transient self-focusing of an Airy beam". In: *Sci. Rep.* (submitted June 2016).

## PRESENTATIONS AT CONFERENCES

- N. Wiersma, N. Marsal, M. Sciamanna, D. Wolfersberger, "Counterpropagating Airy beams in nonlinear media". In: *Nonlinear Photonics OSA* (2014), Barcelona, Spain. pp.NM4A.7. DOI: 10.1364/NP.2014.NM4A.7.

- D. Wolfersberger, N. Wiersma, N. Marsal, M. Sciamanna, "Counterpropagating Airy beams interactions in nonlinear media". In: *International Workshop on Optical Wave & Waveguide Theory and Numerical Theory - OWTNM* (2015), London, United Kingdom.

- N. Wiersma, N. Marsal, M. Sciamanna, D. Wolfersberger, "Spatiotemporal dynamics of counterpropagating Airy beams". In: *CLEO/Europe-EQEC Conference 2015* (2015), Munich, Germany. pp.EF_6_1.

- N. Marsal, N. Wiersma, M. Sciamanna, D. Wolfersberger, "Interaction between Airy beams in nonlinear media". In: *Nonlinear Optics* (2015), Kahuai, United States.

- N. Wiersma, N. Marsal, M. Sciamanna, D. Wolfersberger, "Spatiotemporal interactions of Airy beams". In: *WASTOS* (2015), Berlin, Germany.

- N. Wiersma, N. Marsal, M. Sciamanna, D. Wolfersberger, "Nonlinear Interactions of Accelerating Beams". In: *ISPALD* (2015), Metz, France.

- N. Wiersma, N. Marsal, M. Sciamanna, D. Wolfersberger, "Airy-induced dynamics in nonlinear media". In: *SPIE Photonics Europe* (2016), Bruxelles, Belgium.

- D. Wolfersberger, N. Wiersma, N. Marsal, M. Sciamanna, "Dynamical interactions of counterpropagating Airy beams". In: *Chaos* (2015), London, United Kingdom.

- M. Sciamanna, N. Wiersma, N. Marsal, D. Wolfersberger. In: *Pattern Dynamics in Nonlinear Optical Cavities* (2016), Dresden, Germany (invited).

- M. Sciamanna, N. Wiersma, N. Marsal, D. Wolfersberger, "Spatiotemporal dynamics of nonlinear Airy beam interactions". In: *Nonlinear photonics OSA* (2016), Sydney, Australia (invited).

- D. Wolfersberger, N. Wiersma, N. Marsal, M. Sciamanna, "Nonlinear Dynamics of Airy beam interactions". In: *NICE OPTICS* (2016), Nice, France.

## SCIENTIFIC POPULARIZATION CONTESTS

- N. Wiersma, E. Mercier, "En route vers l'ordinateur optique", 2$^{nd}$ price. In: *Trophée mc6* (2014), Club Metz Technopôle, Metz, France.

- N. Wiersma, "La lumière qui ne file pas bien droit", regional finalist. In: *Ma thèse en 180s* (2016), CPU-CNRS, Nancy, France. See comic in chapter E.

## AWARD

- PhD Grant 2016, Association Française des Femmes Diplômées d'Université (AFFDU) Lorraine.

# CONTENTS

PREFACE 1

1 INTRODUCTION 5

- 1.1 Accelerating beams . . . . . 6
  - 1.1.1 Observation in nature . . . . . 6
  - 1.1.2 Accelerating beams in optics . . . . . 9
  - 1.1.3 Applications in optics . . . . . 11
  - 1.1.4 Airy beams . . . . . 13
- 1.2 Photorefractive effect . . . . . 23
  - 1.2.1 Physical mechanisms . . . . . 23
  - 1.2.2 Optical applications . . . . . 27
- 1.3 Propagation of solitons . . . . . 28
  - 1.3.1 Observation in the nature . . . . . 28
  - 1.3.2 Theoretical mechanisms . . . . . 29
  - 1.3.3 Optical solitons . . . . . 29
- 1.4 Motivations . . . . . 35

I SELF-FOCUSING OF A SINGLE AIRY BEAM 37

2 SOLITONIC PROPERTIES OF A SINGLE SELF-FOCUSING AIRY BEAM 39

- 2.1 Nonlinear Airy propagation . . . . . 40
  - 2.1.1 Self-trapping effect . . . . . 40
  - 2.1.2 Solitonic regime . . . . . 43
  - 2.1.3 Photorefractive vs. Kerr nonlinearity . . . . . 45
- 2.2 Experimental study . . . . . 49
  - 2.2.1 Experimental setup . . . . . 49
  - 2.2.2 Observation of Airy-solitons . . . . . 51
- 2.3 Comparison with the theory . . . . . 59
  - 2.3.1 Simulation model . . . . . 59
  - 2.3.2 Theoretical solitonic self-focusing . . . . . 61
- 2.4 Conclusion and comparison with Gaussian systems . . . . . 63

3 TRANSIENT PROPERTIES OF A SELF-FOCUSING AIRY BEAM AND ITS ANALOGY WITH OPTICAL GRAVITATIONAL LENSING 67

- 3.1 Gravitational effects and its analogies in physics . . . . . 68
  - 3.1.1 Phenomenon . . . . . 68
  - 3.1.2 Observations in optics . . . . . 70

3.2 Experimental transient self-focusing of an Airy beam . . . . . . . . 73
3.2.1 Experimental setup . . . . . . . . . . . . . . . . . . . . . . . . 73
3.2.2 Transient dynamics of the Airy-soliton . . . . . . . . . . . . 74
3.2.3 Influence of the optical nonlinearity . . . . . . . . . . . . . 76
3.3 Theoretical confirmation . . . . . . . . . . . . . . . . . . . . . . . . 80
3.4 Conclusions . . . . . . . . . . . . . . . . . . . . . . . . . . . . . . . 82

II INTERACTIONS OF TWO AIRY BEAMS 83
4 COUNTERPROPAGATING AIRY BEAMS' INTERACTIONS 85
4.1 Waveguiding by a single Airy beam . . . . . . . . . . . . . . . . . . 86
4.2 Nonlinear multiple beams' interactions . . . . . . . . . . . . . . . . 90
4.2.1 Conventional beams' systems . . . . . . . . . . . . . . . . . . 91
4.2.2 Co-propagating Airy beams' interactions . . . . . . . . . . . 93
4.3 Numerical study of counterpropagating Airy beams . . . . . . . . 97
4.3.1 Coupling equations for the counterpropagating case . . . . 97
4.3.2 Study of the Airy interconnection range . . . . . . . . . . . 99
4.3.3 Waveguiding induced by counterpropagating Airy beams . 102
4.4 Experimental evidence . . . . . . . . . . . . . . . . . . . . . . . . . 107
4.4.1 Experimental setup . . . . . . . . . . . . . . . . . . . . . . . . 107
4.4.2 Results and discussions . . . . . . . . . . . . . . . . . . . . . 108
4.5 Conclusions . . . . . . . . . . . . . . . . . . . . . . . . . . . . . . . 117
5 THEORETICAL SPATIOTEMPORAL DYNAMICS OF COUNTERPROPAGATING AIRY BEAMS 119
5.1 Dynamics of nonlinear systems . . . . . . . . . . . . . . . . . . . . 120
5.1.1 Route to chaos . . . . . . . . . . . . . . . . . . . . . . . . . . 120
5.1.2 Dynamics of interacting Airy beams . . . . . . . . . . . . . . 121
5.2 Theoretical results . . . . . . . . . . . . . . . . . . . . . . . . . . . . 123
5.2.1 General overview . . . . . . . . . . . . . . . . . . . . . . . . . 123
5.2.2 Signature of different regimes . . . . . . . . . . . . . . . . . 127
5.3 Comparison with Gaussian systems . . . . . . . . . . . . . . . . . 130
5.3.1 Re-stabilization of the waveguide for large nonlinearity . . 130
5.3.2 Chaotic motion of Airy-induced soliton . . . . . . . . . . . . 132
5.4 Conclusions . . . . . . . . . . . . . . . . . . . . . . . . . . . . . . . 135

III CONCLUSION 137
6 CONCLUSIONS AND PERSPECTIVES 139
6.1 Conclusions . . . . . . . . . . . . . . . . . . . . . . . . . . . . . . . 139
6.2 Perspectives . . . . . . . . . . . . . . . . . . . . . . . . . . . . . . . 143

6.2.1 Stability control of the Airy-soliton . . . . . . . . . . . . . . 143
6.2.2 Experimental waveguiding of probe beams . . . . . . . . . . 143
6.2.3 Experimental study of spatiotemporal dynamics of counterpropagating Airy beams . . . . . . . . . . . . . . . . . . . . 144
6.2.4 Experimental study of the Airy-soliton in a longer propagation medium . . . . . . . . . . . . . . . . . . . . . . . . . . 144
6.2.5 Influence of the coherence of the interacting beams . . . . . 146
6.2.6 Interactions of Airy beams with opposite bending directions 146
6.2.7 Enlarge the study to 2D-Airy beams in nonlinear media . . 149

IV APPENDIX 151

A AIRY GENERATION USING A SPATIAL LIGHT MODULATOR (SLM) 153

B COUNTERPROPAGATING AIRY BEAMS IN A NONLINEAR MEDIUM: EXPERIMENTAL SETUP 159

C NUMERICAL SIMULATION MODEL 163
C.1 Calculation of the beam propagation . . . . . . . . . . . . . . . . . . 164
C.2 Calculation of the nonlinear photorefractive response of the medium 165
C.3 Initial conditions of the physical system and tuning parameters . . 166

D AUTOFOCALISATION PHOTORÉFRACTIVE DE FAISCEAUX D'AIRY – INTERACTIONS ET GUIDAGE TOUT OPTIQUE 169
D.1 Auto-focalisation d'un faisceau d'Airy . . . . . . . . . . . . . . . . 171
D.1.1 Montage expérimental . . . . . . . . . . . . . . . . . . . . . . . 173
D.1.2 Propriétés solitoniques d'un faisceau d'Airy auto-focalisant 174
D.1.3 Propriétés transitoires d'un faisceau d'Airy auto-focalisant et ses analogies avec le lentillage gravitationnel . . . . . . . 176
D.2 Interactions entre deux faisceaux d'Airy . . . . . . . . . . . . . . . . 180
D.2.1 Interactions de deux faisceaux d'Airy contrapropageants . 180
D.2.2 Dynamiques spatiotemporelles théoriques de deux faisceaux d'Airy contrapropageants . . . . . . . . . . . . . . . . . . . . 184
D.3 Conclusion . . . . . . . . . . . . . . . . . . . . . . . . . . . . . . . . 185

E A LITTLE STORY IN 1808 189

BIBLIOGRAPHY 195

# PREFACE

Light has been a popular medium to transmit information for a long time. The first optical communications are reported in free space, where a light source emits optical rays spreading all around the source. A typical example are guiding systems in maritime/air/land transport, where the light indicates the presence of obstacles and directions to follow. A light beam can also contain a message, such as using Morse code, where the succession of light flashes in time can be first translated into letters and then into words. However free space communications requires large and intense light sources and the message can be intercepted by any receiver around the source.

In the 1960's research first presented optical communications using a guiding material: the optical fiber. With this new technology, optical communication signals can be carried along important distances at low power and addressed to a specific receiver. Since then the development of fibers and devices for optical communications has known a remarkable acceleration and in particular thanks to four milestones:

- The invention of the LASER (in the late 1950's) to generate long range confined light beams.
- The development of low loss optical fibre (1970's) to carry the optical beam with an optimum transmission ratio.
- The invention of the optical fibre amplifier (1980's) to increase the propagation range of optical fiber networks.
- The invention of the in-fibre Bragg grating (1990's) for precise and robust signal sensors.

The exponential increase of fiber-based optical networks has also motivated the research for optical waveguiding at small scale. In particular the discovery of photo-sensitive nonlinear media offers the possibility to investigate optically induced waveguiding structures. Since nearly 50 years, the study and control of the diversity and efficiency of such photo-induced waveguides in nonlinear media have become an important research field for all-optical communications.

Recently the discovery of so-called unconventional beams has introduced a new kick-off in optical physics. The novelty is their shape-preserving propagation and their self-regeneration ability. As they can propagate further and remain unaltered even in presence of obstacles, they enable to deepen the range of optical applications beyond the spatial limitations of conventional beams. One beam type in particular has raised much interest: the *Airy beam*.
Discovered ten years ago, the Airy beam presents, in addition to the shape-preserving and self-healing nature, the unique property to propagate along a parabolic trajectory. The bend propagation of the Airy beam has introduced a new optical wave type, the family of *accelerating beams*. The existence of bending light seems to contradict the fundamental principles of general physics, however these accelerating beams are actually formed by a large number of light rays propagating along different straight trajectories. Therefore the accelerating Airy trajectory owes its curved shape to the summation of all these non-parallel trajectories, called the *caustic* of the accelerating beam.
The introduction of unconventional beams defined by their caustic has opened new research fields and has led to a large number of new applications in optical physics and more generally in wave physics (e.g. plasmonics, electronics).

As introduced previously, an important field of optical physics is the study of optical beams in nonlinear media. During its propagation inside the medium, the optical beam interacts with the matter along its trajectory, which influences its own behavior such as shape and trajectory. Nonlinear photorefractive materials in particular have been extensively studied these last decades, because of their high optical sensitivity and their large applications in particular in all-optical information processing.
So far the state-of-the-art in optical waveguiding physics suggests in particular the use of intense shape-preserving optical beams, called *solitons*, to optically induce guiding structures. Such optical solitons appear in nonlinear media, when the nonlinearity of the medium exactly counterbalances the natural expansion (*diffraction*) of an optical beam to induce a self-focusing effect. To explore the waveguiding possibilities of such conventional soliton-based systems, research has studied their propagation by tuning the nonlinearity of the system and in interaction with multiple solitons. The conventional beam's nature however spatially limits the interconnection range, even for multiple interacting beams.

In this thesis we suggest to study the nonlinear propagation of Airy beams in photorefractive crystals under high-focusing conditions and their waveguiding possibilities. So far the generation and control of Airy beams have been studied in linear media, where the shape-preserving, self-healing and accelerating properties confirm promising applications in spatially long range systems. However, the Airy properties are not maintained under nonlinear focusing conditions. In particular when increasing the focusing nonlinearity, theory predicts the Airy beam to split into a strong off-shooting soliton and a weak accelerating beam.

In a first part (chapters 2 and 3), we experimentally unveil the existence of Airy solitons in high nonlinearity ranges and study their behavior. In particular during the formation of the solitonic structure, we enlighten peculiar spatiotemporal dynamics, where the initial linear Airy beam interacts with the rising solitonic beam. The accelerating feature of the Airy beam suggests an analogy with the gravitational interactions between a mass and a wave propagating in a curved spacetime.

In a second step, we more generally demonstrate the formation of complex waveguiding structures for Airy beams propagating under highly self-focusing conditions in photorefractive media (chapter 4). By tuning the balance between the accelerating and solitonic behavior, we present multiple types of guiding while using a single Airy beam. To enlarge the interconnection range, a second Airy beam is added in the photorefractive crystal with a counterpropagating direction. The accelerating properties of the Airy beams enable to significantly reduce the spatial limitations encountered in conventional all-optical waveguiding systems.

In addition, we show that the stability of a system in nonlinear optics is guaranteed up to a nonlinearity threshold, above which the optical beams begin to spatially evolve along time (chapter 5). As the threshold nonlinearity decreases for longer propagation media where the diffraction is higher, we compare the stability range of the shape-preserving Airy beam to the conventional beam in the counterpropagating configuration. Besides much higher stability range (and therefore guiding strength) of the Airy system, we present peculiar spatiotemporal dynamics above the stability threshold. In particular the beam evolves along spatially organized trajectories, which coincide with the multiple lobes structure of the counterpropagating Airy beam. The spatial control of the Airy beam from a stable dynamics up to a chaotic regime suggests innovative ways of performing optical computing based on spatiotemporal chaos.

Thanks to this thesis of three years we demonstrate that the Airy beam offers promising alternatives in general physics and more specifically in photonics for all-optical routing. The shape-preserving, self-healing and accelerating properties of the Airy beam enable to enlarge the range of optical propagation. In particular thanks to the use of nonlinear media, large curved multi-channel waveguides can be optically induced to interconnect or separate an optical signal into multiple beams. Finally the nonlinear interaction of multiple counterpropagating Airy beams increases the optical interconnection types and range for steady-state or dynamical routing. Therefore the first theoretical and experimental results presented in the following chapters confirm the promising implementation of Airy beams in all-optical computing.

# 1

# INTRODUCTION

This chapter first presents the unconventional self-accelerating wave forms discovered in physics and more recently in optics. Then in a second part we focus on the physics of optical solitons which offers in nonlinear optics interesting all-optical processing solutions. The introduction illustrates the cross-fertilization between two topics : the physics of accelerating Airy beams at the solitonic scale and the applications of nonlinear light propagation.

## 1.1 ACCELERATING BEAMS

### 1.1.1 *Observation in nature*

Light is known to propagate along straight trajectories. However, nature can be misleading, as light beams appear to form curved trajectories. The observation of peculiar curved light shapes in nature has led to the study of a new wave form defined by its caustic.

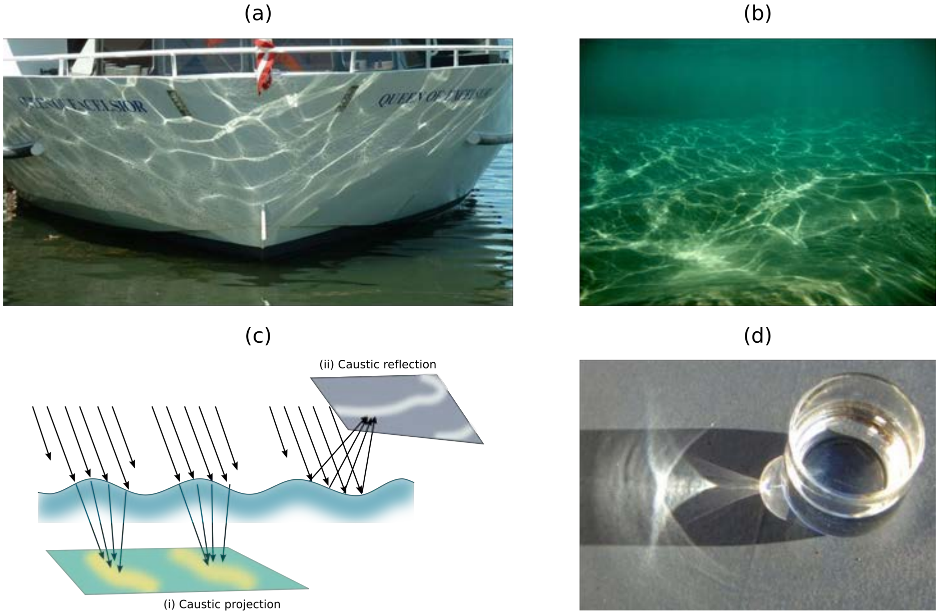

Figure 1.1: (a) Caustic network by reflection created by an undulating water surface. Source: simonhood.org. (b) Caustic network by refraction created by an undulating water surface. Source: sdm.scad.edu. (c) Schematic illustration of the formation of optical caustic networks by (i) refraction or (ii) reflection. Inspired by Ref. [1]. (d) Example of caustics observed through a glass of water.

A caustic is the envelope formed of multiple light rays which have been reflected or refracted by a curved surface or object [1] and their projection on a plane surface displays a so-called caustic network [Figs. 1.1(a)-1.1(d)]. A typical example of optical caustic are the light patterns induced by ripples at the surface of water as depicted on Figures 1.1(a), 1.1(b). When the incident straight propagating light rays reach the water surface, the undulating air-water surface breaks the uniform propagation direction of the light beams [Fig. 1.1(c)]. Because the reflected/transmitted rays do not keep a parallel propagation, their crossing sections appear very bright while the left areas are dark. As a result their incident pattern is not uniform anymore but forms a bright network showing curved light shapes on the projection surface (bottom of the boat in Figure 1.1(a) or of the water in Figure 1.1(b)).

In the case of a glass filled with water displayed on Figure 1.1(d), the light beams falling on the object meet two curved matter interfaces. These non-planar surfaces induce lensing effects and the light rays are diverted from their parallel trajectory to meet along a parabolic-shaped concentration area.

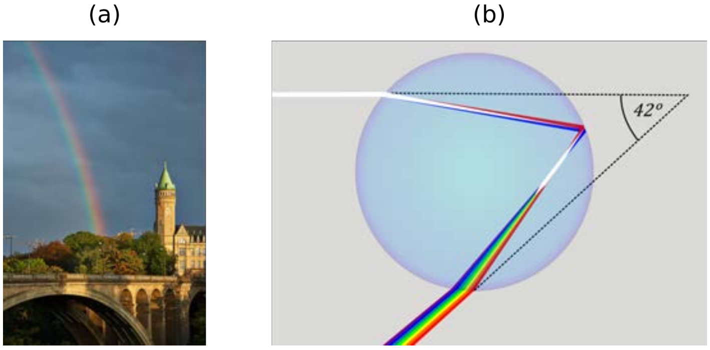

Figure 1.2: (a) Rainbow above the Adolphe bridge in Luxembourg city. Source: Pinterest. (b) Light dispersion and propagation in a raindrop. Source: Wikipedia.

Another example in nature is the rainbow [Fig. 1.2(a)], where the reflection, the refraction and the dispersion of sunlight through the rain drops lead to the formation of a colored spectrum in the sky [Fig. 1.2(b)]. But to understand how each color is so sharp and intense for the observer, the caustic approach needs to be included in a theoretical study. The mathematical formulation and explanation for this phenomenon has been found in the 1820s by the British astronomer and physicist George Biddell Airy who developed the nowadays called Airy function in his early study of optics in physics [2].

Without going into mathematical details about the nature and properties of the Airy function, this function is a solution of the following differential equation:

$$\frac{\partial^2 y}{\partial^2 x} - xy = 0, \tag{1.1}$$

known as the Airy equation or Stokes equation [3], with $x$ and $y$ the spatial transverse and propagation axis. The Airy function enables to explain the caustic observed in rainbows, but until recently the Airy function did not raise much more interest in optical physics.

It was only almost four decades ago that Berry and Balazs have suggested a larger existence field for this function: in the general wave physics. In 1979 the two physicists theoretically predicted in quantum mechanics that the Schrödinger equation describing a free particle can exhibit a non spreading Airy wave packet solution [4] [Eqs. 1.2,1.3] with an Airy function distribution as depicted on Figure 1.3(a). The 1D-solution system is described by the following equations:

$$-\frac{\hbar^2}{2m}\frac{\partial^2\psi}{\partial x^2} = i\hbar\frac{\partial\psi}{\partial t}, \tag{1.2}$$

$$\psi(x,0) = Ai(Bx/\hbar^{2/3}), \tag{1.3}$$

with $\hbar$ the Planck constant, $m$ the mass of the particle, $\psi$ the field envelope, $Ai(x)$ the Airy function, $B$ an arbitrary constant and $x$ the transverse axis. If we consider a one-dimensional wave packet with the probability density distributed along an Airy function in the spatial $x$-direction (as depicted on Figure 1.3(a)), it evolves along time following the equation

$$\psi(x,t) = Ai\left(\frac{B}{\hbar^{2/3}}\left(x^2 - \frac{B^3t^2}{4m^2}\right)\right) e^{iB^3t/2m\hbar\left(x-\left(B^3t^2/6m^2\right)\right)}. \tag{1.4}$$

The equation 1.4 shows a nonlinear propagation, where the probability density distribution shifts along the transverse $x$-axis for increasing time with the velocity $B^3t^2/2m^2$ without additional external forces. However, Berry *et al.* show that quantum wave functions do not correspond to individual classical particles, but to families of particles' orbits. As depicted on the spacetime diagram on Figure 1.3(b), the trajectory lines taken by the Airy wave packet are not parallel but their caustic (orange curve) follows a parabolic acceleration $x \to B^3t^2/2m^2$ along the $x$-axis centered around $t = 0$ [Eqs. 1.3,1.4]. Besides the free acceleration (i.e. without external forces), Berry *et al.* also demonstrated the diffraction-free property of the Airy wave function.

These unique features have motivated research to explore analogies of non spreading accelerating wave propagation in other physical domains such as optics (as we will detail in the following section) and atom physics.

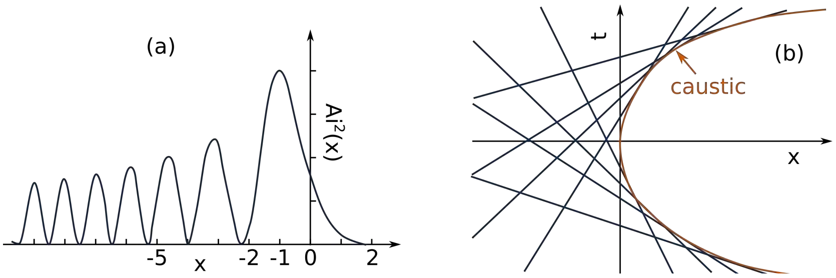

Figure 1.3: Properties of an Airy wave packet in quantum mechanics. (a) Probability density function of the Airy wave packet with $B/\hbar^{2/3} = 1$ [Eq. 1.3]. (b) Parabolic caustic enveloping the straight trajectories of particles in force-free spacetime. Adapted from [4].

### 1.1.2 *Accelerating beams in optics*

In optics, a conventional beam is known to diffract when propagating over a large distance: its size expands and the intensity at the center of the beam decreases over the propagation. For a Gaussian beam the characteristic diffraction-free length is proportional to $\pi\omega_0{}^2/\lambda$, where $\lambda$ is the wavelength and $\omega_0$ the beam waist at its focal point. The diffraction increases when using smaller beam sizes, but many applications, such as in nonlinear optics, colloidal science or biophysics, require small optical rays with as well a long interaction range. Since the discovery of Airy waves in quantum physics being invariant along their propagation [4], research in optics has investigated the analogy in optical beam propagation. Indeed it is well known that the quantum physics and optical physics are governed by mathematically equivalent mechanisms [5]: the quantum mechanical equation for the first and the paraxial propagation equation of diffraction for the second case.

In 1987 Durnin *et. al.* first theoretically and experimentally demonstrated the existence of shape-preserving optical beams [6, 7]: the Bessel beam whose amplitude is defined by the zero-order Bessel function of the first order. Figure 1.4(a) compares the intensity shape of a Bessel beam (solid curve) with a Gaussian one along a free space propagation of $z = 100$ cm. The shape of the Bessel beam appears to be invariant all along while the Gaussian beam has spread and its intensity maximum at $z = 100$ cm has decreased down to less than 0.025% of the initial value. The originality of Durnin's experiment is the generation method for the Bessel beam as the latter is a superposition of confocal planar waves. As

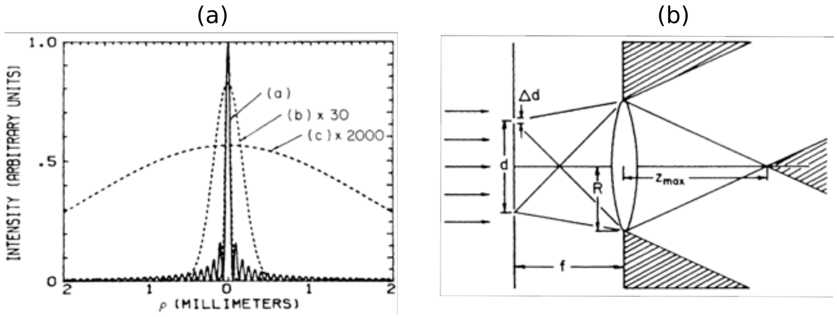

Figure 1.4: Experimental zero-order Bessel beam. (a) Transverse intensity profiles of a diffraction-free Bessel beam (plane curve) and a diffracting Gaussian beam (dashed curves) with the same initial spot size ($FWHM = 70$ µm, $\lambda = 632.8$ nm) along their $z$-propagation (a: $z = 0$, b: $z = 10$cm, c: $z = 100$ cm). (b) Experimental arrangement for the creation of a Bessel beam. Extracted from [6].

a matter of fact the two-dimensional zero-order Bessel beam is composed of concentric rings with increasing radii (see the transverse intensity profile on Figure 1.4(a)). Such an intensity distribution can be shaped using the interference pattern of two spheric waves and a lens placed at the focal distance [Fig. 1.4(b)]. To that aim Durnin *et al.* used a planar wave propagating through two circular slits, with $\Delta d$ each diameter and $d$ the separation distance between both slits. The lens then transforms the circular interference pattern growing over the propagation into a shape preserving interference pattern of a conical superposition of planar waves. The dashed zones indicates the shadow areas, i.e. where no light propagates, and $z_{max}$ defines the propagation distance of an effective experimental Bessel beam. Later other generation methods have been suggested and in particular the use of an axicon enables to transform a planar wave into a Bessel beam (with the same existence area as for the Durnin method) [8].

This result has raised much interest in optical research and led to the discovery of other propagation-invariant beams [9–11] [Figs. 1.5(a), 1.5(b)]. While these beams present very different intensity shapes, they are all formed by a conical superposition of planar waves and their caustic defines the beam type (see the Bessel beam [Fig. 1.5(a)] and the Mathieu beam [Fig. 1.5(b)]). As these caustics are formed by planar waves, they owe their peculiar features to them. The shape invariance of planar beams induces a diffraction-free caustic wave form, which grants the family of beams defined by their caustic the name of "shape-

preserving beams".
In addition the shape-preserving beam is able to regenerate itself after passing an obstacle, as the intensity distribution induced at $z$ and $z + \delta z$ are formed by different regions of the crossing planar beams [Fig. 1.5(c)]. The regeneration distance of the beam depends on the size of the obstacle and the angle defining the conical superposition of the planar beams.
Finally these beams also carry infinite power, as they are formed by planar waves (which ideally contain an infinite power). While this last property could be questioned (the initial optical beam is truncated [Fig. 1.4(b)]), the finite energy induced by the aperture does not affect the ideal shape-preserving property over a large distance.

### 1.1.3 *Applications in optics*

The discovery of beams that not only propagate diffraction-free, but also present a self-healing ability has raised much interest since almost two decades and suggested many technical as well as physical applications in particular in biomedical physics, laser processing and metrology [12].

If we consider in particular the evolution of optical tweezers since their introduction in 1986 [14], they have become one of the core research field with applications in biology, physical chemistry, and soft condensed matter physics [13]. As depicted on Figure 1.6(a), the idea is to use a strongly focused beam to trap particles near the focal point. By creating a strong intensity gradient using a converging beam, small objects, such as a colloidal particle, are drawn towards the focused region. For lower intensity gradient, the radiation pressure of the optical beam tends to blow down the particle. Because the optical tweezing is effective in the optically high-focused region, its trapping effect depends on the spatial focusing range of the optical system. In the case of a Gaussian-based system, the particle is trapped in three dimensions near the focal point [Fig. 1.6(b1)]. By taking advantage of the shape-preserving property of Bessel beams for example, the focused trapping zone is enlarged along the propagation direction $z$ [Fig. 1.6(b2)]. By its shape-preserving and self-healing properties, the Bessel beam increases the manipulation range and enables the manipulation of ensembles of particles simultaneously in multiple planes [15].
The unique propagation and shape properties of accelerating beams has opened

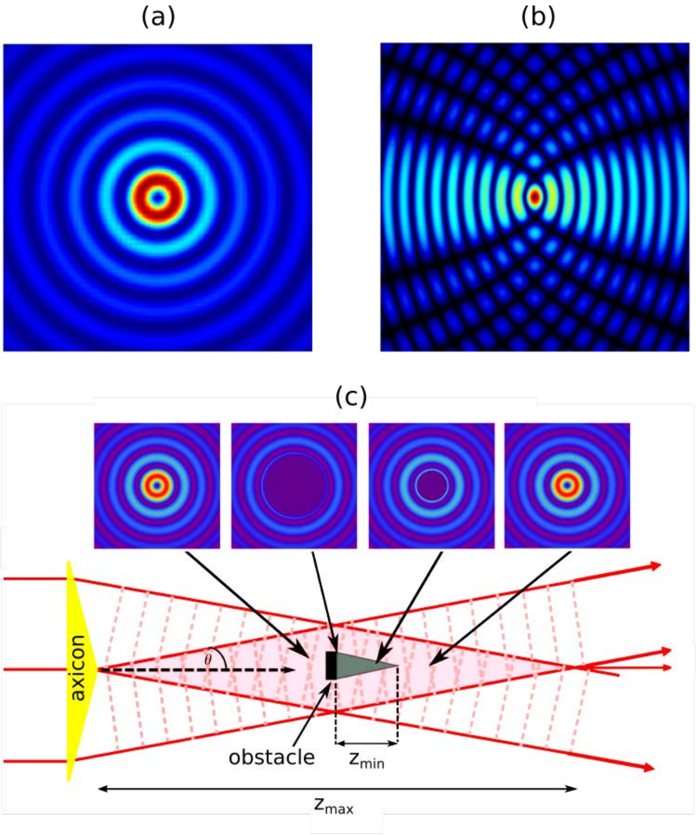

Figure 1.5: Example of diffraction-free propagating beams. Intensity distribution of (a) a Bessel beam and (b) a Mathieu beam. (c) Self-healing property of an axicon-generated Bessel beam: an obstacle placed in the center of the Bessel region (black rectangle) obstructs the beam for a minimum distance, $zmin$ (grey triangle), after which the Bessel field reforms. The insets display the expected image of the beam at four different planes [8].

a large variety of applications in many fields, however one wave function remained unresolved: the Airy function.

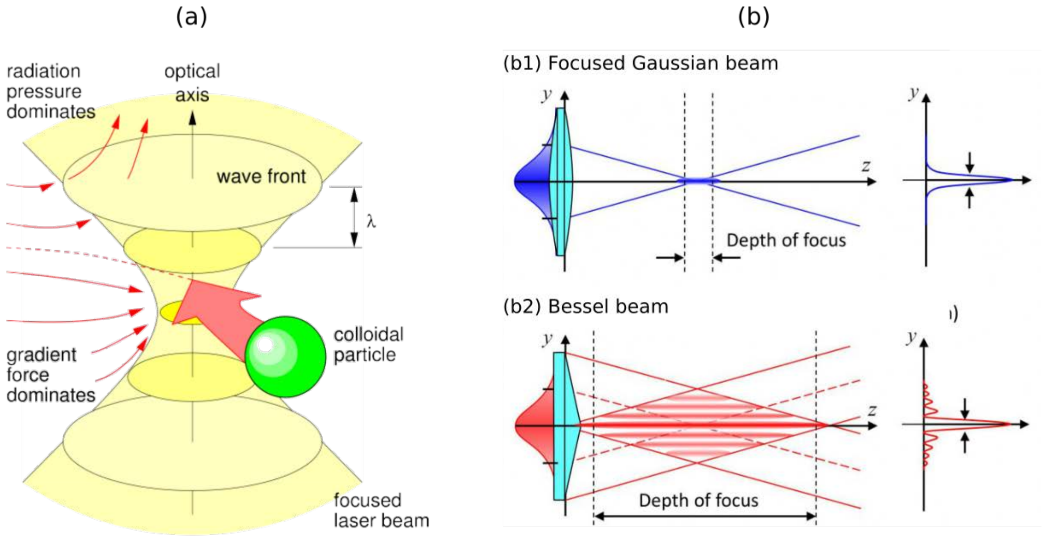
(a)
radiation pressure dominates
optical axis
wave front
λ
gradient force dominates
colloidal particle
focused laser beam
(b)
(b1) Focused Gaussian beam
y
z
y
Depth of focus
(b2) Bessel beam
y
z
y
Depth of focus

Figure 1.6: Optical tweezers. (a) Schematic layout of the mechanisms [13]. (b) Comparison between the Gaussian- and Bessel-based focused regimes. Source: obel.ee.uwa.edu.au.

### 1.1.4 *Airy beams*

#### *Optical Airy properties*

First discovered in quantum mechanics [4], the Airy wave packet has been suggested as a non-spreading and self-healing solution of the Schrödinger equation with a parabolic propagation (see Section 1.1). In 2007 Christodoulides *et al.* suggested the existence of optical Airy beams presenting the same properties as the Airy wave packet in quantum mechanics: shape-preserving propagation and parabolic acceleration [16]. However, the Airy distribution theoretically contains an infinite energy, which can not be obtained in optics. As for other shape-preserving optical beams, Christodoulides *et al.* considered a truncated form of the Airy function with finite energy to overcome this obstacle. The mathematical solution is an association of the Airy function with an exponential decay function:

$$\psi\left(s,\xi=0\right)=\mathrm{Ai}\left(s\right)\exp\left(as\right), \tag{1.5}$$

where $s=x/x_A$ is the normalized transverse dimension, $x_A$ the arbitrary transverse Airy scale, $\xi=z/kx_A{}^2$ the normalized propagation direction and $a>0$ the exponential truncation factor. As depicted on Figure 1.7, the exponential decay function truncates the tail of the Airy distribution along the higher lobe orders. The first lobe with the maximum peak at $x/x_A = -1$ is defined as the main lobe.

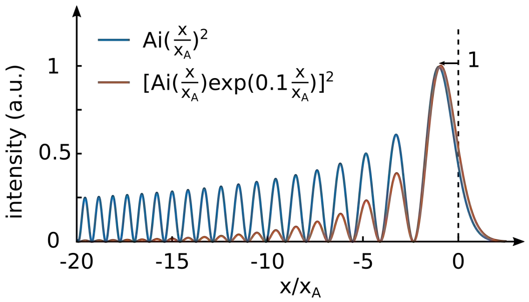

Figure 1.7: Truncation of the Airy. Intensity profiles of an ideal Airy beam (infinite energy, blue line) and a truncated Airy beam with $a = 0.1$ (finite energy, orange line).

Figures 1.8(a) and 1.8(b) display the propagation along the $z$-axis of an ideal infinite-energy Airy beam ($a = 0$) and with a truncated Airy beam ($a = 0.05$) respectively. The comparison shows that the finite-energy Airy beam (one-dimensional as well as two-dimensional) can retain its intensity features over several diffraction lengths and can still accelerate in the transverse $x$-direction. If we focus on the evolution of the transverse intensity distribution along $z$ of the truncated Airy beam, it has been shown that the beam's deterioration starts first at the higher lobes orders as the truncation starts at the tail of the beam [Figs. 1.8(c), 1.8(d)]. The Airy beam displayed in this example is defined by $x_A = 100$ μm, $a = 0.1$, $\lambda = 0.5$ μm and propagates in free space along 1.25 m. As a comparison with Figs. 1.8(a) and 1.8(b), a deflection of $x = 2$ mm corresponds to $s(x_A = 100\ \mu m) = 20$ and $\xi(z = 1.25m) = 10$.

As a truncated solution of the ideal Airy waveform, the optical Airy beam has the advantage of combining the parabolic trajectory and self-healing properties of the Airy wave solution over a finite distance with the diffractive beam properties for larger propagation distances.
As for other shape preserving beams defined by their caustics, the Airy beam is able to regenerate itself after passing an obstacle. If we consider the caustic of the Airy wave form studied by Berry *et al.* in 1979 [Fig. 1.3], the propagation lines of the particles are not parallel. In optics the parabolic caustic of the Airy

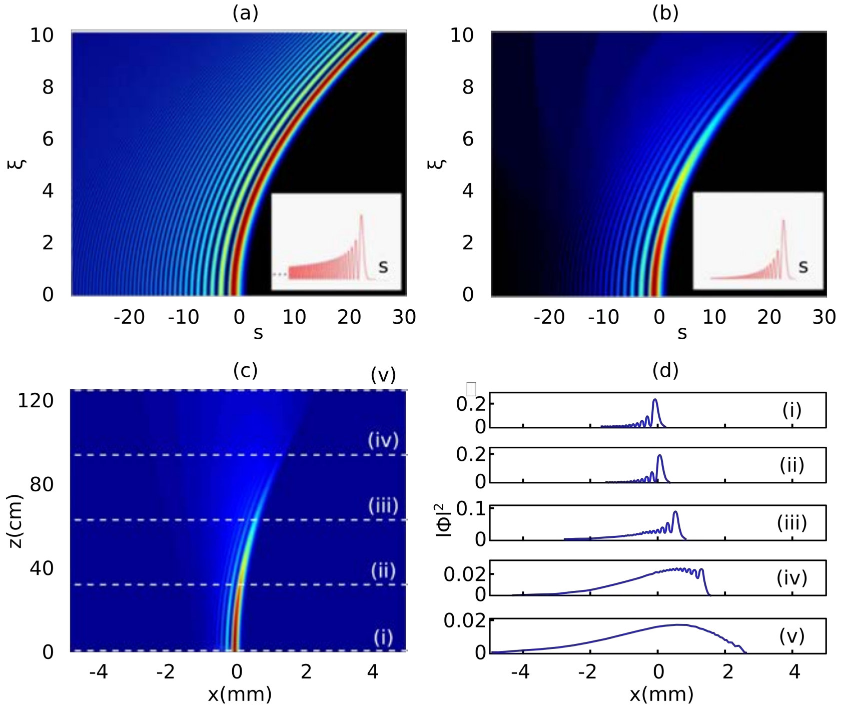

Figure 1.8: Optical Airy beam. Propagation dynamics of (a) a diffraction-free Airy wave and (b) a finite-energy Airy packet when $a = 0.05$. The corresponding input intensities of these beams are shown in the insets. Extracted from [17], with $s = x/x_A$ and $\xi = z/kx_A{}^2$ the normalized transverse and longitudinal dimensions. (c) Propagation dynamics of a finite energy Airy beam as a function of distance. (d) Cross- sections of the normalized beam intensity at (i) z=0 cm, (ii) 31.4 cm, (iii) 62.8 cm, (iv) 94.3 cm, and (v) 125.7 cm. Extracted from [16].

beam is also formed by non parallel trajectory lines, meaning that the photons shaping the main lobe at $z = 0$ and at $z > 0$ are not strictly the same. As shown on Figure 1.9(a), the trajectory lines of the Airy caustic are not a conical superposition of multiple plane waves as in the case of Bessel beams. The individual slopes of each straight trajectory (related to the transverse $x$-axis) decrease for the higher Airy lobe orders. As a consequence, when an obstacle is placed at the initial main lobe's position as depicted on Figure 1.9, Christodoulides *et al.* demonstrated that after $z = 11$ cm the beam starts reforming until $z = 30$ cm, where the Airy beam is completely regenerated [18].

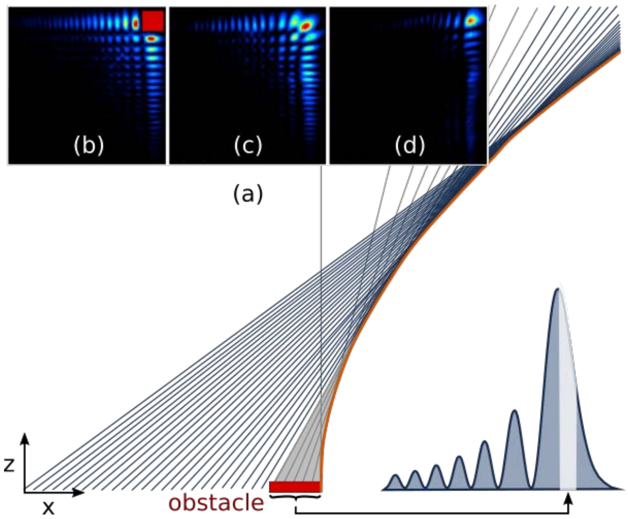

Figure 1.9: Propagation properties of Airy beams. (a) Schematic caustic and intensity profile of the Airy beam, displaying self-healing ability. The gbolic acceleration of the wave form is displayed by the orange line. (b)-(d) Intensity distribution of an 2D-Airy beam with the main lobe initially obstructed ($x_A = 77$ µm) at (b) $z = 0$ cm, (c) $z = 11$ cm and (d) $z = 30$ cm. Adapted from [18].

### *Airy generation methods*

The discovery of an optical finite energy Airy beam solution has encouraged various generation methods. As we will detail in the next paragraphs, an Airy beam can be generated using a conventional Gaussian laser beam which is then spatially modulated. In this section we will focus on the two most widely spread solutions: the SLM-based method (Spatial Light Modulator) and the modulation using asymmetric nonlinear photonic crystals.

### MODULATION USING A SPATIAL LIGHT MODULATOR (SLM)

In 2007, Christodoulides *et al.* have generated the first optical Airy beam in one as well as in two dimensions [Fig. 1.10(b)] using a spatial light modulator (SLM) [17]. The genuine idea is to generate the truncated Airy beam $\mathtt{Ai}(\frac{x}{x_A})\mathtt{exp}(a\frac{x}{x_A})$ in the $k$-space, as the Fourier transform in the $k$-space of an infinite Airy beam is a cubic exponential $\mathcal{TF}\left(\mathtt{Ai}(\frac{x}{x_A})\right) \propto \mathtt{exp}(ik^3/3)$. Therefore, the Fourier transform of the truncated Airy beam, $\psi(k)$, is a Gaussian beam modulated with a cubic phase in Fourier space:

$$\psi(k) \propto \exp\left(-ak^2\right) \exp\left(ik^3/3\right) . \tag{1.6}$$

As shown in equation 1.6, the Fourier transform of the truncated Airy beam is proportional to the product of the Fourier transform of a Gaussian beam and an exponential with cubic phase, which is the Fourier transform of the mathematical Airy function. An optical Airy beam can therefore be generated from a broad Gaussian beam first modulated with a cubic phase then Fourier transformed.

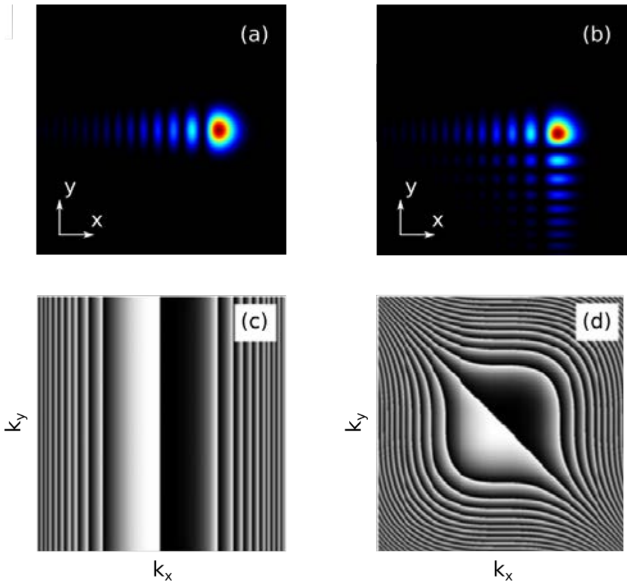

Figure 1.10: Airy beam generation using a spatial light modulator. Intensity distribution of a (a) 1D-Airy beam and (b) 2D-Airy beam. Phase mask on the spatial light modulator for the generation of (c) 1D-Airy beams and (d) 2D-Airy beams [17].

The cubic phase modulation is induced via the SLM on which a 1D- or 2-cubic phase modulation is applied for a 1D- or 2D-Airy beam. The cubic phase pattern is displayed on Figure 1.10(c) for the one-dimensional as well as the two-dimensional case on Figure 1.10(d), which is the summation of a cubic phase modulation along both orthogonal transverse $x$- and $y$-axes. Then to apply a Fourier transformation on the modulated optical beam, a converging lens is placed after the SLM-modulation at the focal distance $f$ as depicted on Figure

1.11. Finally the Airy beam, whose initial intensity distribution is defined in equation 1.5, starts its propagation at the distance $f$ after the Fourier-Transform-lens.

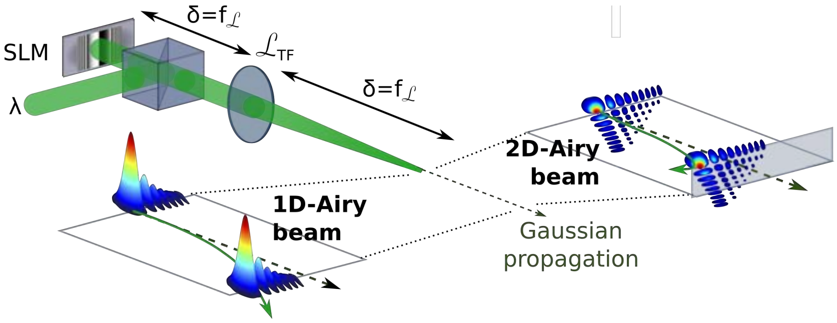

Figure 1.11: Experimental setup to generate 1D- or 2D-Airy beams using a SLM-modulation in Fourier space.

The experimental results are in agreement with the theoretical predictions, as the generated Airy beam propagates along a parabolic accelerating trajectory. In the 2D-case, the acceleration rate of the Airy beam is higher than for the one-dimensional case, because the acceleration is along both transverse dimension, $x$ and $y$:

$$\overrightarrow{\mathrm{acceleration}_{1D}} = \frac{z^2}{4k^2{x_A}^3}\vec{x}, \tag{1.7}$$

$$\overrightarrow{\mathrm{acceleration}_{2D}} = \frac{z^2}{4k^2{x_A}^3}\vec{x} + \frac{z^2}{4k^2{x_A}^3}\vec{y}, \tag{1.8}$$

$$|\,\overrightarrow{\mathrm{acceleration}_{1D}}\,| = \frac{z^2}{4k^2{x_A}^3}, \tag{1.9}$$

$$|\,\overrightarrow{\mathrm{acceleration}_{2D}}\,| = \sqrt{2}\frac{z^2}{4k^2{x_A}^3}. \tag{1.10}$$

As illustrated by these equations and experimentally confirmed, the acceleration depends on the optical wavelength (through $k$) and mainly on the Airy beam's size (characterized by $x_A$). Thanks to the use of an SLM, this modulation technique offers an instantly and precise external tuning tool as demonstrated by Morris *et al.* [19]. They presented the mathematical link between the desired Airy parameters ($a$, $x_A$) and the system's range (Gaussian waist $\omega_0$, Fourier lens $f$) through the SLM-modulation. Thanks to these results, it facilitates the setup

of an Airy beam experiment aiming peculiar applications, which require specific beam's features (e.g. size).
The ballistic behavior described above defines an Airy beam launched parallel to the propagation $z$-axis, when all the opto-mechanical components are perfectly aligned. However, the accelerating properties of the beam can be also tuned by misaligning the Fourier lens or the SLM in the transverse $x, y$-plane to mimic the ballistic dynamics of projectiles moving under the action of gravity [20, 21].

### Modulation using an asymmetric nonlinear photonic crystal

Besides the SLM-based modulation technique introduced by Christodoulides *et al.*, an other Airy generation method has been suggested. In 2009 Arie *et al.* suggested the nonlinear modulation via three-wave mixing processes taking place in an asymmetrically modulated quadratic optical media. In reference [22], they induce a two-dimensional poling of a quadratic medium with the following space-dependent quadratic nonlinear coefficient:

$$\chi^{(2)}(x, y) = d_{ij} \mathrm{sign}\left(\cos\left(2\pi f_x x + f_c y^3\right)\right), \tag{1.11}$$

where $d_{ij}$ is an element of the quadratic susceptibility $\chi^{(2)}$ tensor, $f_x$ is the spatial frequency of the modulation in the beam's propagation $x$-direction and $f_c$ represents the strength of the cubic modulation in the transverse $y$-direction. As depicted on Figure 1.12, a Gaussian pump beam is injected in the crystal along the $x$-direction. Through the asymmetric nonlinear photonic structure the beam is converted to a second-harmonic Airy beam (in the $k$-space). As for the SLM-modulation process, a converging lens is then placed at the output of the photonic crystal to perform a Fourier transform.

To control the free space propagation of the generated Airy beam, various external parameters of the systems can be considered. The idea is to change the quasi-phase matching conditions, by tuning the crystal temperature or pump wavelength, which alters the location of the Airy beam peak intensity along the same curved trajectory. Shortly after, the group has also shown that these tuning parameters can be adjusted to switch the acceleration direction of the Airy beam [23, 24].
This second method therefore offers an interesting alternative for the Airy generation with all-optical control of the Airy features. The advantage of this Airy

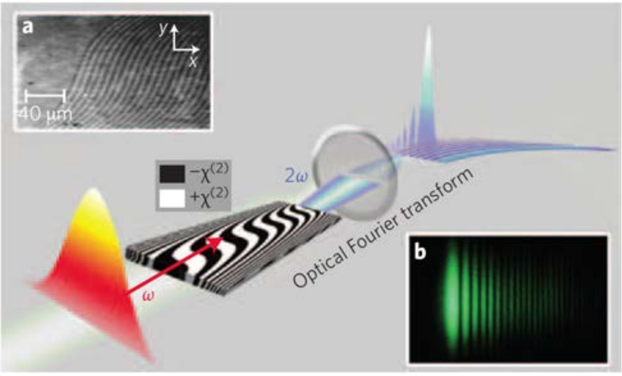

Figure 1.12: (a) Microscope photograph of the quadratic crystal, after selective etching (which reveals the inverted domain pattern). The $x$- and $y$-axes were rescaled for viewing purposes and are not comparable. (b), Profile photograph of the green second-harmonic Airy beam. Extracted from [22].

generation technique is the ability to create Airy beams at new wavelengths and high intensities that are not supported by the SLM-method (maximum intensity around $1\ W/cm^2$).

Quickly after the beam's ballistics and shape-preserving features have been confirmed [18–20], the general study of diffraction-free and self-accelerating beams has experienced an rising interest. Besides the two generation methods presented previously, other techniques have also been suggested using various electro-optical tools such as liquid crystal displays [25], a diffraction grating [26] or a waveguide array [27]. However, the most commonly used techniques are the SLM-based method and the use of quadratic nonlinear crystals.
For our experimental work in the next chapters we chose the SLM-based generation method, because the optical power needed is low (max $100\ \mu W$ at the entrance of the crystal) and because of the easy control and the tuning precision offered by the SLM.

### *Applications*

The discovery of the parabolic accelerating Airy beam has opened a new optical wave type, the non-paraxial accelerating waves. Their existence have been theoretically and experimentally demonstrated [28–30] and has led to numerous applications. Among others we can cite optical micromanipulation of particles [31],

where the large Airy shape and its parabolic propagation enables optical path clearing of particles in suspension in turbid medium with higher performances and efficiency [Fig. 1.13(a)]. In laser processing the non-diffracting propagation offers a larger depth and precision for micromachining various materia and the non-paraxial beam trajectory enables smooth curved sculpting of material edges as depicted on Figure 1.13(b) [32–34].
In biomedical physics Airy beams have also suggested interesting applications such as in light-sheet microscopy, which facilitates rapid, high-contrast, volumetric imaging with minimal sample exposure [35]. Figure 1.13(c) illustrates a light-sheet microscopy scan of a juvenile amphioxus and compares two volumetric images acquired using Gaussian (upper images) and Airy (images below) illumination beams. By this study, Vettenburg *et al.* show that the diffraction-free Airy beam yields high contrast and resolution up to a tenfold larger field of view contrary to the conventional Gaussian physics undergoing rapid divergence.

In optical routing several application fields have already been explored such as in all-optical communications to induce switches using the accelerating property of Airy beams [36] or for information encoding in linear media [37]. Finally other research areas have also studied the unique properties of these accelerating beams such as in plasmonic, including plasmonic circuitry [38] and surface tweezers using Airy plasmons [39, 40]. These promising results have suggested to enlarge the optical applications also to the electronic domain for steering electronic wave packets like their photonic counterparts [41].

In the previous section, we have presented a new family of optical non conventional beams with peculiar properties in free space (diffraction-free, self-healing and non-paraxial propagation, see Section 1.1). A large number of applications suggested in sections 1.1.3 and D.2 deal with the nonlinear propagation of optical accelerating beams in various nonlinear materials. Nonlinear optics is the study of phenomena that occur when the optical properties of a material are modified by light. Different mechanisms can occur depending on the material type. In this thesis we will focus on photorefractive materials and in particular on the propagation of Airy beams under increasing self-focusing nonlinearity.

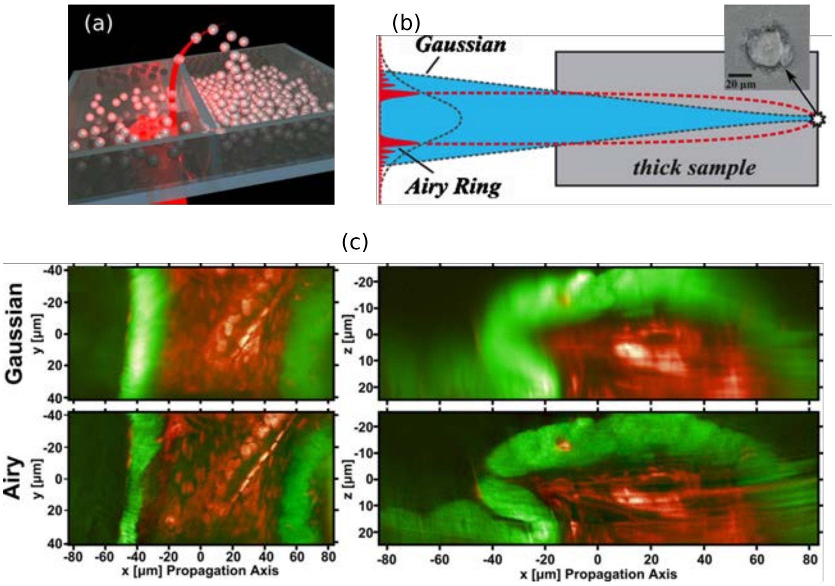
(a)
(b)
Gaussian
Airy Ring
thick sample
20 µm
(c)
Gaussian
Airy
y [µm]
z [µm]
-40
-20
0
20
40
-20
-10
0
10
20
-80
-60
-40
-20
0
20
40
60
80
x [µm] Propagation Axis

Figure 1.13: Examples of applications of Airy beams: (a) for micromanipulation [31], (b) laser processing [33] and (c) light-sheet microscopy [35].

## 1.2 PHOTOREFRACTIVE EFFECT

The photorefractive effect is a nonlinear process where light induces a charge transport in an electro-optic material. Through several effects, as described in Section 1.2.1, the non uniform illumination of such a material leads to a non uniform variation of the refractive index structure inside the crystal: this effect is called the "photorefractive" effect.

The photorefractive effect has been discovered in 1966 by Ashkin *et al.* in lithium niobate ($LiNbO_3$) and lithium tantalate ($LiTaO_3$), where they considered this effect as "optical damage": the quality of the phase-matching second harmonic generation they were studying was reduced by the inhomogeneous refractive index structure photoinduced [42]. In particular they discovered that this degradation occurs when the beam is linearly polarized in the c-axis direction (extraordinary ray), while a beam perpendicularly polarized undergoes conventional diffraction. Nevertheless this damage has quickly turned into an interesting electro-optic feature, as two years later Chen *et al.* suggested photorefractive crystals as storage media for optical holography [43]. The holograms can be photoinduced as a refractive index structure written in the three dimensions of the crystal without any processing. Thanks to the high diffraction efficiency and the easy erasability of the refractive index structure, the photorefractive crystal appears as an ideal tool for dynamic data storage. As this physical process appears for very low optical powers (μW), photorefractive media have become very attractive and their physical mechanisms have been extensively explored. A variety of materials have been explored such as inorganic insulators (e.g. Strontium-Barium Niobate (SBN), Barium Titanate ($BaTiO_3$) crystals), semiconductors (e.g. Indium phosphide (InP) or Cadmium telluride (CdTe) crystals) and also organic compounds [44].

### 1.2.1 *Physical mechanisms*

The conventional photorefractive effect is observed in dielectric or semiconductor material. Many models have been suggested to describe the physical mechanisms since 1969 , but the most widely accepted nowadays is the band transport model of Kukhtarev [45]. While the first physical model considered the photorefractive effect as the result of a general redistribution of trapped charge under nonuniform illumination [42, 46], the Kukhtarev model presents a detailed band conduction model taking into account charge transport, static electric fields, electro-optic index modulation. The photorefractive effect can be described as a sequence of three processes for the charge carriers:

- Photo-excitation of free charge carriers,
- Transport of the free charge carriers due to diffusion, electric forces (drift effect), and photovoltaïc effect,
- Recombination of the excited charge carriers (electron or holes) into a trapped state.

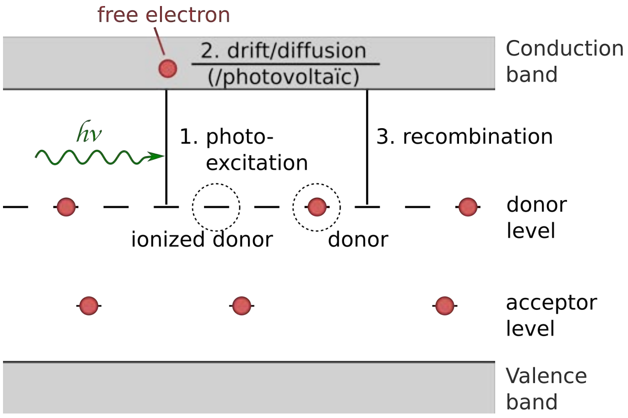

Figure 1.14: Schematic overview of the Kukhtarev band conduction model [45].

Figure 1.14 depicts the schematic photorefractive process of the Kukhtarev's model [45]. When an optical field with enough energy is injected inside the photorefractive crystal, the photoionization promotes the photo-excitation of the free carriers (for example electrons) from their initial filled donor sites ($N_D$ being the initial density) and their migration to the conduction band. As the non-ionized donors contain a negative charge, we add in the model acceptors (density $N_A$) with a positive ionized charge to maintain the electrical neutrality of the medium. These acceptors however do not play any direct role in the photorefractive process in our model. The ionized donors then become empty trap sites ($N_{D^+}$). Then the charges, with density $n$ and mobility $\mu$, diffuse (under random thermal influence) or move under the drift effect (when a bias electric field $E_0$ is applied) or under the photovoltaïc effect through the crystal. At their new position, the mobile charges will then fill empty sites to recombine into a relaxed state.

The charge gradient created results in a space charge field which modulates the refractive index via the linear electro-optic effect. This last process is called the Pockels effect and will be discussed further in this section.

To mathematically model the photorefractive effect, we consider the equations describing the charge transport when an electro-optical field is applied on the medium [47].
The evolution of the production of free carriers $N_{D^+}$ is the difference between those generated by photoionization and by thermal ionization and those trapped [Eq. 1.12]. The charge transport induces a current density $J$ resulting from the diffusion effect $j_{diff}$ and from the drift effect, $j_{drift}$ proportional to the total electric field, along the photorefractive $x$-axis (in the case of the crystals we study the photovoltaïc effect can be neglected $j_{pv} = -\beta I$) [Eq. 1.13]. Equation 1.14 ensures by continuity the conservation of charges in the system. Finally the interactions of carriers with each other and with an external electric field are described through the Maxwell equation 1.15.

$$\frac{\partial N_{D^+}}{\partial t} = (N_D - N_{D^+})(sI + \beta) - \gamma N_{D^+} n, \tag{1.12}$$

$$J = ne\mu E + \mu k_B T \frac{\partial n}{\partial x} + J_{pv}, \tag{1.13}$$

$$\frac{\partial n}{\partial t} = \frac{\partial N_{D^+}}{\partial t} + \frac{\partial}{\partial x}\left(\mu k_B T \frac{\partial n}{\partial x} + \mu n E\right), \tag{1.14}$$

$$\epsilon_{eff}\epsilon_0 \frac{\partial E}{\partial x} = -e\,(N_{D^+} - N_A - n), \tag{1.15}$$

where

| | | | |
|---|---|---|---|
| $E$ | electric field | $\beta_0$ | probability rate of thermal excitation |
| $I$ | light intensity | $\gamma$ | recombination constant |
| $J$ | current density | $\mu$ | mobility |
| $n$ | free electron number density | $s$ | photoexcitation constant |
| $N_A$ | density of acceptors | $\epsilon_{eff}$ | effective static dielectric constant |
| $N_D$ | total density of donors | $\epsilon_0$ | permittivity of free air |
| $N_{D^+}$ | density of ionized donors | | |

The four equations Eqs. 1.12-1.15 are referred to as the fundamental equations of the Kukhtarev's model.

We will now detail the mechanisms induced by the Pockels effect, i.e. the influence of the optical field on the refractive index structure inside the crystal.

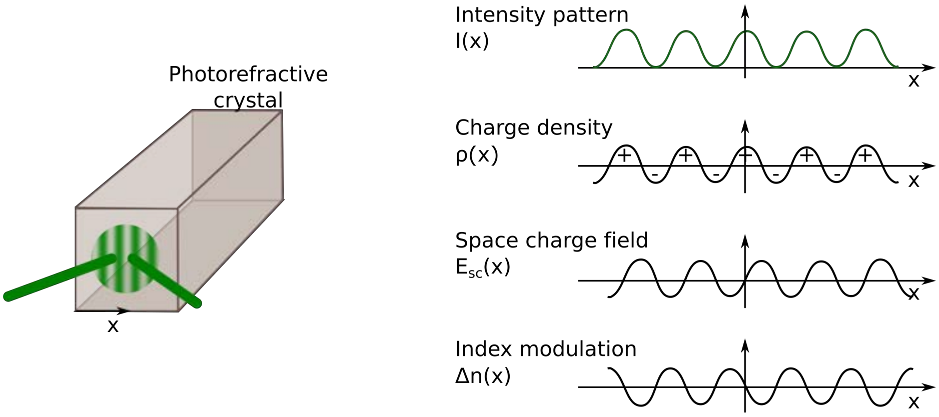

Figure 1.15: Photorefractive effect illustrated with two coherent laser beams injected in a crystal: schematic overview and transverse distribution of the different physical parameters from the optical intensity to the refractive index variation.

Let us consider a non uniform optical illumination on the photorefractive medium. We launch a sinusoïdal optical pattern induced for example by the intersection of two mutually coherent laser beams with their total intensity $I_0 = I_1 + I_2$ [Fig. 1.15]. Their interference pattern is equal to $I = I_0(1 + m * \cos(\phi x))$, with $m = \sqrt{I_1 I_2}/I_0$ the modulation depth and $\phi$ the spatial frequency of the interference grating. The total electric field $E$ is the sum of the externally applied electric field $E_e$ and the photoinduced space charge field $E_{sc}$. Through the Pockels effect the space charge field linearly induces a refractive index variation as follows:

$$\Delta n = \pm \frac{{n_0}^3}{2} r_{eff}(E), \tag{1.16}$$

with $n_0$ the linear refractive index value of the photorefractive crystal, $r_{eff}$ the electro-optical coefficient of the material and the sign ± depends on the polarization of the optical field. The electro-optical coefficient $r_{eff}$ is unique for each material composition and depends on the optical beam's parameters (propagation direction, polarization, wavelength). In the typical case of a SBN-crystal (Strontium-Baryium-Niobate), the highest electro-optical coefficient $r_{eff,max}$ is $r_{33} = 235pm/V$, with $\lambda = 532nm$, considering a horizontal polarization and the propagation direction perpendicular to the c-axis.

Figure 1.15 illustrates the mechanisms leading to an optically induced refractive index variation. The sinusoidal optical interference pattern formed by the two incident beams induces a charge transport and the gradient of charges leads to a space charge field $E_{sc}$ out-of-phase with the optical intensity. Through the Pockels effect the refractive index is modulated according to the induced space charge field. An additional external bias electric field enables to realign the refractive index structure and the illumination pattern.

The refractive index distribution can be engineered by reshaping the optical beam's intensity at the entry of the crystal. As propagation of light depends on the refractive index structure of its propagation medium, its trajectory and shape will be altered and then modify again the propagation structure. This beam-matter-interaction has been extensively studied since the 1970's and suggested a large number of applications as detailed below.

### 1.2.2 *Optical applications*

Photorefractive media are therefore a promising candidate for optical information processing because of their unique properties for low optical power. Besides the first suggested application, volume holographic data storage [49], their massive storage capacity and real-time response have led to applications in optical amplifiers [50] and phase conjugation [51]. More recently the physics of optical tweezers has also raised much interest using such media to trap matter [52].

In addition photorefractive crystals have been studied for all-optical processing and computing such as data storage through pattern formations [53, 54], image processing, optical interconnects [55] and neural networks [56]. As the space charge field induced by the propagating light beam can be controlled via an external bias electric field, the natural diffraction of the beam can be erased leading to the formation of so-called optical spatial solitons [79, 80]. As we will see in the next section, the shape-preserving propagation of these beams in nonlinear media has led to a precise and dynamic solution for efficient real-time all-optical communications.

## 1.3 PROPAGATION OF SOLITONS

In this section we will introduce the soliton, a nonlinear self-trapped wave packet. The first soliton, or solitary wave, has been observed in 1834 by the engineer Scott Russel on the Union Canal near Edinburgh. He observed a boat pulled by horses forming a wave on the water. As the horses and the boat stopped, this wave continued propagating *"at great velocity, assuming the form of a large solitary elevation, a well-defined heap of water which continued its course along the channel apparently without change of form or diminution of speed"* [57]. As we will see in the following sections, this phenomenon has also been observed afterwards for other wave types and in particular in optics.

### 1.3.1 *Observation in the nature*

The propagation of solitary waves have been observed in various media. After the discovery of Russell in 1834 [Fig. 1.16(a)], other singular water waves have been observed. Called tidal bore nowadays, these singular waves are the consequence of the tidal force exerted on shallow water surfaces. The wave of water then travels up a river or narrow bay against the direction of the river or bay's current over several kilometers.

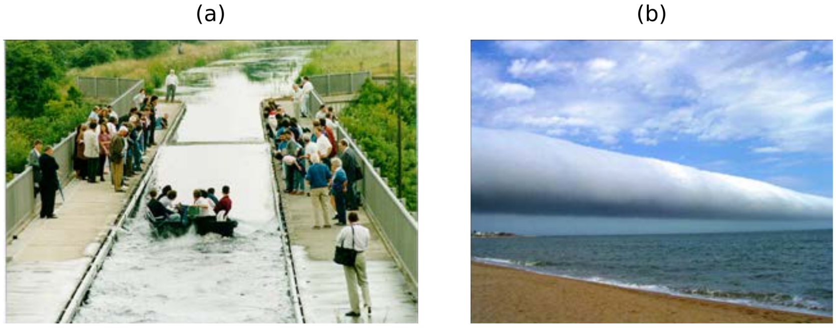

Figure 1.16: Observation of solitons in nature. (a) Soliton on the Scott Russell Aqueduct on the Union Canal near Heriot-Watt University, 12 July 1995 (reproduction of the observation of Russell in 1834 [57]). Source: ma.hw.ac.uk. (b) Coastal roll cloud in Uruguay. Source: Wikipedia.

As depicted on Figure 1.16(b), the atmospheric convection also offers its soliton type: roll clouds. These low, horizontal, tube-shaped clouds appear very

rarely and propagate rolling around a horizontal axis, separated from other clouds.
The presence of sustainable and high energetic waves has raised curiosity since their discovery, but as they where in contradiction with the theoretical models, one had to wait the development of computer-based modeling in the 1960s.

### 1.3.2 *Theoretical mechanisms*

After the discovery of the solitary wave by Russell in 1834, the study of solitons did not progress for more than one century until 1965, when Zabusky *et al.* first demonstrated soliton behavior in media subject to the Korteweg–de Vries equation using a finite difference approach [58]. The Korteweg-de Vries equation has been developed in 1895 by the mathematician Diederik Korteweg and Gustav de Vries to mathematically model waves on shallow water surfaces and includes solitary wave among the solutions [59].

Usually a single wave undergoes dispersion along its trajectory. It is formed by the infinite superposition of harmonic waves (a wave packet), each propagating at a different velocity. Along the propagation the wave packet tends to crush while broadening (i.e. dispersion effect). But when propagating in a shallow canal, the relative depth varies significantly which increases the group velocity ($v = \sqrt{gh}$, with $v$ the velocity, $g$ the g-force and $h$ the depth) leading to a tightening of the wave packet. But in the solitonic case, both effects (dispersion and tightening) balance out each other enabling therefore the invariant propagation of a solitary wave in a nonlinear system.

### 1.3.3 *Optical solitons*

#### ***Temporal and spatial solitons: definition***

In optics we consider two types of solitons: "temporal" solitons in pulsed optics (where the nonlinearity compensates the dispersion) in comparison with the "spatial" soliton. Spatial solitons are observed in wave optics, where the natural diffraction (spatial beam expansion) can be counterbalanced by the nonlinearity of the system [Fig. 1.17].
Besides the Korteweg-de Vries model, several mathematical exactly solvable models, such as the nonlinear Schrödinger equation [60–63], present the soliton as an exact solution. In 1973 Hasegawa *et al.* suggested that the pulse propa-

gation in optical fibers is also governed by the nonlinear Schrödinger equation [64]. As for solitonic water waves in the previous Section 1.3.2, a solitonic optical pulse is a superposition of light waves of different frequencies, thus propagating at different velocities. The nonlinearity of the propagation medium enables under certain conditions to balance with the linear dispersion of the optical pulse, leading to the formation of soliton pulses. In 1980 Mollenauer *et al.* observed the first experimental bright solitons [65] in a single-mode optical fiber (Kerr nonlinearity) using pico-second pulses.

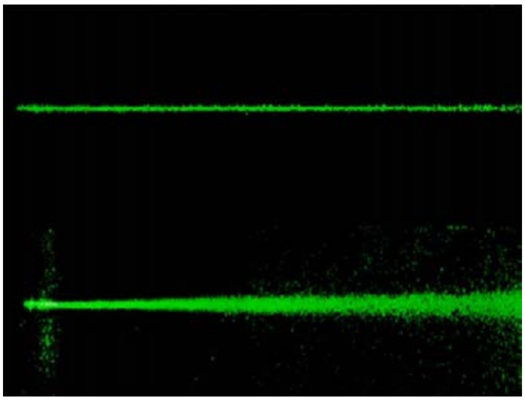

Figure 1.17: Experimental observation of an optical spatial soliton propagating through a 5 mm long nonlinear photorefractive crystal. Top: side-view of the soliton beam from scattered light; bottom: normal diffraction of the same beam when the nonlinearity is 'turned off'. Extracted from [66, 67].

Experimental spatial soliton have also been observed in Kerr [68, 69] and later in photorefractive media [70]. Contrary to temporal solitons in pulsed optics, where the solitonic confinement is only one-dimensional (temporal), the spatial domain offers 2D- and even 3D-self-trapping possibilities.

It is worth mentioning that initially the term "soliton" was only used for self-trapped optical wave packets that are solution of integrable nonlinear partial differential equations. One-dimensional optical soliton pulses in a fiber is an example of such a solution of the nonlinear Schrödinger equation. However, most of the physical systems are governed by non integrable equation, while presenting shape-preserving beam's solutions, first called *solitary waves*. Because the physical behavior of these solitary waves is similar to the mathematical solitons, the definition of an optical *soliton* has been generalized to all self-trapped beams.

For studying the propagation of optical soliton, media with a saturable nonlinearity have raised much interest. Saturable media (i.e. where the nonlinearity saturates above a certain intensity), such as photorefractive systems, support stable 2D-solitons [71], whereas only 1D-soliton can be stable in Kerr media (unless there is already a waveguide structure along one dimension) [72]. Besides the Kerr and photorefractive nonlinearities, which are the most common explored propagation media, optical solitons have also been discovered in a large range of systems, such as atomic vapors [73], quadratic electro-optic effects in paraelectric nonlinear crystals [74], orientational enhanced photorefraction in organic nonlinear materials [75, 76], and thermal nonlinear effects in liquid crystals [67, 77, 78].

### *Photorefractive solitons*

Photorefractive solitons have raised much interest since the 90's [79, 80], as the photorefractive nonlinearity enables the formation of solitons of multiple spatial dimensions, contrary to Kerr nonlinearity. Also the photoinduced nonlinearity required for a solitonic behavior appears for low optical power (a few microwatts [81] contrary to Watts in the Kerr-case). In that case the nonlinearity is increased via an external bias electric field, which offers an additional tuning parameter. The first solitons experimentally observed in photorefractive media however were of transient nature (so called "quasisteady state") and existed only within a narrow temporal window. To reach the steady-state regime, an external background illumination enables to adjust the soliton formation and its dynamics [66]. In general photorefractive solitons are very interesting for experimental implementations, as weak continuous sources lasing at a weak power (a few mW) are sufficient to reach and explore the solitonic physics and its applications [82].

### *Applications*

#### PARTICLE-LIKE INTERACTIONS

The discovery of spatial solitons and its associated discovered phenomena have led to explore many applications. Their self-trapped nature has drawn the attention to the domain of fundamental physics, such as the comparison between the collision of solitons and of particles. This optics-particle equivalence has been first suggested in 1965, where the outcome of soliton collisions has been studied [58]. Colliding solitons appear to interact very similarly to particles, as they may repel or attract each other depending on their distance between each other, their phase-matching and size [83–85]. Theoretical and experimental studies have been done in various nonlinearity types and have led, in particular in photorefractive media, to a larger number of interaction types [55, 86, 87].

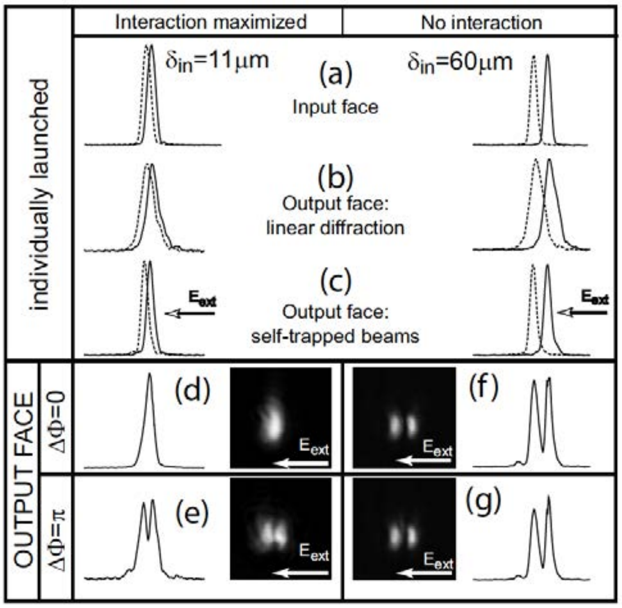

Figure 1.18: Influence of the phase matching $\Delta\Phi$ between two co-propagating solitons for a small and large inter-beams distance. Typical intensity profiles along the transverse axis displaying the interaction process. Extracted from [55].

An example is given on Figure 1.18, where two parallel coherent Gaussian beams are launched in a photorefractive crystal (semiconductor InP:Fe) along the same direction, with an identical waist of 25 μm. As presented in reference [55] and depicted on Figure 1.18(b), the beams diffract and propagate along each other under linear conditions. However, when applying an external bias electric field (here 10kV/cm), they turn into solitons. For a transverse beams' separation of $\delta_{in} = 60$ μm, the beams do not see each other and propagate without interactions [Figs. 1.18(f), 1.18(g)]. On the other hand for smaller transverse shifts, $\delta_{in} = 11$ μm, the interference pattern leads to either mutual attraction for in-phase beams, or repulsive forces when the beams are out-of-phase. This example demonstrates the diversity of particle-like interactions that can be observed for photorefractive solitonic collisions.

### ALL-OPTICAL ROUTING

As detailed in previous subsection 1.2.1, the photorefractive effect is optimal for a precise combination of beam's parameters, in particular the wavelength of the optical beam. If we consider the SBN-crystal used later in our experiment, its optimal photorefractive effect appears for $\lambda = 532$ nm. At this wavelength, $\lambda = 532$ nm, we can observe nonlinear self-focusing solitonic effect of an optical beam and induce waveguiding structures. On the contrary if we propagate an optical beam at an other wavelength (e.g.in the infrared range, $\lambda = 1.55$ $\mu$m), the crystal will have a linear response and the refractive index structure remains unchanged. This sensitivity to the wavelength enables a weak soliton beam at $\lambda = 532$ nm to induce a waveguide that can be used to guide other more intense beams at other wavelengths for which the photorefractive effect is less sensitive [88–90].

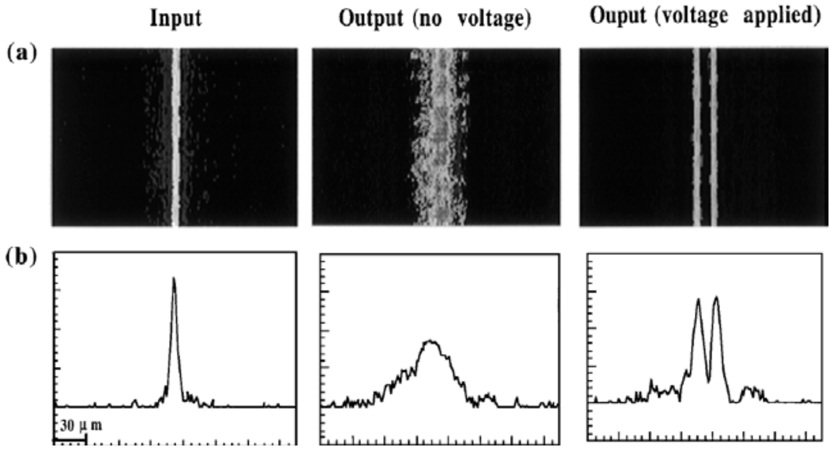

Figure 1.19: (a) Photographs and (b) horizontal profiles of the red beam guided by the waveguide induced by the Y-junction induced by a solitonic propagation of an initial Gaussian beam. Extracted from [89].

Photorefractive solitons appear therefore as an ideal candidate for waveguiding and steering applications. An example is given by Chen *et al.* in reference [89], where they generate a pair of anti-phased dark solitons diverging from each other leading to a Y-junction soliton (using a dark notch on an otherwise-uniform Gaussian beam). The optically created waveguiding structure then form a Y-junction in the solitonic regime as illustrated in Figure 1.19. Such photorefractive soliton-induced waveguides can be used for device applications as experimentally studied by the group of Segev and Chen in references [91] and [92], where directional couplers and high-efficiency frequency converters have been demonstrated.

## 1.4 MOTIVATIONS

In this thesis we study the nonlinear propagation of Airy beams in photorefractive crystals. Considering the state-of-the-art of the control of the accelerating features of the Airy beam, we have focused our research on the propagation of Airy beams under high focusing conditions similar to the solitonic behavior in classical Gaussian systems. First we consider the behavior and features of a single strong self-focused Airy beam in chapters 2 and 3. In a second part we explore the interaction scheme of two Airy beams propagating in opposite directions (chapters 4,5,6).

Under a nonlinear focusing strength, literature has theoretically predicted the existence of a superimposed solution of a soliton and an accelerating beam, both issued from the same initial linear Airy beam [93]. In Chapter 2 we experimentally study an Airy beam under strong nonlinear conditions leading to a solitonic solution. We show that the position and shape of the Airy-soliton beam at the output of the photorefractive crystal can be tuned using various system's parameters.

During the experimental study of the solitonic behavior of Airy beams, we observed a peculiar spatiotemporal response of the output beam. In Chapter 3 we show that the transient behavior of the Airy beam involves both self-bending and acceleration of the initially launched Airy beam. This can be explained by the onset of an off-shooting soliton and the resulting large refractive index perturbation, which acts as a gravitational potential in an accelerating framework. Besides its interest for the analogy with gravitation, the build-up dynamics of the focused beam provides a deeper insight into the subject of accelerating beams in nonlinear focusing media.

As detailed in previous Section 1.3 (paragraph 1.3.3), photorefractive solitons offer interesting solutions for all-optical routing. After the extensive study and characterization of the Airy soliton behavior, we propose to analyze in Chapter 4 waveguides optically induced by a single optical Airy beam in a photorefractive crystal. The results highlight the diversity of waveguides created by a single Airy beam thanks to its multi-lobe structure. In a second step we inject an incoherent counterpropagating Airy beam. By taking advantage of the large transverse Airy distribution and the parabolic trajectory, we investigate the waveguide structures photoinduced by their interconnections. We show that the interaction schemes between two Airy beams offer multiple waveguide possibilities even for large transverse shifts of the interacting beams.

As the waveguide structures induced by two Airy beams present a complex and large transverse spatial distribution due to the shape and properties of the Airy beams, we question about their stability for increasing focusing nonlinearity. In Chapter 5 we present the emergence of peculiar spatiotemporal dynamics. The system evolves from static to time-periodic then chaotic waveguides when increasing the nonlinearity strength and the crystal length. Contrary to Gaussian systems, we show that the Airy properties enable a larger stability range (i.e. more efficient waveguiding). Also under extreme focusing conditions, the resulting chaotic regime does not display randomly distributed dynamics, but appears to be spatially organized with an Airy distribution. Such spatially localized instabilities suggest innovative ways of performing optical computing based on spatiotemporal chaos.

# Part I

# SELF-FOCUSING OF A SINGLE AIRY BEAM

# 2

# SOLITONIC PROPERTIES OF A SINGLE SELF-FOCUSING AIRY BEAM

In this chapter we analyze the existence of Airy-solitons in a photorefractive crystal when increasing the self-focusing nonlinearity. First experimental results show that under a nonlinear positive bias electric field, the photorefractive effect turns the Airy beam into a combination of an off-shooting soliton and an accelerating beam. The Airy-soliton appears for a range of parameters similar to those leading to a Gaussian soliton. Its output position and intensity can be engineered via several external parameters. The experimental findings are then confirmed by numerical simulations.

The numerical context of this chapter is related to the following publication: Noémi Wiersma, Nicolas Marsal, Marc Sciamanna, Delphine Wolfersberger, "All-optical interconnects using Airy beams". In: *Opt. Lett.*, 39.20 (2014), pp 5997-6000.

## 2.1 NONLINEAR AIRY PROPAGATION

In this chapter we will study the self-focusing of an Airy beam towards a so-called solitonic structure. In comparison with Gaussian solitons, the Airy soliton does not preserve the Airy profile and does no longer follow a curved trajectory, but propagates along a straight line. While self-trapping and self-focusing depict the same behavior for a Gaussian beam (i.e. solitonic propagation), we need to set a distinction for Airy beams. We consider self-trapping, when the Airy beam preserves its multi-lobe shape and its curved trajectory over a longer distance than in free space (see next Section 2.1.1). By opposition, the self-focusing effect appears when the Airy beam quits its shape and curved trajectory to form a single soliton along a straight line (combined with a weak accelerating structure, see Section 2.1.2).

### 2.1.1 *Self-trapping effect*

As a truncated solution of the ideal Airy waveform, the optical Airy beam has the advantage of combining the parabolic trajectory and self-healing properties of the Airy wave solution over a finite distance with the diffractive beam properties for larger propagation distances. Unlike conventional beams, such as Gaussian beams, an Airy beam propagating in a linear medium will maintain its shape over a much larger distance. When propagating in an unbiased photorefractive medium, an optical beam is mainly subject to the diffusion effect. Because of the asymmetry of this phenomenon, a Gaussian beam presents various transverse effects such as self-trapping and self-bending [48, 94]. In particular to preserve the shape of the Gaussian spatial profile, an externally applied voltage enables to counterbalance the diffraction effect [81]: the propagating beam then turns into an optical spatial soliton. While conventional beams present a symmetrical energy distribution, it is interesting to first study how the asymmetrical intensity profile of the Airy beam is interacting with the diffusion effect only (i.e. without external bias electric field).

This question has been answered in Ref. [95, 96], where it has been numerically demonstrated that, precisely thanks to the asymmetry of its shape, the Airy beam can undergo self-trapping (i.e. a shape-preserving accelerating propagation over a longer distance). For example reference [95] numerically and experimentally shows that the diffraction of an Airy beam can be annihilated via

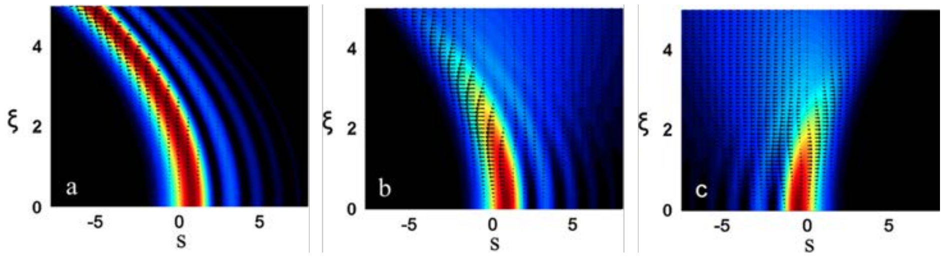

Figure 2.1: Transverse energy power flow. (a) The intensity profile of a self-trapped Airy state during propagation in a diffusive medium. (b, c) The propagation of this same beam (b) in the absence of diffusion and (c) when the phase profile is reversed (with s (resp. ξ) the normalized transverse (resp. propagation) axis). Extracted from [95].

the diffusion effect in a photorefractive medium [Figs. 2.1(a), 2.1(b)]. However, the self-trapping effect appears only when the acceleration is opposite to the diffusive effect [Figs. 2.1(a), 2.1(c)]. An Airy beam propagating in a diffusive medium (e.g. an unbiased photorefractive crystal) therefore preserves its shape much better than propagating in free space. While the self-trapping of conventional beams requires a nonlinear transport effect to counterbalance the diffusion, this new class of self-localized beams owes its existence to carrier diffusion effects only (this observation is also valid for Airy pulses [97]).

Besides the linear shape-preserving propagation of an Airy beam in diffusive media, the propagation direction of the accelerating beam can also be altered via an externally applied nonlinearity. By studying further the impact of the nonlinearity of the medium on the propagation of an Airy beam, various theoretical as well as experimental studies have demonstrated that the shape and trajectory of the Airy beam can be engineered via a refractive index variation [21, 99–101]. The first experimental studies done by Chen's group [21] have shown that an Airy beam as it propagates from an electrically biased medium to a linear medium experiences anomalous diffraction enabling it to maintain its shape, when under self-defocusing nonlinearity. On the other hand a self-focusing nonlinearity prevents the stability of the Airy-accelerating shape and properties for a linear propagation after the crystal [21].

More generally the trajectory of an optical beam is altered by the refractive index variations along the propagation medium. Figure 2.2 depicts how peculiar refractive index gradients can lead to very exotic trajectories of the Airy beam

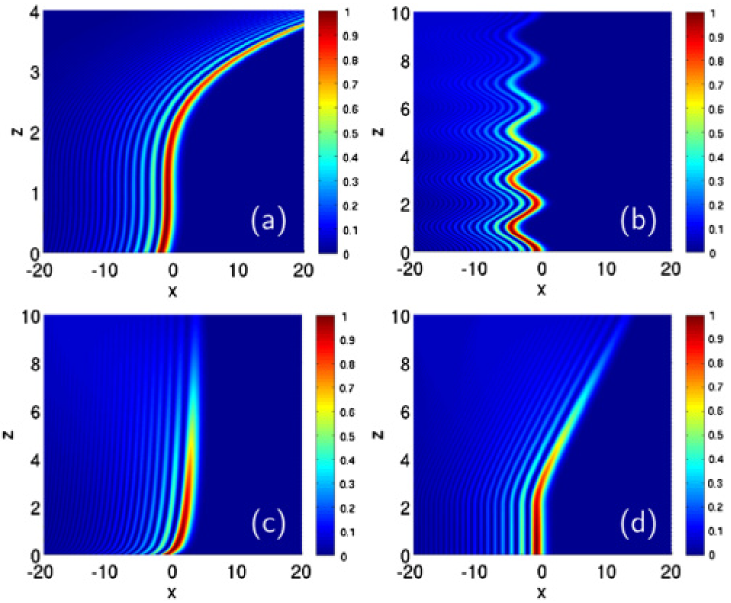

Figure 2.2: Exponentially apodized Airy beam propagation along predefined paths (using a transversely linear index potential): (a) power law trajectory, (b) sinusoidal trajectory, (c) logarithmic trajectory, (d) hyperbolic trajectory. Extracted from [98].

[98]. By dynamically changing the refractive index structure along the propagation direction $z$, Efremidis *et al.* suggest to annihilate the transverse acceleration over a finite distance [Figs. 2.2(a), 2.2(d)] or all along the medium [Fig. 2.2(b)]. They also predict transverse accelerations opposite to the Airy direction for the whole multi-lobe structure [Fig. 2.2(c)].

Inside a nonlinear biased medium, the photorefractive effect enables to photoinduce a local variation of the refractive index structure. By applying a bias electric field, a tunable waveguide structure is photoinduced by the optical beam inside the nonlinear medium (via the Pockels effect). In addition Chen *et al.* experimentally and theoretically demonstrated that a background illumination can also modify the acceleration of the Airy beam [100]. To that aim they optically modify the refractive index distribution along the transverse Airy axis $x$ with an index gradient $\delta n$ using a white light gradient and a bias electric field. As illustrated on Figure 2.3, the acceleration factor of the Airy beam is increased when the gradient increases along the Airy acceleration direction $+x$ [Fig. 2.3(b)]. But if the gradient increases along the higher lobe orders, the Airy beam accelerates less along the $+x$-direction [Fig. 2.3(c)] up to a zero-deflection propagation [Fig. 2.3(d)]. As the acceleration rate of the Airy beam depends on the spatial parameter $x_A$ (see Section 1.1.4), the index gradient values $\delta n$ has to be increased to enhance the initial acceleration of larger Airy beams, while smaller Airy beams need a lower negative index gradient to reach the zero-deflection propagation [Fig. 2.3(e)].

Adding these externally tunable waveguiding and trapping possibilities to the inherent Airy self-trapping effect, the control and tuning of the beam's ballistic using the medium's nonlinearity (or photonic lattices [102, 103]) offer new possibilities in waveguiding solutions such as in all-optical routing.

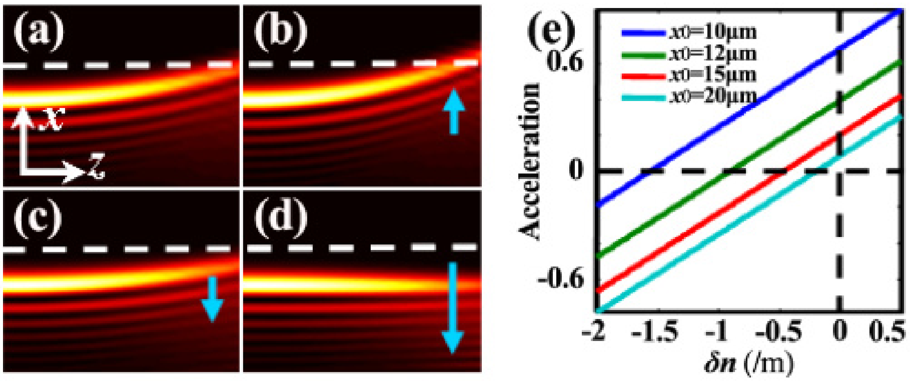

Figure 2.3: 1D Airy beams propagating in an electrically biased medium with different index gradients ($\delta n$ oriented along $x$). (a) Normal propagation. (b) Enhanced and (c) reduced acceleration at $\delta n > 0$ and $\delta n < 0$, respectively; (d) no acceleration at $\delta n = -{}^{n}/_{2k^2 x_A{}^3}$. (e) Plot of acceleration as a function of $\delta n > 0$ under different $x_A$. The white dashed lines mark the position of the central lobe at the output in (a), and the arrows illustrate the index gradient. Extracted from Ref. [100].

## 2.1.2 *Solitonic regime*

Previously we have considered the nonlinear propagation of an Airy beam, where the beam preserves its multi-lobe distribution and its curved trajectory (i.e. a self-trapped regime) [Fig. 2.3]. In the first case, the diffusion effect leads to a self-trapped Airy propagation: the intensity shape remains invariant along the parabolic trajectory. When a small bias electric field is applied on the Airy beam, the beam still undergoes self-focusing and the main lobe is narrower, while still accelerating [96]. However, first studies predict peculiar dynamics of the Airy beam, when propagating under high focusing conditions. Recent works have shown the possibility to induce spatial solitons through self-focusing of ideally non-diffractive beam profiles including optical Airy beams [96, 104]. As depicted on Figure 2.4, Segev *et al.* theoretically present the propagation of an Airy beam in a Kerr medium under a strong self-focusing (left column), a weak focusing (middle column) and a strong defocusing nonlinearity (right column). By comparing the two focusing cases, while the weak focusing conditions preserve the Airy shape and propagation (i.e. self-trapping effect), the increase of nonlinearity turns the Airy beam into multiple off-shooting solitons. In particular the finite-energy Airy beam undergoes stronger self-focusing effect, as the truncation decreases the diffraction-free property of the Airy beam.

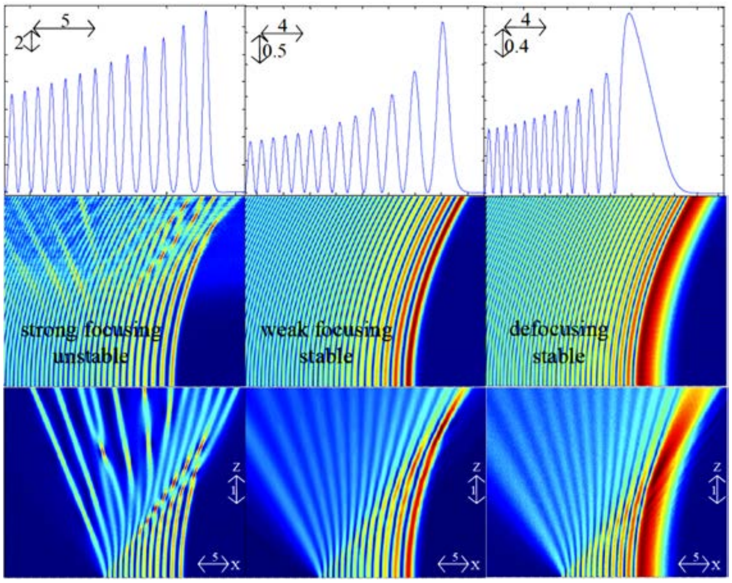

Figure 2.4: Self-accelerating beams in Kerr media. Top row: Intensity profiles at z ¼ 0. Middle row: Propagation of self-accelerating beams with infinite tails and 2 % noise. Bottom row: Propagation of self-accelerating beams with finite tails. Left column: Strong focusing nonlinearity. Middle column: Weak focusing nonlinearity. Right column: Defocusing nonlinearity. Extracted from Ref. [97].

Contrary to the self-trapping effect, where the beam remains Airy-like under a weak nonlinearity [36, 95], we consider strong self-focusing as a nonlinear effect leading to the breakdown of the Airy behavior (in particular the acceleration and Airy-distribution). It has been theoretically demonstrated that finite-energy Airy beams do also undergo solitonic self-focusing when a high positive bias electric field is applied to the nonlinear medium [93, 104, 105]. As depicted on Figure 2.5, by increasing the self-focusing nonlinearity of the medium, the initial linear Airy beam [Fig. 2.5(a)] does not follow the initial self-trapping regime and, similar to Gaussian beams, undergoes a soliton-like behavior [Fig. 2.5(c)].

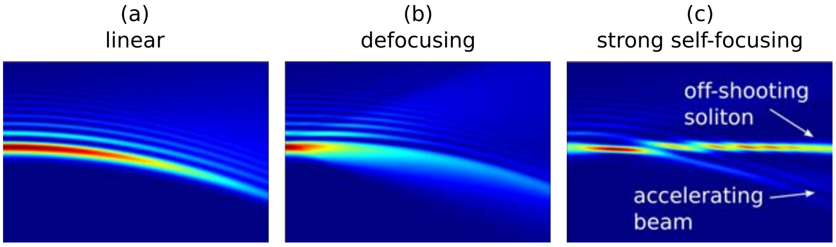

Figure 2.5: Theoretical propagation of an Airy beam in a photorefractive crystal under (a) linear, (b) defocusing and (c) strong focusing conditions.

Contrary to conventional beams, when applying a bias electric field in the direction of the c-axis of the nonlinear medium, the Airy beam does not entirely turn into a soliton, but decomposes itself into a so-called off-shooting soliton and an accelerating wave packet [93, 96, 104–106]. This co-existence of two beam types induced by the same Airy beam is unique in solitonic physics and has raised several questions: what are the existence conditions ? how does the Airy-solitonic behavior differ from the one of a Gaussian soliton ?

### 2.1.3 *Photorefractive vs. Kerr nonlinearity*

The solitonic propagation of Airy beams has been studied in various types of nonlinearities such as in Kerr and photorefractive media. Recently, Segev's group theoretically studied self-accelerating self-focused beams in nonlinear optical media, exhibiting self-focusing and self-defocusing Kerr and saturable nonlinearities, as well as a quadratic response [104]. In particular in the self-focusing case, they have predicted that Airy beams are stable for weak self-focusing in Kerr and saturable nonlinear media. However, under strong self-focusing conditions the Airy beam off-shoots a localized soliton while its main lobe continues to accelerate (see Figure 2.4). Figure 2.6 illustrates the propagation of an Airy beam in a photorefractive medium. Compared to the linear and defocusing propagation, the Airy behavior breaks down under strong photorefractive self-focusing conditions as theoretically predicted by Chen *et al.* [93].

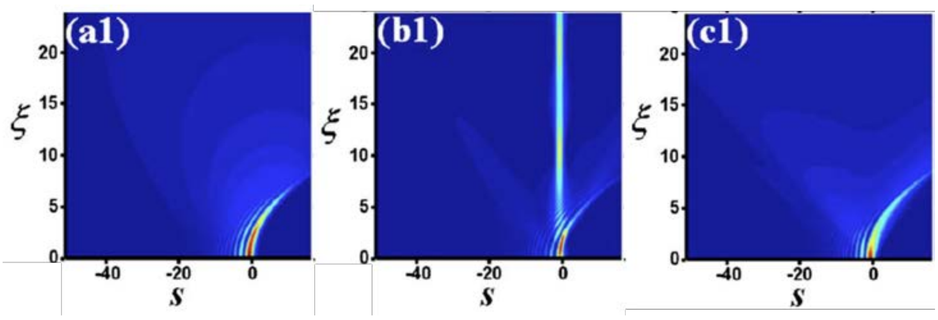

Figure 2.6: Theoretical propagation of an Airy beam in a photorefractive crystal under (a1) linear, (b1) strong focusing and (c1) defocusing conditions. Extracted from Ref. [93].

In Kerr high focusing media an intense solitonic Airy beam can present various spatiotemporal dynamics such as filamentation [105] or oscillations [104, 107] (so-called moving solitons), which is similar to the Gaussian beam case. Figure 2.7 shows the theoretical study of Airy beams in Kerr media [107]. For a weak self-focusing nonlinearity, the Airy beam maintains its Airy-like behavior [Fig. 2.7(a)]. Then under Kerr strong self-focusing nonlinearity the Airy beam splits into an accelerating and a solitonic structure [Fig. 2.7(b)]. However, the soliton is not steady-state, but shoots off towards various transverse output positions. On Figure 2.7(b) we observe one strong static soliton and two weak moving solitons, but the self-accelerating linear packet exists in all cases [Figs. 2.7(a), 2.7(b)]. If we increase the nonlinearity (here the optical intensity $u_0$), the Airy beam undergoes peculiar bifurcation routes. Figure 2.7(c) illustrates the intensity and dynamics of the off-shooting soliton structure for increasing optical intensity $u_0$. It shows that first the Airy beam turns into a steady-state off-shooting soliton with increasing intensity (thick solid line). Then at $u_0 = 2.8$ a soliton pair appears at lower intensity (thin solid line) and moving at a velocity $\mid v \mid = 1.88$. When further increasing the optical intensity $u_0$, additional steady-state solitons and moving soliton pairs appear and eventually die out.
To summarize the dynamics observed for a single strong self-focusing Airy beam

in a Kerr medium, the off-shooting soliton structure presents large and complex dynamics. As depicted on Figure 2.7(d), when decreasing the size of the Airy lobes ($x_A$, here called $\omega_0$), the dynamics observed are similar however shifted along the $u_0$-axis and with less moving soliton pairs.

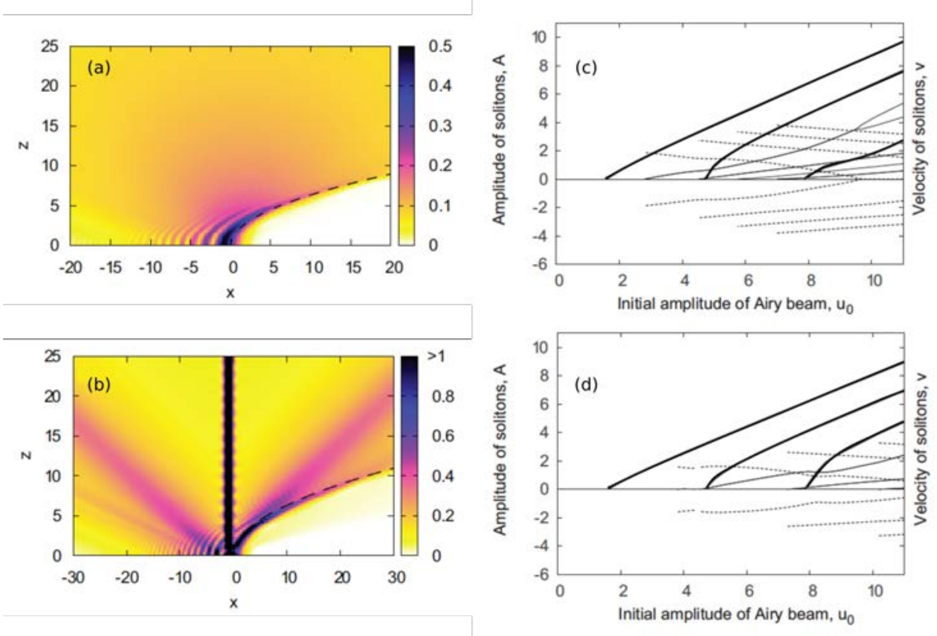

Figure 2.7: (a)-(b) Intensity distribution of an Airy beam propagating in a Kerr medium under (a) weak ($u_0 = 1$) and (b) strong ($u_0 = 4$) nonlinear self-focusing conditions. The thick dashed line is a trajectory $x = z^2/4$ of the truncated Airy beam in a linear medium [17]. (c)-(d) Dependence of the amplitude (solid lines) and velocity (dashed lines) of solitons, emerging from an initial truncated Airy beam, on the amplitude $u_0$ for (a) $w_0 = 10$ and (b) $w_0 = 5.4$. Thick (thin) solid lines correspond to amplitudes of static (moving) solitons. Extracted from Ref. [107].

For both photorefractive and Kerr nonlinearity, the outcome of the dynamics depends on the equilibrium between linear and nonlinear effects, as well as on the power distribution between the different lobes of the Airy beam. As for Gaussian solitons, the solitonic dynamics of Airy beams can be scaled using two beam parameters: the beam's waist and the optical power.

So far the study of Gaussian solitons in photorefractive crystals has shown that, contrary to Kerr media, 2D stable spatial solitons do exist and have been experimentally observed [67]. In the Airy beam case, when it undergoes a photorefractive nonlinearity, its off-shooting soliton propagates along a single direction, tangential to the initial input Airy beam (here along the $z$-axis) [93]. In the following section we will present and study the first experimental Airy-solitons, in particular in a photorefractive medium.

While we were not able to observe a steady-state solitonic regime (to be detailed in Chapter 3), we study in this chapter the behavior of the self-focusing Airy beam at the solitonic peak (highest intensity peak with strongest shift toward the theoretical soliton's position).

## 2.2 EXPERIMENTAL STUDY

### 2.2.1 *Experimental setup*

To observe the outcome of an optical Airy beam after propagating in a focusing nonlinear medium, we use an experimental setup, where we inject a one-dimensional Airy beam in a photorefractive crystal. As depicted on Figure 2.8, the Airy beam is generated using a phase only spatial light modulator (PLUTO Holoeye) in the visible wavelength range ($\lambda = 532$ nm) and the Fourier transformation is induced by the lens $\mathcal{L}_{TF}$. The input face of the SBN-photorefractive crystal (dimensions 5mm*5mm*1cm and $n_{SBN} = 2.3$) is placed at the focal distance of the lens therefore the Airy propagation starts at the entrance of the crystal at $z = 0$. The Airy generation method as well as the experimental setup are detailed in Appendix A.

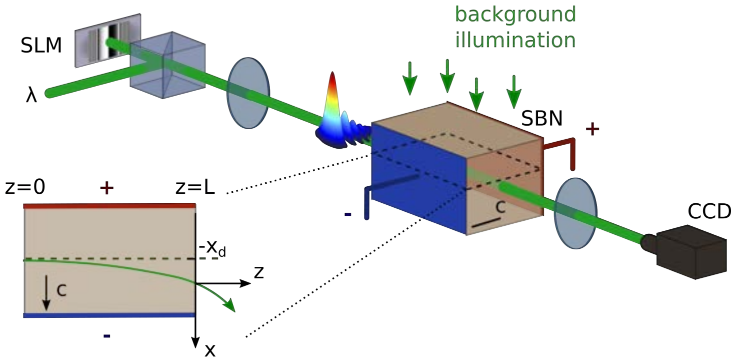

Figure 2.8: Experimental observation of the self-focusing 1D-Airy beam propagating in a biased photorefractive crystal: zoom on the Airy beam's propagation inside the photorefractive crystal.

Along the c-axis of the crystal, we apply an external bias electric field to excite the focusing photorefractive nonlinearity ($E_e \in [0, 4]$ kV/cm). To study the focusing effect on the Airy properties, we orientate the Airy distribution in the c-direction, parallel to the $x$-axis. The beam propagates along the $z$-axis, from $z = 0$ to $z = L$ (where $L$ is the crystal length) and its optical field $\psi(x)$ is defined the following initial conditions:

$$\psi(x)_{z=0,t=0} = \mathrm{Ai}\left(\frac{x+x_d}{x_A}\right)\exp\left(a\frac{x+x_d}{x_A}\right), \tag{2.1}$$

where $x_A$ is the main lobe's waist, $a$ the truncation parameter and $x_d$ the linear transverse deflection of the Airy beam. As for the solitonic Gaussian regime, we set the characteristic transverse beam dimension around $x_A = 10$ µm. The ideal Airy profile is truncated with the aperture parameter $a \approx 0.05$ and we set the transverse origin $x = 0$ at the linear output position of the Airy beam. The linear output Airy beam, in particular the main lobe, therefore sets the reference for the transverse shift along $x$ and for the intensity peak as the output profiles are normalized with the linear main lobe.

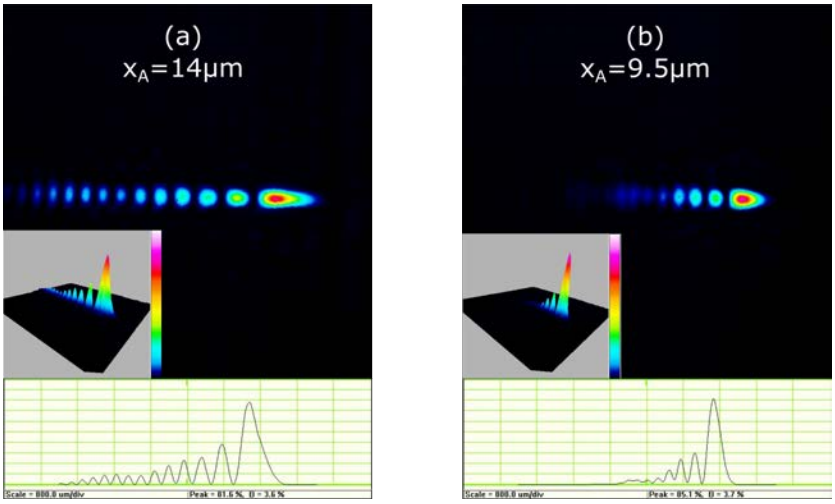

Figure 2.9: Observation of the SLM-generated Airy beam at the input side of the crystal with a CCD camera (20-times magnitude). Intensity distribution and profile of (a) the largest generated Airy beam ($x_A = 14$ µm) and of (b) the smallest generated Airy beam ($x_A = 9.5$ µm) using the experimental setup of Fig. 2.8.

To study the impact of the Airy properties on the solitonic regime, we optimize our Airy shape quality by maximizing the size of the modulated Gaussian beam on the SLM (active area: 15.36 mm $*$ 8.64 mm). To that aim the initial laser beam is expanded to a waist of $w_{SLM} = 3.2$ mm. Then the Fourier Transform lens is set at $f_{TF} = 7.4$ cm to reach the "$x_A = 10$ µm"-range. As depicted on Figure 2.9, the Airy beam presents over ten lobes, guaranteeing a good approximation of the ideal Airy propagation.

Under linear conditions, the beam propagates along the z-axis of the crystal with a transverse parabolic acceleration along the c-axis (parallel to the x-axis) [Fig. 2.8]. In our experiment we set $x = 0$ as the transverse output position of the linear Airy beam. The parabolic acceleration of the beam along the x-axis, described by the linear main lobe, mathematically follows the equation:

$$x_{peak}(z < L) = -\frac{(L-z)^2}{4k^2 x_A^3}, \tag{2.2}$$

where $k = 2\pi n/\lambda$ is the wave vector. All along the study, the main lobe of the linear output Airy beam exits the crystal at $x = 0$. As the deflection $x_d$ varies with the beam's size $x_A$, the input position of the Airy beam at $z = 0$ changes. For example in a 1cm-crystal length and with $x_A = 14$ µm, the Airy main lobe has initially been launched at $-x_{peak}(z = 0) = 12.4$ µm. As indicated in Eq. 2.2, decreasing the beam's size via the lobe's waist $x_A$ leads to a larger deflection, e.g. for $x_A = 10$ µm the beam's deflection equals to $x_d(z = L) = -x_{peak}(z = 0) = 34$ µm.

Figure 2.10 depicts for two different optical powers the output Airy beam after propagating in a 1 cm-long crystal first under linear conditions [Figs. 2.10(a), 2.10(d)], then with a positive focusing nonlinearity ($E_e = 4$ kV/cm) 10 s after the bias voltage has been switched on [Figs. 2.10(b), 2.10(e)]. As presented in Ref. [99], the nonlinear output beam presents an Airy-like intensity profile, similar to the linear output Airy beam, but with narrower and higher peaks showing the weak self-focusing effect [Figs. 2.10(c), 2.10(f)]. The self-focusing behavior appears for a large range of optical power (here $P_A \in [1; 4.3]$ µW). While the optical power increases the nonlinearity of the medium, the lobe tightening effect is however stronger for a lower input power [Figs. 2.10(c), 2.10(f)]. On the first sight, this result may surprise, but it can be explained by the transient spatiotemporal dynamics of our system. This question will be answered later in Chapter 3.

### 2.2.2 *Observation of Airy-solitons*

Theoretically an Airy beam undergoes a solitonic behavior when under strong self-focusing conditions [93, 96, 104]. So far the experimental research has demonstrated shape-preserving weak self-focusing behavior (i.e. tightening of the Airy lobes), when a weak external bias electric field is applied. This effect is observed in the steady-state regime for a weak focusing nonlinearity or for a larger Airy

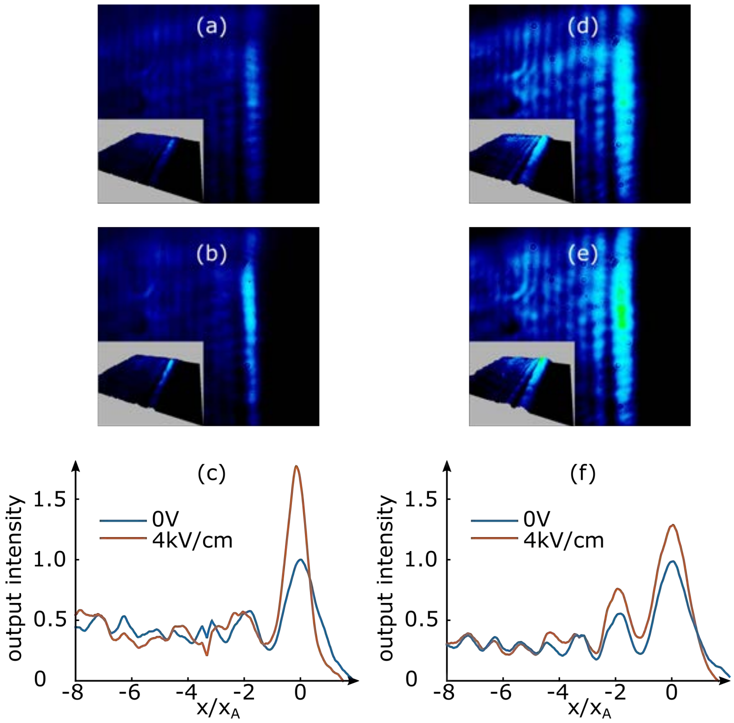

Figure 2.10: Experimental observation of a steady-state Airy beam after self-focusing for two different powers [Fig. 2.8] after 10 s: (a)-(c) $P_A = 1$ µW, (d)-(f) $P_A = 43$ µW. Output intensity distribution of the Airy beam at $z = L$ ($x_A = 14$ µm) (a),(d) after a linear propagation, (b),(e) after biased nonlinear propagation ($E_e = 4$ kV/cm). (c),(f) Intensity profiles of the linear and focused output beams.

beam. But what happens above this limit ? While the previous Figure 2.10 shows an Airy beam with a high voltage ($E_e = 4$ kV/cm), it is worth noting that the measure has been taken far after the biased voltage has been switched on ($t = 10$ s). As we will present in the next Chapter 3, the Airy beam first turns into an off-shooting soliton under high-focusing conditions ($E_e > 2$ kV/cm) before relaxing into a steady-state Airy-like beam with tightened lobes or even, when further increasing the self-focusing strength, with defocused lobes. In Chapter 3 we will also discuss the decrease of stability of the self-focused solitonic regime when increasing the nonlinear focusing strength. As the aim of this Chapter 2 is to enhance the solitonic self-focusing effect, the study of the Airy-soliton here will be concentrated on a transient state of the self-focusing Airy beam.

Therefore, the experimental Airy-solitons observed in this chapter are extracted during the transient self-focusing of the beam. The complete dynamics of the solitonic self-focusing of the Airy beam will be detailed in Chapter 3. In this chapter we will now study the peak solution of the transient off-shooting soliton.

### *Propagation over a short distance*

In this paragraph, we study the case of an Airy beam propagating in a 1cm-crystal ($L = 1$ cm) under an external focusing bias field and Figure 2.11 depicts the soliton off-shooting from the initial Airy beam. On Figures 2.11(b), 2.11(c) we see that a high peak appears between the first and second lobe of the linear output Airy profile, which differs from the self-focusing multi-lobe structure of Figure 2.10.

Because the propagation of the Airy-soliton is theoretically predicted tangential to the initial propagation direction, its output position is expected to be shifted of exactly the transverse deflection between the input and linear output Airy beam. On Figure 2.11 we study two Airy beam sizes: $x_A = 14$ µm [Figs. 2.11(a)-2.11(c)] and $x_A = 9.5$ µm [Figs. 2.11(d)-2.11(f)].
While the optical powers $P_A$ and the bias electric fields $E_e$ are also different in both cases, we concentrate our analysis on the beam's size variation $x_A$. Indeed in the small Airy beam case, $x_A = 9.5$ µm [Figs. 2.11(d)-2.11(f)], the voltage has been decreased to observe an off-shooting soliton (green arrow on Figures 2.11(d)-2.11(f)). Otherwise the transient dynamics are too fast to capture the Airy-soliton on the CCD-camera. As a consequence the optical power has been adjusted to optimize the solitonic self-focusing and the maximum solitonic peak is already reached for $E_e = 3$ kV/cm.

As the acceleration rate of the Airy trajectory depends on the $x_A$-parameter [Eq. 2.2], both Airy beams have different transverse deflection distances [Figs. 2.11(a), 2.11(d)] and their off-shooting solitons are respectively expected at $x_{sol,14\mu m} = -12.4\ \mu m = -0.8 x_A$ and $x_{sol,9.5\ \mu m} = -39.7\ \mu m = -4.2 x_A$. If we compare the theoretical expected and experimental peak positions of the Airy beam in both cases [Figs. 2.11(b), 2.11(e)], they match exactly and the peaks can therefore be identified as their respective off-shooting solitons.
The intensity peaks of the off-shooting solitons are almost three times higher than the linear main lobe's intensity at $z = L$ as they concentrate the energy of

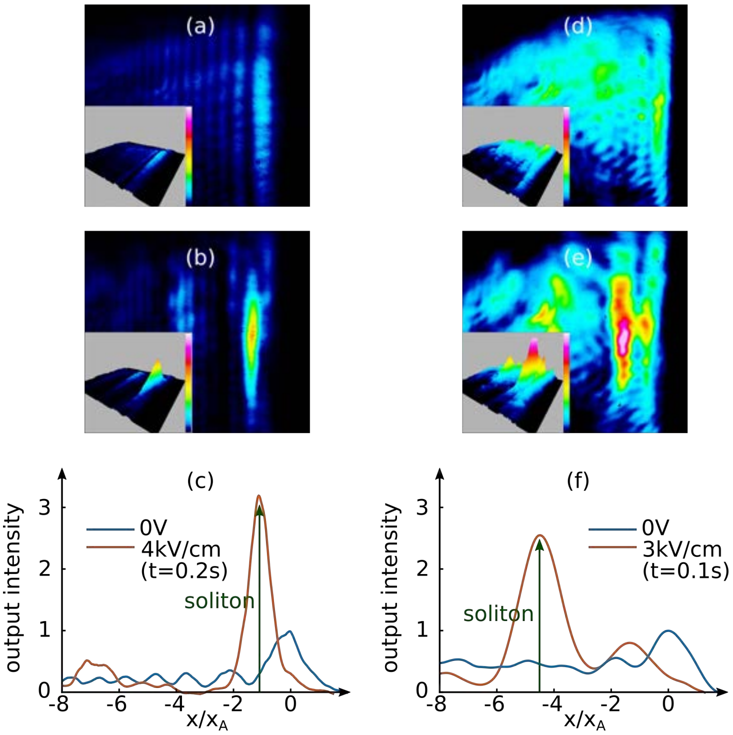

Figure 2.11: Experimental soliton off-shooting from a self-focusing Airy beam for decreasing beam's waist [Fig. 2.8]: (a)-(c) $x_A = 14$ µm, $P_A = 7$ µW (d)-(f) $x_A = 9.5$ µm, $P_A = 43$ µW. Intensity distribution of the Airy beam at $z = L$ (a),(d) after a linear propagation, (b),(e) during high-focused propagation and (c),(f) transverse intensity profile of the linear and solitonic output beams.

several lobe orders. However, the small Airy beam case, $x_A = 9.5$ µm, presents a secondary beam in the solitonic regime [Figs. 2.11(e), 2.11(f)]. This secondary lobe is observed at $x/x_A = -1.5$, between the linear main lobe $x/x_A = 0$ of the accelerating beam and the not accelerating off-shooting soliton $x/x_A = -4.2$. As a consequence this secondary beam also presents a transverse acceleration along the crystal and can be identified as the theoretically predicted accelerating beam co-existing with the off-shooting soliton [93].

As for Gaussian solitons, we study now the impact of the nonlinearity through different parameters on the self-focusing of the Airy-soliton for a fixed beam's size (via $x_A$). Figure 2.12 depicts the transverse intensity profiles of the self-

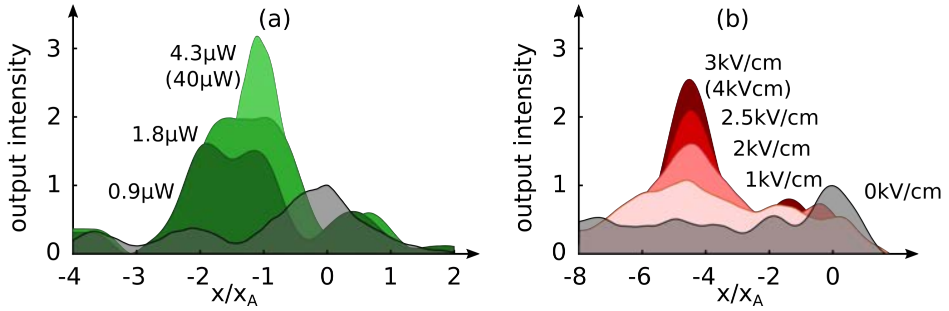

Figure 2.12: Influence of the electro-optical nonlinearity on the Airy-soliton at the output of the crystal [Fig. 2.8]. Transverse intensity profile of the off-shooting soliton (a) for increasing optical input power (with $x_A = 14$ µm and $E_e = 4$ kV/cm) and (b) for increasing bias electric field $E_e$ (with $x_A = 9.5$ µm and $P_A = 7$ µW). The linear output profile is represented in black.

focused beam, first for increasing optical power [Fig. 2.12(a)], then for increasing bias electric field [Fig. 2.12(b)]. The solitonic self-focusing of the beam is induced by the photorefractive effect, which can be mainly tuned via these two parameters (see Section 1.2). Similar to Gaussian physics, the influence of the optical power and of the bias electric field qualitatively play symmetrical roles: they both enhance the formation of a high peak soliton at the zero-deflection-position of the Airy beam.

When increasing the optical power $P_A$ [Fig. 2.12(a)] ($E_e = 4$ kV/cm fixed), the Airy beam splits into a strong solitonic beam around the zero-deflection position $x = -0.8x_A$ and an accelerating beam at $x = 0.7x_A$. The solitonic structure increases from 1.5-times ($P_A = 0.9$ µW) to 3.2-times ($P_A = 4.3$ µW) the intensity of the linear main lobe (gray curve on Fig. 2.12(a)) with a strong tightening up to a waist equal to $0.5x_A$. The accelerating beam then nearly disappears during the solitonic peak when $P_A \geqslant 4.3$ µW (hidden on this Figure), but only for a short transient time ($\approx 100$ ms) as shown in the next chapter.

On Figure we consider an Airy beam of $x_A = 9.5$ µm, with a fixed optical power $P_A = 7$ µW and increasing bias electric field $E_e$. For a qualitatively low electric field $E_e = 1$ kV/cm, the self-focusing peak of the Airy does not present any solitonic beam, but we observe a large energy concentration around the zero-deflection position $x = -4.2x_A$. By increasing $E_e$, the wide beam shape around $x = -4.2x_A$ starts increasing in intensity and tightens towards a solitonic beam with up to 2.5-times the initial main lobe and a waist similar to $x_A$. Besides the solitonic beam, the remaining accelerating structure is observed near $x = -x_A$

even for increasing electric field. This result can be explained by the larger distance between the off-shooting soliton and the accelerating structure.
It is worth noting that we have used two different sizes of Airy beams to analyze the influence of the optical power and the bias electric field on the self-focusing effect. While a small Airy beam, such as $x_A = 9.5\ \mu\text{m}$ in Fig. 2.12(b), has the advantage to off-shoot a soliton far shifted from the linear main lobe which facilitates its identification, the higher truncation leads to stronger diffraction and prevents us from well detecting the off-shooting soliton for low power $P_A$. As a consequence we used a larger Airy beam to study the role of the optical power $P_A$ [Fig. 2.12(a)].

However, in both cases we observe a saturation of the self-focusing effect when further increasing the optical power (same solitonic peak for $P_A = 4.3\ \mu\text{W}$ and $P_A = 40\ \mu\text{W}$, Fig. 2.12(a)) or the external electric field $E_e$ ($E_e = 3$ kV/cm and $E_e = 4$ kV/cm, Fig. 2.12(b)).

This result shows us that the solitonic propagation of Airy beams can be tuned via external system's parameters. But as Figure 2.11(e)-(f) has already indicated, the beam's size and therefore the propagation distance can lead to the formation of a high peak far away from the linear output position. In our 1cm-crystal this scenario requires the use of very small Airy beams ($x_A < 10\ \mu\text{m}$). But if we want to keep the same deflection shift between the input and the output of our nonlinear medium, the Airy beam's properties can offer an other equivalent option [Eq. 2.2]:

- propagating a small Airy beam in a short crystal,
- propagating a larger Airy beam in a long crystal.

As an example a propagation in a (1 cm)-long crystal for an Airy beam with $x_A = 7.5\ \mu\text{m}$ equals to 3.5-times the diffraction length ($L_d = 2k{x_A}^2$), whereas the equivalent $L/L_d$-ratio in a (2 cm)-long crystal is obtained for an Airy beam beam with $x_A = 11\ \mu\text{m}$. It is interesting to question now whether both options lead to the same solitonic behavior.

### *Propagation over a long distance*

To compare the effects of increasing the propagation length regarding the Airy beam's size, we now inject an Airy beam with $x_A = 11\ \mu\text{m}$ inside a SBN-crystal with a doubled length: $L = 2$ cm. Following the equation of the parabolic trajectory [Eq.2.2], the doubling of the propagation distance of the Airy beam leads to the increase of four times of the transverse acceleration reached in a crystal of 1 cm: $x_{sol,11\ \mu m,2\ cm} = -103\ \mu m = -9.3x_A$.

Similar to the previous section, we observe the output beam under biased focusing conditions and the results are presented on Figure 2.13. As depicted on Figures 2.13(a), 2.13(b) the Airy beam also undergoes self-focusing and off-shoots a soliton at $x_{sol,11\ \mu m,2\ cm} \approx -9.5x_A$, matching with the theoretical output position. If we compare the soliton beam in a short and long crystal, the solitonic intensity peak increases with the crystal length (300 % for $L = 1$ cm [Fig. 2.12] to 1000 % for $L = 2$cm [Fig. 2.13(c)]). This observation leads us to the conclusion that the propagation length increases the self-focusing effect on the Airy beam.
But the most striking result is the low bias voltage enabling the formation of an Airy-soliton: in the 2cm-crystal we already observe the solitonic peak at a voltage value ten times lower than in the 1cm-crystal. This phenomenon is due to the higher sensitivity to the self-focusing effect induced by the bias external voltage as the propagating beam undergoes stronger diffraction due to the longer crystal length L. The propagation length offers an interesting parameter to optimize the solitonic behavior as it enables to create an off-shooting soliton over a much larger transverse distance from the linear output position.

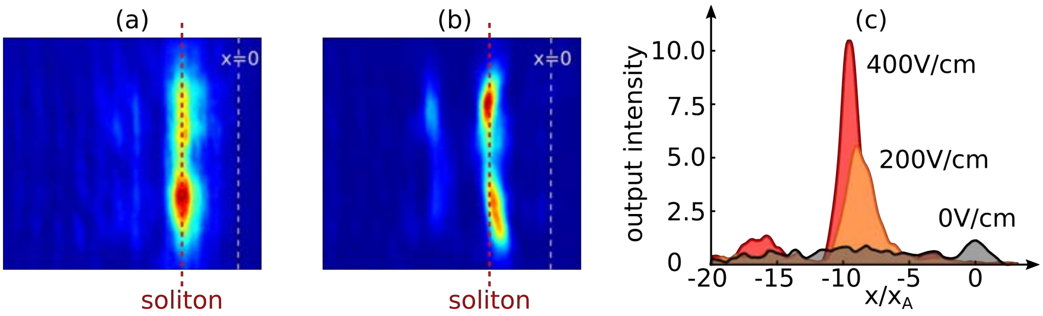

Figure 2.13: Influence of the nonlinear propagation length on the Airy-soliton at the output of the 2cm-crystal (with $x_A = 11\ \mu$m and $P_A = 50\ \mu$W). Optical intensity distribution of the superimposed off-shooting soliton and accelerating beam (a) for $E_e = 200$ V/cm and (b) for $E_e = 4$ kV/cm. (c) Transverse intensity profile of the output Airy-soliton for increasing bias electric field $E_e$.

Finally we here report on the first experimental Airy-soliton observed during the self-focusing process of an Airy beam under biased nonlinear conditions.

The solitonic structure confirms the theoretical prediction, where an Airy beam turns into an off-shooting soliton and an accelerating structure. By tuning the nonlinearity parameters (optical power and electric bias voltage) or the diffraction parameters (beam's size and propagation length), the self-focusing into the Airy-soliton can be enhanced and reach high intense beams shifted over several lobe's sizes along the transverse axis. This solution differs from a self-trapping Airy beam structure, as the solitonic structure does not preserve the Airy shape and is, so far, only observed during the transient self-focusing regime.

While the existence of the Airy-soliton has been predicted in literature, the influence of the system's parameters has not been explored. In the next section we introduce a numerical model to analyze the self-focusing of an Airy beam in a biased photorefractive crystal.

## 2.3 COMPARISON WITH THE THEORY

In this section, we analyze numerically optical waveguide structures created in photorefractive media by one Airy beam under nonlinear self-focusing conditions. When a positive external electric field is applied to the photorefractive crystal, we show that multiple waveguiding structures are photoinduced by a single Airy beam. In that way, an optical Gaussian beam can be linearly guided along a deflecting trajectory or split into several output beams.

### 2.3.1 *Simulation model*

Our typical interaction scheme is depicted on Figure 2.8. It illustrates the linear propagation of an Airy beam in an unbiased photorefractive crystal. To simulate the propagation of the Airy beam along the crystal we consider the normalized numerical model suggested by Belić *et al.* [138], where an optical beam $F(x,t)$ propagates following the nonlinear paraxial wave equation in a photorefractive crystal can be modelled using the following equations:

$$i\partial_z F + \partial_x^2 F = \Gamma E_0 F, \tag{2.3}$$

$$F(x, z=0) = F_0 Ai\left(\frac{x}{x_A}\right) \exp\left(a\frac{x}{x_A}\right), \tag{2.4}$$

$$\Gamma = (knx_A)^2 \, r_{eff} E_e, \tag{2.5}$$

$$\tag{2.6}$$

where $\Gamma$ is the nonlinear photorefractive coupling strength, $r_{eff}$ is the effective component of the electro-optic tensor, $E_e$ the external electric field and $E_0 = E_{sc}/E_e$ is the homogeneous part of the x-component of the photorefractive space charge field. As the optical intensity modulates the space charge field, the steady-state $E_0$ is equal to $E_0 = -I_0/(1+I_0)$. The time-dependency of the space charge field $E_0$ is calculated from :

$$\tau\partial_t E_0 + E_0 = - \mid F \mid^2 / \left(1 + \mid F \mid^2\right), \tag{2.7}$$

where $\tau = \tau_0/(1+I_0)$ is the relaxation time of the crystal, with $\tau_0$ the characteristic response time of the crystal ($\approx 100$ ms in the SBN). The numerical system is completely dimension-free, in particular the propagation $z$-axis is normalized to the diffraction length $L_d = 2kx_A{}^2$ and the transverse $x$-axis is normalized to the beam's waist being the lobe's waist $x_A$ in the case of the Airy beam.

This kind of nonlinear propagation of non conventional beam enables us to optically induce complex waveguiding structures in the photorefractive material through the Pockels effect. The induced refractive index distribution is then related to the combination of the accelerating Airy beam and its off-shooting soliton superimposed in $F$ [Eqs. 2.3,2.5,2.7].

The induced refractive index profile is numerically simulated via a Fast Fourier Transform Beam Propagation Method. We fix the crystal length $L = 1$ cm, $\Gamma = 9$, $a = 0.09$, $x_A = 7.5$ µm, the normalized input electric field of a beam $F_0 = \sqrt{2.5}$. The simulation algorithm is detailed in Appendix C.

In this paragraph we consider optical waveguides created by a single Airy beam $F$ propagating from $z = 0$ to $z = L$ ($z = 0 \to L$) with a focusing nonlinearity. Figure 2.14 displays the intensity of the self-focused Airy beam. This results concern the stationary state that is reached after a transient duration equal to $6\tau$. At $z = 0$, we indicate only 2 positions of high index variations corresponding to the two first lobe orders of the input Airy function (1,2 in Figure 2.14). Interestingly and similar to the references [93, 96], the initial Airy beam with its curved trajectory turns into an "off-shooting" soliton as it propagates along the $z$-axis ($1'$ at $z = L$ in Figure 2.14). To better understand the roles of the system's parameters, we will analyze in the next section the soliton structure of an Airy beam at the output of a biased medium.

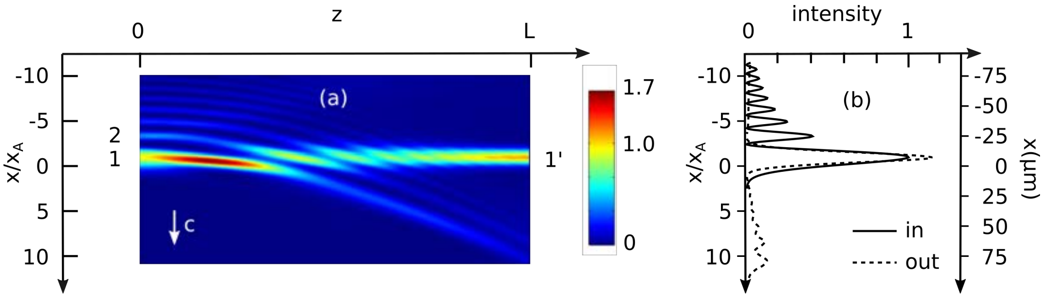

Figure 2.14: (a) Normalized intensity distribution of a self-focused Airy beam propagating in a focusing photorefractive crystal with $x_A = 10$ µm and $L = 1$ cm, (b) corresponding transverse intensity profiles.

### 2.3.2 *Theoretical solitonic self-focusing*

The experimental study in Section 2.2 has shown that the solitonic self-focusing strength of the Airy beam can be mainly tuned via two parameters: the external bias electric field $E_e$ and the optical power of the propagating beam $P_A$. In our theoretical model these parameters are related to $\Gamma$ and $F_0$ and Figure 2.15 illustrates the outcome of the study.

Under linear conditions $\Gamma = 0$, the Airy beam propagates along the crystal without self-focusing [Fig. 2.15(a)]. At the output of the crystal, $z = L$, the accelerating beam (black solid line in Figures 2.15(e) and 2.15(f)) has shifted of 34 µm and the peak intensity is at 60 % of the initial maximum value. When adding an external bias electric field, the nonlinearity strength $\Gamma$ increases and leads to a self-focusing of the Airy beam along the transverse $x$-axis of the crystal. As depicted on Figures 2.15(b) to 2.15(d), the optical field shifts towards the higher lobe orders to focus into a strong solitonic beam at the zero-deflection position $x/x_A = -3.4$ for $\Gamma \geqslant 10$.

The positive influence of $\Gamma$ on the solitonic self-focusing effect is highlighted on Figure 2.15(e), where the transverse intensity profile of the output beam at $t_f = 6\tau$ is plotted for increasing $\Gamma$-values. In comparison with the experimental observations presented previously on Figure 2.12(b), the theory presents the same results. The solitonic peak is enhanced by the external electric field (proportional to the $\Gamma$-parameter) up to 160 % of the input peak and 260 % of the linear output peak. Interestingly this maximum ratio at $\Gamma = 15$ exactly matches the experimental value for $E_e = 3$ kV/cm.

Secondly Figure 2.15(f) depicts the evolution of the off-shooting soliton for an increasing electric field $F_0$ for $\Gamma = 10$. As for the experimental results [Fig. 2.12(a)], the optical power increases the nonlinearity of the photorefractive system hence the self-focusing strength. Similar to the peak range reached for high $\Gamma$-values, we can confirm that the optical power plays a similar role in the nonlinear photorefractive self-focusing effect as the bias electric field.

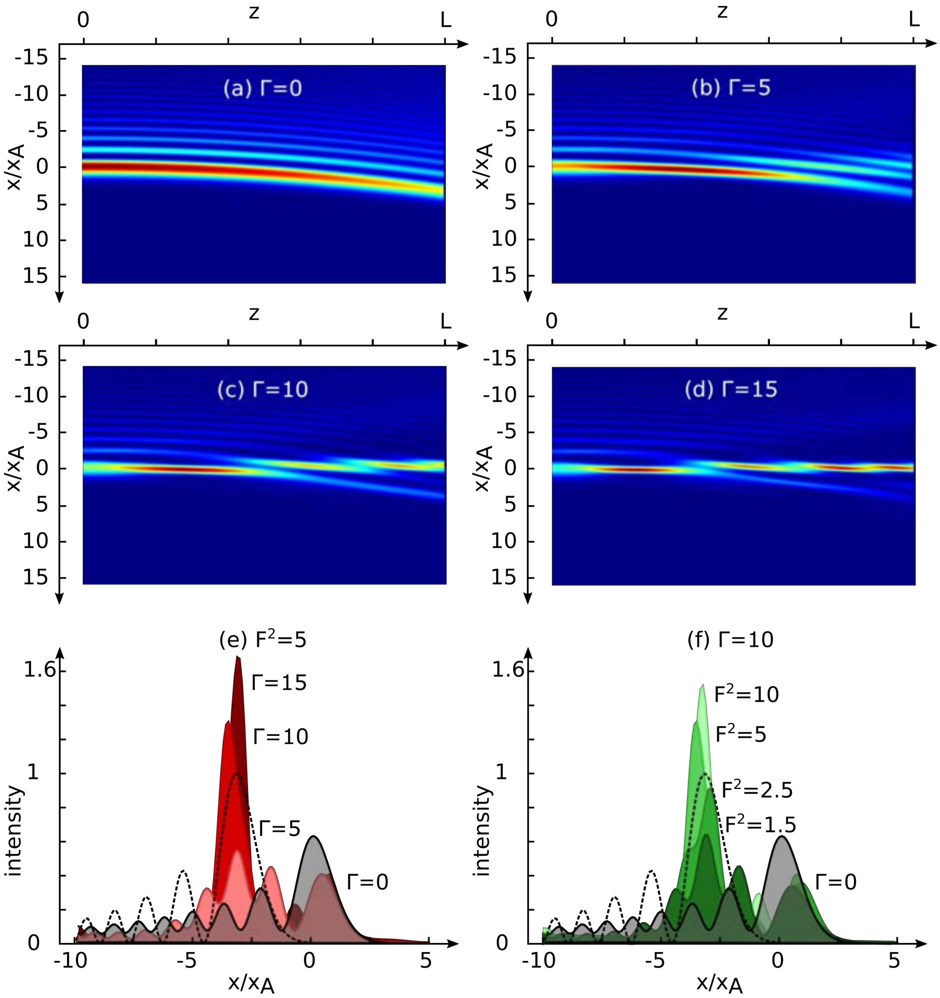

Figure 2.15: Propagation of a self-focused Airy beam propagating in a photorefractive crystal, with $x_A = 10\ \mu m$, $L = 1$ cm and $t_f = 6\tau$. Intensity distribution along the crystal with $F_A = \sqrt{5}$ under (a) linear and (b)-(d) nonlinear condition with an increasing bias electric field ($\Gamma = (knx_A)^2 r_{eff} E_e$). Transverse intensity profiles of the off-shooting soliton at the output of the crystal, $z = L$ and $t_f = 6\tau$, for (e) increasing electric field and (f) increasing optical power. The input Airy profile at $z = 0$ is plotted by a dashed line.

## 2.4 CONCLUSION AND COMPARISON WITH GAUSSIAN SYSTEMS

To conclude, we have experimentally demonstrated the existence of solitonic beam structures induced by an Airy beam under strong nonlinear self-focusing conditions. These results match the theoretical predictions in the literature: the Airy beam splits into a weak accelerating structure and an off-shooting soliton propagating along the crystal without transverse acceleration.
While the experimental Airy-soliton is only transient contrary to our theoretical results, this chapter enables to further deepen the analysis of the self-focusing nonlinearity on an accelerating Airy beam. In particular the outcomes enlighten the complementary roles of the optical field of the propagating Airy beam and the external bias electric field. Both parameters enhance the self-focusing of the Airy beam into mainly a strong and narrow soliton. If we consider the application in all-optical waveguiding, these results suggest the study of the waveguiding properties of the photoinduced in the photorefractive crystal. This question will be answered later in Chapter 4.

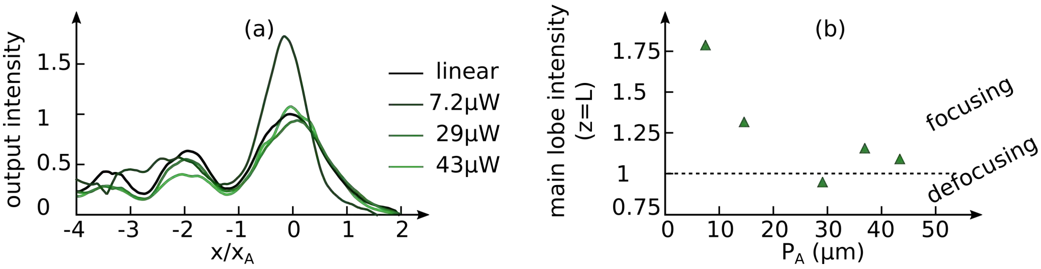

Figure 2.16: (a) Normalized intensity distribution of a self-trapped Airy beam propagating in a focusing photorefractive crystal at $t = 30$ s, with $x_A = 14$ μm, $E_e = 4$ kV/cm and $L = 1$ cm, (b) detailed evolution of the normalized maximum peak value of the self-focused Airy beam for increasing optical power.

Nevertheless the stability of the solitonic self-focusing appears to be power-dependent. In particular if we focus on the output beam 30 s after the electric field has been switched on, the beam does not remain in a self-focused regime for higher power. While Figure 2.12(a) indicates a continuous increase of the solitonic peak for $P_A \in [0.9W; 4.3]$ μW, when further increasing the optical power, the steady-state intensity distribution of the nonlinear Airy beam evolves towards an Airy-like defocused energy profile as depicted on Figure

2.16(a). The increase of the defocusing effect with optical power depicted on Figure 2.16(b) seems to be in contradiction with the aforementioned results, as the optical power increases the self-focusing nonlinearity. But as we will detail in the next chapter, the study of the transient self-focusing of the Airy beam reveals several mechanisms as in Gaussian soliton physics.

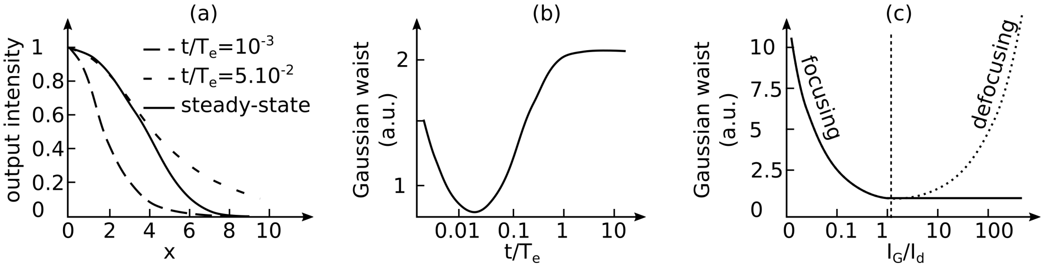

Figure 2.17: (a) Time evolution of the normalized soliton profile issued from a Gaussian beam. (b) Time evolution of the normalized soliton waist for the same conditions as in (a). (c) Evolution of the output beam's waist in the transient (solid line) and in the final steady-state (dashed line) regime for increasing optical power. (a) and (b) extracted from [108] and (c) extracted from [109].

When a Gaussian beam propagates under a strong self-focusing nonlinear effect above a threshold value, the output beam first presents a solitonic self-focused behavior but then relaxes towards a defocused regime as depicted on Figures 2.17(a) and 2.17(b) [108]. More generally the study of the self-focusing of a Gaussian beam has been extensively studied. In particular it has been shown that the solitonic beam can reach the steady-state regime when a background illumination is applied along the crystal [110–114]. Figure 2.17 depicts the evolution of the maximum self-focusing of the Gaussian beam (i.e. the minimal waist) in the transient regime (dashed line) and the final steady-state regime (solid line) for increasing intensity ratio $I_G/I_d$. First the self-focusing effect is enhanced by $I_G/I_d$ until reaching a minimum beam size. Because the transient and final regimes are superimposed, the solitonic structure is stabilized in the medium. But for $I_G/I_d > 3$, the final beam waist starts increasing even further than the initial size, while the transient self-focusing value remains at the minimum. The nonlinear system then has reached the saturation limit for the self-focusing effect, which is not steady-state anymore. In absence of background illumination, the system therefore can not present steady-state Gaussian solitons.

While the aim of this chapter was to observe and analyze solitonic structures from initial Airy beams, the results do not represent the steady-state regime, but transient instants of the self-focusing Airy beam. These observations lead us to consider the temporal evolution of the Airy beam under self-focusing conditions in the next chapter. We will show that a too high nonlinearity can lead to first over-focusing of the Airy-soliton then relaxing into a defocused regime.

# 3

# TRANSIENT PROPERTIES OF A SELF-FOCUSING AIRY BEAM AND ITS ANALOGY WITH OPTICAL GRAVITATIONAL LENSING

We unveil experimentally the transient self-focusing properties of a 1D-Airy beam in a photorefractive crystal under focusing conditions. The transient evolution involves both self-bending and acceleration of the initially launched Airy beam. This is due to the onset of an off-shooting soliton and the resulting nonlocal refractive index perturbation, which acts as a gravitational potential in an accelerating framework. The gravitational lensing and tidal forces resulting from a single light beam can be controlled all-optically through the photorefractive nonlinearity by varying the Airy beam's intensity.

The context of this chapter is related to the following publication:
Noémi Wiersma, Nicolas Marsal, Marc Sciamanna, Delphine Wolfersberger, "Optical gravitational lensing in the transient self-focusing of an Airy beam", *submitted for publication*, 2016).

## 3.1 GRAVITATIONAL EFFECTS AND ITS ANALOGIES IN PHYSICS

### 3.1.1 *Phenomenon*

How wave propagation is modified in the presence of a gravitational field remains one of the central questions of modern physics. Most probably the most satisfactory answer was given by Einstein's general relativity theory [115], the foundation of which being the principle that acceleration and gravitational field are equivalent. The significance of the general relativity theory was confirmed shortly afterwards by the observation of light gravitational lensing [116], i.e. light bending induced by the long-range interaction with matter, and most recently drew cheers with the observation of gravitational waves [117].

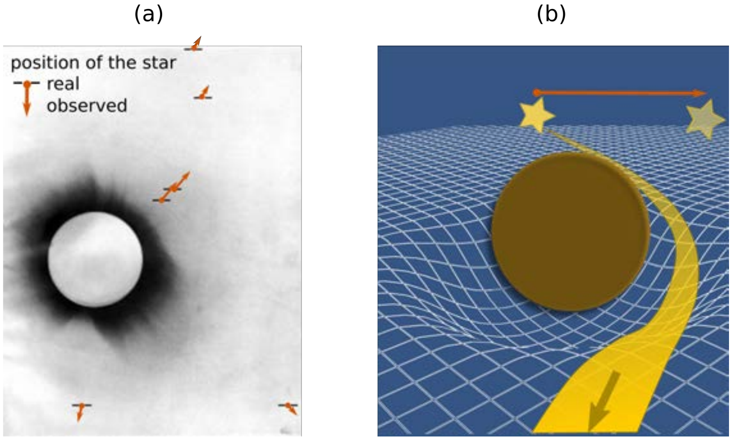

Figure 3.1: Gravitational lensing in space. (a) Negative of the solar eclipse of May 29, 1919 on the Island of Principe. The star shifts are magnified to better visualize the lensing effect. Source: light2015blog.org. (b) Schematic bending of light induced by the gravitational lensing effect when approaching a massive object. The orange arrow illustrates the magnified shift between the real and observed position of the star (similar to Fig 3.1(a)).

Figure 3.1(a) presents the total solar eclipse of May 29th 1919 observed by the English scientific Sir Arthur Eddington on the Island of Principe near the African west coast. During the eclipse, he took pictures of the stars near the sun, which are marked by horizontal lines on Figure 3.1(a). Afterwards he compared the positions of these stars during the eclipse and the night (in absence of sun). As depicted on Figure 3.1(a) the stars appeared shifted away from the sun with

an angle up to 1.75 arc seconds during the eclipse. This optical shift effect of light around massive object is due to the gravitational lensing effect theoretically predicted by Albert Einstein in 1916.
To picture the phenomenon binding acceleration of light to gravitation in spacetime, the universe should be imagined empty as a flat sheet in spacetime, where light propagates along straight lines. The presence of massive objects, such as stars or planets as on Figure 3.1(b), induces a distortion in the spacetime "sheet". As depicted on the schematic illustration of Figure 3.1(b), when light approaches a massive object its trajectory will be deviated. The consequence of star light bending is that stars normally seen at one position in the "empty" sky, will appear shifted at an other position, when the sun is in front of them.

The questions surrounding the necessity for a quantum description of gravitation have recently motivated the study of an alternative, non relativistic approach with the so-called Schrödinger-Newton equation [118]. The suggested model is a nonlinear modification of the Schrödinger equation with a Newtonian gravitational potential where the gravitational potential $\Phi$ emerges from the treatment of the wave function $\psi$ as a mass density:

$$i\hbar\frac{\partial\psi}{\partial t} = -\frac{\hbar^2}{2m}\Delta\psi + m\Phi\psi, \tag{3.1}$$

where $\Delta\Phi = 4\pi G m|\psi^2|$. $G$ is the gravitational constant and $m$ is the particle's mass. Inserting a potential that depends on the expectation value of the wavefunction makes the Schrödinger equation non-linear and changes its properties. The gravitational interaction is always attractive and thus tends to contract matter distributions eventually counter-balancing the wave function spreading from the linear Schrödinger equation.

Although Equation 3.1 has been developed in the context of quantum gravitation, Equation 3.1 is a specific form of the nonlinear Schrödinger equation, which is familiar to us in many fields of science. It is used in hydrodynamics to model the dynamics of envelope of modulated water waves and is thought to explain the emergence of rogue waves [119]. In optics, the nonlinear Schrödinger equation has been first introduced for the nonlinear propagation model in optical fiber (see Section 1.3.3, [64]), where a particular solution are one-dimensional optical soliton pulses. The mathematical analogy between quantum gravitation and nonlinear optics has raised much interest in physics and in particular encouraged the development of optical experimental systems to study the gravitational physics.

### 3.1.2 *Observations in optics*

In optics, the Schrödinger-Newton equation suggests that a nonlocal refractive index perturbation acts as a gravitational potential that perturbs wave propagation in an accelerating or gravitational framework, hence allowing for laboratory investigations of analogous gravitational effects.

In that context, it is remarkable to develop laboratory-scale experiments in which analogous gravitational effects can be observed and related physics be tested more systematically. Thanks to the most recent developments in material engineering, nonlinear optics and light shaping, optics has offered numerous analogies with gravitational effects [120–123]. The fundamental principle is that waves in moving media behave like waves in gravitational fields (i.e. in curved spacetime geometry). For example in reference [120] Leonhardt *et al.* demonstrate an event horizon analogous to the one experienced when approaching a black hole using intense light pulses propagating in optical fiber. Another optical system has been suggested in reference [121] based on ultrashort intensity filaments propagating in bulk medium. The propagating light pulse then interacts linearly with a refractive index grating induced by Kerr optical nonlinearity that operates like a moving medium travelling faster than light, hence preventing light pulses to propagate backwards.

Other optical experiments showing gravitational effects include light bending and trapping in specifically designed metamaterials that mimic curved spacetime geometries [124, 125] and gravitational pull of accelerating solitons in optical fiber supercontinuum generation [126]. As an example, reference [125] suggests a direct investigation of light trapping around a microsphere to mimic the gravitational lensing effect in a curved spacetime as depicted on Figure 3.2. As the microsphere is embedded into the planar grated polymer waveguide, surface tension effects induce a distortion of the waveguide around it. Hence, light propagation will undergo lensing and be eventually captured in unstable circular orbits.

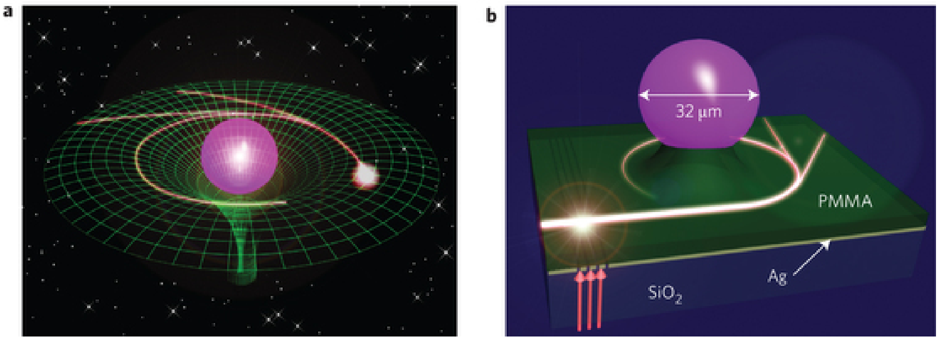

Figure 3.2: Analogue of light deflection in a gravitational field and microstructured optical waveguide. (a) Scheme of light bending due to the gravitational field induced by a massive stellar object. (b) Schematic view of the microstructured optical waveguide formed around a microsphere. In the experimental set-up, a grating is drilled across a silver layer, which is then used to couple the incident laser light (red arrows) into the waveguide. Extracted from [125].

Very recently, the long-range interactions inherent to gravitational lensing were analyzed in the nonlinear interaction between an accelerating (Airy) beam and a spatial soliton created by self-focusing of a Gaussian beam through thermal nonlinearity [Fig. 3.3(a)] [123]. As introduced in Section D.2, an optical Airy beam consists of a main lobe and a tail of smaller lobes that provide acceleration to the main lobe, hence the parabolic trajectory in the spatial domain. As depicted on Figure 3.3(b), the nonlocal refractive index change related to the self-focused intense soliton acts like a mass whose gravitational field deviates the incoming accelerating light beam. As a result the physics mimics the predictions of the so-called Schrödinger-Newton equation.

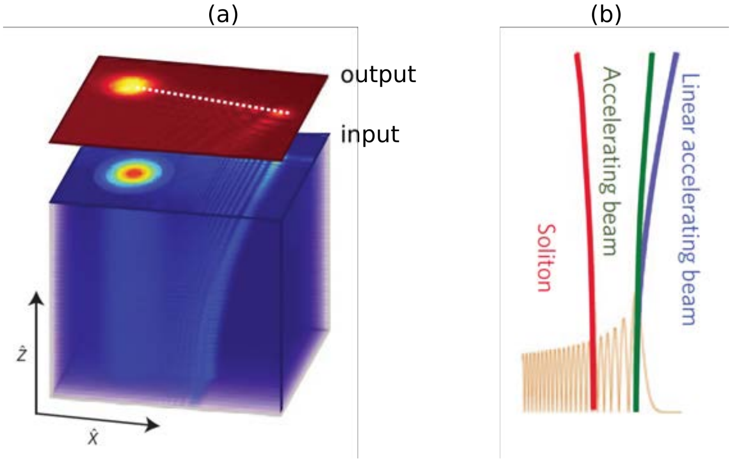
(a)
output
input
$\hat{z}$
$\hat{x}$
(b)
Soliton
Accelerating beam
Linear accelerating beam

Figure 3.3: Optical analogy with gravitational lensing between a powerful soliton beam ('star') and a 2D accelerating Airy beam in a nonlinear Kerr medium. (a) Numerical intensity distribution at the input plane of the medium (blue) and experimental intensity distribution at the output plane (red). (b) Schematic top-view sketch of the accelerating Airy beam interacting with the soliton-"star" in the linear (blue curve) and the nonlinear (green curve) regimes. Extracted from Ref. [123].

## 3.2 EXPERIMENTAL TRANSIENT SELF-FOCUSING OF AN AIRY BEAM

In this chapter we study the transient self-focusing properties of an Airy beam in a photorefractive medium. We report on the first theoretical and experimental analysis of the Airy beam after a nonlinear propagation through a biased crystal. In particular we focus on the transient evolution from the linear accelerating beam towards the self-focused solitonic regime and analyze the influence of the nonlinear strength (optical power) on the spatiotemporal dynamics and the self-focusing strength.

Recent work has shown that propagation in a nonlinear medium (thermal nonlocal nonlinearity) results in a non local refractive index change that acts as a gravitational potential hence altering the Airy beam propagation in a similar way as what can be concluded from general relativity theory. In particular the refractive index changes plays the role of a massive object that, following general relativity theory, induces gravitational lensing and tidal forces on light rays as a result of the space-time curvature. In that context it is interesting to analyze to which extent the above mentioned findings share indeed a similar analogy in optics with gravitational effects.

### 3.2.1 *Experimental setup*

As already detailed in the previous Chapter 2, we consider the propagation a one-dimensional Airy beam into a biased photorefractive SBN-crystal with dimensions 5 mm*5 mm*1 cm ($n_{SBN} = 2.3$) as depicted on Fig. 3.4. The field distribution of a one-dimensional Airy beam $\psi$ is defined by the initial condition:

$$\psi(x)_{z=0,t=0} = Ai\left(\frac{x+x_A}{x_A}\right) exp\left(a\frac{x+x_A}{x_A}\right), \tag{3.2}$$

where $x_A = 10$ µm is the main lobe's waist and $a = 0.04$ the truncation parameter of the Airy beam. Under linear conditions, the beam propagates along the z-axis of the crystal with a transverse parabolic acceleration along the c-axis (parallel to the x-axis) of the photorefractive crystal. In our experiment we set $x = 0$ as the transverse output position of the linear Airy beam. The transverse parabolic acceleration is mathematically described by the equation 2.2. As shown above, the Airy main lobe has initially been launched at $-x_{peak}(z=0) = 34$ µm

[Fig. 3.4]. At the end of previous Chapter 2 we have observed a defocusing behavior of the Airy beam under focusing bias electric field [Fig. 2.16]. To study and enhance the stability of the self-focusing effect of the Airy beam, we will therefore also consider an additional background illumination $I_d$ (as for "dark intensity") along the (x,z)-plane as illustrated on Figure 3.4.

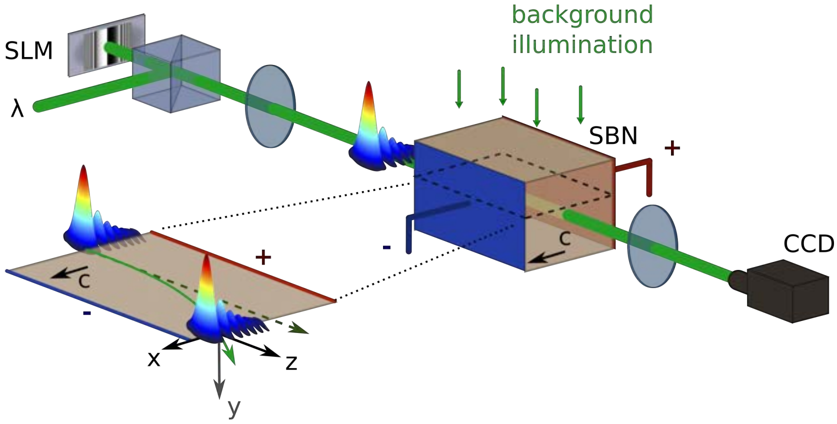

Figure 3.4: Observation of the self-focusing 1D-Airy beam propagating in a biased photorefractive crystal: experimental setup.

### 3.2.2 *Transient dynamics of the Airy-soliton*

When an external bias electric field $E_e$ is applied along the x-axis at $t = 0$ s, the optical Airy beam photoinduces a refractive index variation in the crystal through the Pockels effect. The photorefractive effect in the SBN-crystal induces both a focusing and a shift of the optical energy along the transverse c-axis thanks to mainly two contributions: the drift effect induced by the bias electric field and the diffusion effect [108]. To optimize the nonlinear photorefractive and solitonic effects of our system, the external bias electric field is set to $E_e = 4$ kV/cm.

Figures 3.5(a)-3.5(e) show the evolution of the intensity profile of the output beam versus time. Starting at $t = 0$ s, the intensity shifts towards the position of the linear second Airy lobe, further towards the higher lobe's orders [Fig. 3.5(a)-3.5(b)] and finally reaches a maximum transverse shift $x = -34$ µm at $t = 640$ ms [Fig. 3.5(c)]. We will further refer to this position as the off-shooting soliton's po-

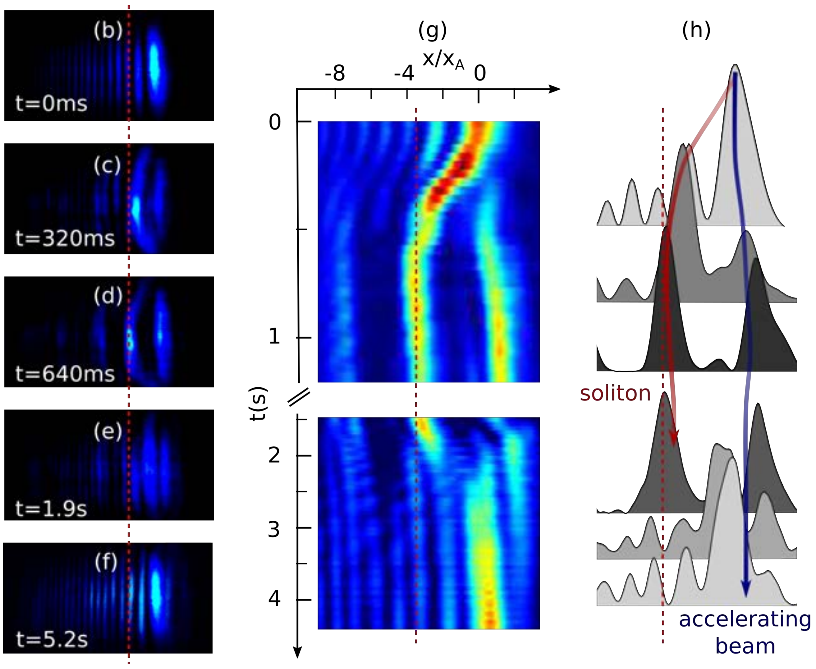

Figure 3.5: Transient dynamics of the Airy-soliton ($x_A = 10$ μm). (a)-(e) Transverse intensity profile of the output beam under nonlinear focusing conditions ($E_e = 4$ kV/cm, $P_A = 400$ μW) for increasing times. (f) 1D intensity profile along time. (g) Top-view sketch of the accelerating beam interacting with the off-shooting soliton, superimposed with their intensity profiles along time.

sition (red dashed line). Then, on a longer time-scale a relaxation-type dynamics is observed towards a redistributed Airy-like profile similar to the input beam at $t = 0$ s [Fig. 3.5(d)-3.5(e)].

The spatiotemporal dynamics of the nonlinearly propagating Airy beam can therefore be summarized in three stages. (i) First the output beam focuses towards the red dashed line of Fig. 3.5(b). (ii) Then we observe two co-existing beam's structures [Figs. 3.5(c), 3.5(d)]: the so-called off-shooting soliton at $x/x_A = -3.7$ and an accelerating structure at $x/x_A = 0.5$ with similar intensities. (iii) Finally the two previous solutions merge and form a new Airy-like structure on a longer time scale. Similar to the relaxation dynamics of a spatial soliton formed by self-focused Gaussian beam [48, 108, 113, 128, 129], the accelerating beam therefore relaxes for longer times into a less focused multi-lobe beam with a peak intensity that shifts back towards the $+x$-axis [Fig. 3.5(f)].

### 3.2.3 *Influence of the optical nonlinearity*

As we will now detail, the nonlinear interactions that emerge from the transient behavior of a single self focused Airy beam [(i) to (ii)] can be compared to the gravitational interactions such as gravitational lensing induced by a massive object (the off-shooting soliton) that attracts and deflects light from its own curved trajectory (the Airy beam).

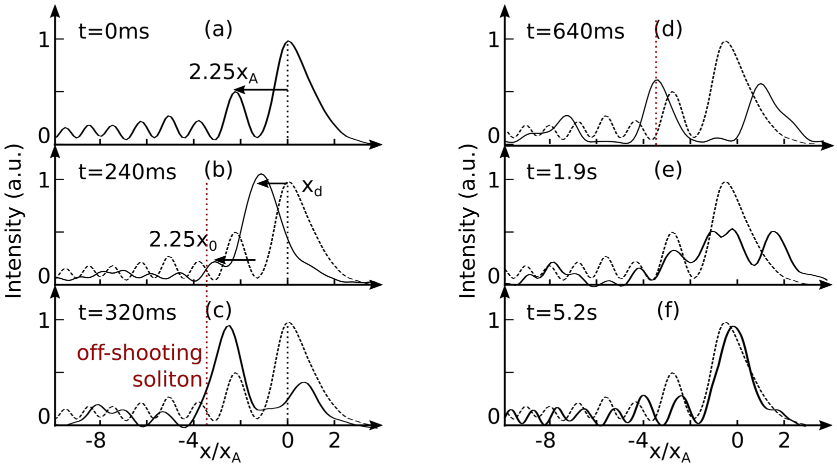

Figure 3.6: Intensity profile of the self-focused output Airy beam along time, $P_A = 400\ \mu W$. (a) Linear intensity profile, (b)-(d) build-up of the off-shooting soliton, (e)-(f) relaxation into a multi-lobe stationary solution. The dashed lines correspond to the linear profile.

In order to characterize the attraction and deflection, we plot in Fig. 3.6 the nonlinear transverse intensity profile of the output beam for increasing times compared to the linear case at $t = 0$ s [Fig. 3.6(a)]. $x_d$ corresponds to the shift of the accelerating wave packet induced by the attraction of the off-shooting soliton (the massive object) with respect to the initial launched Airy beam. The position of the initial Airy main lobe defines the zero attraction position. Thus, $x_d < 0$ illustrates the attraction of the Airy beam towards the off-shooting soliton's position ($x/x_A = -3.7$, see Figs. 3.6(c), 3.6(d)).

It is worth mentioning that on Figs. 3.6(c)-3.6(e) the output profile of the accelerating structure does not match with an Airy distribution anymore, but the output beam still presents secondary lobes. This is due to the multi-channel waveguiding structure photoinduced by the multi-lobe structure of the Airy beam at $t = 0$ s. After $t = 1.9$ s, the solitonic structure vanishes and the intensity redistributes into an Airy-like profile [Fig. 3.6(f)].

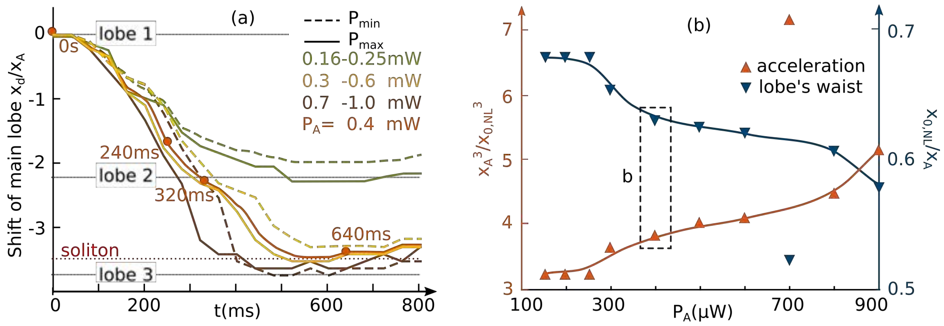

Figure 3.7: Experimental lensing effect self-induced by a self-focused Airy beam. (a) Normalized transverse position $x_d$ of the output intensity peak versus time for different input powers. (b) Normalized acceleration effect: normalized acceleration and main lobe's waist $x_0$ of the Airy beam nonlinearly attracted towards its off-shooting soliton for increasing input power $P_A$.

Figure 3.7(a) details the temporal evolution of the transverse intensity peak's position at the output of the crystal during the transient build-up regime of the off-shooting soliton ($t < 800$ ms, stages (i)-(ii)). Initially the Airy-distributed energy is mainly concentrated in the first lobe at $x = 0$. After the focusing nonlinearity of the system is electrically switched on at $t = 0$ s, the position corresponding to the peak intensity shifts towards the position of the higher lobes' orders along the $-x$-axis (bending effect). Then, around $t = 500$ ms, the position of the peak intensity reaches a quasi-steady position corresponding to the location of the off-shooting soliton until, as depicted on Fig. 3.5(f), for longer times beyond t=1 s, the position of the peak intensity shifts back into the position of the main lobe of the accelerating beam.

As observed in recent experiments using Kerr thermal nonlinearity [123], our experiment suggests that the nonlocal photorefractive nonlinearity acts as a gravitational potential in an accelerating framework. To further support this statement, we now analyze whether the gravitational effects can be tuned by varying the nonlinearity. In what follows we vary the intensity of the input Airy beam to tune the refractive index modulation depth and analyze the corresponding self gravitational effects. Figure 3.7(a) shows the gravitational lensing induced through the deflection of the accelerating beam for increasing Airy beam powers. Similarly to the self-focusing properties of Gaussian beams [48, 67], the transient time towards self-focusing is smaller when the input light intensity increases: a higher intensity reduces the response time of the process. In addition the increase of input power modifies the transient self-focusing properties. As depicted on Figure 3.7(a), when the power increases from $P_A = 250$ μW to $P_A = 300$ μW (green and yellow curves), the maximum shift does not increase linearly, but jumps from the former second lobe's position ($x/x_A = -2.25$) to the theoretical output position of the off-shooting soliton. When further increasing the power ($P_A > 700$ μW), the maximal bending of the beam still deviates but saturates at the third lobe's position ($x/x_A = -3.7$). By varying the optical power it is therefore possible to balance between diffraction and nonlinearity and tune our nonlinear system from a weak interaction ($P \leqslant 250$ μW) to a strong attraction ($P > 250$ μW) between the accelerating wave packet and the solitonic structure.

The off-shooting soliton not only attracts the accelerating beam but also influences its acceleration similarly to tidal forces in gravitational lensing. Figure 3.7(b) depicts the normalized peak acceleration for increasing input powers $P_A$, calculated as follows:

$$\left(\frac{\partial^2 x_{peak}}{\partial z^2}\right)_{NL} \Big/ \left(\frac{\partial^2 x_{peak}}{\partial z^2}\right)_{lin} = \left(x_A/x_{0,NL}\right)^3 , \tag{3.3}$$

where $x_0$ is computed by fitting the intensity profile with an Airy beam profile [Fig. 3.6(a)-3.6(b)]. The acceleration rate increases from three ($P_A = 200$ μW ) to seven times ($P_A = 900$ μW) the initial value. On the same graph we also plot the evolution of the interlobes' distance versus power. The data shows on Fig. 3.7(b) a tightening of the interlobes' distance revealing the presence of tidal forces during the solitonic build-up regime ($t < 500$ ms). The gravitational force exerted on the different lobes varies from one lobe to the next, owing to their different lobe-soliton distances and the self-induced gravitational potential of the accelerating beam. This effect gives rise to tidal forces that deform the structure of the wave packet as it propagates and tend to pull the lobes towards one another.

As already mentioned, the photorefractive nonlinearity of our system can be tuned by different physical parameters such as the external bias electric field ($E_e$), the intensity of the launched beam (with $I = P_A/(2\pi {x_A}^2)$ in the main lobe) but also the so-called dark intensity of the photorefractive crystal via an external background illumination [Fig. 3.4]. Such an illumination tends to artificially increase the dark conductivity of the photorefractive crystal which is initially

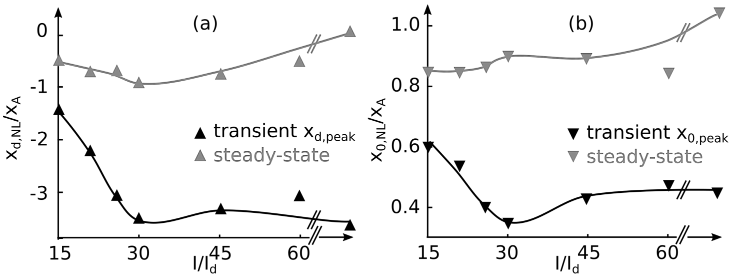

Figure 3.8: Influence of background illumination on the transient and final self-focusing beam: (a) for the transverse beam's shift $x_d$ (attraction parameter) (b) and the interlobes' distance $x_0$ (cubic proportional to the acceleration).

very weak ($I/I_d \approx \infty$). In photorefractive systems using conventional beams it has been shown that $I_d$ plays a significant role during the self-focusing and solitonic regime [67, 109] (see Fig. 2.17(c)). In our Airy beam system, we question how such a background illumination may influence the previous results. Figure 3.8(a)-3.8(b) depict the influence of $I/I_d$ on the transient and corresponding steady state ($t > 8$ s) peak values of $x_d$ and $x_0$.

On Fig. 3.8(a), for $I/I_d = 15$ the self-bending of the Airy beam observed previously is reduced in the transient regime from $x_{d,noI_d} = -3.7x_A$ to $x_{d,I/I_d=15} = -1.5x_A$. Contrary to the case without background illumination, where the Airy-like structure of stage (iii) is superimposed with the initial Airy beam [Fig. 3.6(f)], adding $I_d$ enables the accelerating beam to remain shifted even in the steady-state regime (maximum shift of $-x_A$ for $I/I_d = 30$). As depicted on Fig. 3.8(b), the background illumination also influences the self-focusing effect both in the transient and the steady-state regime. In particular we still observe self-focusing of the accelerating beam after $t > 8$ s.

In terms of optical gravitational lensing, the background illumination enables us to control the nonlinearity of the system and therefore the attraction and tidal force applied on the Airy beam [Fig. 3.8(a)-3.8(b)].

## 3.3 THEORETICAL CONFIRMATION

Our experimental results can be reproduced qualitatively well by numerical simulations (see Figure 3.9). In the paraxial approximation, the nonlinear propagation of the Airy beam in the photorefractive crystal can be simulated by the nonlinear Schrödinger equation using the simulation model described earlier in Chapter 2 with the equations Eq. 2.3-2.7. In this model $\tau$ defines the photorefractive relaxation time and $F_0$ the normalized amplitude of the Airy beam, which is defined by the truncation $a$ and the lobe's waist $x_A$.

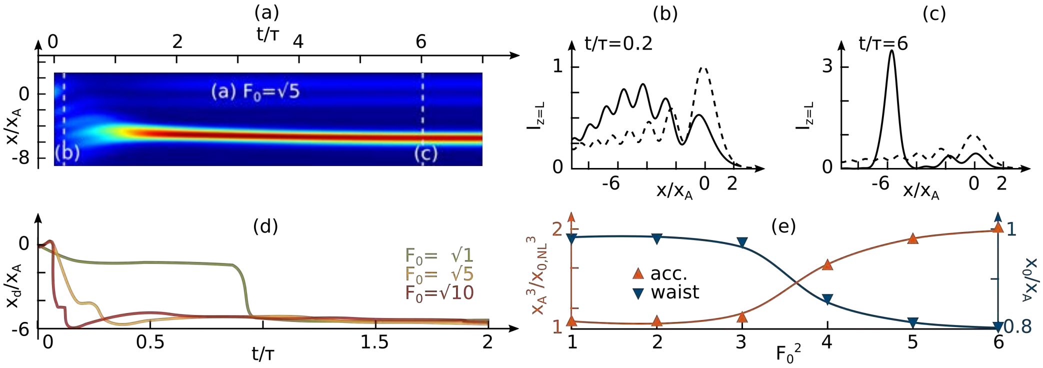

Figure 3.9: Numerical study: Airy-induced optical lensing. (a) Intensity profile of the output beam along time; transverse intensity profiles in the (b) transient and (c) steady-state regime. The dashed lines correspond to the linear profile. (d) Transverse position of the output intensity peak versus time for different input powers. (e) Acceleration effect: normalized acceleration and main lobe's waist $x_0$ of the Airy beam for increasing input intensity.

In this simulation we fix $x_A = 10\ \mu m$, $a = 0.09$, $L = 1$ cm and $\Gamma = 9$. As for the experimental study in previous Section 3.2, we keep the optical power free (here the optical field $F_0$). At $t = 0$ s the bias electric field is applied on the photorefractive crystal via $\Gamma$ and the initial linear 1D-Airy beam self-focuses along the crystal. Figure 3.9(a) depicts the evolution of the spatial distribution of the output beam at $z = L$ along time. Similarly to the experiment, the Airy beam undergoes self-focusing and, as detailed on Figures 3.9(b) and 3.9(c), it turns into an off-shooting soliton (at $x/x_A = -5.5$) and an accelerating beam (at $x/x_A = 0$).

The transient dynamics of the self-focusing output beam can be analyzed via two parameters: the shift of the intensity peak $x_d$ and the inter-lobe distance of the remaining accelerating multi-lobe structure $x_A$. By comparing the transverse shift of the numerical simulations on Figure 3.9(d) with the experimental results [Fig. 3.7(a)], the initial intensity peak at $t = 0$ s (i.e. the linear main lobe) also starts to shift from the linear output position $x/x_A = 0$ along the $-x$-axis towards the zero-deflection position being here $x/x_A = -5.5$. By increasing the optical power via $F_0$, the transient shift is faster as the maximum shift $x/x_A = -5.5$ is reached after $t/\tau = 0.18$ for $F_0 = \sqrt{(10)}$, which is over five times faster than the dynamics for $F_0 = \sqrt{(1)}$. As a consequence we can confirm that the optical power enhances the self-focusing strength and increases the velocity of the transient dynamics.

The analysis of the tightening of the lobes is depicted on Figure 3.9(e), where the minimal $x_A$ values are plotted for increasing optical field $F_0$. As the inter-lobe distance is proportional to $x_A$ and the acceleration rate of an Airy beam proportional to $x_A^{-3}$, Figure 3.9(e) shows that the beam's acceleration during the transient self-focusing regime increases with the optical power hence confirming the experimental results [Fig. 3.7].

If we consider the analogy with gravitational effects the gravitational lensing effect (self-bending and acceleration) induced by the off-shooting soliton is also observed and can be enhanced by increasing the optical power and therefore the refractive index change and the resulting gravitational potential [Figs. 3.9(d), 3.9(e)]. The numerical results are in good qualitative agreement with the experimental observations of the nonlinear interactions between the off-shooting soliton and the accelerating beam (stages (i) and (ii)). However, the numerical simulations do not reproduce the relaxation-type dynamics of the beam (stage (iii)), hence motivating additional theoretical modeling that would take into account carriers diffusion mechanism and also the background intensity $I_d$.

## 3.4 CONCLUSIONS

In summary, this work is the first analysis of the transient self-focusing properties of an Airy beam in a nonlocal nonlinear medium. The transient evolution involves both attraction and acceleration of the initially launched Airy beam due to the onset of an off-shooting soliton. These observations are analogous to gravitational lensing effect being however here self-induced by a single light beam. The accelerating Airy beam creates a transient spacetime curvature that bends light propagation for a short time, before disappearing and restoring an Airy beam profile similar to the launched Airy beam. The properties of the gravitational lensing, i.e. deflection and acceleration, can be both controlled all-optically through the engineering of the optical photorefractive nonlinearity.

When comparing with reference [123], the soliton in our system is not prepared from the self-focusing of a second beam but is created by the accelerating beam itself. Our conclusion is therefore that the analogy with gravitational lensing effects is not limited to the Newton-Schrödinger framework but applies also to nonlinear Schrödinger equation that accounts for a nonlocal nonlinearity (here photorefractive). Although not identical in the details with the Newton-Schrödinger equation, that equation contains all the required ingredients for the observation of the gravitational lensing effects: a focusing nonlinearity that varies with the light intensity and that is nonlocal, i.e. allowing for long-range interactions between the self-focused part of the Airy beam and the remaining accelerating beam. However, the analogy only holds in that time interval during which both the soliton and the accelerating beam interplay nonlinearly.

Besides its interest for the analogy with gravitation, the two-stages build-up dynamics of the focused beam provides a deeper insight into the subject of accelerating beams in nonlinear focusing media, and can be used to photoinduce multiple waveguide structure, as suggested in following Chapter 4.

# Part II

# INTERACTIONS OF TWO AIRY BEAMS

# 4

# COUNTERPROPAGATING AIRY BEAMS' INTERACTIONS

In this chapter we numerically analyze optical waveguide structures created in photorefractive media by one or two incoherent counterpropagating Airy beams under nonlinear self-focusing conditions. First we show that, under the solitonic conditions studied in Chapter 2, a single Airy beam photoinduces multiple waveguiding structures. Gaussian systems would in comparison require at least two beams to create similar waveguides.

In a second part we enlarge the possible interconnection schemes and study the interactions of two self-focused counterpropagating Airy beams both theoretically and experimentally. We demonstrate that for two counterpropagating beams even strongly misaligned, multiple waveguiding structures are photoinduced. In that way, an optical Gaussian beam can be linearly guided along a deflecting trajectory or split into several output beams. These results enable new configurations for all-optical interconnections.

The context of this chapter is related to the following publication:
Noémi Wiersma, Nicolas Marsal, Marc Sciamanna, Delphine Wolfersberger, "All-optical interconnects using Airy beams". In *Optics Letters*, 39.20 (2014).

## 4.1 WAVEGUIDING BY A SINGLE AIRY BEAM

Before analyzing the interaction of multiple Airy beams, we first focus on the waveguide possibilities that a single Airy beam can offer under solitonic conditions. After studying in detail the nature and the tuning of the Airy-solitons, we will now numerically examine the photoinduced refractive index structures inside the nonlinear crystal. So far Airy beams have drawn the attention in particular for their parabolic accelerating property. In reference [36], Denz *et al.* use the parabolic trajectory of the Airy beam to create curved waveguides. As illustrated on Figure 4.1, weak nonlinearity enables to create the waveguide structure and, by switching the Airy orientation using the SLM, they address different output positions at the end of their photorefractive crystal. In this section we increase the nonlinearity to activate the solitonic self-focusing and therefore to obtain a superimposed solitonic and an accelerating profile. Does this configuration also lead to multiple waveguiding structures ? While the curved Airy-induced waveguides in reference [36] have been induced using the linear Airy propagation, we suggest in this chapter the study of waveguides induced by solitonic Airy beams.

First we consider the configuration using a single Airy beam of Chapter 2, where its solitonic behavior has been studied under strong self-focusing conditions (see Section 2.3). The resulting intensity distribution is displayed on Figure 4.2, where the initial linear Airy beam turns into an intense off-shooting soliton and a weak accelerating beam. Through the Pockels effect, the optical electric field induces a refractive index variation [Eqs. 2.3,2.5,2.7]. The induced refractive index profile is numerically simulated via a Fast Fourier Transform Beam Propagation Method. We fix the system's parameters at $L = 1\ \mathrm{cm}$, $\Gamma = 9$, $a = 0.09$, $x_A = 7.5\ \mu\mathrm{m}$ and the normalized input electric field of a beam $F_0 = \sqrt{2.5}$. The crystal length $L = 1$ cm corresponds to $3.3L_d$, with $L_d = 2kx_A^2$ the characteristic diffraction length of the Gaussian beam ($n_0 = 2.3$, $\lambda = 532\ \mathrm{nm}$).
To test the guiding efficiency of the photoinduced waveguide structure, we inject a probe beam at one face of the crystal ($z = 0$ or $z = L$). An efficient waveguide is characterized by guiding an output beam with an intensity peak of similar size and with at least 10 % of the input probe beam. We consider the linear beam propagation by simulating equation 2.3 and keeping the space-charge field $E_0$ equal to the stationary $E_0(x, z)$ resulting from the nonlinear propagation of the

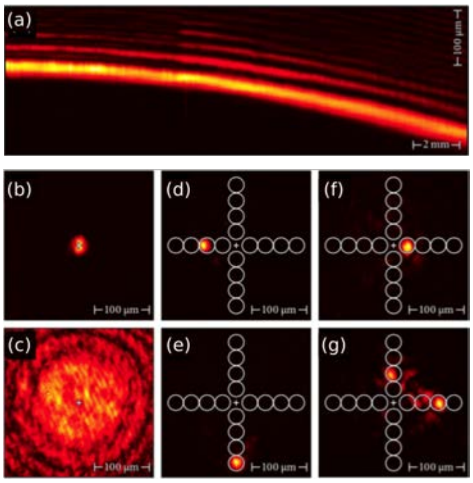

Figure 4.1: Airy-induced all-optical routing. (a) Two dimensional Airy beam propagating along a photorefractive crystal. (b) Gaussian input beam before propagation, (c) diffracted Gaussian output beam at the back face of the crystal without induced refractive index structure. (d)-(g) Propagation of a Gaussian probe beam through Airy-induced waveguide structures (the bending of the Airy beam has been tuned): output intensity distribution. Extracted from [36].

Airy beam (see Appendix C). Three input positions are considered [Fig. 4.2]:

1 main lobe's input ($z = 0$)
2 second lobe's input ($z = 0$)
$1'$ off-shooting soliton's output ($z = L$)

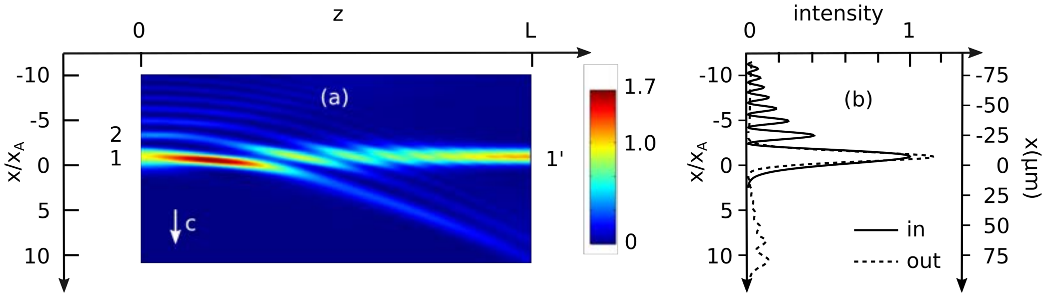

Figure 4.2: (a) Normalized intensity distribution of a self-focused Airy beam propagating in a focusing photorefractive crystal with $x_A = 7.5$ µm and $L = 1$ cm, (b) corresponding transverse intensity profiles.

Figure 4.3 presents the waveguiding results for the three input positions listed above. First we inject the Gaussian probe beam at the guide entry 1 photoinduced by the main lobe of the previous Airy beam (see Figures 4.3(a1) and 4.3(a2)). While the intensity distribution along the crystal shows that the guided beam splits into an accelerating structure and a Gaussian-shaped beam [Fig. 4.3(a1)], the major optical intensity is observed at $1'$. As shown on the intensity profile of the output beam on Figure 4.3(b1), almost 50 % of the beam exits at the soliton's output. This non homogeneous transmission efficiency between the accelerating and the solitonic guide is coherent with the photorefractive physics: the dominant waveguide $1 \to 1'$ has been induced by the most intense beam leading to a waveguide along a straight trajectory. This guiding differs from the situation analyzed in [36] in that, under high-focusing conditions, the output position of the waveguide $1 \to 1'$ does not relate to the deflection of the Airy beam but is rather determined by the position of the off-shooting soliton.

Secondly we consider the input position at $1'$, where the off-shooting soliton has induced a high refractive index variation. The observed scenario appears completely different, as a two-beam structure is observed at the output of the crystal $z = 0$ [Figs. 4.3(a2), 4.3(b2)]. As depicted on Figure 4.3(b2), there is not only an output beam at the guide exit 1 induced by the former main Airy lobe, but nearly 25 % of the initial probe beam appears shifted along the transverse axis. As we can see on Figure 4.3(a2), the output position matches with the initial second Airy lobe order 2. This waveguide presents two advantages comparing to the waveguide $1 \to 1'$ previously studied: a better transmission through the strong guide induced by the off-shooting soliton and furthermore a demultiplex structure allowing for a large spacing between the two outputs ($\approx 3x_A$ between both outputs) [Fig. 4.3(b2)].

Finally we test the guiding efficiency, when the propagation starts at the position 2 induced by the second lobe. The waveguide with the input at $1'$ guides a probe beam to the output positions (1,2) (see Figures 4.3(a2), 4.3(b2)). Because the opposite waveguide $1 \to 1'$ has been demonstrated in Figures 4.3(a1), 4.3(b1), we ask whether the waveguide $2 \to 1'$ is also efficient. Figure 4.3(a3) shows that the energy injected at the entry 2 is no longer confined in a waveguiding structure all along the crystal. As depicted on Figure 4.3(b3), only 8 % of the input intensity peak is observed at the output of the crystal. This low guiding efficiency can be explained by the lower refractive index structure photoinduced by the second lobe order of the Airy beam at $z = 0$ and by the asymmetrical waveg-

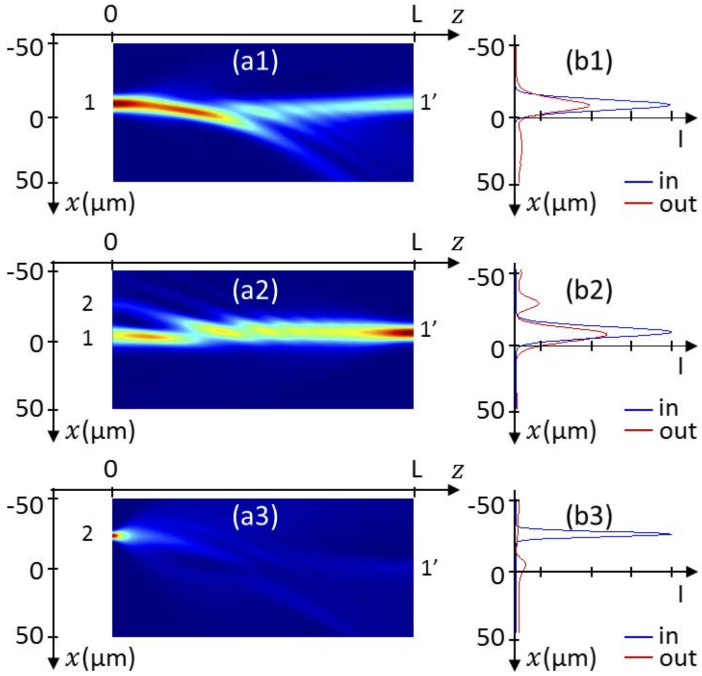

Figure 4.3: Linear probe beam propagation in the waveguide structure of Figure 2.14: (a1) Intensity distribution and (b1) transverse profiles of Gaussian beam guided along $1 \rightarrow 1'$, (a2)-(b2) guided along $1' \rightarrow (1, 2)$, (a3)-(b3) guided along $2 \rightarrow 1'$.

uide structure between $z = 0$ and $z = L$. I In addition this result shows that the intensity required to photoinduce an input guide is more important than for the output guide. As a consequence the guide induced by the soliton offers the best waveguiding efficiency.

To conclude a single Airy beam photoinduces two waveguide types: with one output or with two outputs depending on the input position and side. We have shown that the guiding efficiency is higher when starting through the solitonic guide. In addition the multi-lobe structure of the Airy beam offers a multiple output guiding, which can not be achieved with a single Gaussian beam and therefore utilizes the unique properties of the Airy beam. In comparison with waveguide structures created by Gaussian beams with the same dimensions and focusing conditions, the unique Airy shape and properties offer larger waveguide possibilities. Those results also demonstrate that, although the waveguiding is bidirectional (i.e. a Gaussian probe beam on both crystal sides is guided through the structure), the asymmetry of the waveguide leads to different output positions and guiding efficiencies depending on the input position of the probe beam.

## 4.2 NONLINEAR MULTIPLE BEAMS' INTERACTIONS

As mentioned earlier in the introduction, colliding solitons interact very similarly to particles, as they may repel or attract each other depending on various parameters (see Section 1.3.3). More generally the interactions between multiple solitons have shown fascinating behaviors, which can be tuned via the beams' and system's parameters as well as via the number of interacting beams. In this chapter we will limit our study to the interactions between two optical beams under solitonic focusing conditions.

There are two types of solitonic interactions, coherent and incoherent [87]. In the case of coherent beams, when both beams overlap, their total intensity induces an interference pattern. The photoinduced interference refractive index variation then leads to attractive or repulsive forces between the beams. These coherent interactions can be observed in media with fast response time, such as in Kerr-nonlinearity. However, in materials with a long response time, such as photorefractive and thermal media, these interferences only occur for (quasi-) stationary phase shifts. On the other hand in the case of incoherent interactions, the relative phase shift between the soliton beams varies much faster than the response time of the material. The total intensity corresponds to the sum of both beams' intensities leading to an always attractive force between both bright solitons [130]. In waveguide theory, the collisions of solitons can then be considered as a coupling between the waveguides induced by both beams [131].

In the chapters 4 and 5 we consider the interaction of two counterpropagating incoherent Airy beams. This configuration enables all the lobe orders of each Airy beam to interconnect with all the lobes of the counterpropagating Airy beam.

### 4.2.1 *Conventional beams' systems*

Let us first analyze the interaction scheme of two Gaussian solitons. As detailed below, two configurations can be considered : two solitonic beams propagating in the same and in opposite directions.

#### ***Co-propagating beams***

The collisions of incoherent co-propagating solitons can be induced either through the crossing of two non parallel solitons or by the interactions between slightly shifted parallel solitons. In the case of non parallel solitons, their collision creates an angular momentum and their attraction/repulsion scheme evolves in the 3D-space as they start rotating around each other [128, 132] [Fig. 4.4].

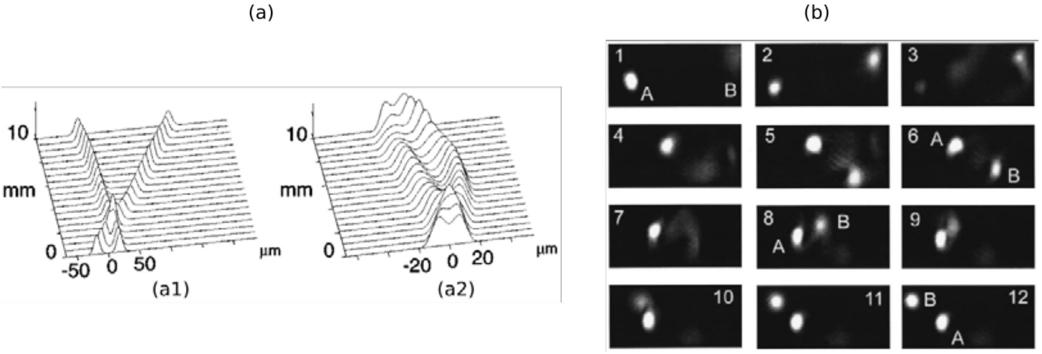

Figure 4.4: Two incoherent co-propagating Gaussian solitons launched along non parallel trajectories in photorefractive media. (a) Typical interaction scheme. Extracted from [66]. (b) Time-resolved complex rotation of a soliton pair. The sequence starts when a second beam is launched onto a steady-state soliton. The time interval between consecutive frames is 0.36 s. Extracted from [128].

If we decrease the angle between the two trajectories (towards a parallel beams' configuration), the solitons stop their orbiting behavior and leave their bound state. Also by narrowing both beams, their individually photoinduced waveguide structures start to overlap leading to a bound-state where they may fuse [133].The tuning of the interaction type and strength enables the creation of all-optical switching and logical gates as suggested in reference [134]. As depicted on Figure 4.5, Assento *et al.* use the interactions between the signal carrying soliton S and other co-propagating solitons, here A and B, to create for example a NOR-gate. Figure 4.5(a) (resp. 4.5(b)) depicts the propagation scheme (resp. experimental propagation) inside the nematic liquid crystal and the different output types of the signal soliton S. In absence of any other beam ("00" on Fig. 4.5), S propagates along a straight line. When a co-propagating beam, A or B, is switched on ("01" or "10" on Fig. 4.5), S is attracted towards the other solitons and follows a curved trajectory. The bending and therefore the output position of S can be tuned by varying the distance between S and the control beam (A or B). The maximum shift is reached when the two control beams are switched on ("11" on Fig. 4.5). The shift of the S-signal reaches then up to 50 µm as presented on Figure 4.5(c), where the four output profiles are displayed.

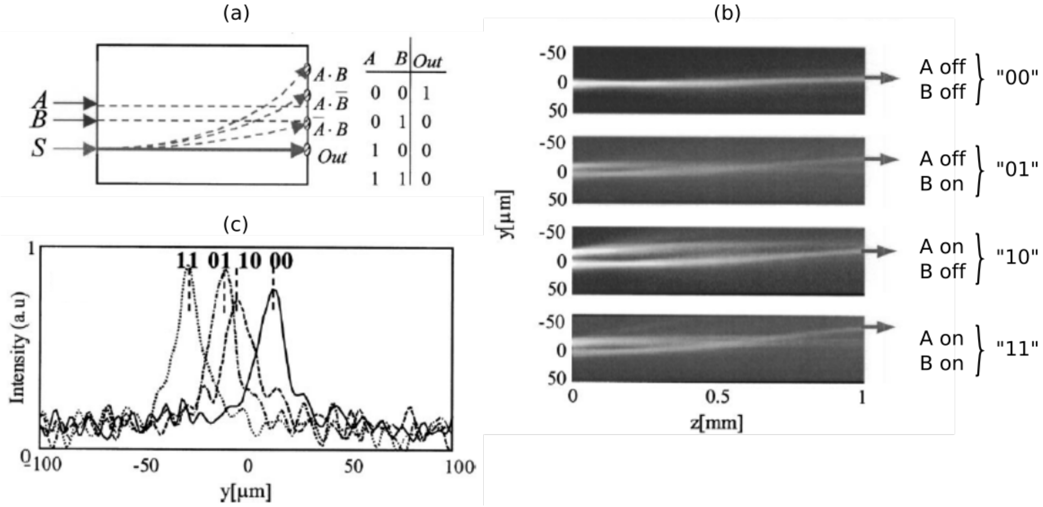

Figure 4.5: Two incoherent parallel co-propagating Gaussian solitons in a nematic liquid crystal. (a) A NOR-gate with three soliton-forming beams: A and B are control inputs, S guides the signal. The truth table refers to the *Out* port. (b) Soliton images along the crystal. The arrow indicates the signal output. (c) Signal profiles at the output (1 mm), corresponding to the input combinations in (b). Extracted from [134].

Finally the tune of the coherence enables the co-propagating Gaussian solitons to attract or repel from each other as demonstrated by Wolfersberger *et al.* (see Fig. 1.18 in Section 1.3.3).

### *Counterpropagating beams*

The scheme of counterpropagating beams allows strong interactions due to cross-coupling of the beams via the combined refractive index structure that is not present in the co-propagating case [135]. Similar to co-propagating solitons, the counterpropagating configuration has been studied for coherent and incoherent solitons with non-parallel crossing and with parallel trajectories [135].

As presented in reference [136] the force between the incoherent counterpropagating beams is always attractive and, as depicted on Figure 4.6(f), the forward beam gradually tunnels into the backward soliton region thus representing a directional coupling behavior. In the case of coherent beams, this Figure illustrates how the coherence of the beams influences the radiation effects in different ways depending on the propagation directions of both beams. As the attraction of both incoherent beams towards each other leads to solutions for optical interconnects, this configuration has been extensively studied for conventional beams (Gaussian beams) [129, 135, 137, 138]. The small transverse spatial range of the solitons used in these systems however limits the interaction range. Belić *et al.* [138] have demonstrated that for a transverse beams' shift exceeding four diameters, each soliton acts as a single soliton. To induce a joint waveguide structure, the beams' separation has to be less than one beam diameter. Later the research group has numerically analyzed the influence of peculiar beams' properties, such as the angular momentum of vortices, on the interaction scheme [139]. They have shown a large diversity of beams' interconnects, with the formation of e.g. dipoles and tripoles, hence demonstrating a new complexity of interactions when using non-Gaussian beams. The spatial limitation of conventional beam solitons and the rich interaction schemes of vortices have led us to the study of counterpropagating Airy beam under solitonic conditions.

### 4.2.2 *Co-propagating Airy beams' interactions*

So far literature has considered the interaction of two Airy beams only in the co-propagating configuration (coherent and incoherent). Before introducing our system with two incoherent counterpropagating Airy beams, let us first study the general behavior of co-propagating Airy beams under solitonic focusing conditions. The advantage of using Airy beams for beams' interaction refers to their complex intensity multi-lobe profile and their parabolic trajectory offering a much larger transverse interconnection range than conventional beams.

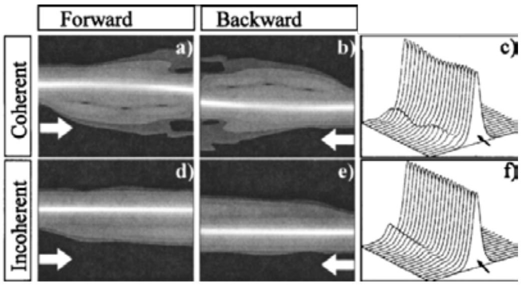

Figure 4.6: (a)–(c) Coherent interactions between the counterpropagating (a),(c) forward and (b) backward solitons. (d) –(f ) Incoherent interactions between the counterpropagating (d),(f ) forward and (e) backward solitons. The plots show absolute values of the field amplitudes. The arrow indicates the propagation direction of each beam. Extracted from [136].

First theoretical research has been done by the group of Belić in 2013, where two coherent Airy beams are launched at the same side of a nonlinear medium under strong self-focusing conditions [140]. They show that bound and unbound soliton pairs, as well as single solitons, can form in such interactions. Figure 4.7 depicts the interaction of two coherent co-propagating Airy beams. In particular

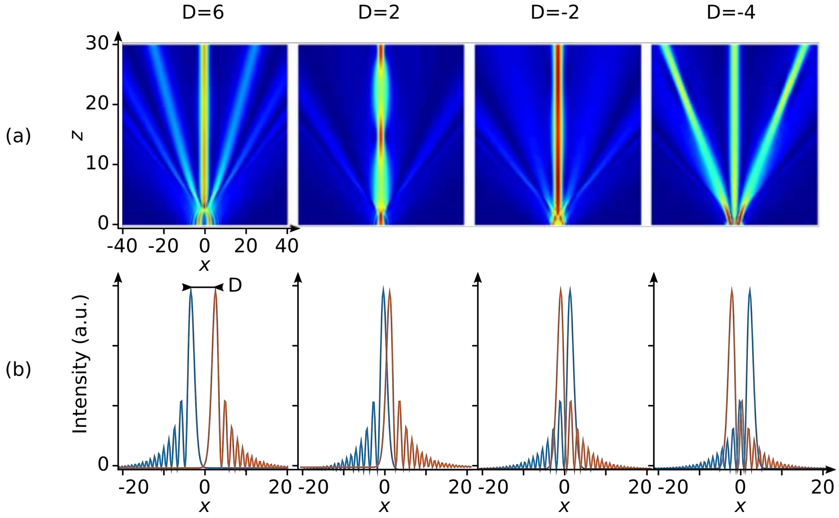

Figure 4.7: Soliton formation through the interaction of two in-phase co-propagating Airy beams in a Kerr medium. D represents the beams' shift. (a) Intensity distribution along the medium. Extracted from [140]. (b) Transverse intensity profiles of both beams at $z = 0$.

the beams' separation D plays an important role in the solitonic interactions. For $D > -4$, both off-shooting solitons are attracted towards each other and form bound solitons. But when the beams' shift decreases, both intensities start to overlap and the linear parabolic trajectories of the Airy beams do not cross any more but diverge from each other. As a result the solitonic interaction structure presents a repulsive behavior when $D \leqslant -4$. In addition the interactions can also be tuned via the phase shift $\Phi$ between both Airy beams. As depicted on Figure 4.8(a), the attractive interactions of in-phase beams turn into repulsive solitons for out-of-phase beams ($\Phi = \pi$). To understand this behavior, Figure 4.8(b) shows the field distribution of both Airy beams. The main lobes of the Airy beams have opposite field signs hence they induce opposite refractive index distributions, leading to repulsive interactions. Finally by varying the beams' spacing, their phase shift and the nonlinearity type (Kerr or saturable), they observe, similar to conventional solitonic systems, attraction/repulsion behaviors between both off-shooting solitons [Fig. 4.8].

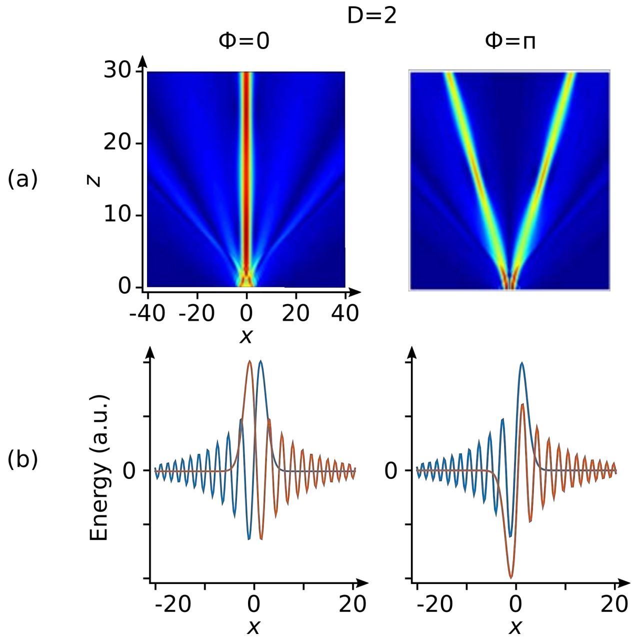

Figure 4.8: Influence of the phase shift of two co-propagating interacting Airy beams in a Kerr medium. In phase: $\Phi = 0$. Out-of-phase: $\Phi = \pi$. (a) Intensity distribution along the medium. Extracted from [140]. (b) Transverse energy profiles of both beams at $z = 0$.

The accelerating feature of Airy beams does not appear in the interacting solitons, however their interaction trajectories are very complex if the separation between initial beams is comparable to the width of the first Airy lobes. This diversity is due to the Airy multi-lobe shape and the beams' coherence which induce complex interactions such as e.g. individual solitons, breathing or merged solitons [141, 142].

The study and control of the interaction between coherent Airy-originated solitons has also been done in highly nonlocal media, where the nonlocality range strongly affects the dynamics of the off-shooting soliton and the interactions between two co-propagating Airy-solitons [143]. Finally the combination of the periodic Airy intensity distribution with an additional coherent Gaussian beam enables to tune the solitonic interactions types (attraction/repulsion) [144].

The co-propagating configuration of Airy beams offers interesting interaction schemes. By contrast a counterpropagating configuration enables optical interactions of a larger distance and, combined with the large transverse dimension of the Airy shape and trajectory, it allows several interaction schemes in all spatial dimensions. While the solitonic interactions in the co-propagating case are mainly controlled by the main lobes, the secondary lobes play an important role in the photoinduction of waveguide structure in the nonlinear medium, when one or several lobes of the counterpropagating beams for example face each other. The interaction of counterpropagating Airy beams opens therefore new interesting fields for optical interconnections.

## 4.3 NUMERICAL STUDY OF COUNTERPROPAGATING AIRY BEAMS

To study the propagation of two self-focusing counterpropagating Airy beams in a photorefractive crystal and the resulting beams-matter interactions, we consider the numerical model already used in Chapter 2 by adding a second beam. Figure 4.9 depicts the typical interaction scheme, where a forward Airy beam is launched at $z = 0$ in the $+z$-direction (forward beam) and the second Airy beam propagates in the opposite $-z$-direction from the other crystal face at $z = L$ (backward beam). The transverse linear accelerations of both Airy beams are in the same $+x$-direction as depicted on Figure 4.9.

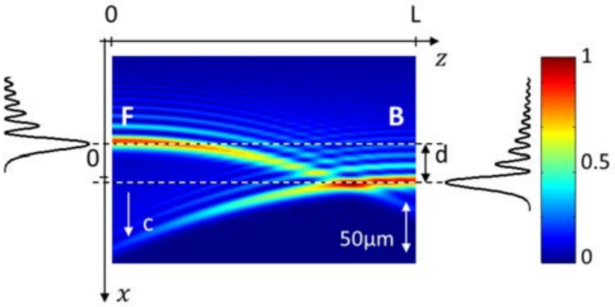

Figure 4.9: Typical interaction scheme of two counterpropagating Airy beams in an unbiased photorefractive crystal.

### 4.3.1 *Coupling equations for the counterpropagating case*

Our numerical simulations are done using the same algorithm as in Chapter 2. The initial Airy profiles of the forward beam $F(x,z)$ and the backward beam $B(x,z)$, are given by the following equations:

$$F(x, z=0) = F_0 \mathrm{Ai}\left(\frac{x}{x_A} + D\right) \exp\left(a\left(\frac{x}{x_A} + D\right)\right), \tag{4.1}$$

$$B(x, z=L) = B_0 \mathrm{Ai}\left(\frac{x}{x_A}\right) \exp\left(a\frac{x}{x_A}\right), \tag{4.2}$$

where $F_0$ and $B_0$ correspond to the wave amplitudes of respectively the forward beam $F$ and the backward beam $B$, $\mathrm{Ai}$ represents the Airy function, $x_A$ an arbitrary transverse scale, $a$ the truncation factor and $D = dx_A$ the additional normalized shifting distance between the initial input beams $F$ and $B$ along the transverse $x$-axis. For $D = 0$, the beams are aligned and each lobe order of the forward Airy beam collides with the same lobe order of the backward beam at $z = L/2$. By shifting the beam $F$ the forward lobes will interconnect with different backward lobe orders and hence induce an asymmetry along the axis $z = L/2$. Similarly to the case of a single Airy beam, the nonlinear propagation of these two incoherent counterpropagating beams can be modelled as follows [138]:

$$i\partial_z F + \partial_x^2 F = \Gamma E_0 F, \tag{4.3}$$

$$-i\partial_z B + \partial_x^2 B = \Gamma E_0 B, \tag{4.4}$$

where $\Gamma = (knx_A)^2 r_{eff} E_e$ is the nonlinear photorefractive coupling strength, $E_0$ is the homogeneous part of the $x$-component of the photorefractive space-charge field (see Section 2.3 ). As the backward beam $B$ propagates along the opposite direction of $F$, the propagation equation of $B$ is equal to the forward equation 4.3 with a sign change concerning the $z$-propagation.
The photorefractive effect is now induced by the sum of the two incoherent beams and the temporal evolution of $E_0$ is calculated using a relaxation-type dynamics given by:

$$\tau \partial_t E_0 + E_0 = -I_0/(1 + I_0), \tag{4.5}$$

$$I_0 = \mid F \mid^2 + \mid B \mid^2, \tag{4.6}$$

where $\tau$ is the relaxation time of the crystal. As illustrated in the equations 4.5 and 4.6, the optical intensity will increase the nonlinearity of our system. By applying a positive external electric field $E_e$ along the c-axis of the crystal (parallel to the $x$-axis [Fig. 4.9]) we will show here that complex waveguiding structures can be optically induced in the photorefractive nonlinear material through the Pockels effect: more complex interconnections can be done over a larger distance thanks to the additional counterpropagating Airy beam. The induced refractive index distribution is then related to the combination of the multiplexed Airy beams $F$ and $B$ and their solitonic interactions.

The induced refractive index profile is numerically simulated via a Fast Fourier Transform Beam Propagation Method detailed in Appendix C. As for the single Airy beam case, we fix the crystal length at $L = 1$ cm, $\Gamma = 9$, $a = 0.09$, $x_0 = 7.5$ µm, the normalized input energy of the beams $F_0 = B_0 = \sqrt{2.5}$ and keep $D$ as a free parameter.

### 4.3.2 *Study of the Airy interconnection range*

We restrict our investigation to two configurations: the first one where the two counterpropagating Airy beams are strictly aligned (transverse shift $D = 0$, [Fig. 4.10]) and secondly with a small misalignment $D = 2$ [Fig. 4.11]. Similarly to the single beam case, we first consider the intensity patterns of the interacting counterpropagating solitonic Airy beams. In a second step we will test these photoinduced waveguide structures at the input positions with the largest guiding efficiency.

#### F AND B INITIALLY ALIGNED ($D = 0$):

As detailed in Chapter 2, each Airy beam turns into a combination of an off-shooting soliton and an accelerating beam under strong self-focusing conditions. In our configuration here both beams have their transverse acceleration along the photorefractive $c$-axis of the crystal, so both undergo a solitonic behavior.
Figure 4.10 depicts the interactions of two aligned Airy beams ($D = 0$). When a focusing nonlinearity is applied on the crystal, the two beams turn into a solitonic beam. As illustrated on Figures 4.10(c)-4.10(d), their intensity pattern does not match with a superposition of two symmetrical single solitonic Airy beam structures presented on Fig. 2.14. Indeed, at $z = L$, the position of the off-shooting soliton (respectively at $z = 0$) is not the same compared to the situation with only one Airy beam, but we notice an additional shift of $+2x_A$. This shift is induced by the presence of the counterpropagating beam and the resulting intensity increases inside the medium. The photoinduced refractive index structures enables us therefore to consider multiple input positions: at the main lobe's input, the soliton's output and we will also test again the second lobe's input, because the intensity pattern of two Airy beams induce larger and stronger refractive index variation.
As for the single Airy waveguide studied earlier in Section 4.1, we number the possible input/output positions [Fig. 4.10(c)]:

1 forward beam: main lobe's input ($z = 0$)
2 forward beam: second lobe's input ($z = 0$)
1′ forward beam: off-shooting soliton′ output ($z = L$)
3 backward beam: main lobe's input ($z = L$)
4 backward beam: second lobe's input ($z = L$)
3′ backward beam: off-shooting soliton's output ($z = 0$).

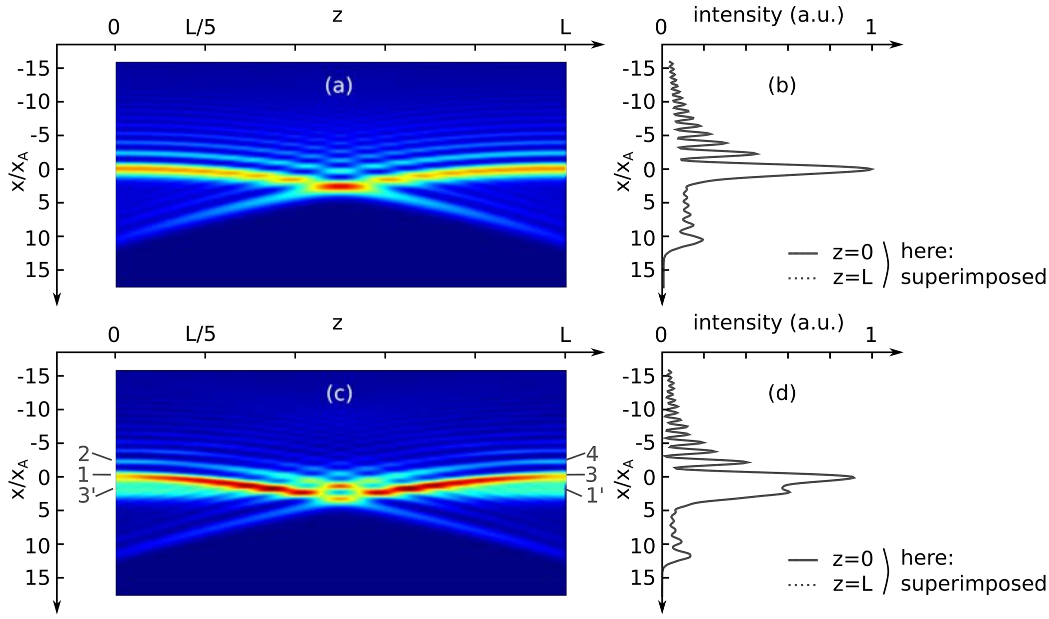

Figure 4.10: Interactions between two aligned counterpropagating Airy beams in a photorefractive crystal ($D = 0$). (a) (resp. (c)) Intensity distribution inside the medium and (b) (resp. (d)) transverse intensity profiles at both ends of the crystal under linear (resp. nonlinear focusing) conditions.

### F AND B INITIALLY MISALIGNED ($D = 2$):

The large transverse intensity distribution of the Airy beam suggests us to test the interconnections between two misaligned counterpropagating incoherent Airy beams. Figure 4.11 presents the interaction scheme of Airy beams misaligned by $D = 2$, which corresponds to a shift of $2x_A$ between both beams. Because of the parabolic trajectories along the $+x$-axis, the intensity pattern is not symmetric any more: the longitudinal intersection area of the main lobes is now shifted towards the $+z$-direction and additional interactions between the self-focused counterpropagating Airy beams appear.

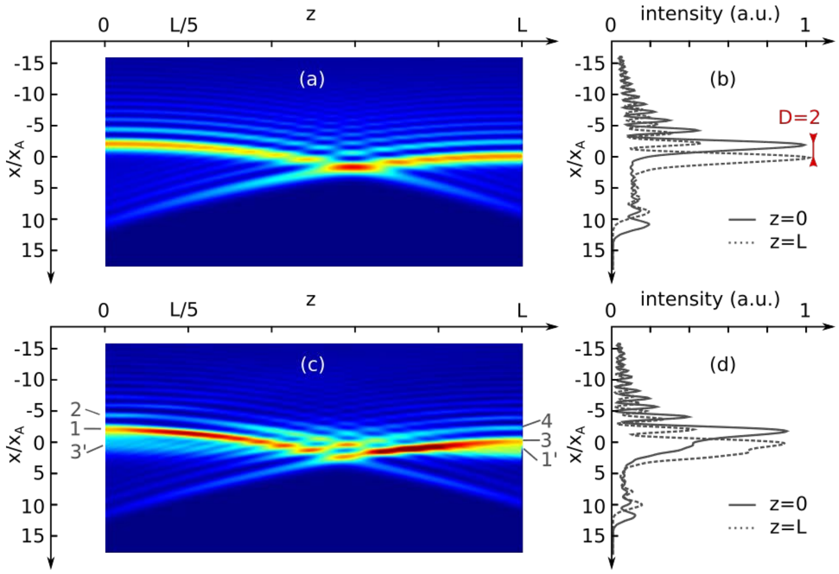

Figure 4.11: Interactions between two misaligned counterpropagating Airy beams in a photorefractive crystal ($D = 2$). (a) (resp. (c)) Intensity distribution inside the medium and (b) (resp. (d)) transverse intensity profiles at the ends of the crystal under linear (resp. nonlinear focusing) conditions.

Under strong self-focusing conditions, both off-shooting solitons appear at different transverse output positions. On one hand the forward solitonic beam has shifted of $2x_A$ similar to the ($D = 0$)-case ($1'$ at $z = L$ [Figs. 4.11(c)-4.11(d)]). On the other hand the backward propagating soliton exits the crystal almost at the same output position as for the single Airy beam case, i.e. the zero-deflection position $x = 0$ at $z = 0$. The shift of the forward Airy beam induces an asymmetric interaction between each soliton and counterpropagating Airy beam. One solitonic output beam almost behaves as a single Airy beam (here B), while the propagation of the other soliton is strongly affected by the multi-lobe structure of the counterpropagating beam [Fig. 4.11(d)]. This more complex intensity distribution results from higher energy exchange within the counterpropagating main and secondary lobes.

### 4.3.3 *Waveguiding induced by counterpropagating Airy beams*

The previous section has presented larger interconnection schemes, where the multi-lobe structure of the Airy beams and their off-shooting solitons induce complex intensity patterns inside the photorefractive medium. The resulting refractive index structure suggests possible waveguiding with multiple input and output positions associated with large transverse shifts. We will now study the waveguiding strength of these structures by propagating a Gaussian probe along the suggested input positions: $1$, $2$ and $3'$.

#### F AND B INITIALLY ALIGNED ($D = 0$):

First we consider the symmetrical waveguide structure induced by two aligned counterpropagating Airy beams [Figs. 4.10(c)-4.10(d)]. As depicted on Figure 4.12, the Gaussian beam propagates along similar trajectories than in the single beam case. Again the guiding structure induced by the second lobe order 2 does not offer efficient waveguiding for the probe beam (despite the larger transverse waveguide structure induced by the second counterpropagating Airy beams) [Figs. 4.12(c)-4.12(d)].

The input positions are associated with output structures induced by the same beams as for the single beam case, $1 \rightarrow 1'$ and $3' \rightarrow (3, 4)$, but with smaller guiding efficiencies. The possible energy loss can be explained by the strong interaction due to cross-coupling of the beams and by the energy flows between the multiple lobe orders [Fig. 4.10(a)] [21]. However, the counterpropagating beams configuration presents several additional advantages:

- Symmetry: we have a single and a demultiplexing waveguiding structure for both $z$-directions,
- Transverse shift: the shifts of the off-shooting solitons enable larger transverse distances for optical guiding and waveguide (over $4x_A$ [Figs. 4.12(e)-4.12(f)]).

As a conclusion we can stress that the use of two counterpropagating Airy beams allows for achieving complex waveguiding structures that would otherwise require the counterpropagating interactions of more than two Gaussian beams.

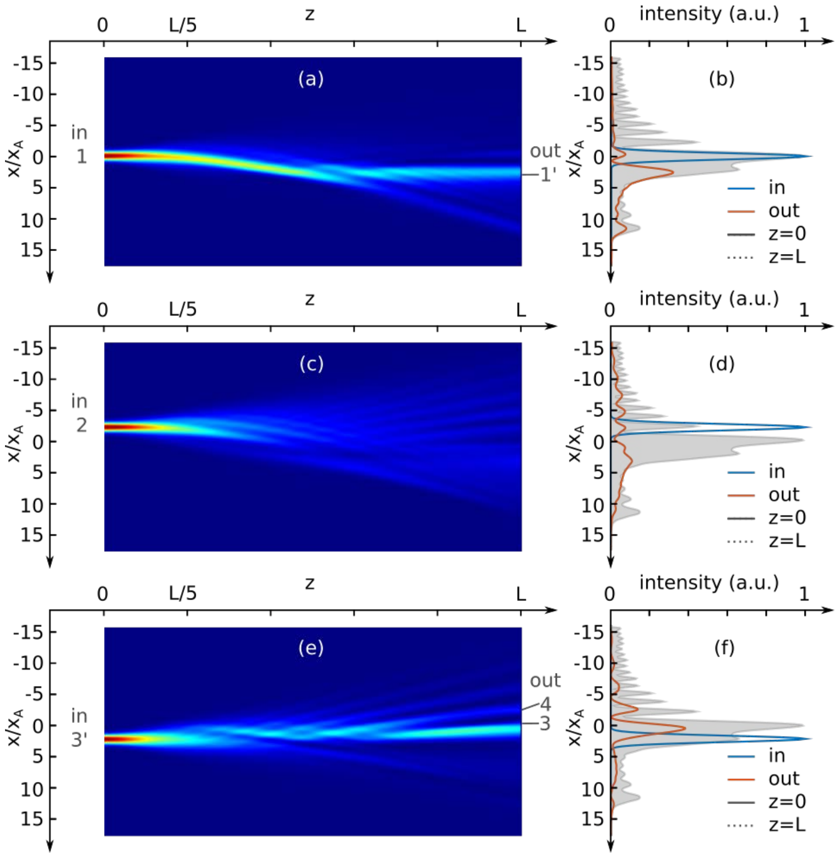

Figure 4.12: Linear probe beam propagation in the waveguide structure induced by aligned Airy beams [Figs. 4.10(c)-(d)]. (a) Intensity distribution and (b) transverse profiles of a Gaussian beam guided along $1 \rightarrow 1'$, (c)-(d) non efficiently guided from 2 to the whole output plane of $z = L$, (e)-(f) guided along $3' \rightarrow (3,4)$.

## F AND B INITIALLY MISALIGNED ($D = 2$):

If now we use the waveguiding structures induced by misaligned beams [Figs. 4.11(c)-4.11(d)], the asymmetry of the system offers new output cases. In Figure 4.13 we display these additional waveguiding results. Similarly to the structure generated when $D = 0$, if the Gaussian beam is first guided by a main Airy lobe (1 or 3), it also exits at the soliton's output ($1'$ or $3'$). But here the single output beam has shifted of $4x_A$, contrary to $2x_A$ in the symmetrical case and $0x_A$ in the single Airy case [Figs. 4.13(a)-4.13(b)]. If the probe beam is injected into inputs formed by off-shooting solitons ($1'$ or $3'$), it will split into two beams at the Airy lobes positions on the other side of the crystal with input-output shifts up to $6x_A$ ($3' \rightarrow (3,4)$ [Fig. 4.13(c)-(d)]). While in the symmetrical case, the input and output positions of the demultiplexing waveguides were defined by the Airy and the soliton profile of the same beam ($3' \rightarrow (3',4)$ [Figs. 4.12(c), 4.12(d)]), the outputs of the demultiplexing waveguide for $D = 2$ are induced by the off-shooting soliton of the forward beam $1'$ and by the main lobe of the counterpropagating beam 3 ($3' \rightarrow (1',3)$ [Figs. 4.13(c), 4.13(d)]).

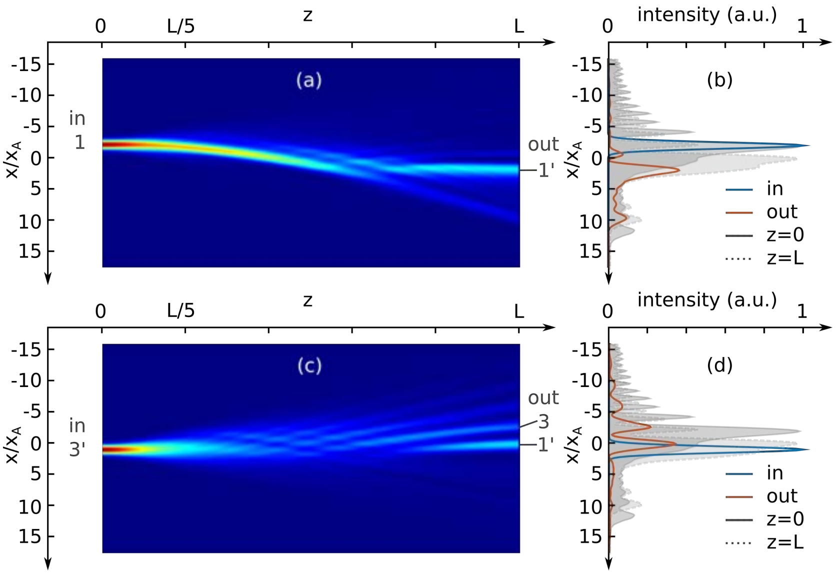

Figure 4.13: Linear probe beam propagation in the waveguide structure induced by misaligned Airy beams [Figs. 4.11(c)-(d)]: (a) Intensity distribution and (b) transverse profiles of a Gaussian beam guided along $1 \rightarrow (1',3)$, (c)-(d) guided along $3' \rightarrow (1',3)$.

## LIMITS OF THE MISALIGNMENT D:

Such a configuration, leading to inter-lobe interaction areas inside the crystal, enables to create 1-to-2-demultiplexers guiding up to half the energy of the input beam with an important transverse shift $x$. The resulting waveguide structures show interesting features. First the waveguide occurs although the positions of the two input beams are largely shifted ($2x_A$). The same simulation but using shifted Gaussian beams at the entrances 1 and 3 does not create any waveguide. Secondly the interaction scheme allows for controlling the spatial positions of the waveguide outputs by varying the transverse shift D between the counterpropagating input beams.

However, the larger the shift D is, the smaller is the area leading to interconnection between the counterpropagating beams. To illustrate this effect, Figure 4.14 depicts the interaction scheme for a transverse shift of $D = 3$. While the linear intensity distribution still shows both Airy beams interconnect [Figs. 4.14(a), 4.14(b)], in the nonlinear regime both off-shooting solitons present a zero-deflection propagation which characterises a single Airy-soliton [Figs. 4.14(c), 4.14(d)]. To test whether the large transverse optical structure still offers efficient waveguiding, we inject a probe beam at the different input positions marked on Figure 4.14(c). As now the cross-coupling of the largely shifted Airy beams is smaller, the waveguides are mainly induced by one beam ($F$ or $B$). However, on Figures 4.14(e) and 4.14(f) we show a waveguide with entries/exits induced by both beams: $1 \to (1', 3)$. In this case the probe beam is equally split into both outputs with a mutual shift of $6x_A$.

To conclude as the guiding efficiency depends on the self-focusing strength of the medium, which also damages the accelerating profile, such a solitonic Airy-waveguiding requires a compromise between the Airy-induced shape diversity (multi-lobe, curved trajectory) and solitonic efficiency.

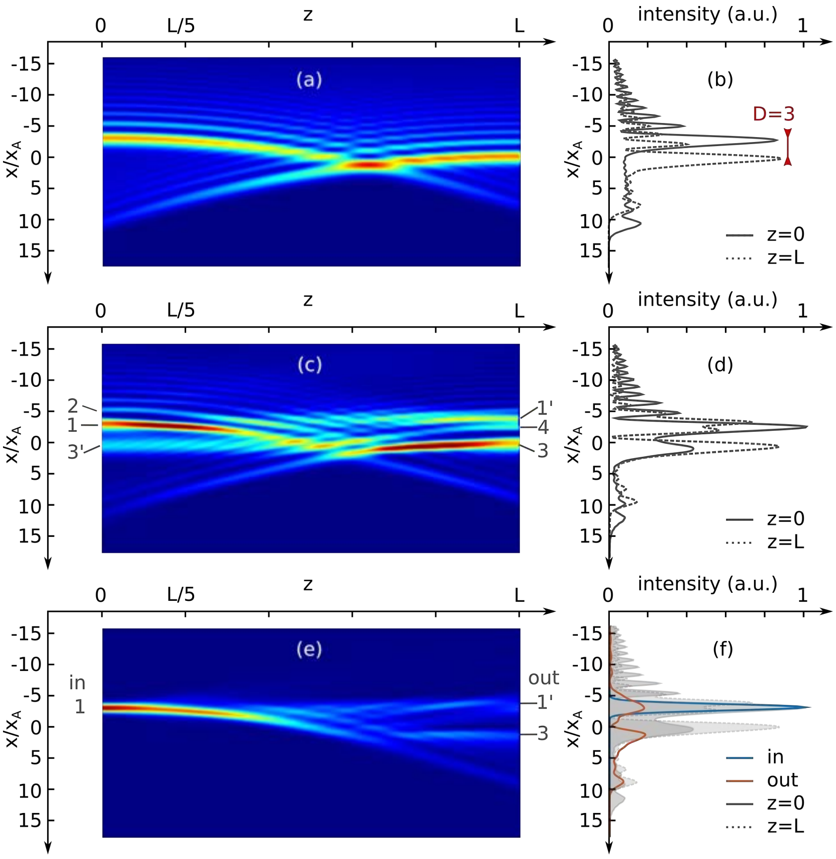

Figure 4.14: Photo-induced waveguides using two misaligned counterpropagating Airy beams in a photorefractive crystal (D = 3). (a) (resp. (c)) Intensity distribution inside the medium and (b) (resp. (d)) transverse intensity profiles at the ends of the crystal under linear (resp. nonlinear focusing) conditions. (e)-(f) Linear probe beam propagation in the waveguide structure (b): (e) intensity distribution and (f) transverse profiles of a Gaussian beam guided along $1 \rightarrow (1',3)$.

## 4.4 EXPERIMENTAL EVIDENCE

### 4.4.1 *Experimental setup*

In previous section we have theoretically demonstrated that counterpropagating Airy beams induce waveguides with a combination of a solitonic and a multi-lobe structure when applying nonlinear focusing conditions. The presence of a second Airy beam optically induces a more complex refractive index structure which modifies the trajectory of the first Airy beam (section 4.3.2).

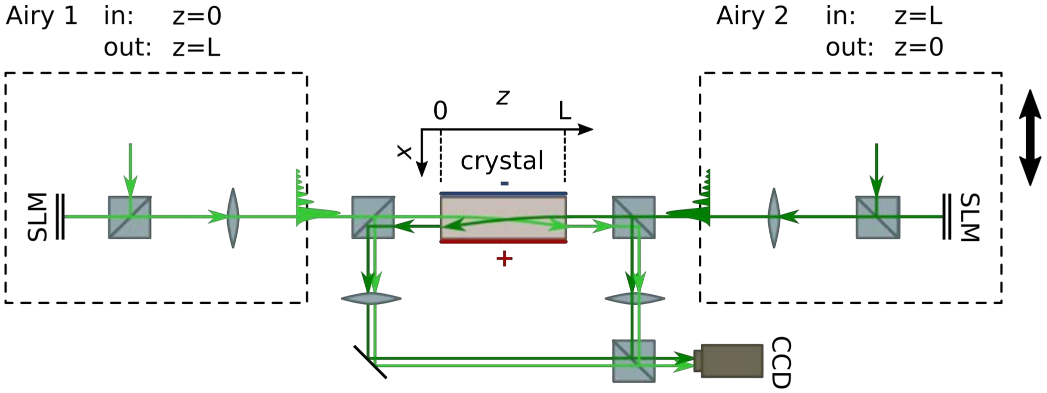

Figure 4.15: Study of two incoherent counterpropagating Airy beams in a biased focusing photorefractive (PR) crystal: experimental setup.

Here we present the first experimental study of two incoherent counterpropagating Airy beams in a biased focusing photorefractive crystal (SBN-crystal already used in chapters 2 and 3) as depicted on Figure 4.15. Both Airy beams propagate in opposite longitudinal $z$-directions and accelerate towards the $+x$-direction with the same parameters:

| Parameter | Variable | Values |
|---|---|---|
| wavelength | $\lambda$ | 532 nm |
| lobe size | $x_A$ | $\in [9.5; 14]$ µm |
| Airy truncation | $a$ | $\approx 0.04$ |
| optical power | $P_A$ | $\in [7.5; 150]$ µW |
| external electric voltage | $U_{SBN}$ | $\in [0; 2]$ kV |

The second Airy beam can be shifted along $x$ to tune the alignment of the beams. To ensure the incoherence of both counterpropagating beams, the second Airy beam is generated by an additional laser.
With two imaging systems and a CCD camera we measure the spatial evolution of the output beams at both sides of the crystal of 1 cm. The large space charge field induced by the bias electric field and the Airy beams prevents us from observing the intensity distribution inside the crystal all along the longitudinal $z$-direction. The description of the experimental setup is detailed in Appendix B.

### 4.4.2 *Results and discussions*

For the following results we study the intensity at the output side $z = L$ of the crystal. As illustrated on Figure 4.15, there are two intensities superimposed on the camera: the forward Airy beam (Airy 1) after propagating through the medium and the reflection of the backward Airy beam (Airy 2) before its crystal propagation. The reflection of the second beam enables us to compare the output position of the forward beam with the counterpropagating Airy lobes. Hence, we can identify the guiding efficiency of the multi-lobe structure of the counterpropagating beam (because of the symmetry of our system, the results at $z = 0$ are identical).

#### ***Comparison of the self-focusing of a single and of two counterpropagating Airy beams***

We start our experiment using counterpropagating Airy beams with $x_A = 14$ µm, $P_A = 60$ µW and $U_{SBN}(t > 0s) = 2$ kV. Figure 4.16 shows a comparison of the spatial output position of the self-focused forward Airy beam propagating along the $+z$-direction with and without a counterpropagating Airy beam [Fig. 4.15]. As detailed in previous Chapter 3, a single propagating Airy beam turns into a solitonic beam at the transverse zero-deflection position. The self-focused beam is a superposition of an off-shooting soliton co-existing with an accelerating beam structure. This dynamics is well reproduced in Figures 4.16(b)-4.16(e), where the intensity is first attracted towards the zero-deflection position [Figs. 4.16(b)-4.16(c)]. At $t = 300$ ms we observe a high and narrow intensity peak at $x_{sol} = -20$ µm and the accelerating beam starts forming its multi-lobe structure at $x = 20$ µm [Fig. 4.16(e)]. The transverse shift of the solitonic peak here is smaller than in our previous analysis in Chapter 3, as the Airy beam in this section is larger ($x_A = 14$ µm contrary to $x_A = 10$ µm leading to a decrease of the transverse acceleration Eq. 2.2). The influence of the $x_A$-parameter will be discussed later in this section.

In the presence of a counterpropagating Airy beam, the evolution of the intensity distribution of the output beam changes significantly [Figs. 4.16(f)-4.16(i)]. In comparison with the single beam case, the optical intensity of the forward beam shifts faster and further towards the higher lobe orders in the $-x$-direction. In particular the maximum peak value has increased from $0.8I_{ini,max}$ in the single beam case to $I_{ini,max}$ and the transverse shift has more than doubled to a maximum value of $-55$ µm. As illustrated on Figures 4.16(f)-4.16(g), the counterpropagating Airy beam is injected at $x = -45$ µm. Through the photorefractive effect and the large transverse dimension of the Airy beam, the photoinduced variation of refractive index also appears beyond the zero-deflection position of the single Airy beam ($x < x_{sol} = -20$ µm). Thanks to the larger propagation schemes of two Airy beams, the forward optical beam is guided into the combined photoinduced waveguide structure along larger transverse distances. If we analyze the intensity shift towards the zero-deflection position $x_{sol}$, the Airy-soliton in the single beam case appears at 300 ms [Fig. 4.16(d)], whereas the intensity has already shifted beyond $x = 50$ µm after 200 ms in the counterpropagating case [Fig. 4.16(i)]. The faster response time can be explained by the quasi-instantaneous waveguide photoinduced by the counterpropagating main lobe at $x = -45$ µm.

Although the experimental setup does not allow us to directly observe and measure the optical waveguides inside the photorefractive crystal, the analysis of the output beam demonstrates the waveguiding effect of a counterpropagating Airy beam. The forward beam is better guided and shifted towards the higher lobes' orders thanks to the backward beam whose main lobe nearly coincides with the output position of the off-shooting soliton in the single Airy beam case. In the next paragraphs we will focus our study on the tuning possibility of our waveguide induced by the counterpropagating beam using three parameters: the mutual transverse shift between both beams D, the beams' size $x_A$ and the external electric bias voltage $U_{SBN}$.

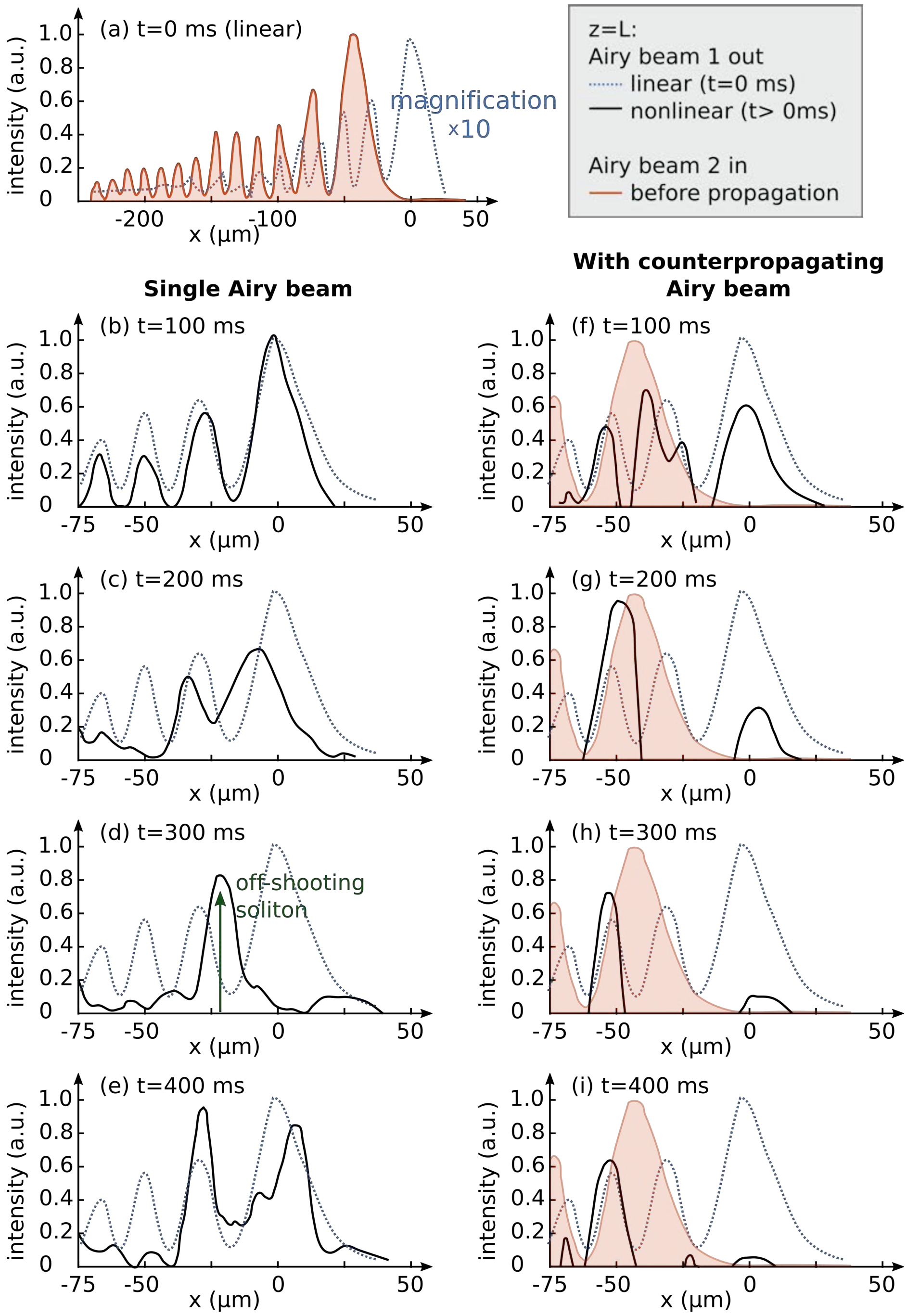

Figure 4.16: Influence of a counterpropagating Airy beam on the propagation of an Airy beam in a focusing biased photorefractive crystal, observation at $z = L$ [Fig. 4.15]. (a) Linear profiles of the forward and backward propagating Airy beams. Spatial evolution of the forward Airy beam along time (b)-(e) stand alone and (f)-(i) interacting with a counterpropagating Airy beam.

### *Influence of the system's parameters on the beams' interactions*

#### INFLUENCE OF THE BEAMS' MISALIGNMENT: D

In previous paragraph we have shown that adding a counterpropagating Airy beam near the output position of the soliton off-shooting from the forward Airy beam enhances the shift and the intensity concentration of the single Airy soliton towards the higher lobe orders. Now we wonder whether the waveguide induced by the backward Airy beam is still efficient, when the main lobe is shifted in the opposite direction of the solitonic drift.

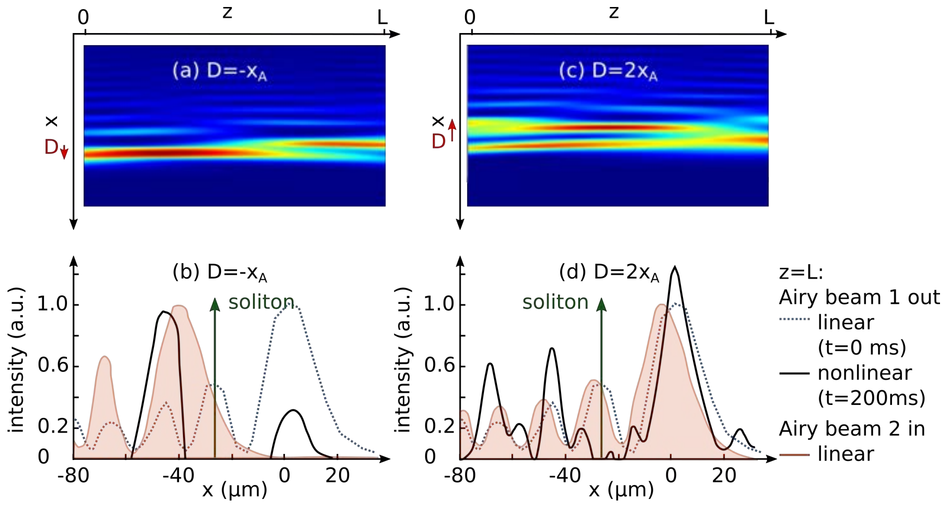

Figure 4.17: Waveguiding effect of two counterpropagating Airy beams in a biased photorefractive crystal for different misalignments, with $x_A = 14$ µm, $P_A = 60$ µW and $U_{SBN} = 2$ kV. (a) (resp. (c)) Numerical intensity distribution inside the crystal and (b) (resp. (d)) experimental transverse intensity profile of the forward output beam at $z = L$ for $D = -x_A$ (resp. $D = 2x_A$) [Eq. 4.1].

Figure 4.17 presents the numerical interaction scheme and the experimental guiding results of counterpropagating Airy beams with a shift along the photorefractive drift direction $-x$ [Figs. 4.17(a)-4.17(b)] and with shifts in opposite direction ($x$ and $-x$) [Figs. 4.17(c)-4.17(d)]. The first case, where the counterpropagating main lobe is beyond the forward zero-deflection position $x_{sol} = -20$ µm, has been discussed in the previous paragraph. In this case the counterpropagating main lobe is before $x_{sol}$. Therefore, we will focus on the second case, where the backward Airy beam is almost superimposed with the linear output Airy beam (see orange plain and blue dashed lines on Fig. 4.17(d). As depicted on the numerical insight of the optical intensity distribution on Fig. 4.17(c), both main lobes and solitonic structures nearly do not interact with each other during their propagation all along the crystal except near the output face $z = L$. At the end of the crystal, the energy of the self-focusing forward beam does not propagate along a straight line, but splits into the counterpropagating main lobe and the second lobe order. This energy split suggests experimental beam's attraction towards both transverse $+x$- (at the main counterpropagating lobe) and $-x$-directions (towards the higher counterpropagating lobe orders). The bidirectional attraction of the forward Airy beam by the backward Airy beam is experimentally confirmed on Figure 4.17(d). The transverse intensity profile of the forward Airy beam at $z = L$ appears to have three output beams, distinctively separated of up to 70 μm. Interestingly these three output do not match the three first lobes of the counterpropagating beam, but the first, third and fourth lobes. The preferred solitonic zero-deflection output position, which coincides with the second backward lobe order, does not present any intensity peak.

This result is striking by the fact that the waveguides at $x = -70$ μm and $x = -45$ μm have been induced by the linear less intense third and fourth lobe orders. This guiding strength may be due to their position along the drift direction. As the forward beam is naturally attracted towards the $-x$-direction, a part of the beam shifts towards its solitonic zero-deflection position and continues its shift towards the linear higher lobe orders of the backward beam. At the same time a large part of the intensity is attracted towards the backward main lobe at $x = 0$ μm, as this lobe contains half of the optical energy of the total Airy beam.

In this paragraph we have demonstrated transient attraction of a self-focused Airy beam towards the multi-lobe counterpropagating Airy beam structure. This attraction is separately induced by multiple lobes of the counterpropagating Airy beam which split the forward output intensity into up to three outputs along the transverse $x$-axis. By tuning the transverse separation distance D between the counterpropagating beams, the attraction can be either towards the main counterpropagating lobe enhancing the solitonic structure or towards multiple lobes leading to a demultiplexing of the soliton into multiple split beams. This diversity of attraction is unique and enabled by the multi-lobe structure of the

Airy beam.

### INFLUENCE OF THE AIRY BEAMS' SIZE: $x_A$

Finally we suggest the study of the balance between the linear accelerating properties and the self-focusing solitonic behavior of the counterpropagating Airy beams' system. To increase the solitonic effect we reduce the Airy beams' size via $x_A$ from 14 µm to 9.5 µm with $D = -x_A$. As depicted on Figure 4.18, the smaller Airy beam [Figs. 4.18(a), 4.18(b)] has more deflected than the Airy beam with $x_A = 14$ µm [Figs. 4.18(c), 4.18(d)]. In the single Airy beam configuration the off-shooting soliton for $x_A = 14$ µm appears at $-28$ µm, while for $x_A = 9.5$ µm the solitonic peak has shifted of $-35$ µm compared to the linear main lobe (see green arrow on Figs. 4.17(b) and 4.17(c)).

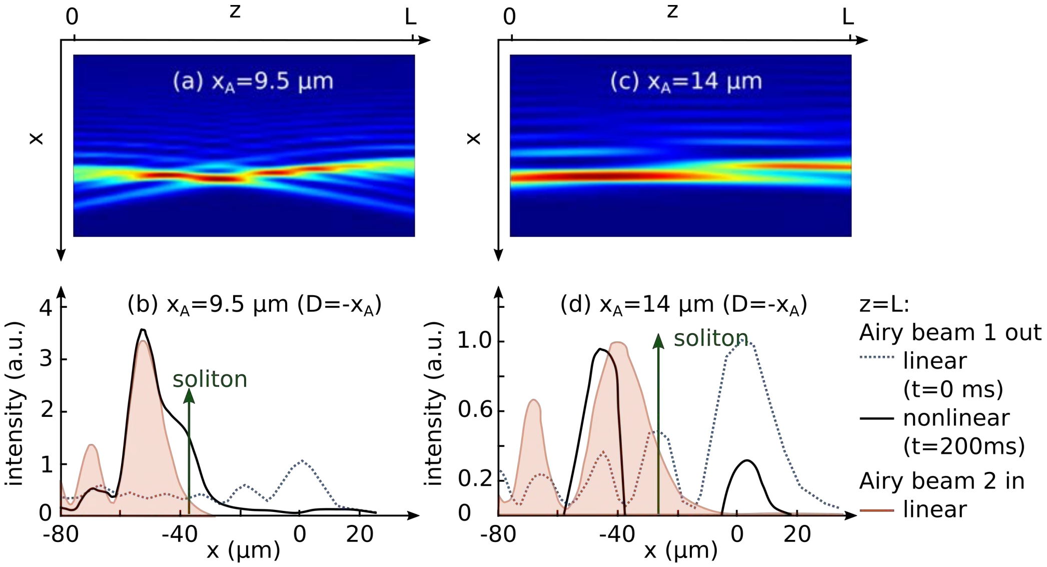

Figure 4.18: Waveguiding effect of two counterpropagating Airy beams in a biased photorefractive crystal for beam sizes, with $D = -x_A$, $P_A = 60$ µW and $U_{SBN} = 2$ kV. (a) (resp. (c)) Numerical intensity distribution inside the crystal and (b) (resp. (d)) experimental transverse intensity profile of the forward output beam at $z = L$ for $x_A = 9.5$ µm (resp. $x_A = 14$ µm).

In both cases the counterpropagating Airy beam is beyond the zero-deflection position of the forward beam, hence we expect an attraction of the forward beam towards the $-x$-direction. When the electric bias voltage $U_{SBN}$ is switched on a $t = 0$ s, we observe in both cases after 200 ms an intensity peak. This peak has shifted in both cases beyond the single soliton's position towards the counterpropagating main lobe [Figs. 4.18(b), 4.18(d)], which confirms the predicted attractive force. In particular for $x_A = 9.5$ µm the intensity peak has shifted of $-55$ µm and increased from 2.5-times to 3.5-times the linear peak intensity.

The nonlocal beam-matter interaction of the single Airy beam case is therefore increased by an additional beam-beam interaction. But if we analyze the intensity distribution of the self-focused Airy beam with $x_A = 14$ µm [Fig. 4.18(d)], only approximately 75 % of the energy is attracted towards the counterpropagating main lobe at $x = -45$ µm while a small beam remains at the linear position of the forward main lobe $x = 5$ µm. By identification this second beam corresponds to the accelerating beam, which co-exists with the Airy-soliton.

In terms of waveguides that can be photoinduced for both Airy beam's sizes, a small Airy beam ($x_A = 9.5$ µm) enhances the guide of the counterpropagating main lobe. A larger Airy beam ($x_A = 14$ µm) however strengthens the same guide induced by the counterpropagating main lobe, but it will also photoinduce a guide at $x = 5$ µm and therefore suggests a demultiplex waveguide structure with a separation distance of 5 µm-($-45$ µm) $= 50$ µm.
As a consequence, the simple decrease of the beams' size (by simply changing the phase mask on the spatial light modulator) enables to switch from a demultiplex solution [Fig. 4.18(d)] to a strong single output waveguide structure [Fig. 4.18(b)].

### Influence of the applied voltage: $U_{SBN}$

The previous analysis of the influence of the shift D and the Airy beam's size $x_A$ has been concentrated on the highest self-focusing of the Airy beam in presence of a counterpropagating Airy beam in the transient regime. As presented in Figure 4.16, the solitonic regime of the counterpropagating Airy beams is not stationary but relaxes after a while (a few seconds) which lowers the waveguiding quality. By applying an external bias electric field along the photorefractive c-axis of the medium, the nonlinearity is enhanced leading to a stronger self-focusing effect.

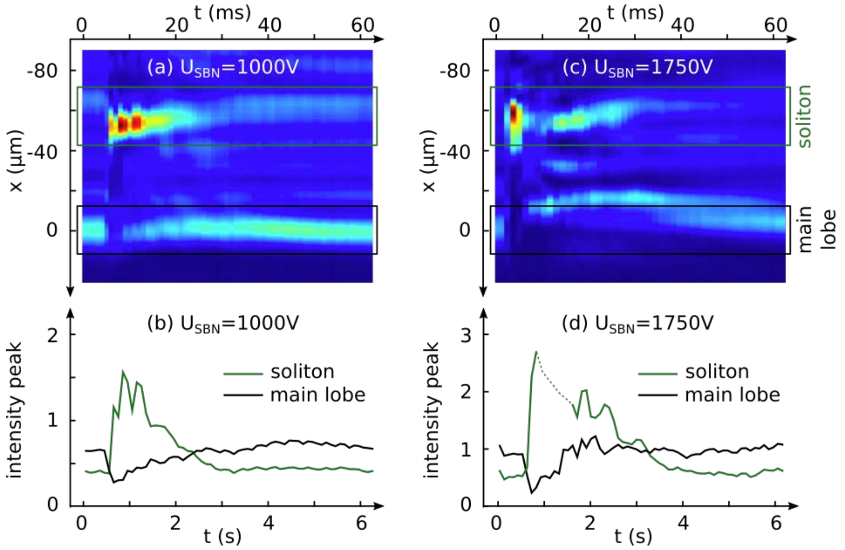

Figure 4.19: Influence of the external bias electric field on the waveguiding strength and stability, with $D = -x_A$, $P_A = 60$ µW and $x_A = 9.5$ µm. (a) (resp. (c)) Experimental transverse intensity distribution of the output beam at $z = L$ along time and (b) (resp. (d)) temporal evolution of the energy concentrated around the linear forward main lobe's position and around the solitonic output position (enhanced by the backward main lobe) for $U_{SBN} = 1000$ V (resp. $U_{SBN} = 1750$ V).

Figure 4.19 illustrates the evolution of the output beam along time, with $D = -x_A$, $P_A = 60$ µW and $x_A = 9.5$ µm for two different external electric bias voltages $U_{SBN} = 1000$ V and $U_{SBN} = 1750$ V. As the counterpropagating Airy beam is injected at $x = -x_A$ (soliton enhanced waveguide structure), the forward output intensity is mainly concentrated around two transverse positions: its linear main lobe's position around $x = 0$ and the position of the backward main lobe. To measure and compare both distributions, we integrate the intensity around both transverse locations as depicted on Figures 4.19(a) and 4.19(c) (green and black frames). The temporal evolution of both outputs appear on Figures 4.19(b) and 4.19(d) for two bias voltage values: $U_{SBN} = 1000$ V and $U_{SBN} = 1750$ V. The external electric field enhances two parameters: the solitonic peak energy value (almost doubling) and foremost the solitonic guide has a better waveguiding efficiency than the linear forward main lobe over a longer time. While the

1 kV-system offers a solitonic output over 1.8 s, the increase to 1750 V maintains the solitonic guide over 2.7 s. The bias voltage presents therefore an interesting tuning parameter to stabilize the waveguide structures over a longer time.

To summarize the influence of the system's parameters, we present a graph here below.

| Parameter | Symbol | Values | Influence |
|---|---|---|---|
| Backward beam | B | | Higher guiding efficiency<br>Larger transverse shift |
| Beams' shift | D | $[0; \approx 10x_A]$ | Tune of the demultiplex waveguiding (1-3 outputs)<br>Larger transverse shift |
| Beam's size | $x_A$ | $[9.5; 14]$ µm | Decrease of the solitonic self-focusing<br>Smaller transverse shift (less deflection)<br>Tune of the demultiplex waveguiding (1-2 outputs) |
| Bias electric voltage | $U_{SBN}$ | $[0; 2]$ kV | Increase of the solitonic self-focusing<br>Higher temporal stability of the soliton |

## 4.5 CONCLUSIONS

To conclude, we have demonstrated waveguiding achieved by a single Airy beam and by the nonlinear interactions of counterpropagating Airy beams. In comparison with waveguide structures created by Gaussian beams with the same dimensions and focusing conditions, the interaction schemes between two Airy beams offer larger waveguide possibilities thanks to their unique Airy shape and properties. (i) A single Airy beam photoinduces a waveguide with two outputs (see Chapter 2). (ii) Two counterpropagating Airy beams induce multiple output waveguiding structures that cannot be achieved with only two counterpropagating Gaussian beams. (iii) The resulting waveguiding remains possible even for transverse shifts of the interacting beams that by far exceed the beam waist. The numerical simulations presented in this paper motivate an experimental implementation of counterpropagating Airy beams induced optical routing.

In a second step we have demonstrated large multi-scale incoherent interactions between two counterpropagating Airy beams. By tuning the transverse shift, the beams' size and the nonlinearity strength, the self-focusing Airy beam is attracted towards the multiple lobes of the counterpropagating Airy beam.
The experimental results confirm the complex and various waveguide structures achievable by only the interaction of two counterpropagating Airy beams. We present a number of easy-to-tune parameters that enable to photoinduce efficient waveguides with large transverse shifts, with multiple outputs and stable over a few seconds. Unfortunately these solitonic structures are not steady-state and therefore do not enable the waveguide study using a Gaussian probe beam.

It is worth stressing that all previous cases of the numerical simulations of this chapter correspond to stationary situations in that the waveguide remains fixed when time increases above a transient duration of several order of the relaxation time of the crystal [Fig. 4.20(a)]. As we will discuss in detail in the next Chapter 5, we do find parameters where the waveguiding is not stationary anymore. In Figures 4.20(b) and 4.20(c) when increasing the nonlinear parameter $\Gamma$, we observe a situation where the intensity profile at the crystal output varies periodically [Fig. 4.20(b)] or irregularly [Fig. 4.20(c)] over time. These first spatiotemporal dynamics observed in a counterpropagating Airy beam system encourage further investigation into the relations between the Airy properties and the solitonic interactions.

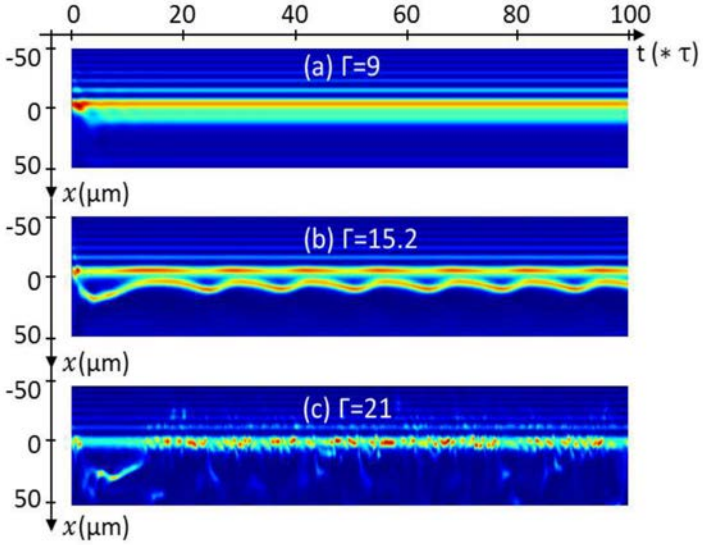

Figure 4.20: Spatiotemporal dynamics for counterpropagating aligned Airy beams. Normalized transverse intensity at $z = L$ (output of F and input of B) versus time: (a) stationary ($\Gamma = 9$), (b) time periodic ($\Gamma = 15.2$), (c) irregular ($\Gamma = 21$).

# 5

# THEORETICAL SPATIOTEMPORAL DYNAMICS OF COUNTERPROPAGATING AIRY BEAMS

We analyze theoretically the spatiotemporal dynamics of two incoherent counterpropagating Airy beams interacting in a photorefractive crystal under focusing conditions. For a large enough nonlinearity strength the interaction between the two Airy beams leads to light-induced waveguiding. The stability of the waveguide can be tuned via the crystal length, the nonlinearity strength and the beam's intensities and is improved when comparing to the situation using Gaussian beams. We further identify the threshold above which the waveguide is no longer static but evolves dynamically either time-periodically or even chaotically. Above the stability threshold, each Airy-soliton moves erratically between privileged output positions that correspond to the spatial positions of the lobes of the counterpropagating Airy beam. These results suggest new ways of creating dynamically varying waveguides, optical logic gates and chaos-based computing.

The context of this chapter is related to the following publication:
Noémi Wiersma, Nicolas Marsal, Marc Sciamanna, Delphine Wolfersberger, "Spatiotemporal dynamics of counterpropagating Airy beams”. In *Scientific Reports*, 5.2011 (2015).

## 5.1 DYNAMICS OF NONLINEAR SYSTEMS

Instabilities, self-oscillations and chaos are fundamental processes in nonlinear optics. Multiple beams' interactions in nonlinear media, even without external feedback, can give rise to beam self-trapping and spatial solitons that may further destabilise to spatiotemporal dynamics and then, eventually, chaos [145–147]. Multiple parameters, such as the optical intensity or the misalignment of the interacting beams [148, 149], enable to control the sequence of bifurcations from stationary dynamics to deterministic chaos [150].

### 5.1.1 *Route to chaos*

As seen in Chapter 1 (see Section 1.3.3), interacting solitons enable various optically induced waveguiding structures in the nonlinear media. The control of the mutual exchange of energy between interacting solitons enables to create all-optical guiding, dividing and switching devices [129, 134] and even over large distances in different media [151].

Interestingly the onset of spatiotemporal instabilities observed for various beams' configurations in different nonlinear media presents the same evolution scenario: initial diffraction, collapse to the soliton shape, then time-periodic dynamics to chaotic instabilities, where the interacting solitons rotate and twist around each other in an erratic way [67, 128, 135, 138, 152].

As an example Figure 5.1 depicts the numerical evolution of dynamics of two aligned counterpropagating Gaussian solitons in a biased photorefractive medium for increasing crystal length [153]. While Figure 5.1(a) summarizes all the encountered dynamics of the output beam on a so-called bifurcation diagram, Figures 5.1(b) to 5.1(e) depict the intensities at one output face of the crystal along time. The displayed intensity is the sum of the output beam (red plot) and the counterpropagating input beam (green plot). When both intensity distributions overlap, the resulting plot is yellow. This case is first seen on Figure 5.1(b), where the both intensities are constant along time and remain at the transverse position $\Delta x/w = 0$. The first change is observed at $L/L_d = 0.5$, where the output beam (red) shifts towards $\Delta x/w = -1$. In particular Figure 5.1(c) depicts the spatiotemporal evolution of the optical intensity along time for $L/L_d = 1$, where the beam's shift reaches $\Delta x/w = -2$. It is worth noting that this shift does not

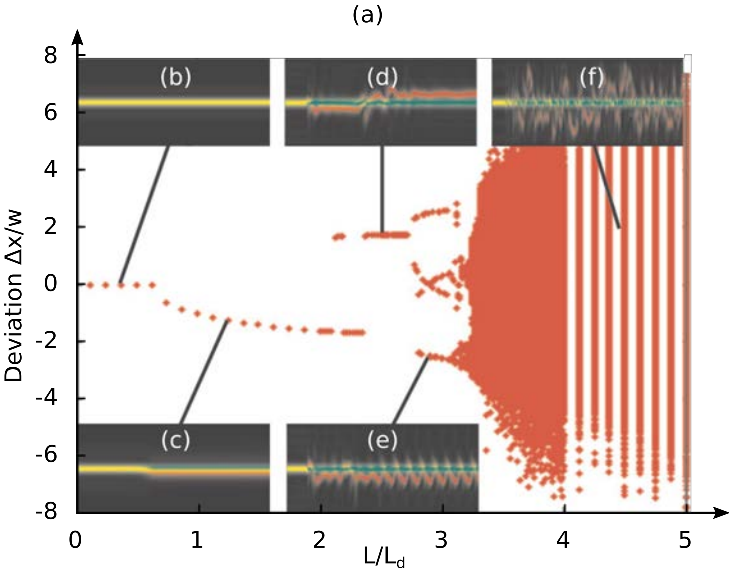

Figure 5.1: Bifurcation diagram, displaying transition to chaos in a 1D model of counter-propagating self-trapped beams. Insets depict characteristic time dependence of the beams along the diagram, at one of the crystal faces. The steady beam (green) is the entering beam, the unsteady beam (red) is the exiting beam. Adopted from [153], source: `www.lpr-journal.org`.

appear immediately in time. However, the shifted position remains steady-state afterwards, hence only the final shifted position is marked on the bifurcation diagram. When further increasing the crystal length, the system starts to evolve towards oscillating dynamics 5.1(e) and finally bifurcates to chaotic dynamics as the output beam moves erratically along the transverse $x$-axis [Fig. 5.1(f)].
The gradual bifurcation from a stable steady-state then oscillating regime to unstable dynamics represents a typical route to chaos of an optical system. Apart from Gaussian beams, other diffractive beam profiles such as optical vortices present solitonic behavior under self-focusing conditions and exhibit similar dynamical routes to instabilities [139].

### 5.1.2 *Dynamics of interacting Airy beams*

As already mentioned, under high-focusing conditions the Airy beam undergoes soliton-like behavior. The collision of two Airy beams also suggests a large variety of interaction schemes. The solitonic interactions have been demonstrated in the spatial domain using co-propagating Airy beams [140–143] and in the temporal domain using Airy pulses [154, 155]. In Chapter 4 we have studied the counterpropagating configuration in photorefractive media and we have shown more complex stationary waveguide structures than those induced by interacting Gaussian beams. A single Airy beam leads to waveguiding structures with multiple outputs [127]. The additional interactions induced by a counterpropagating beam allows for achieving complex waveguiding structures that would otherwise require the counterpropagating interactions of more than two Gaussian beams. But these stationary structures only exist for a limited range of the nonlinearity strength.

As the interactions of two counterpropagating conventional beams lead to spatiotemporal dynamics, we question whether self-accelerating Airy beams undergo a similar spatiotemporal behavior and how the Airy properties influence the dynamics. To describe these dynamics, we analyze the spatiotemporal evolution of the output position of the forward off-shooting soliton at the crystal's output plane $z = L$.

## 5.2 THEORETICAL RESULTS

### 5.2.1 *General overview*

As in previous Chapter 4, we study the nonlinear interactions of two counterpropagating Airy beams in a photorefractive medium. We consider the propagation of two identical one-dimensional Airy beams along the longitudinal *z*-axis. The two Airy beams are initially injected at each side of the crystal and are both defined by the lobe size $x_A$ and aperture parameter $a$.

The interaction scheme and evolution are illustrated on Figure 5.2. As presented on Figure 5.2(a), both Airy beams are aligned with their deflection along the direction of the photorefractive c-axis. When a positive external electric field is applied on the crystal, both Airy beams turn into off-shooting solitons [Fig. 5.2(b)]. Through the Pockels effect multiple waveguiding structures are photoinduced, which have been extensively studied in the previous Chapter 4. If we increase the nonlinearity of the system via the parameter $\Gamma$ ($\Gamma > 10$), we demonstrate the existence of a threshold curve above which non steady-state dynamics appear. To describe the dynamics observed, we study the spatiotemporal evolution of the off-shooting soliton at $z = L$. As illustrated on Figure 5.2(c), the soliton's output position starts evolving along time presenting, amongst others, an oscillating behavior.

We have identified that the interaction schemes of two counterpropagating beams depend on two main control parameters, that are the nonlinear coupling constant $\Gamma$ and the crystal length $L$ (as in reference [153]). Figure 5.3 shows a stability diagram in the plane of the following parameters: $(\Gamma, L)$. It depicts the various spatiotemporal dynamics of the forward-propagating "off-shooting" soliton's intensity at the output $I(x, z = L)$ for two different intensities $F_0 = B_0 = \sqrt{1.5}$ [Fig. 5.3(a)] and $F_0 = B_0 = \sqrt{6}$ [Fig. 5.3(b)]. For an Airy lobe's waist $x_A = 10\ \mu m$ ($a = 0.1$), the parameter range corresponds to $1\ cm \leqslant L \leqslant 10\ cm$ and to an external bias electric field of a few $kV/cm$ ($\Gamma \in [3, 30]$).
For low $\Gamma$-values ($\Gamma = 3$), the nonlinearity $\Gamma$ applied on the system is not high enough to create locally a large refractive index variation inside the crystal by the photorefractive effect and therefore to induce an off-shooting soliton. Still, the propagation of each Airy beam optically induces a curved waveguide along the deflecting Airy trajectory [36]. We call this region 'static waveguide without off-shooting soliton'.

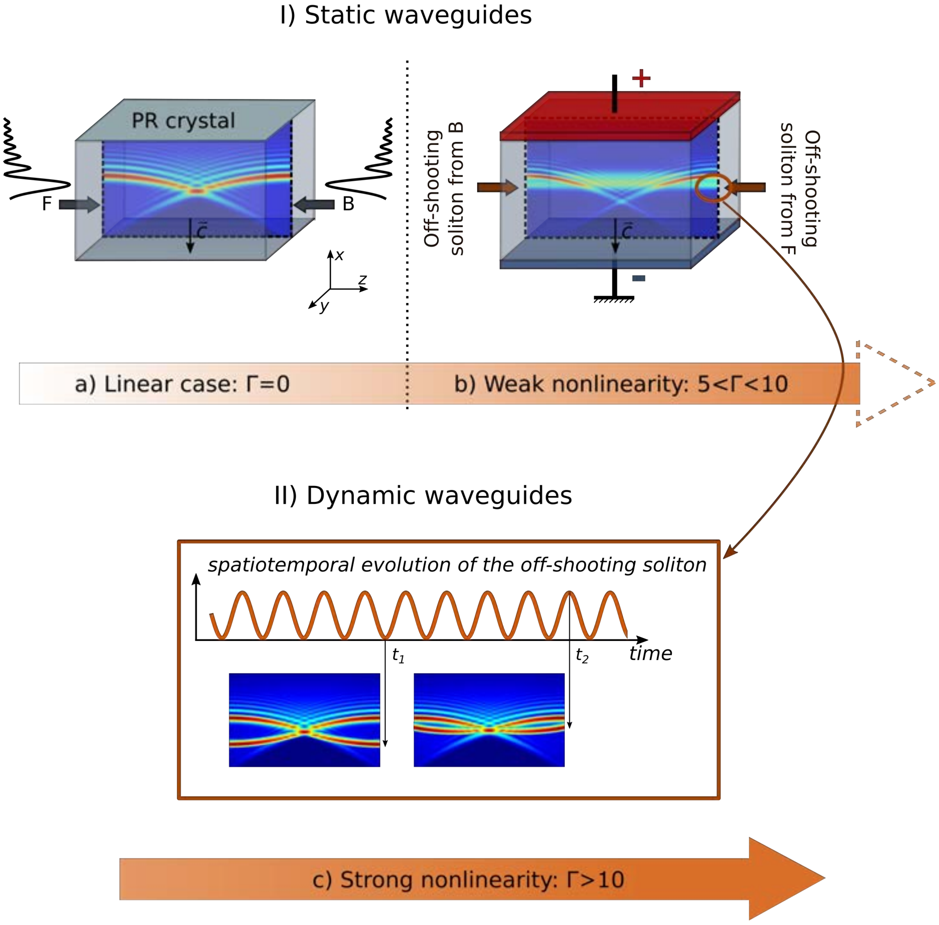
I) Static waveguides
PR crystal
F
B
$\bar{c}$
x
z
y
Off-shooting soliton from B
Off-shooting soliton from F
+
-
a) Linear case: Γ=0
b) Weak nonlinearity: 5<Γ<10
II) Dynamic waveguides
spatiotemporal evolution of the off-shooting soliton
$t_1$
$t_2$
time
c) Strong nonlinearity: Γ>10

Figure 5.2: Two counterpropagating Airy beams' configuration in a photorefractive crystal. (a) Linear propagation in an unbiased photorefractive crystal ($\Gamma = 0$). (b)-(c) Nonlinear interaction scheme of two counterpropagating Airy beams in an externally biased photorefractive crystal: (b) intensity field inside the crystal induced by weak nonlinear interactions, (c) spatiotemporal evolution of the forward "off-shooting soliton" for stronger nonlinear interactions at $z = L$.

For a larger nonlinearity strength, each counterpropagating Airy beam undergoes self-focusing and a part of the beam's energy turns into an "off-shooting" soliton [Fig. 5.2(b)]. We define the existence of an off-shooting soliton, when a peak of at least 10 % of the input intensity exits at the crystal's side $z = L$ and can be clearly distinguished from the linear output beam. Since almost half of the

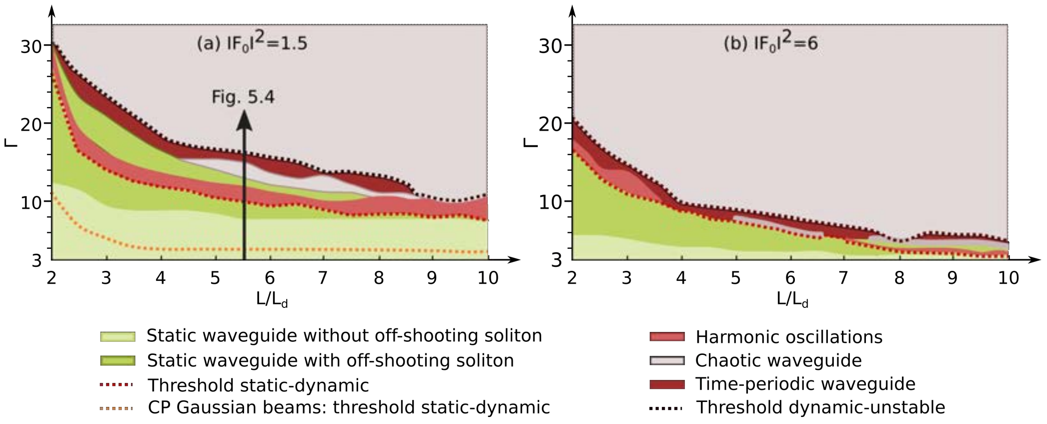

Figure 5.3: Typical dynamical behavior of counterpropagating Airy beams in the parameter plane (Γ, L): (a) with low input intensities ($F_0 = B_0 = \sqrt{1.5}$), (b) with high input intensities ($F_0 = B_0 = \sqrt{6}$).

energy is stored in the first Airy lobe [107], the nonlinearity of the system mostly influences the main lobes and the off-shooting solitons. The interaction of the two counterpropagating Airy beams then leads to various new static waveguide structures and we call this region 'static waveguide with off-shooting soliton'.

As presented in Chapter 4, the photoinduced waveguide structure enables a Gaussian beam to exit the crystal at a single or at two output positions simultaneously. The parabolic trajectory of the counterpropagating Airy beams enables waveguiding structures even for transverse shifts of the interacting beams that by far exceed the beam waist.

When we further increase the nonlinearity Γ, the waveguide is no longer constant with time but rather shows stable time-periodic dynamics: the off-shooting soliton evolves from a constant transverse output position to an output position that oscillates harmonically in time along the x-axis [Figs. 5.2(c), 5.4(c)]. We call this region 'harmonic oscillations'.

Similar to the case of counterpropagating Gaussian beams [138], the critical nonlinearity strength that delimits the onset of time-periodic oscillations of the waveguide decreases with the increase of the crystal length L, see the line labeled 'threshold static-dynamic' in Fig. 5.3.

For an even larger Γ and/or crystal length L, the time-periodic waveguide dynamics is replaced by chaotic-like spatiotemporal dynamics. The position of the

off-shooting soliton does not vary periodically in time but rather in an erratic way. As will be shown later, while the trajectory is erratic in time, the motion of the off-shooting soliton is attracted towards the input positions of the lobes of the counterpropagating Airy beam. We call this parameter region 'chaotic waveguide'.
The critical nonlinearity leading to unstable waveguiding decreases with the increase of the crystal length L, as is also true for counterpropagating Gaussian [138] and vortex beams (see the line labeled 'threshold dynamic-unstable' in Fig. 5.3).

Interestingly, we identify two additional regions. In both cases 5.3(a) and 5.3(b) the time-periodic dynamically varying waveguide may re-stabilize to a static waveguide when increasing the nonlinearity. The off-shooting soliton stabilizes again at a constant output position. The possibility to stabilize again the photoinduced waveguiding by increasing the nonlinearity strength has not been observed earlier with counterpropagating Gaussian beams and is related to the multilobe shape of the Airy beams. Therefore, this suggests an advantage in using counterpropagating Airy beams. We also identify another parameter region where the position of the off-shooting soliton varies periodically in time but not in an harmonic way. We have simply called this region 'time-periodic waveguide'. This specific dynamics bifurcates from the harmonic waveguide case but is also observed as a bifurcation of the chaotic waveguide case. We shall detail these dynamics and their bifurcations in the next section.

Similarly to other counterpropagating beams' systems, the intensity of the input beams is an important parameter. When increasing the total optical intensity injected in the crystal through the counterpropagating beams the refractive index variations increases, hence resulting in more nonlinear interactions; see [Fig. 5.3(b)]. When we compare the Figures 5.3 (a) and (b), the critical nonlinearity that leads to either a time-periodic waveguide or even chaotic waveguide for a normalized intensity $|F_0|^2 = 1.5$ [Fig. 5.3 (a)] is larger than for $|F_0|^2 = 6$ [Fig. 5.3 (b)]. The stability of the waveguide is therefore reduced by the increase of the optical intensity.
Finally it is worth comparing the critical nonlinearity that leads to dynamically varying waveguide (our dashed line) in the case of counterpropagating Airy beams with the one computed for counterpropagating Gaussian beams (dotted line). Besides the fact that Airy-induced waveguides have more complex features than Gaussian-induced waveguides, it appears also that, the Airy-induced

waveguides are stable in a large range of parameters and in particular for a large range of nonlinearity strength $\Gamma$ and/or crystal length $L$. This unique property of Airy-induced waveguides is related to the diffraction-free propagation and multilobe shape of Airy beams.

### 5.2.2 *Signature of different regimes*

In this section, we analyze the nature and the evolution of the spatiotemporal dynamics of two counterpropagating Airy beams for a fixed crystal length $L$ when the nonlinear coupling strength $\Gamma$ is increased. Physically the nonlinearity is increased through the positive bias electric field applied on the crystal or the intensity of the laser beam. Although as mentioned earlier the stability of the photoinduced waveguide depends on the crystal length $L$, the nonlinearity $\Gamma$ and the beam intensities, we shall restrict ourselves to one case where $F_0 = B_0 = \sqrt{1.5}$ and $L = 5.5L_d$. For Airy beams with the parameters $x_A = 10\mu m$, $a = 0.1$, it corresponds to a crystal length of $L = 28mm$ (see arrow [Fig. 5.3(a)]). This case illustrates the complexity underlying the sequence of bifurcations to spatiotemporal instabilities of the waveguide [Fig. 5.4(a)]. A similar sequence of bifurcations occurs when varying the system parameters. For each $\Gamma$-value, we simulate the propagation of two counterpropagating Airy beams over $t_f = 100\tau_0$, where at each crystal's side the main lobe of the counterpropagating Airy beams is centered around $x = -x_A$ for its input position. We then display the spatiotemporal dynamics of the forward off-shooting soliton at the crystal's output side $z = L$ along the transverse $x$-axis by plotting the off-shooting transverse position versus time [Figs. 5.4(b)-(g)]. To avoid the transient dynamics, we detect the extreme $x$-positions taken by the off-shooting soliton within the times $t_1 = 20\tau_0$ and $t_f = 100\tau_0$. The bifurcation diagram on Figure 5.4(a) resumes the position of the spatial output of the off-shooting soliton during time: for each $\Gamma$-value, the $x$-extrema taken by the off-shooting soliton along time are represented with black dots.

The diagram on Figure 5.4(a) displays the route to instabilities from a system with a weak nonlinearity ($\Gamma = 9$) to a highly nonlinear system ($\Gamma > 16$). For $\Gamma \in [9, 10.2]$, the bifurcation diagram displays a steady-state transverse output position of the off-shooting soliton during time [Fig. 5.4(b)]. The steady-state case depicted in Figure 5.4(b) corresponds to the waveguide structures demonstrated

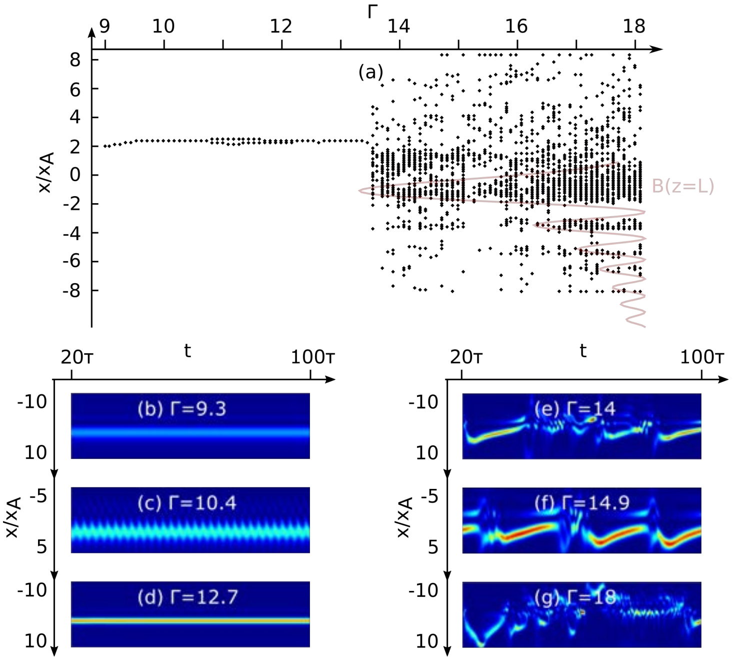

Figure 5.4: Spatiotemporal dynamics of two counterpropagating Airy beams in a long crystal $L = 5.5L_d$, with the normalized intensities $F_0 = B_0 = \sqrt{1.5}$. (a) Bifurcation diagram of the transverse output position of the forward off-shooting soliton at $z = L$, with the transverse normalized intensity profile of backward Airy beam at $z = L$. (b)-(g) Temporal evolution of the transverse output position of the forward off-shooting soliton at $z = L$: (b) steady-state ($\Gamma = 9.3$), (c) sinusoidal oscillations ($\Gamma = 10.4$), (d) second steady-state ($\Gamma = 12.7$), (e) first instabilities ($\Gamma = 14$), (f) periodical non-sinusoidal oscillations ($\Gamma = 14.9$) and (g) instabilities ($\Gamma = 18$). E.g. experimentally for counterpropagating Airy beams in a SBN:75 crystal ($L * 5\ mm * 5\ mm$) with $x_A = 10\ \mu m$: $L = 28mm$, $U_{ext} \in [500V, 900V]$.

in [127], where the counterpropagating Airy beams and their off-shooting solitons co-exist in the crystal. When $\Gamma \in [10.3, 11.8]$, two extrema of the $x$ position of the off-shooting soliton appear for a given $\Gamma$ value. The time-trace of the $x$ position of the off-shooting soliton displays a sinusoidal evolution [Fig. 5.4(c)]. We observe a stable oscillating dynamics, where the off-shooting soliton oscillates periodically around its characteristic position $x = 2.5x_A$. The period of the sinusoidal oscillation is about $3.5\tau_0$, i.e. is of the same order of magnitude than the material nonlinear optics time-scale. The amplitude of the oscillation is determined by the Airy properties and in particular their deflection characteristics.

Indeed the amplitude of the oscillation is larger for a longer crystal since by increasing the crystal length, the counterpropagating Airy beams deflect more before colliding. The Figure 5.4(d) shows that this oscillating soliton dynamics re-stabilizes when increasing the nonlinearity leading to a new static waveguide structure. This singular case will be explained in details and illustrated in Figure 5.5 (b) of the next section.

When increasing the nonlinearity strength above $\Gamma = 13$, the position of the off-shooting soliton presents an erratic motion along the output axis $x$ [Fig. 5.4 (a)]. Figure 5.4(e) indicates that the soliton tends to follow alternatively a complex time-periodic, then a chaotic-like behavior. As depicted on Figure 5.4(f), when we increase the nonlinearity ($\Gamma = 14.8$), the chaotic-like evolution of the position of the off-shooting solution stabilizes to a time-periodic dynamics where oscillations at a slower time-scale modulate the dynamics with a higher amplitude than for the harmonic oscillation depicted in Figure 5.4 (c).

Finally when $\Gamma > 15.3$, the time-periodic dynamically varying waveguide becomes unstable and the position of the off-shooting soliton rotates in an erratic way around the single Airy case position $x = 0$ and the counterpropagating main lobe's position $x = -x_A$ [Fig. 5.4(g)]. It is worth noting that for a very high coupling strength ($\Gamma > 16.3$) the erratic motion of the off-shooting soliton encompasses additional attractive $x$-values at $x \in \{-3.2x_A, -4.8x_A, -6.2x_A\}$. Interestingly these $x$-values correspond to the respective input positions of the second, third and fourth lobe orders of the counterpropagating Airy beam [Fig. 5.4(a)]. The characteristics of this chaotic soliton motion will be further discussed in the next sections.

## 5.3 COMPARISON WITH GAUSSIAN SYSTEMS

In the previous Section 5.2 we have demonstrated the existence of a threshold curve above which non steady-state dynamics appear. For similar operating conditions, this threshold is larger for interacting Airy beams when compared to interacting Gaussian beams [Fig.5.3], hence demonstrating the larger stability range of the photoinduced Airy waveguides.

### 5.3.1 *Re-stabilization of the waveguide for large nonlinearity*

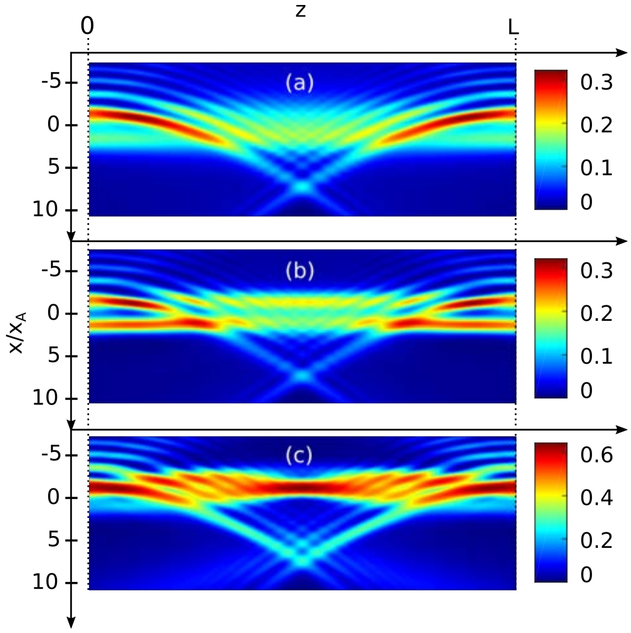

Figure 5.5: Static waveguides: intensity fields of two counterpropagating Airy beams inside a PR crystal under focusing conditions ($L = 5.5L_d$). With initial intensity $F_0 = B_0 = \sqrt{1.5}$ [Fig. 5.3(a)]: (a) below the static-dynamic threshold curve ($\Gamma = 10$), (b) re-stabilization above the static-dynamic threshold curve ($\Gamma = 12.5$). (c) With initial intensity $F_0 = B_0 = \sqrt{6}$, on the static-dynamic threshold curve ($\Gamma = 7$) [Fig. 5.3(b)].

As previously emphasized in Figure 5.3, dynamically varying waveguides photoinduced by two counterpropagating Airy beams can re-stabilise when the nonlinearity $\Gamma$ increases. So far, the dynamical behavior of two counterpropagating Gaussian beams has only shown an evolution from a steady-state, then time-

periodic to chaotic like regimes [153]. The Figure 5.5 compares the typical static waveguides with off-shooting soliton that can be observed in the two stability $(\Gamma, L)$-diagrams [Figs. 5.3 (a)-(b)]. Figure 5.5(a) corresponds to the waveguide structures presented in [127] where a Gaussian probe beam can be guided along the crystal to one or two outputs.
Fig. 5.5(b) illustrates the new waveguide structure in the re-stabilization zone ('static waveguide with off shooting soliton' above the line labeled 'threshold static-dynamic' [Fig. 5.3]). This waveguide structure offers the same type of photoinduced waveguides as in Fig. 5.5(a) but with a better coupling efficiency (up to 55% instead of 40%) in the off-shooting solitons due to the stronger focusing nonlinearity.

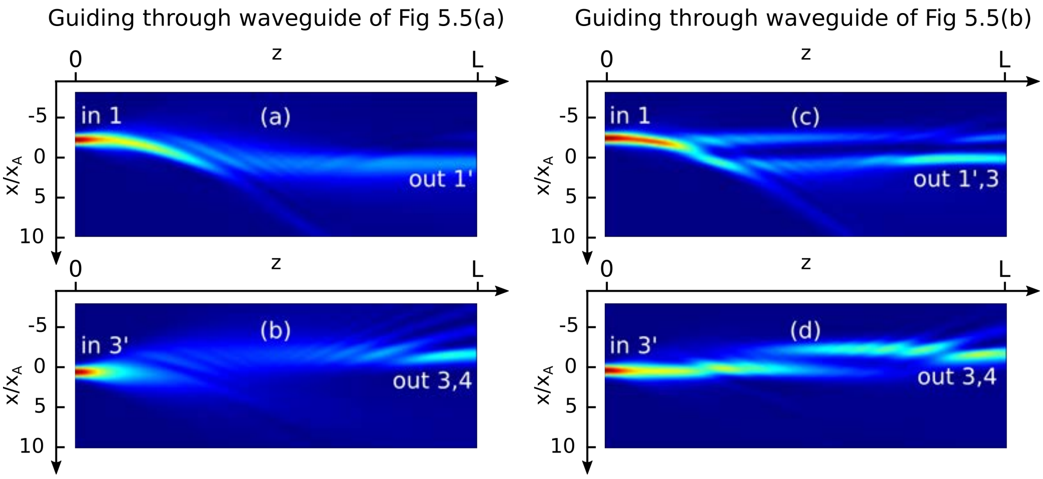

Figure 5.6: Linear propagation of a Gaussian probe beam through the waveguide structures induced (a),(b) in Figure 5.5(a) (below the static-dynamic threshold) and (c),(d) in Figure 5.5(b) (above the static-dynamic threshold). Intensity field of the guided Gaussian beam through the waveguide structure for an input position on the $(z = 0)$-face of the crystal (a),(c) at 1 (induced by the main lobe of F) and (b),(d) at $3'$ (induced by the off-shooting soliton of B).

The waveguide strengths of the structures induced below and above the static-dynamic threshold curves [Figs. 5.5(a), 5.5(b)] are illustrated on Figure 5.6. The first structures in Figures 5.6(a) and 5.6(b) have already been studied in previous Chapter 4 (see Section 4.3.3, Figure 4.12). If we compare the results with an output beam guided through a waveguide structure induced in the re-stabilization regime in Figures 5.6(c) and 5.6(d), the first observation is that the intensity transmitted is significantly higher. In addition we note a change in the spatial intensity distribution of the output beam injected at 1. While one output beam is observed at $1'$ in the steady-state structure of 5.5(a) [Fig. 5.6(a)], the re-stabilized waveguide of Figure 5.5(b) splits the Gaussian probe beam in two output beams at $1'$ and 3 hence demonstrating a stronger cross-coupling of the Airy beams for higher self-focusing nonlinearity [Fig. 5.6(c)].

Figure 5.5(c) also presents a particular steady-state structure in the strong intensity case $F_0 = B_0 = \sqrt{6}$ at two parameter points: $(L = 5, \Gamma = 7.5)$ and $(L = 5.5, \Gamma = 7)$. Contrary to the usual steady-state case, where the counterpropagating Airy beam induces a transverse shift of the off-shooting soliton [127], the off-shooting soliton changes its output position and merges exactly into the main lobe of the counterpropagating Airy beam. In the configurations (b) and (c) where the nonlinearity of the system is increased through $\Gamma$ or the initial intensity, the space-charge field photoinduced by the multiple lobe orders of the two counterpropagating Airy beams has a significant role in the interaction schemes in the photorefractive crystal. Although the main power is transferred into the off-shooting soliton during the nonlinear propagation of the Airy beams [107], the secondary lobes of the Airy beams are essential for the re-stabilization of our system above the conventional steady-state threshold curve.

### 5.3.2 *Chaotic motion of Airy-induced soliton*

As already emphasized in Section 5.2.1, the dynamical behavior of the photoinduced waveguide significantly depends on the crystal length. In the 'chaotic waveguide' region [Fig. 5.3], we propose therefore to compare the situation of a short crystal (e.g. $L = 2.5L_d = 13mm$) and the one of a long crystal (e.g. $L = 5.5Ld = 28mm$). It is worth mentioning that due to their parabolic trajectory, the two counterpropagating Airy beams intersect at $x_{L=2.5L_d} = 0.7x_A$ for the short crystal and at $x_{L=5.5L_d} = 7x_A$ for the long crystal. As a result, the photoinduced waveguides originate mostly from the interaction of the first and second lobe orders of the counterpropagating Airy beams in the case of a short crystal, and from the interaction of the four first lobe orders of the counterpropagating Airy beam in the case of a longer crystal. The resulting waveguiding structure in the case of a longer crystal will be larger along the transverse $x$-axis ($\Delta x_{L=5.5L_d} \approx 7x_A$ instead of $\Delta x_{L=2.5L_d} \approx x_A$ in the case of a short crystal). Sim-

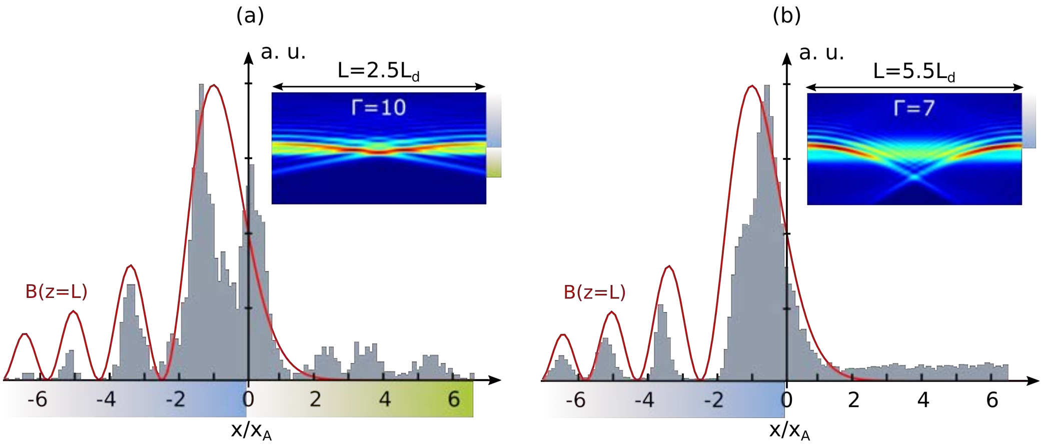

Figure 5.7: Probability of occurrence of the position of the off-shooting soliton at the output face of (a) a short crystal ($L = 2.5L_d$; $\Gamma > 26.6$) and (b) a long crystal ($L = 5.5L_d$; $\Gamma > 15.3$), with $F_0 = B_0 = \sqrt{1.5}$ in both cases. The red curve indicates as a guide for the eyes the position of the counterpropagating Airy beam at the crystal output face. Insets represent the photoinduced waveguide in a situation before the onset of spatiotemporal dynamics.

ilarly, in the case of a long crystal, the transverse trajectory of the off-shooting solitons will shift from its typical transverse position $x_{soliton} = 0$ towards the $+x$-direction.

In particular, as illustrated in Figures 5.4 (a) and (g) for a long crystal, under high nonlinear conditions, the system of two counterpropagating Airy beams shows a peculiar instability pattern: the output positions of the off-shooting soliton in the unstable regime appear to be attracted toward very specific output positions, which correspond to the respective input positions of the different lobe orders of the counterpropagating Airy beam. Figure 5.7 depicts the statistical distribution of the output position of the off-shooting soliton in (a) a short crystal ($L = 2.5L_d$) and (b) in a long crystal ($L = 5.5L_d$) with $F_0 = B_0 = \sqrt{1.5}$. The output positions of the off-shooting soliton are not distributed in a continuous way but rather in a discrete way. The privileged output positions match with the input positions of the Airy lobes of the counterpropagating backward beam (blue zone). Also the attraction strength, measured by the highest probability in the plotted histograms, decreases for the higher lobe orders, as the space-charge field related to the energy distribution of the Airy beam decreases along the $-x$-axis. In the short crystal case (a), the off-shooting soliton is also attracted towards the $+x$-axis, at the output positions of the Airy lobes of the forward beam (green zone).

Such spatially localized instabilities have never been observed in an optical system using counterpropagating beams [135, 138]. Our system based of counterpropagating Airy beams therefore creates a chaotic motion of the off-shooting soliton whose topology can be engineered by both the Airy beam properties and the photorefractive crystal nonlinearity strength and length. Recent years have seen a tremendous interest in applications of optical chaos for all-optical signal processing including optical generation of random numbers. The most conclusive proposals so far have used the temporal chaotic output of semiconductor lasers [156]. The digital sampling of optical chaos allows to extract random bits at high bit rate [157]. The extension to massive parallel computing is however limited in that it requires either a large number of such chaotic lasers or the use of uncorrelated emission from individual laser longitudinal or transverse modes. In the present scheme, one has access to a chaotic output (the erratic motion of the off-shooting soliton) that is by essence spatially multiplexed at discrete positions that match the locations of Airy beam lobes. Our findings therefore suggest innovative ways of performing multiplexed chaos-based optical computing.

## 5.4 CONCLUSIONS

To conclude, the interaction of two counterpropagating Airy beams in a photorefractive crystal leads to peculiar spatiotemporal dynamics. The system evolves from static to time-periodic then chaotic waveguides when increasing the nonlinearity strength and the crystal length. We demonstrated the existence of a threshold curve above which non steady-state dynamics appear. By comparison to similar studies using counterpropagating Gaussian beams, photoinduced Airy waveguides are stable for a larger range of parameters. Also on the route to instabilities, we identify a singular additional region where dynamical waveguides re-stabilize to static waveguides with a better coupling efficiency. When the system bifurcates to the chaotic-like dynamics, the off-shooting soliton moves in an erratic way with privileged positions that match the input positions of the multiple lobes of the counterpropagating Airy beams. Such spatially localized instabilities suggest innovative ways of performing optical computing based on spatiotemporal chaos. The unique properties of static and dynamic Airy waveguide structures motivate experimental demonstration and implementation in different nonlinear optical media.

# Part III

# CONCLUSION

# 6

# CONCLUSIONS AND PERSPECTIVES

## 6.1 CONCLUSIONS

This thesis resumes three years of research studies in essentially three fields:

- the self-focusing of an accelerating 1D-Airy beam into a solitonic structure in photorefractive media,
- the spatiotemporal interactions of two counterpropagating solitonic 1D-Airy beams in the nonlinear crystal,
- and the waveguiding structures induced in the medium by the propagating Airy beams.

First we have both experimentally and theoretically analyzed the solitonic beam when off-shooting from an Airy beam propagating in a nonlinear biased photorefractive crystal. While we were not able to observe a steady-state solitonic regime experimentally, we have demonstrated in Chapter 2 the influence of the parameters enhancing the nonlinearity of the system or thus the diffraction of the beam. Because solitons are defined by the exact balance between the nonlinearity of the medium and the diffraction of the beam, we scanned the strength of both effects by tuning the system's parameters. On one hand the nonlinearity, hence the photorefractive effect, can be increased using the external bias electric field and the optical power. On the other hand a smaller beam's size and a longer propagation medium induce a larger diffraction effect, leading to stronger self-focusing for similar or lower nonlinearity. Experimentally the high self-focusing regime has only been observed in the transient regime. By comparison with the Gaussian beam, the Airy beam requires a higher nonlinearity because of its almost diffraction-free propagation. In addition we have shown a *large transverse mobility* of the output beam during the transient self-focusing regime thanks to the parabolic trajectory and the multi-lobe structure of the Airy beam.

Afterwards in Chapter 3 we have focused our study on the transient self-focusing regime towards the solitonic structure. As an Airy beam splits into an off-shooting soliton and a linear accelerating multi-lobe beam, we have analyzed the behavior of the accelerating structure in the presence of the solitonic beam at the output of the biased crystal. First the multi-lobe structure is attracted towards the off-shooting soliton. Because the transverse beam size is simultaneously tightening, its acceleration also increases. In relation to previous chapter, we have also studied the influence of a background illumination on the transient dynamics as steady-state photorefractive Gaussian solitons require a background illumination on the medium to remain stable. While we have not been able to stabilize the solitonic structure, the dark intensity enables the steady-state output beam to remain in a focused multi-lobe regime instead of the defocusing structure observed in Chapter 2.

The combined attraction and acceleration of the linear multi-lobe beam near the intense off-shooting soliton can find analogies in the gravitational lensing effect in spacetime. This phenomenon was first predicted in the general relativity theory of Albert Einstein and describes the attraction and acceleration of a wave when approaching a massive object such as a star in spacetime. By tuning the nonlinearity of our optical system via the optical power, the self-focusing effect, hence the gravitational lensing in our analogy, can be enhanced.

In a second step the better understanding of the physics of the self-focusing (and in particular the solitonic) regime has encouraged us to study the guiding structures photo-induced by the Airy beam in Chapter 4. Numerically we have propagated a Gaussian probe beam in the waveguide created by a steady-state off-shooting Airy-soliton. Thanks to the multi-lobe Airy-structure on one side and the single solitonic guide on the other side of the crystal, we have observed multiple types of waveguiding inside the same structure. Depending on the input position, a probe beam is single-guided or demultiplexed (two output beams).

In addition the configuration using two incoherent counterpropagating Airy beams offers larger optical interconnects. In comparison with the beam-matter interactions studied previously, the presence of a second beam influences the propagation of each Airy beam and therefore of the off-shooting solitons. Experimentally we can tune the output distribution of the Airy beam by shifting both counterpropagating beams from each other along the transverse axis. The output beam can be shifted along the transverse axis, split into multiple beams or concentrate into a more intense beam. The diversity of the output beam in a counterpropagating configuration can be explained by the multi-lobe waveguiding structures induced by the second beam at the output face for the off-shooting soliton. By tuning the transverse shift between the two counterpropagating Airy beams and the beams' size, we can reach larger output positions. In addition the waveguiding effect is increased via the optical power and the electric bias field. While we did not reach the stability of our counterpropagating solitonic beams in the experiment, we numerically tested the photoinduced waveguide structures in the case of aligned and misaligned Airy beams. Similar to the single Airy beam's case, a probe beam may exit the crystal as one or two output beams. The additional counterpropagating Airy beam however offers these two types of waveguide for both propagation directions. Such waveguiding structures are unique for Airy beams and could not be achieved using only two Gaussian beams. Also experience and theory have shown that the large intensity field induced by both Airy beams enables them to interconnect even when strongly misaligned. *Airy beams are therefore excellent candidates for large and complex waveguiding solutions.*

Finally we have analyzed the interactions of the counterpropagating Airy beams' configuration for increasing nonlinearity. While conventional counterpropagating beams present an evolution from a steady-state regime to unstable chaotic dynamics, we have questioned whether the nearly diffraction-free property of an optical Airy beam offers a larger stability range. This matter has been addressed in Chapter 5, where we have numerically studied the spatiotemporal behavior of the off-shooting solitons for increasing electro-optical nonlinearity $\Gamma$ (optical power and bias electric field) and diffraction (via the length of the crystal L). As for conventional beams, the off-shooting soliton is more unstable for higher electro-optical nonlinearity and propagation distance. We have demonstrated the existence of a threshold curve in the $(\Gamma - L)$-diagram, above which the steady-state off-shooting soliton, studied for waveguiding in previous chapters, first bifurcates towards oscillating dynamics. When further increasing the nonlinearity of the system, the output beam evolves towards an unstable then chaotic-like behavior. By comparison with the bifurcation route in the Gaussian case, counterpropagating Airy beams are much more stable, hence they induce stronger steady-state waveguiding structures. In addition the Airy properties offer a few interesting singularities. Indeed we have demonstrated the existence of peculiar steady-state regimes above the steady-state threshold. Finally the multilobe structure of the counterpropagating Airy beams enable to spatially organize the output position of the off-shooting soliton even in the chaotic-like regime. As a consequence, the question about the stability has opened a much larger field of spatiotemporal interactions. Interestingly the Airy distribution and properties increase the complexity of the system, however the second Airy spatially organizes the spatiotemporal dynamics on the system.

All along the thesis, we have considered the solitonic regime of an Airy beam, which theoretically annihilates the fascinating properties of the Airy beam. Instead the intrinsic Airy features have remained throughout our experimental and numerical work:

- multi-lobe Airy distribution: creation of demultiplexing waveguides, larger transverse waveguiding, spatial localization of instabilities

- diffraction-free propagation: interconnection of multiple lobes of the counterpropagating Airy beams over a longer distance, larger stability range

- accelerating propagation: larger transverse beams' interconnections, support for the analogy with the gravitational framework

The results confirm the Airy beam as an ideal candidate for all-optical waveguiding and suggest to deepen its study in larger optical configurations.

## 6.2 PERSPECTIVES

### 6.2.1 *Stability control of the Airy-soliton*

#### *Experimental stabilization of the Airy-soliton*

As emphasized all along the manuscript, the off-shooting soliton regime suggests a large range of optical interconnects. Nevertheless we have not been able to experimentally obtain a steady-state soliton. This issue should be further studied in following work as we now have a better knowledge of the origins and the mechanisms of the self-focusing effect leading to the off-shooting Airy-soliton. Furthermore it would be interesting to compare the stability of the solitonic structure in the single Airy beam case and with a counterpropagating Airy beam.

#### *Theory of the self-focusing dynamics*

The theoretical model used for our numerical simulations does not show a relaxed regime of the Airy-soliton into an accelerating Airy-like structure. As the photorefractive effect is considered to be dominated by the drift effect (induced by the electric bias field), we suggest to add the neglected diffusion effect in the propagation algorithm. As shown for Gaussian solitons, both types of charge transports have to be considered for a complete understanding of the nonlinear photorefractive mechanisms [48]. In the Airy case the decomposition of the self-focusing Airy beam into two beams may activate different physical mechanisms, such as the drift effect for the off-shooting soliton and the diffusion effect for the remaining accelerating beam.

### 6.2.2 *Experimental waveguiding of probe beams*

Theory predicts efficient single and demultiplex waveguiding structures photoinduced by one or two counterpropagating Airy beams. However the unstable transient regime of the off-shooting soliton in both configurations prevents us to test the waveguiding effect with a Gaussian probe beam. While a counterpropagating Airy beam already strongly affects the output position of the forward Airy beam (i.e. large shifts, split of the soliton's outputs), the guiding effects of the photoinduced structure need to be studied and confirmed with conventional linearly propagating probe beams.

### 6.2.3 *Experimental study of spatiotemporal dynamics of counterpropagating Airy beams*

While we have not been able to stabilize the solitonic structure of counterpropagating Airy beams in the photorefractive medium, we have explored the evolution of the system when increasing the nonlinearity of the system. By tuning the optical power, the external bias electric field and the beams' size, we have studied the evolution of the intensity at the output of the crystal. So far the results have not been conclusive. Indeed the output intensity seems to evolve along the output plane and in particular along the positions of the entering counterpropagating Airy beam.
But the exact observation has been prevented by mainly two obstacles. First the imaging system used to observe the output beam also displays the reflected input of the counterpropagating Airy beam, which is ten times more intense as the output beam. As a consequence the CCD-display saturates because of the input beam's reflection before reaching a sufficient intensity level to analyze the output beam.

Furthermore the SLM-modulated Airy beams are not exactly steady-state. The intensity distribution presents fluctuations along the lobe orders which prevents us from studying the relative evolution of the intensity distribution of the output beam along time. While time fluctuation of an SLM-modulated optical beam can be reduced via an appropriate calibration of the SLM, we also observed a variation of the fluctuation frequency for increasing nonlinearity. This completely decorrelated result encourages further study of the spatiotemporal dynamics of counterpropagating Airy beam.

### 6.2.4 *Experimental study of the Airy-soliton in a longer propagation medium*

First results presented in Chapter 2 have shown stronger self-focusing of the Airy beam when propagating in a longer medium (here $L = 2$ cm instead of $L = 1$ cm). In addition the experimental study of the temporal evolution of the output beam unveils the first stable off-shooting soliton from an initial Airy beam, i.e. when the off-shooting soliton exists over several seconds.

Figures 6.1(a)-(e) depict the output intensity of an Airy beam self-focusing through a 2 cm-long SBN-crystal after the external bias electric field is applied at $t = 0$ s. While in the 1 cm-case the off-shooting soliton only remains up to 1 s, we observe a steady-state soliton over 15 s [Fig. 6.1(f)]. As the bias electric field is very low ($U_{SBN} = 100$ V), the new observed steady-state regime suggests that the crystal length could enhance the nonlinear self-focusing of the Airy without crossing the saturation threshold of the photorefractive effect. A complete study of the influence of the system's parameters (beam's size and power, bias electric field) on the self-focusing effect would enhance the comprehension of the balance of the nonlinearity strength and the beam's diffraction to obtain a stable and strong soliton off-shooting from an Airy beam.

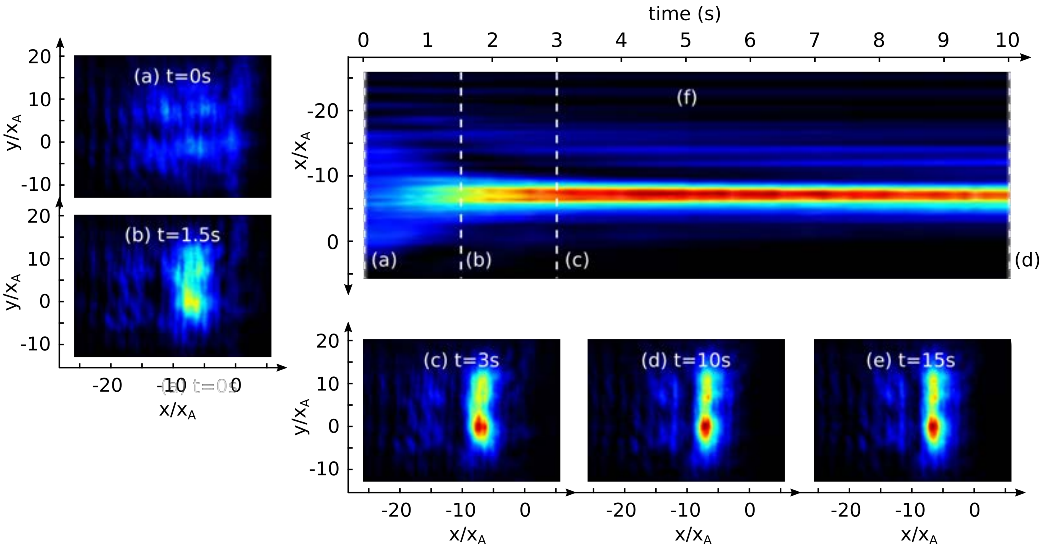

Figure 6.1: Propagation of an Airy beam through a 2 cm-long biased photorefractive crystal, with $x_A = 11$ µm, $P_A = 50$ µW and $U_{SBN} = 100$ V. (a)-(e) Intensity distribution of the output beam at different times. (f) Spatial evolution of the self-focusing Airy beam at the output along time.

Furthermore the longer crystal enables the study of the possibilities of interconnects in the configuration using two counterpropagating Airy beams. The longer propagation induces a larger transverse acceleration of both beams hence suggesting larger interaction schemes combined with stronger solitonic effect (see Fig. 6.1). Finally the theoretical study of counterpropagating Airy beams predicts a higher instability in long media (see Chapter 5). As the behavior of a single self-focusing Airy beam already shows significant differences from the 1 cm-case, the experimental setup could display instabilities while avoiding the saturation of the photorefractive effect.

### 6.2.5 *Influence of the coherence of the interacting beams*

The study of incoherent counterpropagating Airy beams has given us an extensive insight in the balance between the conventional beams' interactions and the Airy properties. As co-propagating Airy beams present various solitonic interactions when varying their transverse shift and their phase-shift, it would be interesting to consider the impact of coherently interacting Airy beams in our configuration.

Furthermore our study of spatiotemporal dynamics in the unstable regime has shown a spatial distribution of the output position of the beam along all the lobe orders of the counterpropagating Airy beam. In the case of coherent beams, the phase is not constant along the lobe orders and suggest an alternative spatial distribution in the high nonlinear range.

### 6.2.6 *Interactions of Airy beams with opposite bending directions*

Finally the asymmetry of the Airy beam offers a large variety of interconnections. While we have studied Airy beams accelerating along the same transverse direction, we question whether Airy beams with opposite acceleration directions such as on Figure 6.2(a) can interconnect and form waveguiding structures through cross-coupling.

The first results presented in the following have been done during two student projects I supervised:

- Thomas Bouchet, Final study projet, 2014-2015
- Quentin Groshens and Edouard Zerdoun, first year master, 2015

#### *Study of the linear Airy beams' interconnection range*

To establish an interconnection between both counterpropagating beams, the transverse shift D between them is tuned according to the Airy beams' deflection. As depicted on Figures 6.2(b)-6.2(d), the normalized shift depends on the

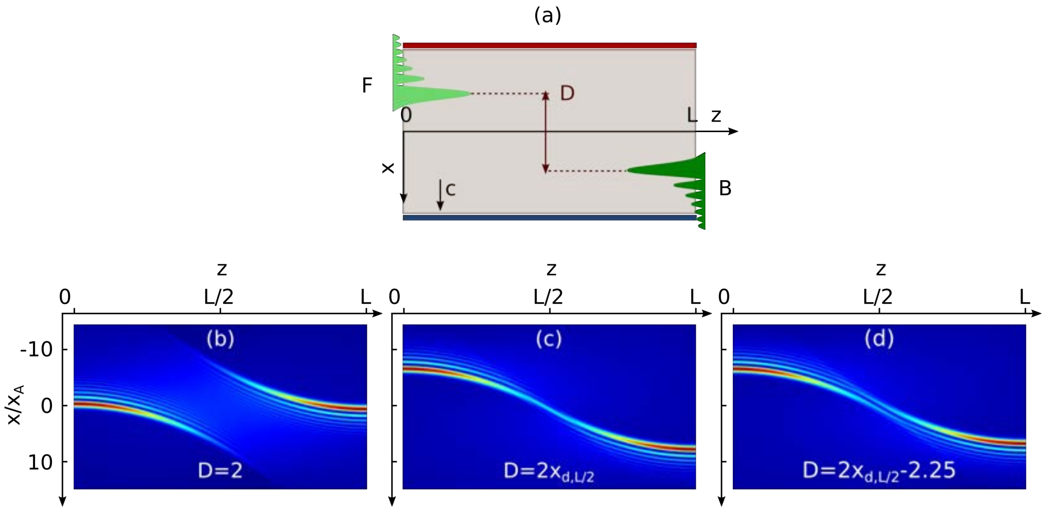

Figure 6.2: Interaction of counterpropagating Airy beams with opposite acceleration directions in a biased photorefractive medium. (a) Interaction scheme before propagation. (b)-(d) Intensity distribution under linear conditions when the two Airy beams (b) do not meet ($D = 2$), (c) interconnect with their main lobes ($D = 2x_d$) and (c) interconnect with their main and second lobes ($D = 2x_d - 2.25$) with $x_d$ being the normalized transverse deflection of each Airy beam.

deflection of the Airy beams hence its size $x_A$ and propagation distance (here $L/2$ as they meet in the middle of the crystal). Considering $L = \alpha L_d$, the deflection of an Airy beam at the middle of the crystal is equal to $x_d(z = \alpha L/2) = \alpha^2/4$. As a consequence the connection of both main lobes requires a shift of $D = \alpha^2/2$ as depicted on Figure 6.2(c). In the case of two interconnections, the transverse shift is reduced by the distance between the first and second lobe orders being $2.25x_A$ (here normalized at 2.25) [Fig. 6.2(d)].

### *Nonlinear interactions and waveguiding*

The configuration of opposite accelerating Airy beams induces smaller cross-coupling areas than in the configuration studied in our work previously. Here the interconnection appears between the linear component of both beams. As a consequence this study enlarges the results presented in reference [36], where the parabolic trajectory of a single main lobe is used to create curved waveguides.

On Figure 6.3 we depict a few propagations of a probe beam through the multi-lobe and curved guiding structure induced by two opposite Airy beams as

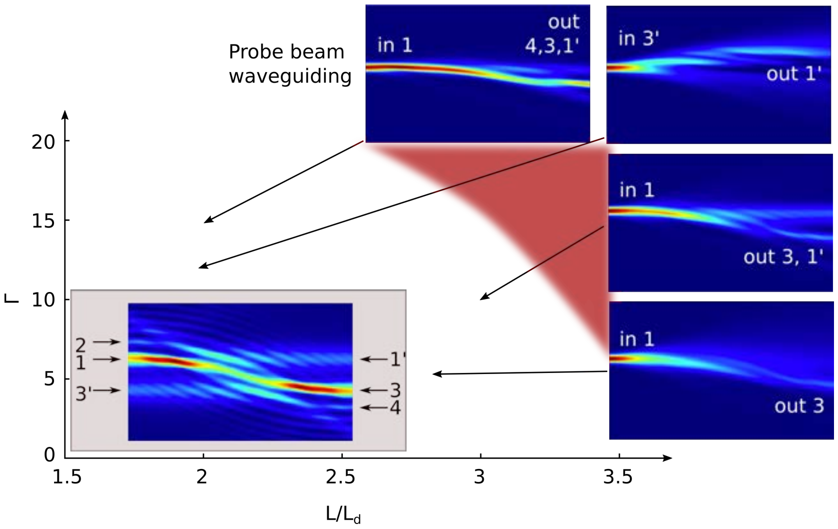

Figure 6.3: Nonlinear interactions of counterpropagating Airy beams with opposite bending directions and their waveguiding effect. Gray frame: intensity distribution of the interacting Airy beams in the biased photorefractive medium ($L = 3, \Gamma = 10$). The other intensity distributions depict the waveguiding of a probe beam through structures photoinduced by cross-coupling of both Airy beams for various $(\Gamma, L)$-parameters. In the red zone, no waveguides induced by both interconnecting beams have been observed.

illustrated in the gray frame. By varying the crystal length $L$ and the photorefractive nonlinearity $\Gamma$ (through the external bias electric field), the interconnecting the main lobes of the opposite beams photoinduce waveguiding structures (see gray frame, where the significant entries are indicated with numbers). Figure 6.3 does not represent all guiding types, but already shows how a probe beam can be guided with different output schemes depending on the $(\Gamma, L)$-values:

- single output ($\Gamma = 5, L/L_d = 2.75$): $1 \rightarrow 3$ or ($\Gamma = 12, L/L_d = 2$): $3' \rightarrow 1'$
- two outputs ($\Gamma = 10, L/L_d = 3$): $1 \rightarrow (3, 1')$
- three outputs ($\Gamma = 15, L/L_d = 2$): $1 \rightarrow (4, 3, 1')$

These first results suggest a smaller guiding range along the propagation direction but with possible larger transverse shifts. The experimental implementation as well as the study of spatiotemporal dynamics suggest interesting outcomes.

### 6.2.7 *Enlarge the study to 2D-Airy beams in nonlinear media*

More generally in this thesis we have focused our study on one-dimensional Airy beams and their interactions in the counterpropagating configuration. The introduction of a second dimension, i.e. using two-dimensional Airy beams, offers larger interconnections between the beams because of the two-dimensional structure and also the higher deflection of the Airy beam. In particular multiple Airy beams can merge into a single or multiple solitons in the co-propagating case [158]. It would be therefore interesting to study multiple two-dimensional Airy beams in the counterpropagating case.

In addition the self-focusing effect has been studied for an Airy distribution along the photorefractive c-axis of the crystal. Using a two-dimensional Airy beam, one could better analyze the balance between the Airy properties and the photorefractive nonlinear effects. In particular as depicted on Figure 6.4, the self-focusing of the 2D-Airy beam defined along the $x, y$-axes only occurs along the $x$-axis, which coincides with the c-axis of the photorefractive crystal. The setup is identical to the one studied in chapters 2 and 3 [Fig. 6.4(f)].Similar to the 1D-case, the Airy beam first undergoes transient self-focusing, where the intensity of the first row (i.e. most intense row on the right [Fig. 6.4(a)]) shifts along the $-x$-direction towards the higher lobes' orders [Figs. 6.4(b)-6.4(d)]. In a second step the output beam relaxes into a defocused 2D-accelerating structure [Figs. 6.4(e)-6.4(f)].
The second dimension of the Airy beam could offer a better understanding of the physics of the self-focusing as we could spatially decorrelate the accelerating Airy properties (here $y$-axis) from the solitonic behavior (along the photorefractive c-axis of the crystal, here $x$-axis).

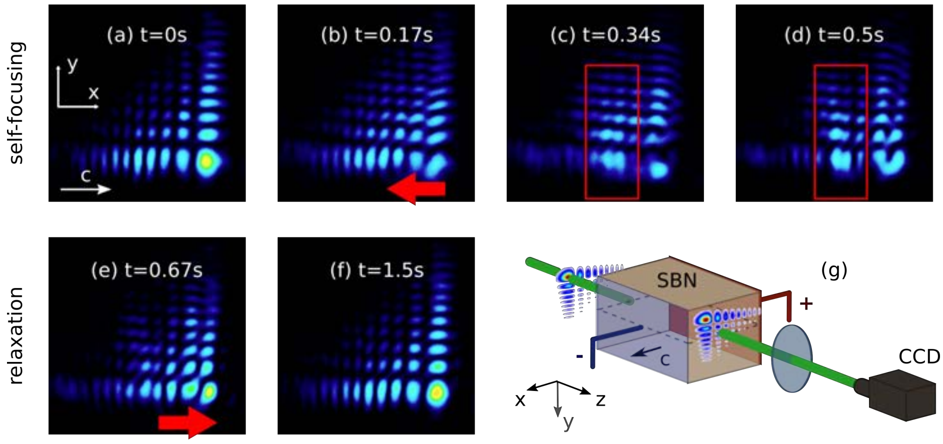
self-focusing
relaxation
(a) t=0s
(b) t=0.17s
(c) t=0.34s
(d) t=0.5s
(e) t=0.67s
(f) t=1.5s
(g)
y
x
c
SBN
+
-
c
CCD
x
z
y

Figure 6.4: Self-focusing of an 2D-Airy beam in a biased photorefractive crystal, with $x_A = 11\ \mu\text{m}$, $P_A = 50\ \mu\text{W}$, $L = 1$ cm and $U_{SBN} = 4$ kV. (a)-(f) Intensity profile of the output beam for different times. (g) Schematic propagation setup of an 2D-Airy beam in the SBN-crystal.

# Part IV

# APPENDIX

# A

# AIRY GENERATION USING A SPATIAL LIGHT MODULATOR (SLM)

Since the discovery of the existence of optical truncated Airy beams, many generation methods have been explored. The general principle is to modulate a Gaussian beam with a cubic phase and to Fourier transform the modulated beam to obtain an Airy beam. As mentioned in section 1.1.4, the techniques most commonly studied are:

- a modulation of a free-space propagating Gaussian beam with a spatial light modulator,
- a nonlinear propagation of a Gaussian beam through a asymmetric photonic crystal.

For our experimental work, we chose the SLM-based method for the precision and speed of the modulation.
The spatial light modulator PLUTO of Holoeye is a phase only spatial light modulator, where the Gaussian beam is modulated through reflection, defined by following parameters:

| PLUTO Spatial Light Modulator – Microdisplay Features | |
|---|---|
| Display type | Reflective Liquid Crystal on Silicon (LCOS) (Phase only) |
| Resolution | $1920 * 1080$ |
| Pixel Pitch | 8.0 μm |
| Fill factor | 87 % |
| Active area | $15.36 * 8.64$ mm |
| Addressing | 8 bits (256 gray levels) |
| Frame rate | 60 kHz |

Figure A.1 presents the tool and the setup used in our experiment. Thanks to a beam splitter placed in front of the SLM, the incident Gaussian beam and its modulated reflection are perpendicular to the SLM-plane to optimize the phase modulation. The best resolution is guaranteed by the maximization of the incident Gaussian beam size without reaching the edges of the active area. After an expansion of the initial laser beam, the radius of the incident Gaussian waist is equal to $\omega_{\mathrm{SLM}} = 3.2$ mm. Because the phase modulation is optimized for an optical polarization along the larger side (horizontal in our experiment), a polarizer is also placed after the beam expansion (not illustrated on figure A.1).

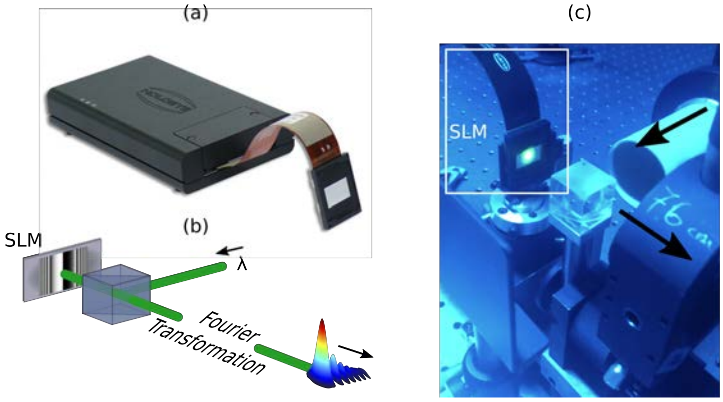

Figure A.1: SLM-based Airy beam generation. (a) Spatial Light Modulator PLUTO Holoeye. (b) Schematic view of the experimental setup. (c) Illustration of the SLM-setup in our experiment.

In reference [17], Christodoulides *et al.* introduces the modulation phase for a one- or two-dimensional Airy beam. The modulation device is addressed with phase functions via standard graphics cards as extended monitor device. Then we use a Matlab-generated grey-level image to induce a spatial phase modulation with following script:

```
%% Generation of the SLM mask

% number of points on the x- and y-direction mask
pix_SLM = 1080;

% phase modulation of Christodoulides [-20pi:+20pi]
% to be modified for other Airy sizes
phase_max=4*pi;

% Creation of the 1D axis
x=linspace(-phase_max/2,phase_max/2,pix_SLM);

% Creation of the mask matrix
phi_1D= repmat((x.^3)/3,pix_SLM,1);
```

```
phi_2D=phi_1D+phi_1D';
phi_1D = mod(phi_1D, 2*pi);
phi_2D = mod(phi_2D, 2*pi);

% Save image in the folder
g1=figure;
imagesc(phi_1D), colormap(gray);
axis off
fnum='airy_1D_mask.png';
print(g1,'-dpng',fnum);

g2=figure;
imagesc(phi_2D), colormap(gray);
axis off
fnum='airy_2D_mask.png';
print(g2,'-dpng',fnum);
```

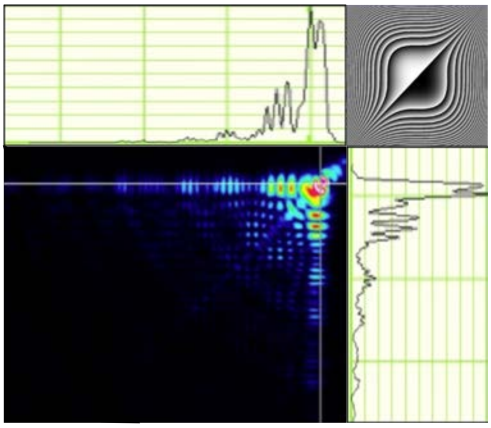

Figure A.2: Experimental optical beam after a 2D cubic phase modulation through the SLM. Airy-like intensity distribution after the Fourier transformation. Right corner: phase modulation applied on the SLM.

The SLM-modulation masks obtained correspond to those presented in reference [17] by Christodoulides. However, a post-modulation has to be added. As illustrated on figure A.2, the outcome beam does not have the predicted Airy profile, but seems to have an additional modulation along both transverse axes. In reality the SLM reflects not only the Airy beam, but many diffraction orders. Therefore the output beam observed in figure A.2 contains multiple superimposed diffraction orders of the modulated beam. To only keep one Airy beam, we need to select the first diffraction order of the output beam.

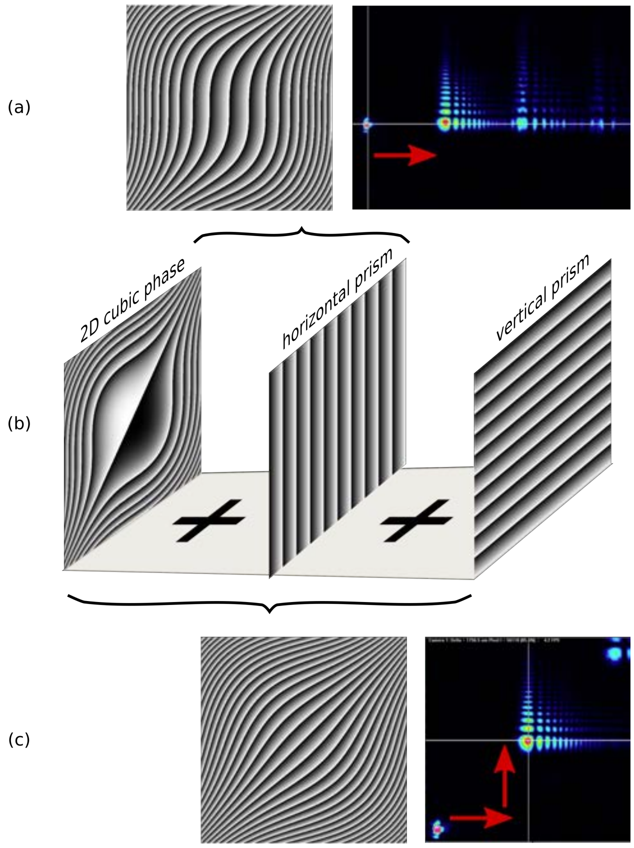

Figure A.3: Airy beam generation and isolation through a cubic phase and a phase grating using an SLM.

A classical method is the use of a prism, but its separation effect can also be induced by the SLM as illustrated on figure A.3. Indeed by adding a phase grating in the beam modulation, which is summed to the initial cubic phase mask [Fig. A.3(b)], the superimposed diffraction orders can be separated as depicted on figures A.3(a) and A.3(c). Afterwards we select the first order diffraction beam, presenting an Airy distribution, using a slit (for the 1D-case) or a hole (for the 2D-case).

As introduced in Chapter 2, the analysis of the solitonic behavior of an Airy beam requires a lobe's waist around $10\ \mu m$. Intuitively the Airy beam's parameters, the truncation $a$ and the lobe's waist $x_A$, depend on the focusing power of the Fourier transform lens and the SLM-modulation. A theoretical approach is also suggested by Mazilu *et al.* in reference [19], where the initial and output parameters are linked through following equations:

$$x_A = \frac{c_m f_{\mathcal{TF}}}{k}, \tag{A.1}$$

$$a = \frac{1 + (M^2)^2}{2{c_m}^2 \omega_{SLM}} \tag{A.2}$$

where $k = 2\pi/\lambda$ is the wave vector of the optical beam, $f_{\mathcal{TF}}$ the focal length of the Fourier transform lens, $M$ the beam quality factor (ideally assumed equal to 1) and $c_m$ the modulation parameter of the SLM. This last parameter is equal to $c_m = \sqrt[3]{6\Phi_{SLM}}/l$, where $l$ is the hologram side length and $\Phi$ the maximal phase shift across the hologram ("phase max" in our Matlab script).

To better understand the intrinsic link between the different parameters, we first consider the SLM-modulation $c_m$ fixed. The Gaussian beam size is also maximized to enhance the spatial modulation resolution, therefore $\omega_{SLM}$ also remains unchanged.

As shown in equation A.1, the focal length $f_{\mathcal{TF}}$ needs to be minimized to reach the solitonic dimensions for the Airy beam: $x_A \approx 10\ \mu m$. Due to space restrictions induced by the opto-mechanical devices, we select $f_{\mathcal{TF}} = 7.5$ cm. In a second step we tune the SLM-modulation by reducing the maximal phase shift along the LCOS-display. However this leads to an increase of the truncation factor $a$, as described in equation A.2. As the truncation of the Airy beam has to be limited to approach the ideal Airy profile, we have to make a compromise between the size and the quality of the generated Airy beam. Experimentally our system generates Airy profiles in the range of $x_A \in [9.5; 14]\ \mu m$.

# B

# COUNTERPROPAGATING AIRY BEAMS IN A NONLINEAR MEDIUM: EXPERIMENTAL SETUP

In this section we detail the experimental setup to study two incoherent counterpropagating Airy beams under solitonic conditions as depicted on the schematic illustration of figure 4.15 in Chapter 4. Appendix A has shown that the generation of Airy beams with $x_A \approx 10\ \mu\text{m}$ requires a small focal length of the Fourier Transform lenses, here $f_{\mathcal{TF}} = 7.5$ cm. As a consequence the distance between each Fourier lens and the respective crystal input is equal to 7.5 cm. In addition we place a slit after the Fourier lens and the closest to the crystal for an optimized filtering of the first order diffraction of the SLM-modulated beam (being the Airy beam here).

In the counterpropagating Airy beam case however the Airy beam generation setup is placed on both sides of the crystal: at $z = 0$ and $z = L$. As a consequence the two filtering slits should be placed at both ends of the crystal hence preventing any imaging setup of the output beams at $z = 0$ and $z = L$.
To overcome this problem we have added a confocal ($4f$)-lensing system between the slit and the crystal on both sides. The Airy beam is therefore deferred from the slit's position to the input face of the crystal placed $4 * f_{4f}$ further along $z$. As depicted on the experimental scheme of figure B.1, this $4f$-based configuration enables us to place beam splitters at each crystal's end for the imaging system. Thanks to a careful choice of imaging lenses ($f_{CCD1} = 14.9$ cm and $f_{CCD2} = 15.7$ cm), both crystal ends are observed on the same CCD-camera with a 20-times magnification.

On figure B.2(a) we see photographs of the complete experimental setup. The Nd:Yag-laser "Genesis MX SLM" in the front is the light source for generating the counterpropagating beam ($\lambda_2$ on figure B.1). The photorefractive crystal is placed further away on the photograph and figure B.2(b) presents a zoomed picture of the crystal. As illustrated on figure B.1 both Airy beams are injected in counterpropagating directions and their linear deflection is towards the positive voltage side. To better link the experimental setup to the scheme of figure B.1, the Airy beam generated with the laser $\lambda_1$ and propagating along the $+z$-direction

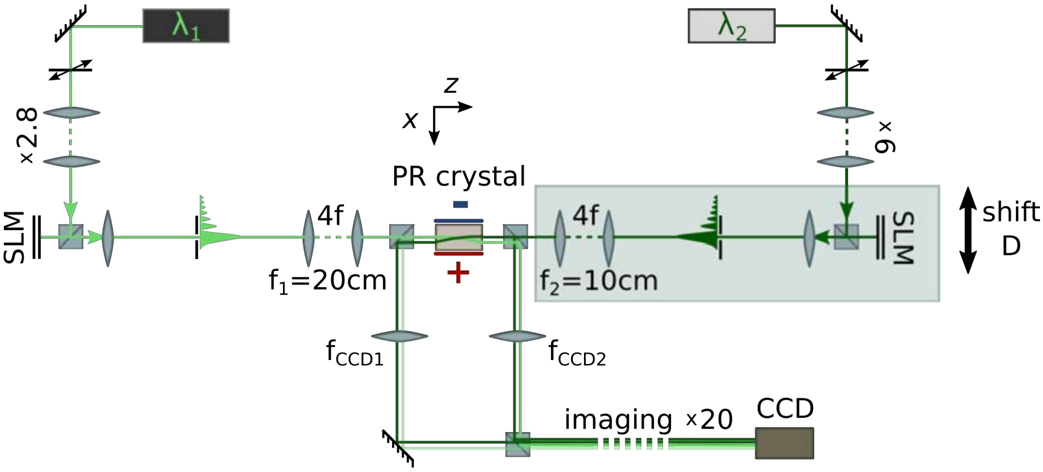

Figure B.1: Scheme of the experimental setup to study counterpropagating Airy beams in a biased photorefractive medium.

(resp. $-z$-direction for the Airy beam generated using the $\lambda_2$-laser) is marked in bright (resp. dark) green.

As illustrated on figure B.2(c), the small focal length of the Fourier transform lens induces a small spacing for the SLM-modulation (SLM-screen, beam splitter and Fourier transform lens). After the lens, we see the slit placed at the focal distance of the lens.

Finally we focus on the setup of the counterpropagating Airy beam. As depicted on figure B.3, the complete SLM-modulation and the 4f-system are placed on a single rail to optimize the tuning of the beam along $z$. As the Airy beam's deflection depends on the $z$-distance from its generation position, the crystal has to be exactly at the distance $f_{TF} + 4f_{4f}$ from the Fourier lens. The $z$-position of the crystal being already fixed during the setup of the first Airy beam, the rail enables the adjustment of the $z$-position of the counterpropagating Airy beam.

In addition the rail-based setup offers an easy-to-use solution to tune the transverse shift D between the counterpropagating Airy beams.

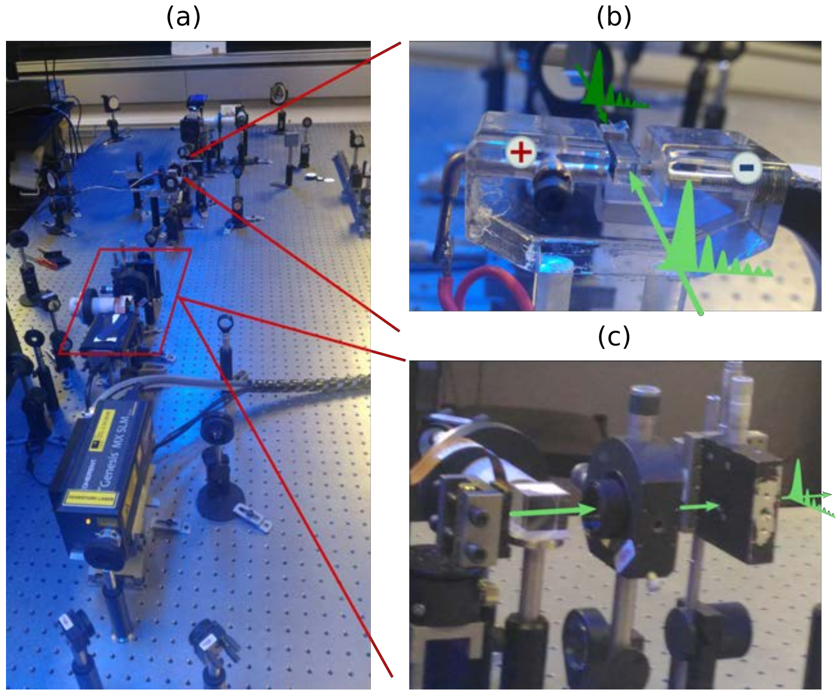

Figure B.2: Pictures of the experimental setup. (a) Overview of the complete experiment (the laser $\lambda_1$ does not appear on the picture). (b) Zoom on the photorefractive SBN-crystal. (c) SLM-based modulation of the first Airy beam using the $\lambda_1$-laser.

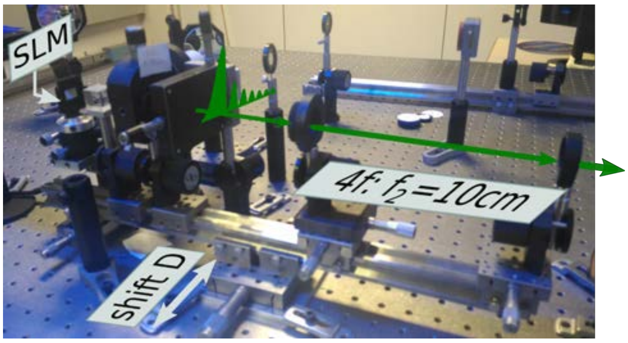

Figure B.3: Zoom on the setup of the counterpropagating Airy beam on a single rail. The Airy beam is generated after the slit (see dark green Airy shape), then deferred $4 * f_2 = 40$cm further at the $(z = L)$-face of the photorefractive crystal.

C

# NUMERICAL SIMULATION MODEL

The theoretical study in this thesis of the propagation of one-dimensional Airy beams in a photorefractive medium is based on a (2D+1)-dimensional simulation model called the Fast Fourier Transform (FFT) Beam Propagation Method (BPM). In this appendix we consider for illustration the configuration of two counterpropagating beams as in chapters 4 and 5 as depicted on figure C.1(a). For the numerical simulations of the single Airy case (chapters 2 and 3), the same algorithm is used but with the backward beam switched off.

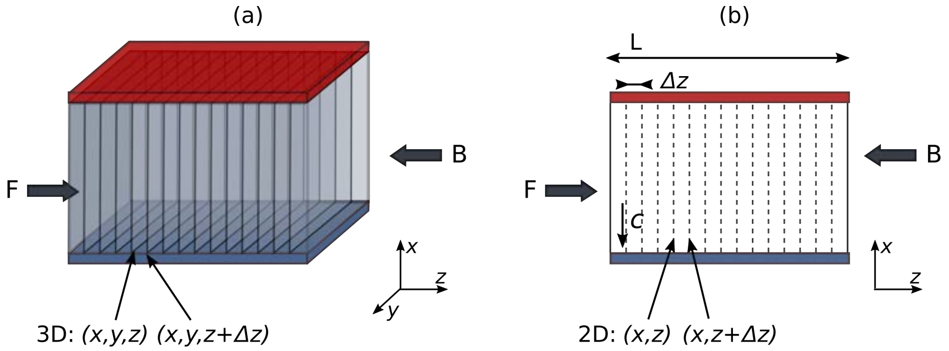

Figure C.1: Interaction scheme of counterpropagating beams in a biased photorefractive medium (a) in 3D and (b) in 2D (used for the numerical calculation in this thesis).

The beam propagation method is generally used to simulate the propagation of optical beams in optical slowly varying medium such as a photorefractive crystal. This numerical technique is based on a two-step principle:

- the spatial propagation of the beam through the medium along $z$ (see figure C.1(b))
- calculating the nonlinear response of the crystal (i.e. the internal space charge field)

As depicted on figure C.2 we calculate the two phases in a loop along time to complete the nonlinear process induced by the beam-matter interactions. As presented in the following paragraphs, both steps can be calculated separately during each time loop using the FFT BPM method and the equations 4.3-4.6 governing our photorefractive system (see Chapter 4).

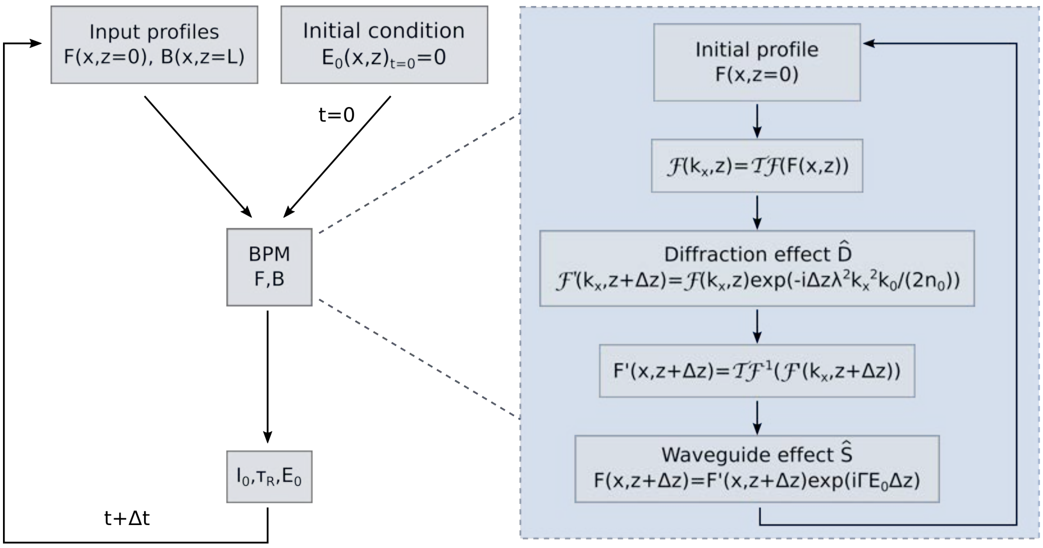
Input profiles
F(x,z=0), B(x,z=L)
Initial condition
$E_0(x,z)_{t=0}=0$
t=0
BPM
F,B
$I_0, \tau_R, E_0$
t+Δt
Initial profile
F(x,z=0)
$\mathcal{F}(k_x,z)=\mathcal{TF}(F(x,z))$
Diffraction effect $\hat{D}$
$\mathcal{F}'(k_x,z+\Delta z)=\mathcal{F}(k_x,z)\exp(-i\Delta z\lambda^2 k_x^2 k_0/(2n_0))$
$F'(x,z+\Delta z)=\mathcal{TF}^{-1}(\mathcal{F}'(k_x,z+\Delta z))$
Waveguide effect $\hat{S}$
$F(x,z+\Delta z)=F'(x,z+\Delta z)\exp(i\Gamma E_0\Delta z)$

Figure C.2: Evolution diagram of the algorithm to simulate the beam propagation in a photorefractive medium. Left: temporal evolution of the space charge field. Right: Fast Fourier Transform Beam Propagation Method at each time step $\Delta t$.

## C.1 CALCULATION OF THE BEAM PROPAGATION

The general mathematical form of an optical beam F propagating in a nonlinear medium is expressed as following:

$$\frac{\partial F}{\partial z} = (\hat{D} + \hat{S})F, \tag{C.1}$$

where $\hat{D}$ is the linear diffraction operator and $\hat{S}$ the nonlinearity operator taking into account the photoinduced refractive index change. As we consider two one-dimensional incoherent beams, there is no interference pattern and we can write their propagation equations as following:

$$i\frac{\partial F}{\partial z}+\frac{\partial^2 F}{\partial x^2}=\Gamma E_0 F, \tag{C.2}$$

$$-i\frac{\partial B}{\partial z}+\frac{\partial^2 B}{\partial x^2}=\Gamma E_0 B, \tag{C.3}$$

By identification, the canonical form of the operators are:

$$\hat{D}_F = i\frac{\partial}{\partial z}, \tag{C.4}$$

$$\hat{S}_F = -\Gamma E_0, \tag{C.5}$$

$$\hat{D}_B = -i\frac{\partial}{\partial z}, \tag{C.6}$$

$$\hat{S}_B = \Gamma E_0. \tag{C.7}$$

Finally the beam propagation calculation along the $z$-direction of equation C.1 can be described as a step-wise propagation from $z$ to $z+\Delta z$ [Fig. C.1(b)] as a combination of the diffraction and nonlinear effects:

$$F(x, z+\Delta z) = \exp\left(\left(\hat{D}+\hat{S}\right)\Delta z\right) F\left(x, z\right), \tag{C.8}$$

$$\approx \exp\left(\hat{D}\Delta z\right)\exp\left(\hat{S}\Delta z\right) F\left(x, z\right), \tag{C.9}$$

where equation C.9 includes the first order simplification of $\exp\left((\hat{D}+\hat{S})\Delta z\right)$. The numerical implementation of the beam propagation is calculated in the Fourier plane for the diffraction effect. Then we add in the spatial domain the guiding effect induced by the refractive index structure. Finally after the propagation from $z = 0$ to $z = L$ (or backward for B) is completed, the optical field distribution $I_0$ is updated using equation 4.6 [Fig. C.2]. Hence the photorefractive space charge field of the medium will be modified as detailed in the next paragraphs.

## C.2 CALCULATION OF THE NONLINEAR PHOTOREFRACTIVE RESPONSE OF THE MEDIUM

As presented in Chapter 4, the evolution of the space charge field inside the photorefractive medium evolves with the optical field distribution $I_0$ and following a relaxation-type dynamics. To approximate the solution $E_0(t)$ of the temporal differential equation 4.5 we consider the numerical Runge-Kutta method RK4. Considering known the value of $E_0$ and the updated intensity distribution $I_0$ at the time t, the new value of the space charge field at the time $t + \Delta t$ is equal to:

$$E_0(t+\Delta t) = E_0(t) + \frac{1}{6}(K_1 + 2K_2 + 2K_3 + K_4), \tag{C.10}$$

(C.11)

where $K_1$, $K_2$, $K_3$ and $K_4$ are the increments gradually based on $E_0$ and the previous increments:

$$K_1 = -\frac{1}{\tau_k}\left(E_0(t) + \frac{I_0(t)}{1+I_0(t)}\right), \tag{C.12}$$

$$K_2 = -\frac{1}{\tau_k}\left(E_0(t) + \frac{\Delta t}{2}K_1 + \frac{I_0(t)}{1+I_0(t)}\right), \tag{C.13}$$

$$K_3 = -\frac{1}{\tau_k}\left(E_0(t) + \frac{\Delta t}{2}K_2 + \frac{I_0(t)}{1+I_0(t)}\right), \tag{C.14}$$

$$K_4 = -\frac{1}{\tau_k}\left(E_0(t) + \Delta t K_3 + \frac{I_0(t)}{1+I_0(t)}\right), \tag{C.15}$$

$$\tau_k = \frac{\tau}{1+I_0}. \tag{C.16}$$

## C.3 INITIAL CONDITIONS OF THE PHYSICAL SYSTEM AND TUNING PARAMETERS

Finally to simulate the spatiotemporal nonlinear beam-matter interactions we compute the presented time-loop algorithm in Matlab. All the physical parameters are normalized and without dimensions in our numerical simulations. In particular we can cite the transverse axis $x/x_A$ ($x_A$ being the waist of a Gaussian beam or of the main lobe of the Airy beam) or the propagation distance $z/L_d$ ($L_d$ the diffraction length).

The steps in the spatial domain ($\Delta x$, $\Delta z$) and in time $\Delta t$ have been chosen to optimize the spatiotemporal resolution and the calculation time. It is worth noticing that the large transverse intensity distribution and its multi-lobe structure impose a very large spatial resolution comparing to the Gaussian beam. As a consequence the calculation time is much larger for Airy beams as a large transverse dimension with high resolution has to be considered. In particular we chose $\Delta x/x_A \in [0.1, 0.2]$, $\Delta z/x_A < 1$ and $\Delta t = \tau/20$.

# AUTOFOCALISATION PHOTORÉFRACTIVE DE FAISCEAUX D'AIRY

Depuis toujours, la lumière est un moyen courant pour transmettre de l'information. Les premières communications optiques connues à ce jour ont eu lieu dans l'espace libre, où une source lumineuse émet des rayons optiques se propageant tout autour de la source. Un fameux exemple sont les systèmes de guidage pour les transports maritimes, aériens et terrestres, dans lesquels une lumière indique la présence d'obstacles et des directions à suivre. Un faisceau lumineux peut également contenir un message, tel en codage Morse, où la succession de flash de lumière dans le temps peut tout d'abord être traduit en lettres, puis en mots. Communiquer dans l'espace libre exige cependant des sources larges et intenses. Par ailleurs le message peut être intercepter par tout récepteur autour de la source.

Dans les années 60 des chercheurs présentent pour la première fois des systèmes de communication optique avec un matériau de guidage: il s'agit de la fibre optique. Grâce à cette nouvelle technologie, il est possible de transporter des signaux optiques de communication sur d'importantes distances à faible puissance et de l'adresser à un récepteur précis. Depuis, le développement de la fibre ainsi que d'appareils pour la communication optique a connu un réel essor et ce notamment au travers de quatre inventions clés:

- L'invention du LASER (fin des années 50) pour la générations de faisceaux confinés sur une longue distance.
- Le développement de la fibre optique à faibles pertes (années 70) pour transporter le signal avec un ratio de transmission optimal.
- L'invention de l'amplificateur à fibre optique (années 80) pour augmenter la portée de transmission dans des réseaux de fibre optique.
- L'invention du réseau de fibre de Bragg (années 90) pour des récepteurs de signaux précis et robustes.

Par ailleurs, la progression exponentielle des réseaux de fibre optique a également encouragé la recherche pour des solutions de guidage optique à petite échelle. En particulier la découverte de matériaux non linéaires photosensibles a conduit à l'étude de structure guidantes photo-induites. Depuis bientôt 50 ans, l'étude et le contrôle de la diversité et de l'efficacité de tels guides photo-induits dans des milieux non linéaires est devenu un domaine de recherche important pour les communications tout-optiques.

Récemment la découverte de faisceaux dits non-conventionnels a entraîné un nouvel essor dans la physique optique. L'innovation réside dans leur propagation invariante et dans leur capacité à se régénérer. Grâce à leur capacité à se propager plus loin et à rester inchangés à l'encontre d'obstacles, ces faisceaux permettent d'approfondir la portée des applications optiques au-delà des limitations spatiales des faisceaux conventionnels. Un type de faisceau en particulier a suscité beaucoup d'intérêt: le *faisceau d'Airy*.
Découvert il y a dix an, le faisceau d'Airy présente, outre son caractère invariant et auto-régénérant, la propriété unique de se propager selon une trajectoire parabolique. La propagation curviligne du faisceau d'Airy a introduit une nouvelle famille d'onde optique, celle des *faisceaux accélérant*. L'existence de lumière courbe semble contredire les principes fondamentaux de la physique générale, ces faisceaux accélérant sont cependant formés par un grand nombre de rayons lumineux se propageant selon différentes trajectoires rectilignes. Ainsi la trajectoire accélérante Airy doit sa forme courbe à la sommation de toutes ces trajectoires non parallèles, ceci définit la *caustique* du faisceau accélérant.
L'introduction de faisceaux non conventionnels définis par leur caustique a ouvert de nouveaux domaines de recherche et a mené à de nombreuses nouvelles applications dans la physique optique et, plus généralement, dans la physique ondulatoire (ex. plasmonique, électronique).

Comme évoqué précédemment, l'étude de faisceaux dans des milieux non linéaires est un domaine important de la physique optique. Lors de sa propagation au sein du matériau, le faisceau optique interagit avec la matière tout au long de sa trajectoire, ce qui, par la suite, influence son propre comportement telles la forme et la trajectoire. Ces dernières décennies, les matériaux non linéaire photoréfractifs ont été l'objet de vastes études, de par leur grande sensibilité optique ainsi que grâce aux nombreuses applications qu'ils offrent, en particulier dans le domaine du traitement tout-optique de l'information.
A ce jour, l'état de l'art dans la physique du routage optique suggère notamment l'emploi de faisceaux intenses invariants, dits*solitons*, pour induire optiquement des structures guidantes. De tels solitons optiques sont présents dans des milieux

non linéaires, dans lesquels la nonlinéarité du matériau compense exactement l'élargissement naturel (la *diffraction*) d'un faisceau optique afin d'induire un effet d'auto-focalisation. Dans le but d'explorer les possibilités de routage dans un tel système solitonique, les chercheurs se sont penchés sur leur propagation en variant la nonlinéarité du système ainsi qu'en faisant interagir plusieurs solitons. Cependant la nature des faisceaux conventionnels limite spatialement la distance d'inter-connections, même pour l'interaction de multiples faisceaux.

Dans ce manuscrit de thèse, j'étudie la propagation non linéaire de faisceaux d'Airy dans des conditions fortement focalisantes ainsi que les possibilités de guidage d'onde qui en résultent. A ce jour, la génération et le contrôle de faisceaux d'Airy ont été étudiés dans des milieux linéaires, dans lesquels les propriétés d'invariance, d'auto-régénération et d'accélération confirment des applications prometteuses dans des systèmes à longue portée. Dans des conditions non linéaires focalisantes cependant, le faisceau d'Airy ne conserve pas ces propriétés. Selon des études théoriques, lorsque l'on augmente la nonlinéarité focalisante, il se divise en un soliton intense émis et un faible faisceau accélérant.

## C.4 AUTO-FOCALISATION D'UN FAISCEAU D'AIRY

En théorie, un faisceau d'Airy suit un comportement solitonique dans des conditions auto-focalisantes [93, 96, 104]. A ce jour, la recherche expérimentale a démontré une faible auto-focalisation accompagnée de la préservation de la forme (i.e. resserrement des lobes Airy) lorsque l'on applique un champ électrique extérieur faible. Cet effet s'observe dans le régime stationnaire pour une faible nonlinéarité focalisante ou pour un faisceau d'Airy de plus grande taille. Mais que se passe-t-il au-delà de cette limite ? Alors que Figure D.1 présente un faisceau d'Airy dans le cas d'un voltage élevé ($E_e = 4$ kV/cm), il est important de souligner que la mesure a été prise bien après l'allumage du champ électrique ($t = 10$ s). Comme nous le montrerons dans la section suivante, sous l'effet d'une forte nonlinéarité focalisante ($E_e > 2\ kV/cm$), le faisceau d'Airy se transforme dans un premier temps en une structure solitonique avant de se relâcher vers une structure stationnaire similaire à celle d'Airy avec des lobes resserrés, voire défocalisés pour une force auto-focalisante supérieure. Dans cette section nous nous intéressons à l'état transitoire solitonique maximal du faisceau d'Airy au cours de son auto-focalisation.

Les résultats ci-dessous sont la première démonstration expérimentale du soliton Airy et nous nous pencherons également sur la forme et le comportement du Airy-soliton en fonction des paramètres du système. Comme la forme solitonique suit théoriquement une propagation rectiligne, contrairement au faisceau Airy qui possède une accélération transverse, un pic d'intensité à la même position transverse que le faisceau d'Airy initial sera étudié comme solution solitonique Airy.

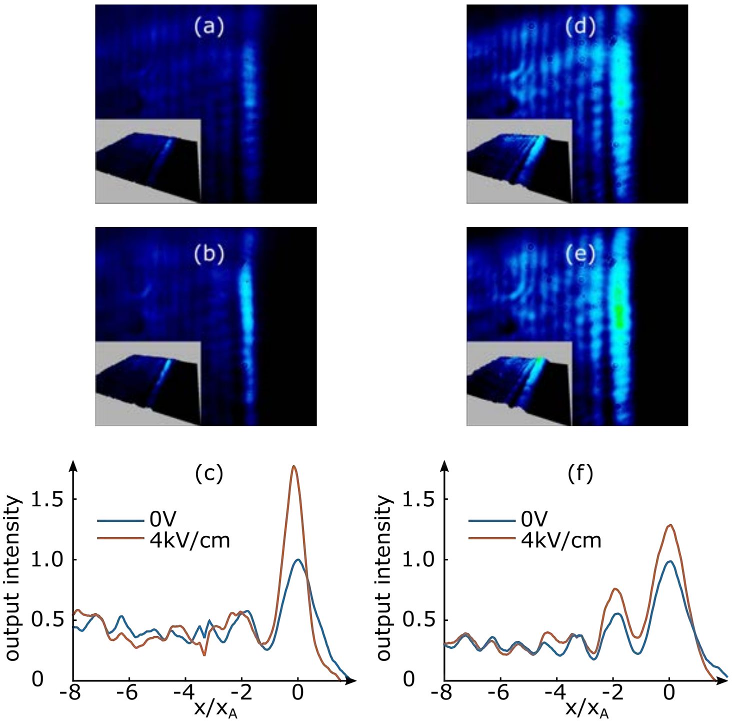

Figure C.3: Observation expériementale d'un faisceau d'Airy stationnaire après autofocalisation à deux puissances optiques différentes [Fig. 2.8] après 10 s: (a)-(c) $P_A = 1$ µW, (d)-(f) $P_A = 43$ µW. Distribution d'intensité de sortie du faisceau d'Airy à $z = L$ ($x_A = 14$ µm) (a),(d) après propagation linéaire, (b),(e) après propagation non linéaire focalisante ($E_e = 4$ kV/cm). (c),(f) Profils d'intensité des faisceaux de sortie linéaire et focalisé.

### C.4.1 *Montage expérimental*

Pour étudier l'existence d'une structure solitonique durant l'auto-focalisation, nous propageons un faisceau d'Airy unidimensionnel dans un cristal SBN photoréfractif. Comme l'indique la Figure D.2, le faisceau d'Airy est généré grâce à une modulation d'un faisceau gaussien dans l'espace de Fourier. La propagation du faisceau d'Airy ainsi que son accélération transverse démarrent à l'entrée du cristal $z = 0$.

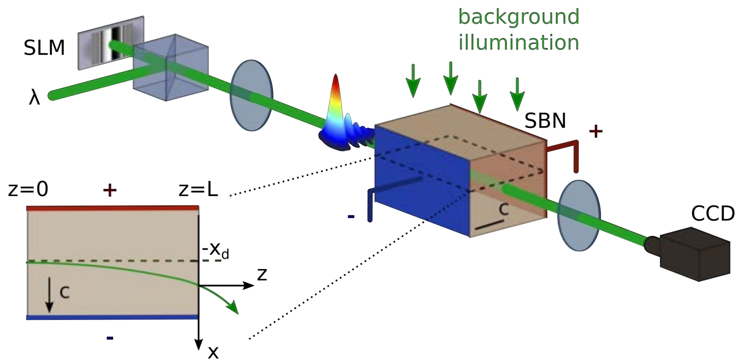

Figure C.4: Observation expérimentale de l'auto-focalisation d'un faisceau d'Airy 1D dans un cristal photoréfractif non linéaire: zoom sur la propagation du faisceau d'Airy à l'intérieur du cristal.

Un champ électrique extérieur est appliqué le long de l'axe $c$ du cristal pour exciter la nonlinéarité photoréfractive focalisante ($E_e \in [0,4]$ kV/cm) et la distribution Airy du faisceau est selon ce même axe. Le faisceau d'Airy se propage donc le long de l'axe $z$, partant de $z = 0$ à $z = L$ ($L$ étant la longueur du cristal) et son champ optique $\psi(x)$ est défini selon les conditions initiales suivantes:

$$\psi(x)_{z=0,t=0} = Ai\left(\frac{x + x_d}{x_A}\right) exp\left(a\frac{x + x_d}{x_A}\right), \tag{C.17}$$

avec $x_A$ le rayon du lobe principal, $a$ le paramètre de troncature et $x_d$ la déflection linéaire transverse du faisceau d'Airy. Comme pour le régime solitonique pour les faisceaux Gaussien conventionnels nous prenons comme longueur caractéristique autour de $x_A = 10\ \mu m$ avec $a \approx 0.05$ et$x = 0$ correspond en $z = L$ à la position linéaire de sortie du faisceau d'Airy.

### C.4.2 *Propriétés solitoniques d'un faisceau d'Airy auto-focalisant*

La Figure D.3 illustre le soliton émis du faisceau d'Airy initial. Sur les Figures D.3(b), D.3(c) on voit apparaître un pic intense entre le premier et le second lobe du profil Airy linéaire de sortie, ce qui diffère de la structure multi-lobe auto-focalisée de Figure D.1.

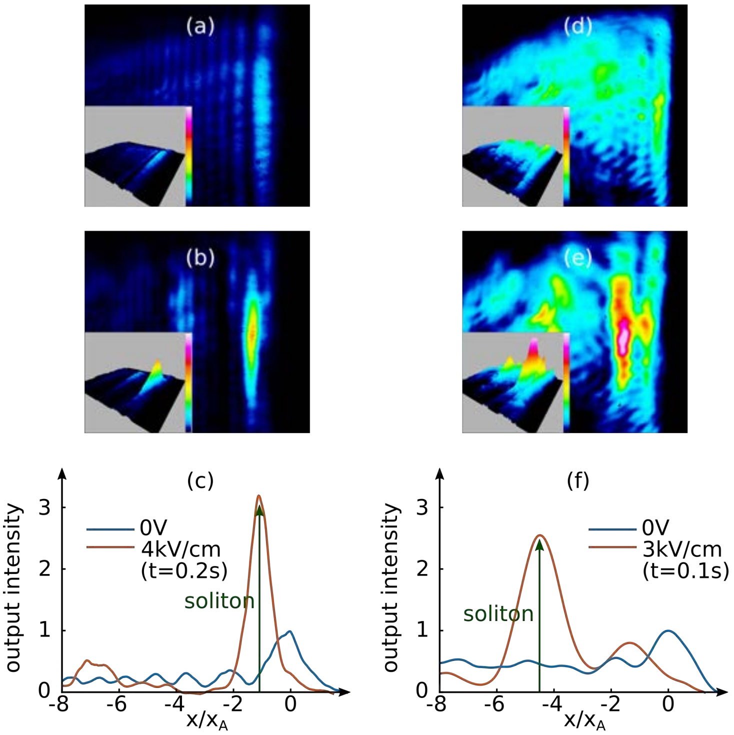

Figure C.5: Soliton expérimental émis d'un faisceau d'Airy auto-focalisant pour un rayon de lobe décroissant [Fig. D.2]: (a)-(c) $x_A = 14$ µm, $P_A = 7$ µW (d)-(f) $x_A = 9.5$ µm, $P_A = 43$ µW. Distribution d'intensité du faisceau d'Airy à $z = L$ (a),(d) après propagation linéaire, (b),(e) durant la propagation fortement non linéaire et (c),(f) profils d'intensité transverse des faisceaux de sortie linéaire et solitonique.

Comme l'accélération du faisceau d'Airy dépend du paramètre $x_A$ (selon $x_A^{(} - 3)$)), les deux faisceaux d'Airy ont des distances de déflections différentes [Figs. D.3(a), D.3(d)] et leurs solitons émis sont prévus respectivement à $x_{sol,14\mu m} = -12.4\ \mu m = -0.8x_A$ et $x_{sol,9.5\ \mu m} = -39.7\ \mu m = -4.2x_A$. Si l'on compare les

positions des pics prédits théoriquement et ceux obtenus expérimentalement, ils coïncident exactement. Ces résultats sont donc la première démonstration expérimentale du soliton Airy.
Tout comme les études théoriques [93, 104, 107], nos résultats expérimentaux présentent également une faible structure accélérante. Cette structure apparaît proche de la sortie linéaire $x = 0$ et est notamment visible dans le cas d'un petit $x_A$, car la déflection plus importante permet de distinguer la sortie linéaire et la position du soliton (flèche verte).

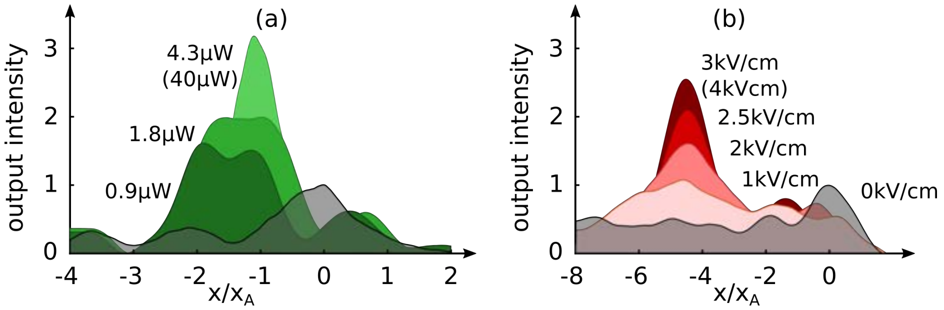

Figure C.6: Influence de la non linéarité électro-optique sur le soliton Airy à la sortie du cristal [Fig. D.2]. Profil d'intensité transverse du soliton émis (a) pour puissance optique croissant ($x_A = 14$ µm, $E_e = 4$ kV/cm) et (b) pour un champ électrique croissant $E_e$ ($x_A = 9.5$ µm et $P_A = 7$ µW). Le profil de sortie linéaire est représenté en noir.

Par ailleurs la Figure D.4 illustre l'influence des paramètres optique (la puissance [Fig. D.4(a)]) et électronique (le champ électrique extérieur [Fig. D.4(b)]) sur le faisceau solitonique transitoire lors de l'auto-focalisation du faisceau d'Airy. Dans les deux cas, nous observons une augmentation de l'effet solitonique, à savoir un pic plus intense et plus resserré à la position théoriquement prédite pour le soliton. Ces résultats sont en accord avec la physique de l'effet photoréfractif, comme la modulation locale de l'indice de réfraction est égale à $\Delta n = \pm\frac{n_0{}^3}{2} r_{eff}(E_{optique} + E_{électrique})$.

Finalement nous présentons le premier soliton Airy expérimental observé durant le processus d'auto-focalisation d'un faisceau d'Airy dans des conditions non linéaires biaisées. La structure solitonique confirme les prédictions théoriques, qu'un faisceau d'Airy se transforme en un soliton émis et une structure accélérante. En jouant sur les paramètres de nonlinéarité (puissance optique et champ électrique) ainsi que sur les paramètres de diffraction (taille du faisceau et la longueur de propagation), il est possible d'améliorer l'auto-focalisation du faisceau d'Airy et d'induire des faisceaux très intenses et fortement décalés (plusieurs multiples de la taille du premier lobe) le long de l'axe transverse du cristal. Cependant cette structure solitonique n'est pas stable et dans la prochaine section nous nous intéressons à l'évolution temporelle de tout le processus d'auto-focalisation du faisceau d'Airy.

### C.4.3 *Propriétés transitoires d'un faisceau d'Airy auto-focalisant et ses analogies avec le lentillage gravitationnel*

Récemment des chercheurs ont démontré que la propagation d'ondes optiques dans un milieu non linéaire (nonlinéarité non locale thermique) mène à une modification non locale de l'indice de réfraction qui agit comme un potentiel gravitationnel et qui, par conséquent, modifie la propagation d'un faisceau d'Airy d'une manière similaire à l'effet résultat de la théorie de la relativité générale. En particulier l'indice de réfraction jour le rôle d'un objet massif qui, d'après la théorie de la relativité générale, induit un effet de lentillage gravitationnel et des forces de marée sur les rayons optiques à cause de l'espace-temps courbe [123]. Dans ce contexte il est intéressant d'analyser en quelle mesure l'auto-focalisation du faisceau d'Airy partage une analogie optique similaire avec les effets de gravitation.

Les Figures D.5(a)-D.5(e) présentent l'évolution du profil d'intensité du faisceau de sortie au cours du temps. A partir de $t = 0$ s, l'intensité se déplace vers la position du seconde lobe Airy linéaire, jusqu'au-delà vers les lobes d'ordre supérieur [Fig. D.5(a)-D.5(b)] et atteint un déplacement transverse maximal à $x = -34$ µm au temps $t = 640$ ms [Fig. D.5(c)]. Par la suite nous nous référons à cette position par 'la position du soliton émis' (ligne pointillée rouge). Puis, sur une durée plus longue, on observe une dynamique de relaxation vers un profil redistribué de type Airy similaire à celui du faisceau linéaire initial à $t = 0$ s [Fig. D.5(d)-D.5(e)].

Les dynamiques spatiotemporelles du faisceau d'Airy non linéaire peuvent se résumer par trois étapes. (i) Tout d'abord le faisceau de sortie se focalise vers la ligne pointillée rouge sur Fig. D.5(b). (ii) Puis on observe deux structures de fais-

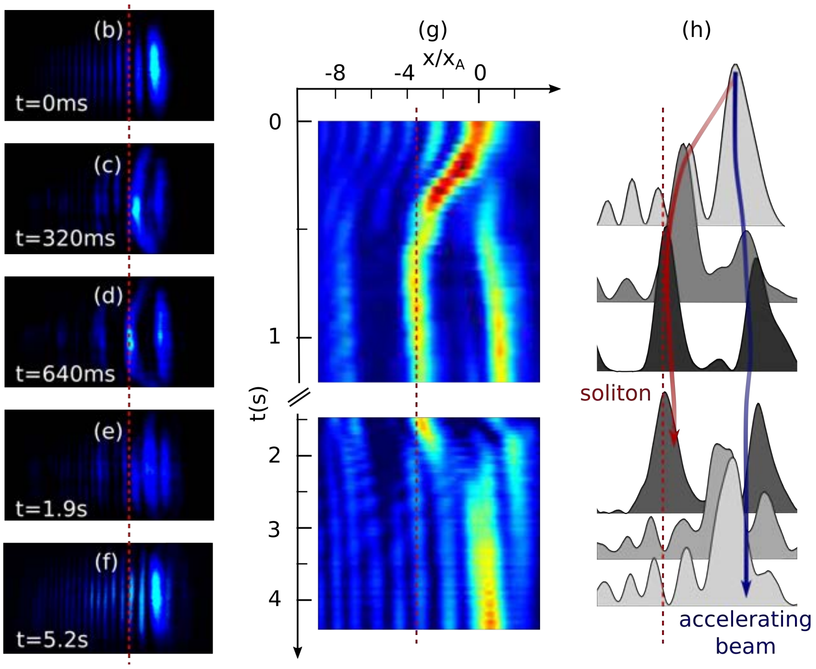

Figure C.7: Dynamique transitoires du soliton Airy ($x_A = 10$ μm). (a)-(e) Profil d'intensité transverse du faisceau de sortie dans des conditions non linéaires focalisantes ($E_e = 4$ kV/cm, $P_A = 400$ μW) au cours du temps. (f) Profil d'intensité 1D au cours du temps. (g) Illustration schématique du faisceau accélérant interagissant avec le soliton d'émission, ainsi que leur profils d'intensité au cours du temps.

ceaux co-existant [Figs. D.5(c), D.5(d)]: le-dit soliton émis à $x/x_A = -3.7$ et une structure accélérante à $x/x_A = 0.5$ avec des intensités similaires. (iii) Finalement les deux solutions précédentes fusionnent et forment une nouvelles structure similaire au Airy sur une durée plus longue. Telles les dynamiques de relaxations d'un soliton spatial issu d'un faisceau Gaussien auto-focalisé [48, 108, 113, 128, 129], le faisceau accélérant se redistribue avec des lobes moins focalisés et un pic d'intensité redéplacé vers l'axe $+x$ [Fig. D.5(f)].

La Figure D.6(a) présente le lentillage gravitationnel induit par la déflection du faisceau accélérant pour une puissance optique croissante. Tel pour les propriétés d'auto-focalisation du faisceau Gaussien [48, 67], le temps du transitoire vers l'auto-focalisation est réduit, lorsque l'intensité optique d'entrée augmente: une plus grande intensité réduit le temps de réponse du processus. Par ailleurs l'augmentation de la puissance optique modifie les propriétés transi-

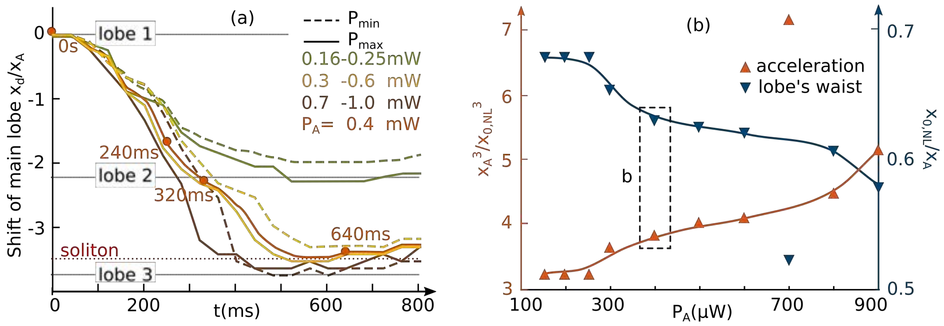

Figure C.8: Effet de lentillage expérimental auto-induit par le faisceau d'Airy autofocalisé. (a) Position transverse normalisée $x_d$ du pic de sortie en fonction du temps pour une puissance optique croissante. (b) Effet d'accélération normalisée: accélération normalisée et rayon du lobe principal $x_0$ du faisceau d'Airy attiré non linéairement vers le soliton émis pour une puissance optique croissant $P_A$.

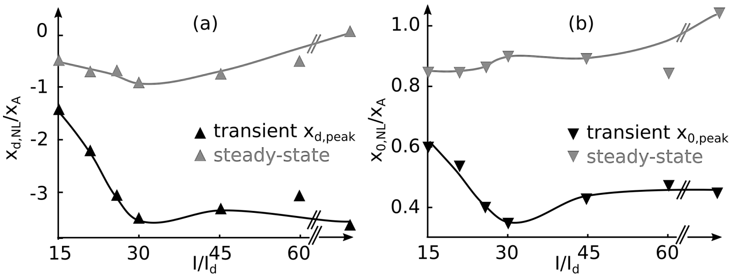

Figure C.9: Influence de l'illumination de fond sur le faisceau auto-focalisé transitoire et final: (a) décalage du faisceau $x_d$ (paramètre d'attraction) (b) et la distance inter-lobes $x_0$ (proportionnelle au cube à l'accélération).

toire d'auto-focalisation. Tel sur la Figure D.6(a), lorsque la puissance augmente de $P_A = 250$ μW à $P_A = 300$ μW (courbes vertes à jaunes), le déplacement maximum n'augmente pas linéairement, mais saute de la position du second lobe précédent ($x/x_A = -2.25$) à la position théorique du soliton émis de sortie. Lorsque la puissance est encore plus grande ($P_A > 700$ μW), le décalage maximal du faisceau continue à croître mais sature au troisième lobe ($x/x_A = -3.7$). En modifiant la puissance optique, il est donc possible d'équilibrer entre la diffraction et la nonlinéarité et ainsi de régler notre système non linéaire d'un faible interaction ($P \leqslant 250$ μW) à une forte interaction($P > 250$ μW) entre le paquet d'onde et la structure solitonique.

Le soliton émis non seulement attire le faisceau accélérant, mais influence également son accélération telles les forces des marée dans le lentillage gravitationnel. La Figure D.6(b) illustre l'accélération maximale normalisée pour une puissance optique croissante $P_A$. L'accélération augmente par trois ($P_A = 200\ \mu W$ ) voire par sept ($P_A = 900\ \mu W$) par rapport à la valeur initiale. Par ailleurs nous observons un resserrement des lobes ce qui traduit une présence de forces de marée durant le régime de formation du soliton ($t < 500$ ms). La force gravitationnelle exercée sur les différents lobes varie d'un lobe à une autre, ce qui est dû à la distance variable entre le lobe et le soliton ainsi qu'à cause de la variation du potentiel gravitationnel photoinduit du faisceau accélérant. Cet effet induit des forces gravitationnelles qui déforment la structure du paquet d'onde lorsqu'il se propage et tendent à resserrer les lobes.
Sur Fig. D.7(a), pour $I/I_d = 15$ l'auto-décalage du faisceau d'Airy observé précédemment est réduit durant le transitoire de $x_{d,noI_d} = -3.7x_A$ à $x_{d,I/I_d=15} = -1.5x_A$. Contrairement à la situation sans illumination de fond, ou la structure de type Airy de la phase (iii) est superposée à celle du faisceau d'Airy initial [Fig. **??**(f)], rajouter $I_d$ permet au faisceau accélérant de rester décalé même dans le régime stationnaire (décalage maximum de $-x_A$ for $I/I_d = 30$). Tel illustré sur Fig. D.7(b), l'éclairage de fond influence également l'effet d'auto-focalisation à la fois durant le régime transitoire comme stationnaire. En particulier nous continuons à observer de l'auto-focalisation du faisceau accélérant après $t > 8$ s. En termes de lentillage gravitationnel, l'éclairage de fond nous permet de contrôler la nonlinéarité du système et ainsi l'attraction et la force des marée appliquée sur la faisceau d'Airy [Fig. D.7(a)-D.7(b)].

En résumé ce travail est la première analyse des propriétés d'auto-focalisation transitoire d'un faisceau d'Airy dans un milieu non local non linéaire. L'évolution transitoire implique à la fois de l'attraction comme l'accélération du faisceau d'Airy initial, effets dus au soliton d'émission. Ces observations sont analogues à l'effet de lentillage gravitationnel quoiqu'auto-induite ici par un seul faisceau optique. Le faisceau d'Airy accélérant crée un espace-temps transitoire courbe qui défléchit la propagation de la lumière durant un court instant, avant de disparaître et de restaurer un profil Airy similaire à celui du début. Les propriétés du lentillage gravitationnel, i.e. déflection et accélération, peuvent être toutes deux contrôlées tout-optiquement en modifiant la nonlinéarité photoréfractive.

## C.5 RÉSUMÉ

### C.5.1 *Interactions de deux faisceaux d'Airy contrapropageants*

GUIDES D'ONDE CRÉÉS PAR UN SEUL FAISCEAU D'AIRY Avant d'analyser l'interaction de multiples faisceaux d'Airy, nous nous concentrons tout d'abord sur les possibilités de guidage que peut offrir un seul faisceau d'Airy dans des conditions solitoniques. Après avoir étudié précédemment la nature et le contrôle du soliton Airy, nous nous examinons numériquement les structures d'indice de réfraction photo-induites à l'intérieur du cristal non linéaire. A ce jour les faisceaux d'Airy ont suscité beaucoup d'intérêt notamment pour leur propriété d'accélération parabolique. Dans la Référence [36], Denz *et al.* utilise la trajectoire parabolique du faisceau d'Airy pour créer des guides d'onde courbes. Dans ce paragraphe nous augmentons la nonlinéarité pour activer l'auto-focalisation solitonique et pour obtenir ainsi un profile solitonique et accélérant superposés. La distribution d'intensité résultant est présentée sur Figure D.8, où le faisceau d'Airy linéaire initial se transforme en un soliton émis intense et un faible faisceau accélérant. Par l'effet photoréfractif, en particulier l'effet Pockels, cette distribution d'intensité photo-induit localement une augmentation d'indice de réfraction. Pour guider un signal optique test dans cette structure, nous considérons trois positions d'entrées [Fig. D.8]:

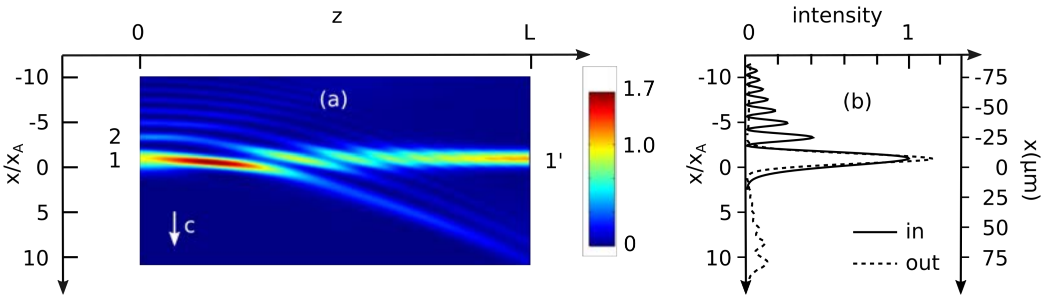

Figure C.10: (a) Distribution d'intensité normalisé d'un faisceau d 'Airy auto-focalisé se propageant dans un cristal photoréfractif non linéaire, $x_A = 7.5$ µm et $L = 1$ cm, (b) profils d'intensité transverses correspondant.

1 Entrée du lobe principal ($z = 0$)
2 Entrée du second lobe ($z = 0$)
1′ Sortie du soliton émis ($z = L$)

Tel présenté sur la Figure D.9, le type et l'efficacité du guide dépend de la po-

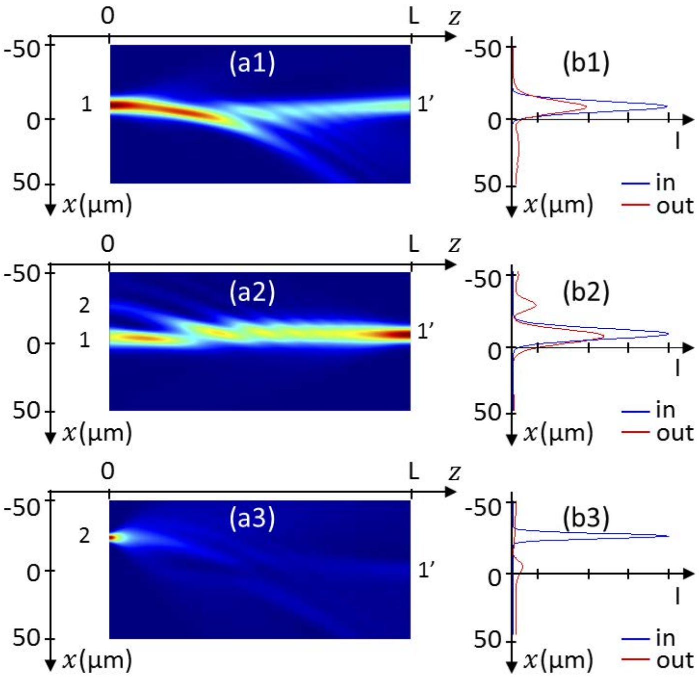

Figure C.11: Propagation linéaire du faisceau test dans la structure guidante de Figure D.8: (a1) distribution d'intensité et (b1) profils d'intensité transverses du faisceau gaussien guidé le long de $1 \to 1'$, (a2)-(b2) guidé le long de $1' \to (1, 2)$, (a3)-(b3) guidé le long de $2 \to 1'$.

sition d'entrée choisie par le faisceau gaussien test. Un faisceau d'Airy photo-induit deux types de guides d'onde: un avec une sortie [Figs. D.9(a1)-(b1)] ou avec deux sorties [Figs. D.9(a2)-(b2)]. Nous démontrons que l'efficacité de guidage est supérieure lorsque la propagation débute dans le guide solitonique. Par ailleurs la structure multi-lobe du faisceau d'Airy offre un guidage à sorties multiples, ce qui ne peut pas être obtenu avec un seul faisceau gaussien, et s'appuie donc sur les propriétés uniques du faisceau d'Airy. En comparaison avec les structures guidantes créées par les faisceaux gaussiens avec les mêmes dimensions et conditions de focalisation, la forme et les propriétés uniques Airy offrent des possibilités de guides d'onde bien plus larges. Ces résultats démontrent également que, bien que le guidage est bi-directionnel (i.e. un faisceau test gaussien est guidé le long de la structure dans les deux directions), l'asymétrie du guide d'onde mène à des positions de sortie ainsi qu'à des efficacités de guidage différentes selon la position d'entrée du faisceau test.

**Étude numérique de l'interactions de deux faisceaux d'Airy contrapropageants** Dans un second temps nous étudions la propagation de deux faisceaux d'Airy auto-focalisés contrapropageants dans un cristal photoréfractif ainsi que les interactions faisceaux-matière. Figure D.10 illustre le schéma-type d'interactions, dans lequel un faisceau d'Airy aller ("*F*" comme *forward* en anglais) est lancé à $z = 0$ dans la direction $+z$et un second faisceau d'Airy se propage dans le sens opposé $-z$ depuis l'autre face du cristal en $z = L$ ("*B*" comme *backward* en anglais) . Les accélérations des deux faisceaux d'Airy sont dans le même sens $+x$ tel présenté sur la Figure D.10.

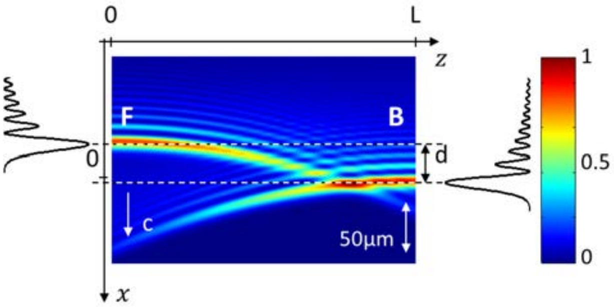

Figure C.12: Schéma d'interaction type de deux faisceaux d'Airy contrapropageants dans un cristal photoréfractif linéaire.

Figure D.11 présente la structure guidante photo-induite par deux faisceau d'Airy contrapropageants désalignés. L'utilisation d'une configuration avec des faisceaux contrapropageants présente plusieurs avantages par rapport au cas "un seul faisceau d'Airy":

- Symétrie: dans le cas où les deux faisceaux d'Airy sont alignés selon l'axe transverse $x$, nous avons des structures guidant à une sortie ainsi qu'à plusieurs sorties dans les deux sens de propagation $+z$ et $-z$,
- Décalage transverse: les décalages transverses des solitons émis (dans les cas F et B alignés comme désalignés) permettent des distance transverses bien plus importantes lors du guidage optique (plus de $4x_A$ dans le cas alignés, plus de $6x_A$ dans le cas désalignés de la Figure D.11).

Deux faisceaux d'Airy contrapropageants permettent de créer des structures de guidage complexes qui, dans le cas de faisceaux gaussiens nécessiterait sinon des interactions de plus de deux faisceaux gaussiens.

Comme l'efficacité de guidage dépend de la force d'auto-focalisation du milieu, qui cependant détériore le profil accélérant, les guides photo-induits par des faisceau d'Airy solitoniques nécessitent de trouver un équilibre entre la diversité de forme proposée par les propriétés Airy (multi-lobes, trajectoire courbe) et l'efficacité solitonique.

Dans un second nous démontrons également expérimentalement des interactions à de larges échelles multiples entre deux faisceaux d'Airy contrapropageants incohérents. Cette configuration et les résultats obtenus sont la première étude expérimentale d'interactions entre des faisceaux d'Airy et la Figure D.12 illustre le schéma du montage. Nous démontrons que la présence du second faisceau d'Airy induit une structure d'indice de réfraction plus complexe, ce qui modifie la trajectoire du premier faisceau d'Airy. En réglant les différents paramètres du système, le faisceau d'Airy auto-focalisant est attiré vers les lobes multiples du faisceau d'Airy contrapropageant.

Les résultats expérimentaux confirment les structures de guidantes complexes et variées qui peuvent être obtenues avec les seules interactions de deux faisceaux d'Airy contrapropageants. Comme l'indique le tableau ci-dessous, nous présentons une série de paramètres facilement réglables permettant de photo-induire des guides d'onde avec de larges décalages, plusieurs sorties et stables sur plusieurs secondes.

| Paramètre | Valeurs | Influence |
|---|---|---|
| Faisceau contrapropageant | | Plus d’efficacité de guidage<br>Plus de décalage transverse |
| Décalage du faisceau | $[0; \approx 10x_A]$ | Réglage du nombre de sorties du guide (1-3 sorties)<br>Plus de décalage transverse |
| Taille du faisceau | $[9.5; 14]$ µm | Moins d’auto-focalisation solitonique<br>Moins de décalage transverse (moins de déflection)<br>Réglage du nombre de sorties du guide (1-3 sorties) |
| Champ électrique $U_{SBN}$ | $[0; 2]$ kV | Plus d’auto-focalisation solitonique<br>Meilleure stabilité temporelle du soliton |

### c.5.2 *Dynamiques spatiotemporelles théoriques de deux faisceaux d’Airy contrapropageants*

Pour approfondir l’étude de l’interaction de deux faisceaux d’Airy, nous intensifions les conditions focalisantes. La stabilité peut être réglée grâce aux paramètres cités ci-dessus. Les guides photoinduits par deux faisceaux d’Airy apparaissent alors plus stables que ceux photoinduits par deux faisceaux gaussiens under focusing conditions. Au cours de notre études exhaustive (évolution de la dynamique spatiotemporelle en fonction de la longueur du cristal et de la nonlinéarité du milieu), nous observons un seuil au-dessus duquel le guide d’onde n’est plus stationnaire, mais évolue selon des dynamiques temporelles périodiques voire même chaotiques tel il est possible d’observer sur la Figure D.13 . Au dessus du seuil de stabilité, chaque soliton Airy se meut de manière erratique autour de positions de sorties privilégiées, qui correspondent aux positions spatiales des lobes du faisceau d’Airy contrapropageant. Ces résultats suggèrent de nouveaux moyens de créer des guides d’onde dynamiques, des portes logiques optiques ainsi que du calcul chaotique.

## C.6 CONCLUSION

Cette thèse résume trois années de recherche essentiellement dans trois domaines:

- l'autofocalisation d'un faisceau d'Airy accélérant unidimensionnel vers une structure solitonique dans des milieux photoréfractifs,
- les interactions spatiotemporelles de deux faisceaux d'Airy 1D contrapopageants dans un cristal non linéaire,
- et les structures de guide d'onde induites dans le milieu par les faisceaux d'Airy.

Tout au long de la thèse nous avons considéré le régime solitonique d'un faisceau d'Airy, ce qui en théorie anihile les propriétés fascinantes d'un faisceau d'Airy. Au contraire les propriétés Airy intrinsèques ont persisté à travers notre travail numérique et expérimental:

- distribution Airy multi-lobe : création de guides démultiplexant, guidage d'onde de plus grande amplitude transverse, localisation spatiale d'instabilités
- propagation sans diffraction : interconnection de multiples lobes des faisceaux d'Airy contrapropageants sur de plus longues distances, plus grande marge de stabilité
- propagation accélérante : meilleure capacité d'interconnection transverse, cadre pour l'analogie avec l'espace gravitationnel

Ces résultats confirment que le faisceau d'Airy est un candidat idéal pour du routage tout-optique et suggèrent son étude approfondie dans des configurations optiques plus larges.

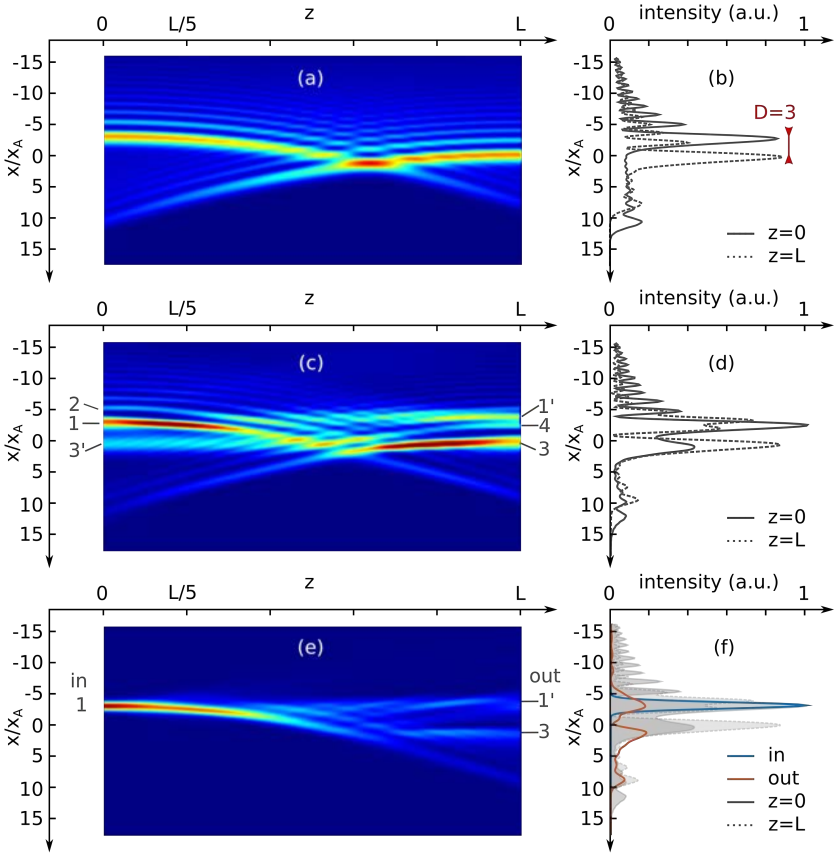

Figure C.13: Guides d'onde photo-induits à l'aide de deux faisceaux d'Airy contrapropageants désalignés dans un cristal photoréfractif (D = 3 normalisé selon $x_A$). (a) (resp. (c)) Distribution d'intensité à l'intérieur du milieu et (b) (resp. (d)) profils d'intensité transverses aux extrémités du cristal dans des conditions linéaires (resp. non linéaires focalisantes). (e)-(f) Propagation linéaire d'un faisceau test dans la structure de guide d'onde (b): (e) distribution d'intensité et (f) profils transverses du faisceau gaussien guidé le long de $1 \to (1', 3)$.

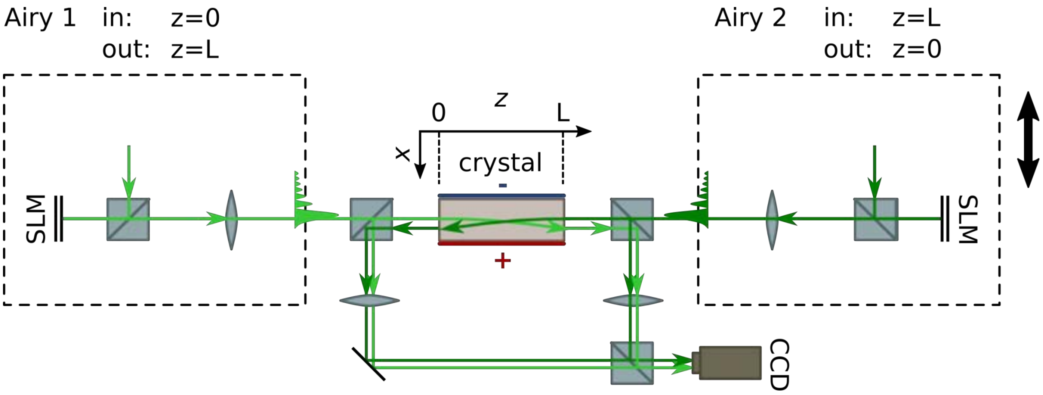
Airy 1 in: z=0
out: z=L
Airy 2 in: z=L
out: z=0
0
z
L
x
crystal
-
+
SLM
SLM
CCD

Figure C.14: Etude de deux faisceaux d'Airy incohérents contrapropageant dans un cristal photoréfractif: montage expérimental.

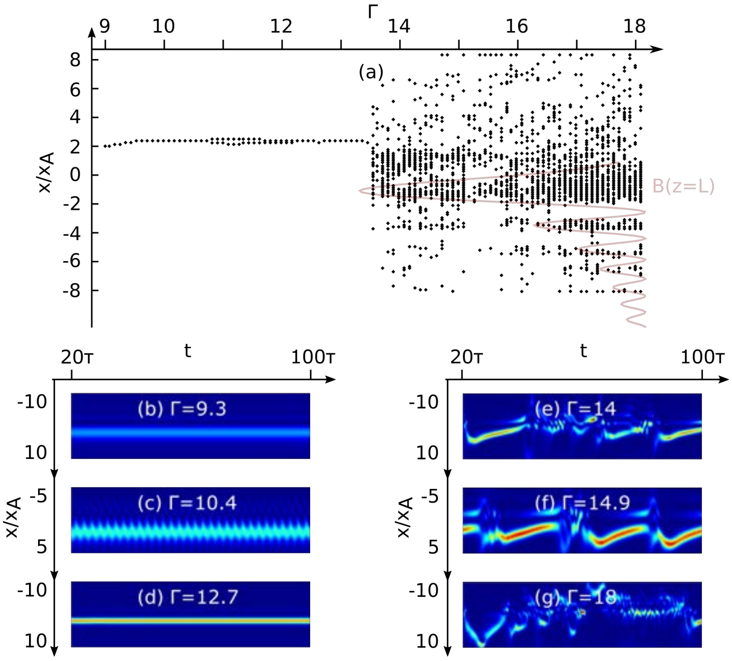

Figure C.15: Dynamiques spatiotemporelles de deux faisceaux d'Airy contrapropageant dans un long cristal $L = 5.5L_d$, d'intensités normalisées $F_0 = B_0 = \sqrt{1.5}$. (a) Diagramme de bifurcation des positions de sortie transverses du soliton Airy à $z = L$, avec le profil d'intensité normalisé du faisceau d'Airy contrapropageant à $z = L$. (b)-(g) Evolution temporelle de la position de sortie transverse du soliton Airy aller à $z = L$: (b) régime stationnaire ($\Gamma = 9.3$), (c) oscillations sinusoidales ($\Gamma = 10.4$), (d) deuxième régime stationnaire ($\Gamma = 12.7$), (e) premières instabilités ($\Gamma = 14$), (f) oscillations non sinusoidales périodiques ($\Gamma = 14.9$) et (g) instabilités ($\Gamma = 18$). P.ex. expérimentation pour des faisceaux d'Airy contrapropageant dans un cristal SBN:75 ($L * 5$ mm $* 5$ mm) avec $x_A = 10$ µm: $L = 28$mm, $U_{ext} \in [500V, 900V]$.

D

# A LITTLE STORY IN 180S

*La lumière qui ne file pas bien droit* - Comic story about the analogy between self-focusing of an optical Airy beam and the gravitational lensing effects in space-time. Edited in the context of a francophone science popularization contest, ”Ma thèse en 180s” 2016.

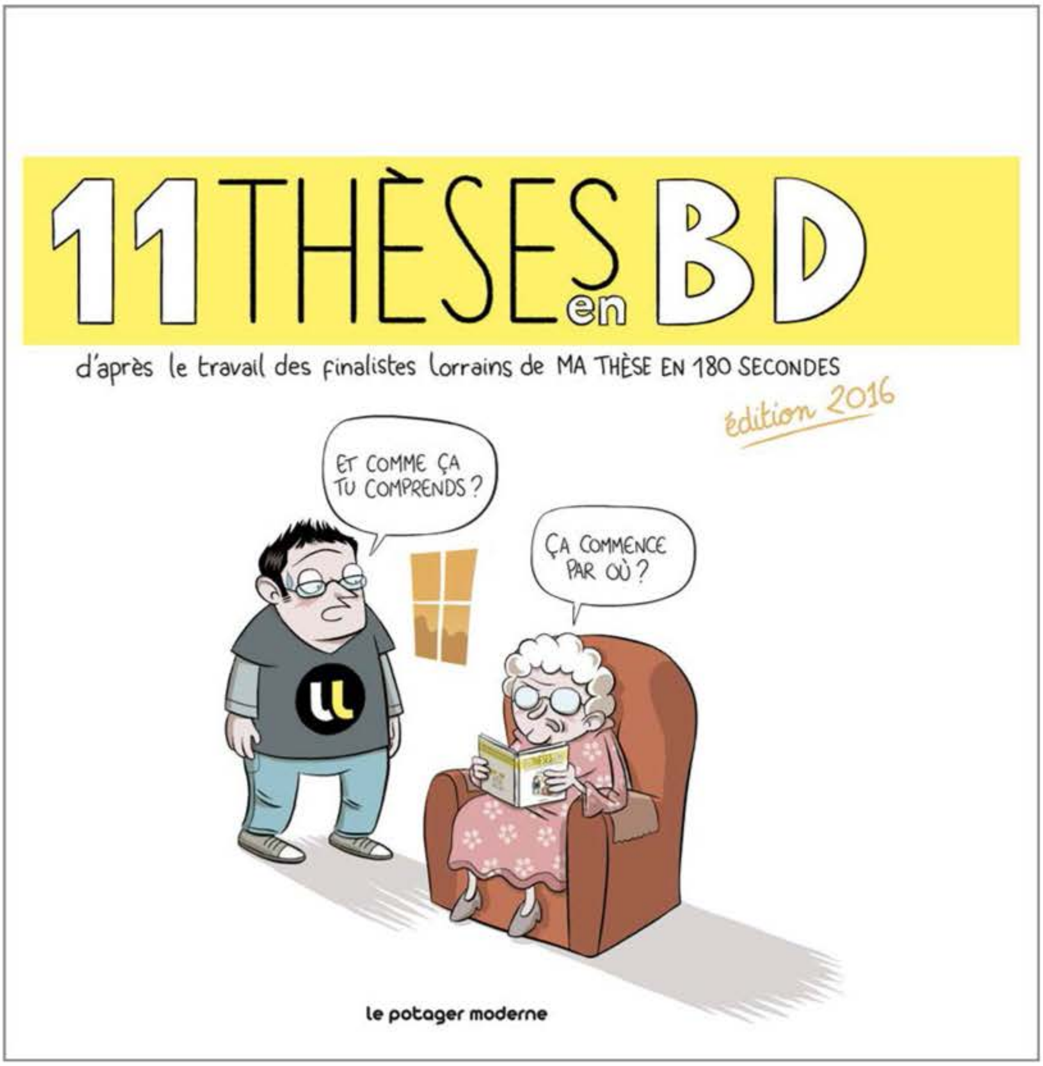
11 THÈSES en BD
d'après le travail des finalistes lorrains de MA THÈSE EN 180 SECONDES
édition 2016
ET COMME ÇA TU COMPRENDS ?
ÇA COMMENCE PAR OÙ ?
le potager moderne

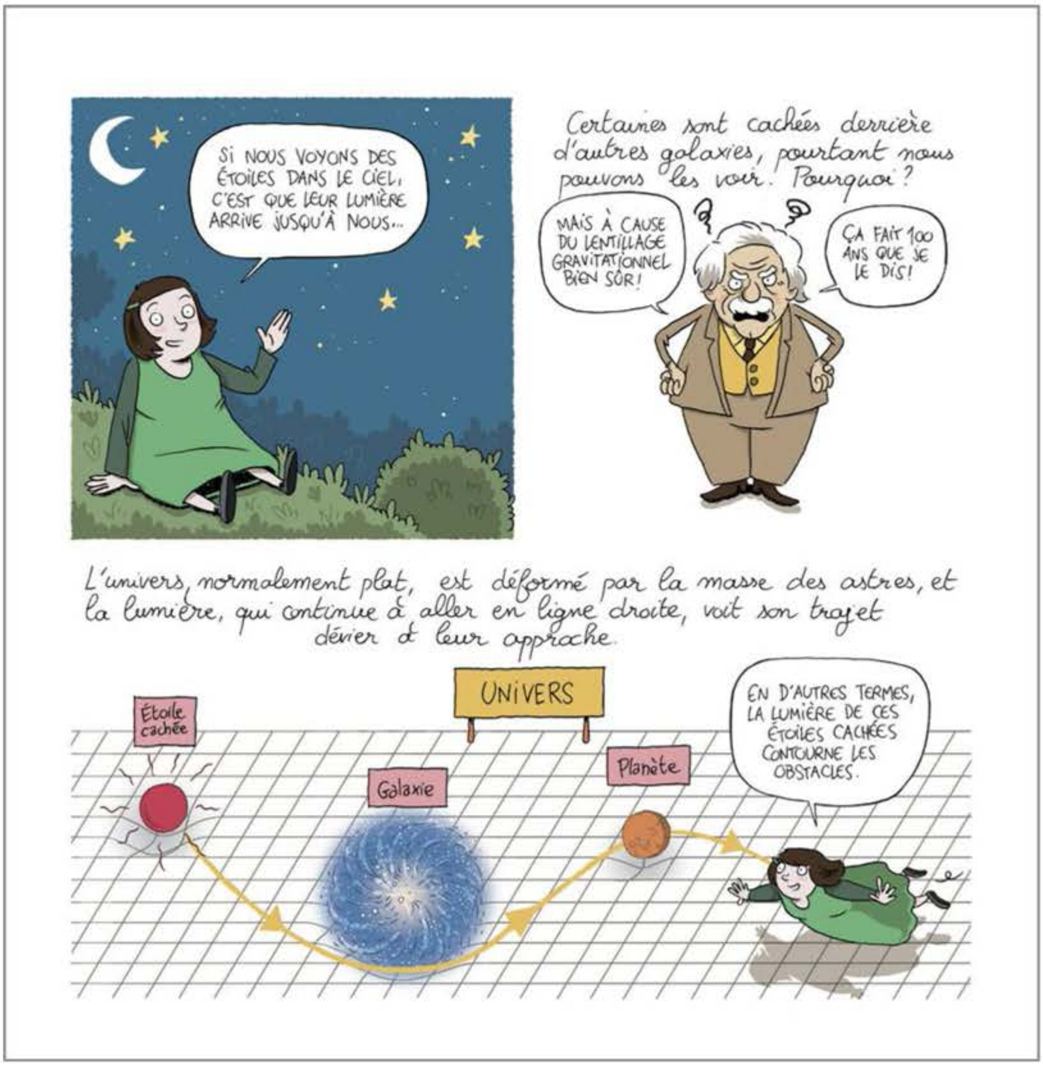
SI NOUS VOYONS DES ÉTOILES DANS LE CIEL, C'EST QUE LEUR LUMIÈRE ARRIVE JUSQU'À NOUS...
Certaines sont cachées derrière d'autres galaxies, pourtant nous pouvons les voir. Pourquoi ?
MAIS À CAUSE DU LENTILLAGE GRAVITATIONNEL BIEN SÛR !
ÇA FAIT 100 ANS QUE JE LE DIS !
L'univers, normalement plat, est déformé par la masse des astres, et la lumière, qui continue d'aller en ligne droite, voit son trajet dévier à leur approche.
UNIVERS
Étoile cachée
Galaxie
Planète
EN D'AUTRES TERMES, LA LUMIÈRE DE CES ÉTOILES CACHÉES CONTOURNE LES OBSTACLES.

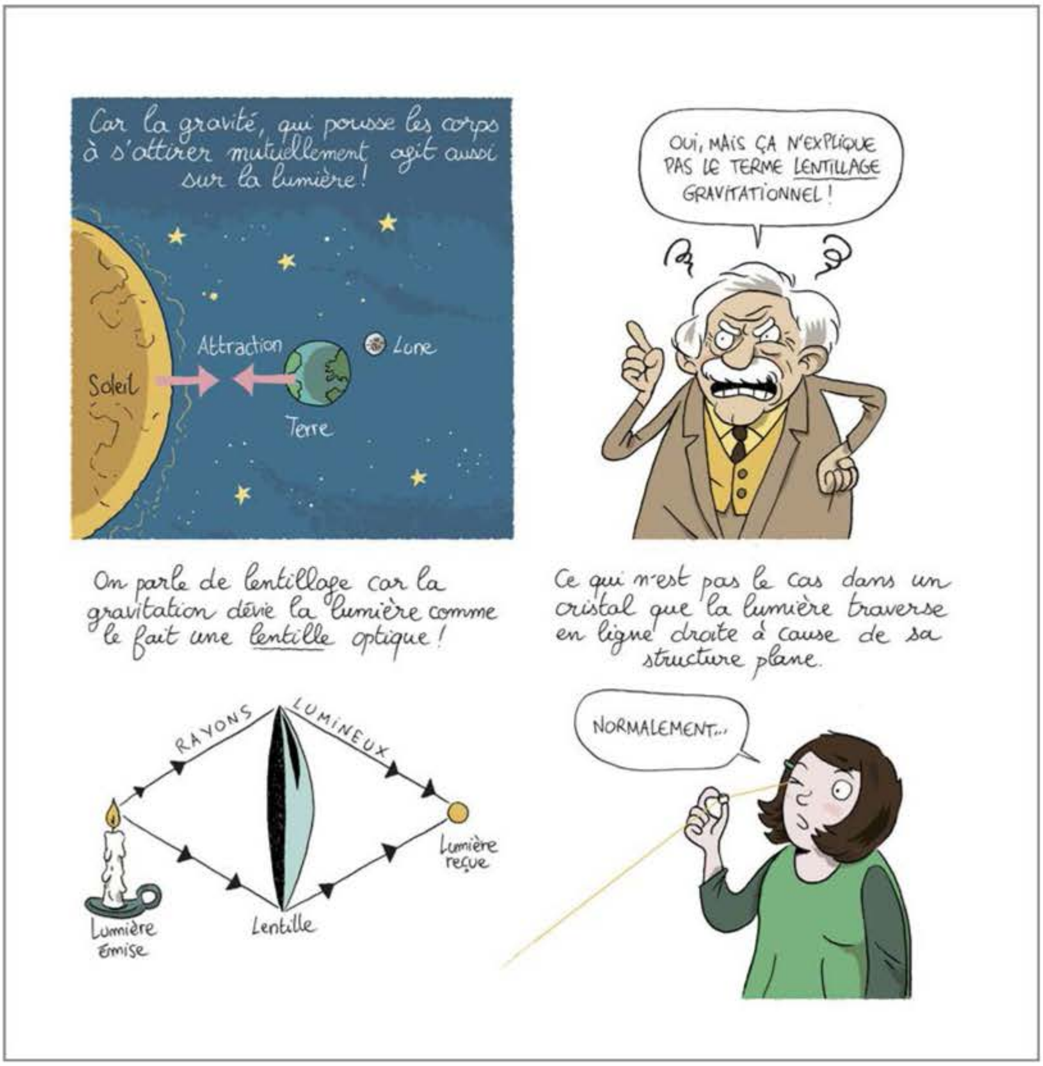
Car la gravité, qui pousse les corps à s'attirer mutuellement agit aussi sur la lumière !
Soleil
Attraction
Lune
Terre
OUI, MAIS ÇA N'EXPLIQUE PAS LE TERME LENTILLAGE GRAVITATIONNEL !
On parle de lentillage car la gravitation dévie la lumière comme le fait une lentille optique !
RAYONS LUMINEUX
Lumière Émise
Lentille
Lumière reçue
Ce qui n'est pas le cas dans un cristal que la lumière traverse en ligne droite à cause de sa structure plane.
NORMALEMENT…

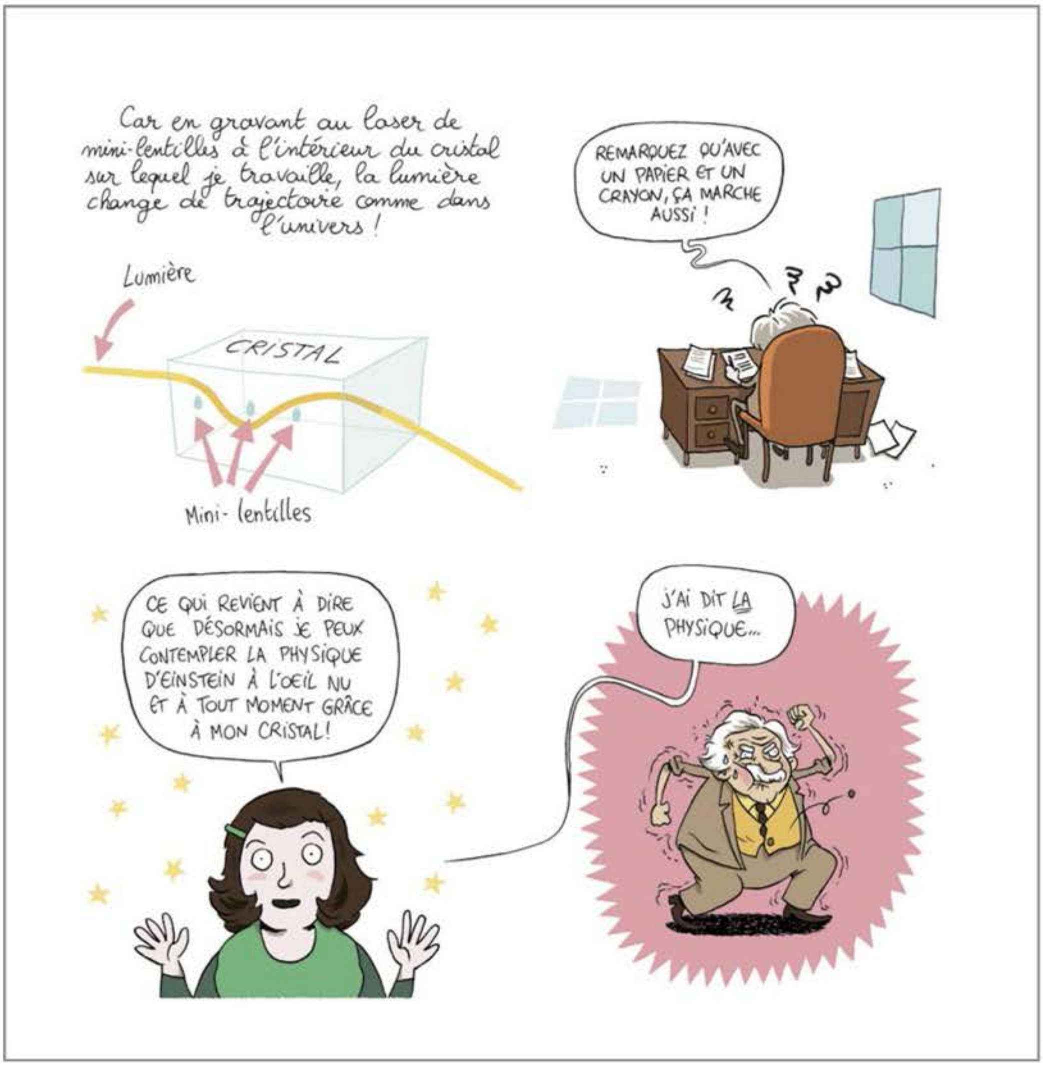
Car en gravant au laser de mini-lentilles à l'intérieur du cristal sur lequel je travaille, la lumière change de trajectoire comme dans l'univers !
Lumière
CRISTAL
Mini-lentilles
REMARQUEZ QU'AVEC UN PAPIER ET UN CRAYON, ÇA MARCHE AUSSI !
CE QUI REVIENT À DIRE QUE DÉSORMAIS JE PEUX CONTEMPLER LA PHYSIQUE D'EINSTEIN À L'OEIL NU ET À TOUT MOMENT GRÂCE À MON CRISTAL !
J'AI DIT LA PHYSIQUE...

# BIBLIOGRAPHY

[1] D. K. Lynch and W. Livingston. *Color and light in nature, 2nd edition*. Vol. 26. 6. 2001, p. 486. DOI: `10.1002/col.1070`.

[2] G. B. Airy. "On the intensity of light in the neighbourhood of a caustic." In: *Trans. Cambridge Phil. Soc.* 6 (1838), pp. 397–403.

[3] O. Vallée and M. Soares. *Airy Functions and Applications to Physics*. EBSCO ebook academic collection. World Scientific, 2004.

[4] M. V. Berry and N. L. Balazs. "Nonspreading wave packets." In: *Am. J. Phys.* 47 (1979), p. 264.

[5] D. Gloge and D. Marcuse. "Formal quantum theory of light rays." In: *J. Opt. Soc. Am.* 59.December (1969), pp. 1629–1631. DOI: `10.1364/JOSA.59.001629`.

[6] J. Durnin, J. Miceli, and J. H. Eberly. "Diffraction-free beams." In: *Phys. Rev. Lett.* 58.15 (1987), pp. 1499–1501. DOI: `10.1103/PhysRevLett.58.1499`.

[7] J. Durnin. "Exact solutions for nondiffracting beams. I. The scalar theory." In: *J. Opt. Soc. Am. A* 4.4 (1987), p. 651. DOI: `10.1364/JOSAA.4.000651`.

[8] M. McLaren et al. "Self-healing of quantum entanglement after an obstruction." In: *Nat. Commun.* 5 (2014). DOI: `10.1038/ncomms4248`.

[9] J. C. Gutiérrez-Vega et al. "Experimental demonstration of optical Mathieu beams." In: *Opt. Commun.* 195.1-4 (2001), pp. 35–40. DOI: `10.1016/S0030-4018(01)01319-0`.

[10] M. A. Bandres, J. C. Gutiérrez-Vega, and S. Chávez-Cerda. "Parabolic nondiffracting optical wave fields." In: *Opt. Lett.* 29.1 (2004), pp. 44–46. DOI: `10.1364/OL.29.000044`.

[11] D McGloin and K Dholakia. "Bessel beams: Diffraction in a new light." In: *Contemp. Phys.* 46.1 (2005), pp. 15–28. DOI: `10.1080/0010751042000275259`.

[12] Z. Bouchal. "Nondiffracting optical beams: Physical properties, experiments, and applications." In: *Czechoslov. J. Phys.* 53.7 (2003), pp. 537–578. DOI: `10.1023/A:1024802801048`.

[13] D. G. Grier. "A revolution in optical manipulation." In: *Nature* 424.6950 (2003), pp. 810–6. DOI: `10.1038/nature01935`.

[14] A Ashkin, J. M. Dziedzic, J. E. Bjorkholm, and S Chu. "Observation of a single-beam gradient force optical trap for dielectric particles." In: *Opt. Lett.* 11.5 (1986), p. 288. DOI: `10.1364/OL.11.000288`.

[15] V. Garcés-Chávez et al. "Simultaneous micromanipulation in multiple planes using a self-reconstructing light beam." In: *Nature* 419.6903 (2002), pp. 145–147. DOI: `10.1038/nature01007`.

[16] G. A. Siviloglou and D. N. Christodoulides. "Accelerating finite energy Airy beams." In: *Opt. Lett.* 32.8 (2007), pp. 979–981. DOI: `10.1364/OL.32.000979`.

[17] G. Siviloglou and J Broky. "Observation of accelerating Airy beams." In: *Phys. Rev. ...* Vol. 213901. November. Optical Society of America. 2007, pp. 23–26. DOI: `10.1103/PhysRevLett.99.213901`.

[18] J. Broky, G. A. Siviloglou, A. Dogariu, and D. N. Christodoulides. "Self-healing properties of optical Airy beams." In: *Opt. Express* 16.17 (2008), pp. 12880–12891. DOI: `10.1364/OE.16.012880`.

[19] J. E. Morris et al. "Propagation characteristics of Airy beams: dependence upon spatial coherence and wavelength." In: *Opt. Express* 17.15 (2009), p. 13236. DOI: `10.1364/OE.17.013236`.

[20] G. A. Siviloglou, J. Broky, A. Dogariu, and D. N. Christodoulides. "Ballistic dynamics of Airy beams." In: *Opt. Lett.* 33.3 (2008), pp. 207–209. DOI: `10.1364/OL.33.000207`.

[21] Y. Hu et al. "Optimal control of the ballistic motion of Airy beams." In: *Opt. Lett.* 35.13 (2010), p. 2260. DOI: `10.1364/OL.35.002260`.

[22] T. Ellenbogen, N. Voloch-Bloch, A. Ganany-Padowicz, and A. Arie. "Nonlinear generation and manipulation of Airy beams." In: *Nat. Photonics* 3.7 (2009), pp. 395–398. DOI: `10.1038/nphoton.2009.95`.

[23] I. Dolev and A. Arie. "Three wave mixing of airy beams in a quadratic nonlinear photonic crystals." In: *Appl. Phys. Lett.* 97.17 (2010), p. 171102. DOI: `10.1063/1.3504247`.

[24] I. Dolev, T. Ellenbogen, and A. Arie. "Switching the acceleration direction of Airy beams by a nonlinear optical process." In: *Opt. Lett.* 35.10 (2010), pp. 1581–1583. DOI: `10.1364/OL.35.001581`.

[25] D. M. Cottrell, J. A. Davis, and T. M. Hazard. "Direct generation of accelerating Airy beams using a 3/2 phase-only pattern." In: *Opt. Lett.* 34.17 (2009), pp. 2634–2636. DOI: `10.1364/OL.34.002634`.

[26] G. Porat, I. Dolev, O. Barlev, and A. Arie. "Airy beam laser." In: *Opt. Lett.* 36.20 (2011), pp. 4119–4121. DOI: `10.1364/OL.36.004119`.

[27] H. Deng and L. Yuan. "Two-dimensional Airy-like beam generation by coupling waveguides." In: *J. Opt. Soc. Am. A* 30.7 (2013), p. 1404. DOI: `10.1364/JOSAA.30.001404`.

[28] M. a. Bandres. "Accelerating parabolic beams." In: *Opt. Lett.* 33.15 (2008), p. 1678. DOI: `10.1364/OL.33.001678`.

[29] E. Greenfield, M. Segev, W. Walasik, and O. Raz. "Accelerating Light Beams along Arbitrary Convex Trajectories." In: *Phys. Rev. Lett.* 106.21 (2011), p. 213902. DOI: `10.1103/PhysRevLett.106.213902`.

[30] I. Kaminer, R. Bekenstein, J. Nemirovsky, and M. Segev. "Nondiffracting Accelerating Wave Packets of Maxwell's Equations." In: *Phys. Rev. Lett.* 108.16 (2012), p. 163901. DOI: `10.1103/PhysRevLett.108.163901`.

[31] J Baumgartl et al. "Optical path clearing and enhanced transmission through colloidal suspensions." In: *Opt. Express* 18.16 (2010), pp. 17130–40. DOI: `10.1364/OE.18.017130`.

[32] "Microscopy with self-reconstructing beams." In: *Nat. Photonics* 4.11 (2010), pp. 780–785. DOI: `10.1038/nphoton.2010.204`.

[33] D. G. Papazoglou, N. K. Efremidis, D. N. Christodoulides, and S. Tzortzakis. "Observation of abruptly autofocusing waves." In: *Opt. Lett.* 36.10 (2011), pp. 1842–1844. DOI: `10.1364/OL.36.001842`.

[34] A. Mathis et al. "Micromachining along a curve: Femtosecond laser micromachining of curved profiles in diamond and silicon using accelerating beams." In: *Appl. Phys. Lett.* 101.7 (2012), p. 071110. DOI: `10.1063/1.4745925`.

[35] T. Vettenburg et al. "Light-sheet microscopy using an Airy beam." In: *Nat. Methods* 11.5 (2014), pp. 541–544. DOI: `10.1038/nmeth.2922`.

[36] P. Rose, F. Diebel, M. Boguslawski, and C. Denz. "Airy beam induced optical routing." In: *Appl. Phys. Lett.* 102.10 (2013), pp. 2013–2016. DOI: `10.1063/1.4793668`.

[37] Y. I. L. Iang et al. "Image signal transmission with Airy beams." In: *Opt. Lett.* 40.23 (2015), pp. 5686–5689. DOI: `10.1364/OL.40.005686`.

[38] P. Polynkin et al. "Curved plasma channel generation using ultraintense Airy beams." In: *Science* 324.5924 (2009), pp. 229–232. DOI: `10.1364/OPN.20.12.000028`.

[39] A. Salandrino and D. N. Christodoulides. "Airy plasmon: a nondiffracting surface wave." In: *Opt. Lett.* 35.12 (2010), pp. 2082–2084. DOI: `10.1364/OL.35.002082`.

[40] A. E. Minovich et al. "Airy plasmons: Non-diffracting optical surface waves." In: *Laser Photonics Rev.* 8.2 (2014), pp. 221–232. DOI: `10.1002/lpor.201300055`.

[41] N. Voloch-Bloch et al. "Generation of electron Airy beams." In: *Nature* 494.7437 (2013), pp. 331–335. DOI: `10.1038/nature11840`.

[42] A. Ashkin et al. "Optically-induced refractive index inhomogeneities in LiNbO3 and LiTaO3." In: *Appl. Phys. Lett.* 9.1 (1966), pp. 72–74. DOI: `10.1063/1.1754607`.

[43] F. S. Chen. "Holographic storage in Lithium Niobate." In: *Appl. Phys. Lett.* 13.7 (1968), p. 223. DOI: `10.1063/1.1652580`.

[44] G. Montemezzani, C. Medrano, M. Zgonik, and P. Günter. "The photorefractive effect in inorganic and organic materials." In: *Nonlinear Opt. Eff. Mater.* 2006, pp. 301–373. DOI: `10.1007/978-3-540-49713-4_4`.

[45] N. V. Kukhtarev et al. "Holographic storage in electrooptic crystals." In: *Ferroelectrics* 22.1 (1978), pp. 961–964. DOI: `10.1080/00150197908239451`.

[46] F. S. Chen. "A Laser-Induced Inhomogeneity of Refractive Indices in KTN." In: *J. Appl. Phys.* 38.8 (1967), p. 3418. DOI: `10.1063/1.1710138`.

[47] F. Agulló-López. *Insulating Materials for Optoelectronics: New Developments*. 1995.

[48] J. Petter et al. "Self-bending of photorefractive solitons." In: *Opt. Commun.* 170.4-6 (1999), pp. 291–297. DOI: `10.1016/S0030-4018(99)00485-X`.

[49] J Ashley et al. *Holographic Data Storage*. Ed. by H. J. Coufal, D. Psaltis, and G. T. Sincerbox. Vol. 44. Springer Series in Optical Sciences 3. Berlin, Heidelberg: Springer Berlin Heidelberg, 2000, pp. 341–368. DOI: `10.1007/978-3-540-47864-5`.

[50] K. Iizuka. "Optical Properties of Crystals Under Various External Fields." In: *Elem. Photonics, Vol. I.* New York, USA: John Wiley & Sons, Inc., pp. 302–361. DOI: `10.1002/0471221074.ch5`.

[51] C. C. Chang. "Photorefractive Multi-Beam Induced Phase Conjugation." In: *Opt. Rev.* 4.5 (1997), pp. 556–560. DOI: `10.1007/s10043-997-0556-5`.

[52] H. A. Eggert et al. "Trapping of dielectric particles with light-induced space-charge fields." In: *Appl. Phys. Lett.* 90.24 (2007), p. 241909. DOI: `10.1063/1.2748089`.

[53] N. Marsal et al. "Experimental control of pattern formation by photonic lattices." In: *Opt. Lett.* 33.21 (2008), p. 2509. DOI: `10.1364/OL.33.002509`.

[54] N. Marsal, D. Wolfersberger, M. Sciamanna, and G. Montemezzani. "Noise- and dynamics-sustained patterns in a nonlinear photorefractive system." In: *Phys. Rev. A* 81.3 (2010), p. 031804. DOI: `10.1103/PhysRevA.81.031804`.

[55] M. Alonzo, C. Dan, D. Wolfersberger, and E. Fazio. "Coherent collisions of infrared self-trapped beams in photorefractive InP:Fe." In: *Appl. Phys. Lett.* 96.12 (2010), p. 121111. DOI: `10.1063/1.3373609`.

[56] C. Denz. *Optical Neural Networks*. Ed. by T. Tschudi. Wiesbaden: Vieweg+Teubner Verlag, 1998. DOI: `10.1007/978-3-663-12272-2`.

[57] J. S. Russell. "Report on waves." In: *14th meeting of the British Association for the Advancement of Science*. Vol. 311. 1844, p. 390.

[58] N. J. Zabusky and M. D. Kruskal. "Interaction of "Solitons" in a Collisionless Plasma and the Recurrence of Initial States." In: *Phys. Rev. Lett.* 15.6 (1965), pp. 240–243. DOI: `10.1103/PhysRevLett.15.240`.

[59] D. J. Korteweg and G. de Vries. "XLI. On the change of form of long waves advancing in a rectangular canal, and on a new type of long stationary waves." In: *Philos. Mag. Ser. 5* 39.240 (1895), pp. 422–443. DOI: `10.1080/14786449508620739`.

[60] V. E. Zakharov. "Kinetic Equation for Solitons." In: *Sov. Phys. - JETP* 60 (1971), pp. 993–1000.

[61] V. F Zakharov and A. B Shabat. "Exact Theory of Two-dimensional Self-focusing and One-dimensional Self-modulation of Wave in Nonlinear Media." In: *Sov. Phys. JETP* 34.1 (1972), p. 62.

[62] R. Dodd, J. Eilbeck, J. Gibbon, and H. Morris. *Solitons and nonlinear wave equations*. 1982, p. 627.

[63] C. Gu. *Soliton Theory and Its Applications*. 2010, p. 416.

[64] A. Hasegawa. "Transmission of stationary nonlinear optical pulses in dispersive dielectric fibers. I. Anomalous dispersion." In: *Appl. Phys. Lett.* 23.3 (1973), p. 142. DOI: `10.1063/1.1654836`.

[65] L. F. Mollenauer, R. H. Stolen, and J. P. Gordon. "Experimental Observation of Picosecond Pulse Narrowing and Solitons in Optical Fibers." In: *Phys. Rev. Lett.* 45.13 (1980), pp. 1095–1098. DOI: `10.1103/PhysRevLett.45.1095`.

[66] M.-f. Shih et al. "Two-dimensional steady-state photorefractive screening solitons." In: *Opt. Lett.* 21.5 (1996), p. 324. DOI: `10.1364/OL.21.000324`.

[67] Z. Chen, M. Segev, and D. N. Christodoulides. "Optical spatial solitons: historical overview and recent advances." In: *Reports Prog. Phys.* 75.8 (2012), p. 086401. DOI: `10.1088/0034-4885/75/8/086401`.

[68] J. E. Bjorkholm and A. A. Ashkin. "cw Self-Focusing and Self-Trapping of Light in Sodium Vapor." In: *Phys. Rev. Lett.* 32.4 (1974), pp. 129–132. DOI: `10.1103/PhysRevLett.32.129`.

[69] A. Barthelemy, S. Maneuf, and C. Froehly. "Propagation soliton et autoconfinement de faisceaux laser par non linearité optique de kerr." In: *Opt. Commun.* 55.3 (1985), pp. 201–206. DOI: `10.1016/0030-4018(85)90047-1`.

[70] M. Segev, B. Crosignani, A. Yariv, and B. Fischer. "Spatial solitons in photorefractive media." In: *Phys. Rev. Lett.* 68.7 (1992), pp. 923–926. DOI: `10.1103/PhysRevLett.68.923`.

[71] E. L. Dawes and J. H. Marburger. "Computer studies in self-focusing." In: *Phys. Rev.* 179.3 (1969), pp. 862–868. DOI: `10.1103/PhysRev.179.862`.

[72] P. L. Kelley. "Self-Focusing of Optical Beams." In: *Phys. Rev. Lett.* 15.26 (1965), pp. 1005–1008. DOI: `10.1103/PhysRevLett.15.1005`.

[73] V. Tikhonenko, J. Christou, and B. Luther-Davies. "Three Dimensional Bright Spatial Soliton Collision and Fusion in a Saturable Nonlinear Medium." In: *Phys. Rev. Lett.* 76.15 (1996), pp. 2698–2701. DOI: `10.1103/PhysRevLett.76.2698`.

[74] E. Del Re et al. "One-dimensional steady-state photorefractive spatial solitons in centrosymmetric paraelectric KLTN." In: *Tech. Dig. Summ. Pap. Present. Conf. Lasers Electro-Optics. Conf. Ed. 1998 Tech. Dig. Ser. Vol.6 (IEEE Cat. No.98CH36178).* Vol. 23. 1. IEEE, 1998, pp. 456–457. DOI: `10.1109/CLEO.1998.676492`.

[75] M. F. Shih and F. W. Sheu. "Photorefractive polymeric optical spatial solitons." In: *Opt. Lett.* 24.24 (1999), pp. 1853–1855. DOI: `10.1364/OL.24.001853`.

[76] Z. Chen et al. "Self-trapping of light in an organic photorefractive glass." In: *Opt. Lett.* 28.24 (2003), p. 2509. DOI: `10.1364/OL.28.002509`.

[77] F Derrien, J. F. Henninot, M Warenghem, and G Abbate. "A thermal (2D+1) spatial optical soliton in a dye doped liquid crystal." In: *J. Opt. A Pure Appl. Opt.* 2.4 (2000), pp. 332–337. DOI: `10.1088/1464-4258/2/4/316`.

[78] J. F. Henninot et al. "Self-waveguiding in an isotropic channel induced in dye doped nematic liquid crystal and a bent self-waveguide." In: *J. Opt. A Pure Appl. Opt.* 6.4 (2004), pp. 315–323. DOI: `10.1088/1464-4258/6/4/005`.

[79] E. DelRe, B. Crosignani, and P. Di Porto. "Photorefractive Spatial Solitons." In: 2001, pp. 61–85. DOI: `10.1007/978-3-540-44582-1_4`.

[80] E. DelRe, B. Crosignani, and P. Di Porto. "Chapter 3 Photorefractive Solitons and Their Underlying Nonlocal Physics." In: *Prog. Opt.* Vol. 53. 2009, pp. 153–200. DOI: `10.1016/S0079-6638(08)00203-5`.

[81] G. C. Duree et al. "Observation of self-trapping of an optical beam due to the photorefractive effect." In: *Phys. Rev. Lett.* 71.4 (1993), pp. 533–536. DOI: `10.1103/PhysRevLett.71.533`.

[82] W. Krolikowski, B. Luther-Davies, and C. Denz. "Photorefractive solitons." In: *IEEE J. Quantum Electron.* 39.1 (2003), pp. 3–12. DOI: `10.1109/JQE.2002.806190`.

[83] J. P. Gordon. "Interaction forces among solitons in optical fibers." In: *Opt. Lett.* 8.11 (1983), p. 596. DOI: `10.1364/OL.8.000596`.

[84] J. S. Aitchison et al. "Experimental observation of spatial soliton interactions." In: *Opt. Lett.* 16.1 (1991), p. 15. DOI: `10.1364/OL.16.000015`.

[85] M Shalaby, F Reynaud, and A Barthelemy. "Experimental observation of spatial soliton interactions with a $\pi/2$ relative phase difference." In: *Opt. Lett.* 17.11 (1992), p. 778. DOI: `10.1364/OL.17.000778`.

[86] M Segev and G Stegeman. "Self-trapping of optical beams: Spatial solitons." In: *Phys. Today* 51.8 (1998), pp. 42–48. DOI: `10.1063/1.882370`.

[87] G. I. Stegeman. "Optical Spatial Solitons and Their Interactions: Universality and Diversity." In: *Science (80-. ).* 286.5444 (1999), pp. 1518–1523. DOI: `10.1126/science.286.5444.1518`.

[88] M. Morin, M. Segev, G. Duree, and G. Salamo. "Waveguides formed by quasi-steady-state photorefractive spatial solitons." In: *Opt. Lett.* 20.20 (1995), p. 2066. DOI: `10.1364/OL.20.002066`.

[89] Z. Chen, M. Mitchell, and M. Segev. “Steady-state photorefractive soliton-induced Y-junction waveguides and high-order dark spatial solitons.” In: *Opt. Lett.* 21.10 (1996), p. 716. DOI: `10.1364/OL.21.000716`.

[90] M.-f. Shih et al. “Waveguides induced by photorefractive screening solitons.” In: *J. Opt. Soc. Am. B* 14.11 (1997), p. 3091. DOI: `10.1364/JOSAB.14.003091`.

[91] S. Lan et al. “Directional coupler with soliton-induced waveguides.” In: *Opt. Lett.* 24.7 (1999), p. 475. DOI: `10.1364/OL.24.000475`.

[92] S. Lan et al. “Second-harmonic generation in waveguides induced by photorefractive spatial solitons.” In: *Opt. Lett.* 24.16 (1999), p. 1145. DOI: `10.1364/OL.24.001145`.

[93] Y. Hu et al. “Reshaping the trajectory and spectrum of nonlinear Airy beams.” In: *Opt. Lett.* 37.15 (2012), p. 3201. DOI: `10.1364/OL.37.003201`.

[94] D. N. Christodoulides and M. I. Carvalho. “Compression, self-bending, and collapse of Gaussian beams in photorefractive crystals.” In: *Opt. Lett.* 19.21 (1994), p. 1714. DOI: `10.1364/OL.19.001714`.

[95] S. Jia et al. “Diffusion-Trapped Airy Beams in Photorefractive Media.” In: *Phys. Rev. Lett.* 104.25 (2010), p. 253904. DOI: `10.1103/PhysRevLett.104.253904`.

[96] I. Kaminer, M. Segev, and D. N. Christodoulides. “Self-Accelerating Self-Trapped Optical Beams.” In: *Phys. Rev. Lett.* 106.21 (2011), p. 213903. DOI: `10.1103/PhysRevLett.106.213903`.

[97] I. Kaminer, Y. Lumer, M. Segev, and D. N. Christodoulides. “Causality effects on accelerating light pulses.” In: *Opt. Express* 19.23 (2011), p. 23132. DOI: `10.1364/OE.19.023132`.

[98] N. K. Efremidis. “Airy trajectory engineering in dynamic linear index potentials.” In: *Opt. Lett.* 36.15 (2011), p. 3006. DOI: `10.1364/OL.36.003006`.

[99] P. Vaity, A. Kumar, S. Prabhakar, and R. P. Singh. “2D Airy beams propagation through photorefractive materials.” In: ed. by S. K. Khijwania, B. D. Gupta, B. P. Pal, and A. Sharma. 2010, 81730N–81730N–6. DOI: `10.1117/12.897797`.

[100] Z. Ye et al. “Acceleration control of Airy beams with optically induced refractive-index gradient.” In: *Opt. Lett.* 36.16 (2011), pp. 3230–3232. DOI: `10.1364/OL.36.003230`.

[101] Y. Y. Zhang et al. "Periodic inversion and phase transition of finite energy Airy beams in a medium with parabolic potential." In: *Opt. Express* 23.8 (2015), p. 10467. DOI: `10.1364/OE.23.010467`.

[102] F. Xiao et al. "Optical Bloch oscillations of an Airy beam in a photonic lattice with a linear transverse index gradient." In: *Opt. Express* 22.19 (2014), p. 22763. DOI: `10.1364/OE.22.022763`.

[103] F. Diebel et al. "Control of Airy-beam self-acceleration by photonic lattices." In: *Phys. Rev. A* 90.3 (2014), p. 033802. DOI: `10.1103/PhysRevA.90.033802`.

[104] R. Bekenstein and M. Segev. "Self-accelerating optical beams in highly nonlocal nonlinear media." In: *Opt. Express19* 19.24 (2011), pp. 23706–23715. DOI: `10.1364/OE.19.023706`.

[105] P. Panagiotopoulos et al. "Nonlinear propagation dynamics of finite-energy Airy beams." In: *Phys. Rev. A - At. Mol. Opt. Phys.* 86.1 (2012), pp. 1–15. DOI: `10.1103/PhysRevA.86.013842`.

[106] A. Lotti et al. "Stationary nonlinear Airy beams." In: *Phys. Rev. A - At. Mol. Opt. Phys.* 84.2 (2011), p. 021807. DOI: `10.1103/PhysRevA.84.021807`.

[107] I. M. Allayarov and E. N. Tsoy. "Dynamics of Airy beams in nonlinear media." In: *Phys. Rev. A* 023852.90 (2014), pp. 1–7. DOI: `10.1103/PhysRevA.90.023852`.

[108] N. Fressengeas, J. Maufoy, and G. Kugel. "Temporal behavior of bidimensional photorefractive bright spatial solitons." In: *Phys. Rev. E* 54.6 (1996), pp. 6866–6875. DOI: `10.1103/PhysRevE.54.6866`.

[109] N. Fressengeas. "Etude expérimentale et théorique de l'auto-focalisation d'un faisceau laser en milieu photoréfractif: convergences spatiale et temporelle vers un soliton." PhD thesis. University of Lorraine, 1997.

[110] N. Fressengeas, D. Wolfersberger, J Maufoy, and G Kugel. "Build up mechanisms of (1+1)-dimensional photorefractive bright spatial quasi-steady-state and screening solitons." In: *Opt. Commun.* 145.January (1998), pp. 393–400. DOI: `10.1016/S0030-4018(97)00455-0`.

[111] J. Maufoy, N. Fressengeas, D. Wolfersberger, and G. Kugel. "Simulation of the temporal behavior of soliton propagation in photorefractive media." In: *Phys. Rev. E* 59.5 (1999), pp. 6116–6121. DOI: `10.1103/PhysRevE.59.6116`.

[112] C. Dan et al. “Near infrared photorefractive self focusing in $Sn_2P_2S_6$:Te crystals.” In: *Opt. Express* 15.20 (2007), p. 12777. DOI: `10.1364/OE.15.012777`.

[113] D. Wolfersberger et al. “Fast photorefractive self-focusing in InP:Fe semiconductor at infrared wavelengths.” In: *Appl. Phys. Lett.* 92.2 (2008), p. 021106. DOI: `10.1063/1.2830989`.

[114] D. Wolfersberger and D. Tranca. “2D infrared self-focusing in bulk photorefractive SBN.” In: *Opt. Mater. Express* 1.7 (2011), p. 1178. DOI: `10.1364/OME.1.001178`.

[115] A. Einstein. “Die Feldgleichungen der Gravitation.” In: *Albert Einstein Akad.* Vol. XLVIII-XLI. Weinheim, FRG: Wiley-VCH Verlag GmbH & Co. KGaA, 2006, pp. 88–92. DOI: `10.1002/3527608958.ch5`.

[116] F. W. Dyson, A. S. Eddington, and C. Davidson. “A Determination of the Deflection of Light by the Sun’s Gravitational Field, from Observations Made at the Total Eclipse of May 29, 1919.” In: *Philos. Trans. R. Soc. A Math. Phys. Eng. Sci.* 220.571-581 (1920), pp. 291–333. DOI: `10.1098/rsta.1920.0009`.

[117] B. P. Abbott et al. “Observation of Gravitational Waves from a Binary Black Hole Merger.” In: *Phys. Rev. Lett.* 116.6 (2016), p. 061102. DOI: `10.1103/PhysRevLett.116.061102`.

[118] R. Penrose. “Quantum computation, entanglement and state reduction.” In: *Philos. Trans. R. Soc. A Math. Phys. Eng. Sci.* 356.1743 (1998), pp. 1927–1939. DOI: `10.1098/rsta.1998.0256`.

[119] D. R. Solli, C. Ropers, P. Koonath, and B. Jalali. “Optical rogue waves.” In: *Nature* 450.7172 (2007), pp. 1054–1057. DOI: `10.1038/nature06402`.

[120] T. G. Philbin et al. “Fiber-Optical Analog of the Event Horizon.” In: *Science (80-. ).* 319.5868 (2008), pp. 1367–1370. DOI: `10.1126/science.1153625`.

[121] D. Faccio et al. “Analogue gravity and ultrashort laser pulse filamentation.” In: ed. by B. J. Eggleton, A. L. Gaeta, and N. G. R. Broderick. 2010, pp. 77280M–77280M–10. DOI: `10.1117/12.855845`.

[122] F. Belgiorno et al. “Hawking Radiation from Ultrashort Laser Pulse Filaments.” In: *Phys. Rev. Lett.* 105.20 (2010), p. 203901. DOI: `10.1103/PhysRevLett.105.203901`.

[123] R. Bekenstein et al. “Optical simulations of gravitational effects in the Newton–Schrödinger system.” In: *Nat. Phys.* 11.10 (2015), pp. 872–878. DOI: `10.1038/nphys3451`.

[124] D. A. Genov, S. Zhang, and X. Zhang. “Mimicking celestial mechanics in metamaterials.” In: *Nat. Phys.* 5.9 (2009), pp. 687–692. DOI: `10.1038/nphys1338`.

[125] C. Sheng et al. “Trapping light by mimicking gravitational lensing.” In: *Nat. Photonics* 7.11 (2013), pp. 902–906. DOI: `10.1038/nphoton.2013.247`.

[126] A. V. Gorbach and D. V. Skryabin. “Light trapping in gravity-like potentials and expansion of supercontinuum spectra in photonic-crystal fibres.” In: *Nat. Photonics* 1.11 (2007), pp. 653–657. DOI: `10.1038/nphoton.2007.202`.

[127] N. Wiersma, N. Marsal, M. Sciamanna, and D. Wolfersberger. “All-optical interconnects using Airy beams.” In: *Opt. Lett.* 39.20 (2014), pp. 5997–6000. DOI: `OL.39.005997`.

[128] C. Denz et al. “Dynamics of formation and interaction of photorefractive screening solitons.” In: *Phys. Rev. E* 60.5 (1999), pp. 6222–6225. DOI: `10.1103/PhysRevE.60.6222`.

[129] J. Petter and C. Denz. “Guiding and dividing waves with photorefractive solitons.” In: *Opt. Commun.* 188.1-4 (2001), pp. 55–61. DOI: `10.1016/S0030-4018(00)01142-1`.

[130] D. Anderson and M. Lisak. “Bandwidth limits due to incoherent soliton interaction in optical-fiber communication systems.” In: *Phys. Rev. A* 32.4 (1985), pp. 2270–2274. DOI: `10.1103/PhysRevA.32.2270`.

[131] A. W. Snyder, D. J. Mitchell, and Y. S. Kivshar. “Unification of linear and nonlinear wave optics.” In: *Mod. Phys. Lett. B* 09.23 (1995), pp. 1479–1506. DOI: `10.1142/S0217984995001480`.

[132] E. DelRe, S. Trillo, and A. J. Agranat. “Collisions and inhomogeneous forces between solitons of different dimensionality.” In: *Opt. Lett.* 25.8 (2000), p. 560. DOI: `10.1364/OL.25.000560`.

[133] W. Królikowski et al. “Interaction of two-dimensional spatial incoherent solitons in photorefractive medium.” In: *Appl. Phys. B Lasers Opt.* 68.5 (1999), pp. 975–982. DOI: `10.1007/s003400050733`.

[134] M. Peccianti et al. "All-optical switching and logic gating with spatial solitons in liquid crystals." In: *Appl. Phys. Lett.* 81.18 (2002), p. 3335. DOI: `10.1063/1.1519101`.

[135] M. S. Petrović, M. R. Belić, C. Denz, and Y. S. Kivshar. "Counterpropagating optical beams and solitons." In: *Laser Photon. Rev.* 5.2 (2011), pp. 214–233. DOI: `10.1002/lpor.200900053`.

[136] O. Cohen et al. "Collisions between Optical Spatial Solitons Propagating in Opposite Directions." In: *Phys. Rev. Lett.* 89.22 (2002), p. 229901. DOI: `10.1103/PhysRevLett.89.229901`.

[137] M. Belić et al. "Self-trapped bidirectional waveguides in a saturable photorefractive medium." In: *Phys. Rev. E* 68.2 (2003), p. 025601. DOI: `10.1103/PhysRevE.68.025601`.

[138] M. R. Belić et al. "Counterpropagating self-trapped beams in photorefractive crystals." In: *J. Opt. B Quantum Semiclassical Opt.* 6.5 (2004), S190–S196. DOI: `10.1088/1464-4266/6/5/005`.

[139] M. Belić et al. "Counterpropagating optical solitons and vortices in photorefractive crystals." In: ed. by Y. Sheng, S. Zhuang, and Y. Zhang. 2006, pp. 602701–602701–9. DOI: `10.1117/12.667694`.

[140] Y. Y. Zhang et al. "Soliton pair generation in the interactions of Airy and nonlinear accelerating beams." In: *Opt. Lett.* 38.22 (2013), pp. 4585–4588. DOI: `10.1364/ol.38.004585`.

[141] Y. Y. Zhang et al. "Interactions of Airy beams, nonlinear accelerating beams, and induced solitons in Kerr and saturable nonlinear media." In: *Opt. Express* 22.6 (2014), pp. 7160–7171. DOI: `10.1364/OE.22.007160`.

[142] R. Driben, V. V. Konotop, and T. Meier. "Coupled Airy breathers." In: *Opt. Lett.* 39.19 (2014), p. 5523. DOI: `10.1364/OL.39.005523`.

[143] M. Shen, J. Gao, and L. Ge. "Solitons shedding from Airy beams and bound states of breathing Airy solitons in nonlocal nonlinear media." In: *Sci. Rep.* 5 (2015), p. 9814. DOI: `10.1038/srep09814`.

[144] M. Shen, W. Li, and R.-K. Lee. "Control on the anomalous interactions of Airy beams in nematic liquid crystals." In: *Opt. Express* 24.8 (2016), p. 8501. DOI: `10.1364/OE.24.008501`.

[145] Y. Silberberg and I. B. Joseph. "Instabilities, Self-Oscillation, and Chaos in a Simple Nonlinear Optical Interaction." In: *Phys. Rev. Lett.* 48.22 (1982), pp. 1541–1543. DOI: `10.1103/PhysRevLett.48.1541`.

[146] W. J. Firth and C Paré. "Transverse modulational instabilities for counterpropagating beams in Kerr media." In: *Opt. Lett.* 13.12 (1988), pp. 1096–1098. DOI: `10.1364/OL.13.001096`.

[147] D. J. Gauthier, M. S. Malcuit, A. L. Gaeta, and R. W. Boyd. "Polarization bistability of counterpropagating laser beams." In: *Phys. Rev. Lett.* 64.15 (1990), pp. 1721–1724. DOI: `10.1103/PhysRevLett.64.1721`.

[148] A. L. Gaeta, R. W. Boyd, J. R. Ackerhalt, and P. W. Milonni. "Instabilities and chaos in the polarizations of counterpropagating light fields." In: *Phys. Rev. Lett.* 58.23 (1987), pp. 2432–2435. DOI: `10.1103/PhysRevLett.58.2432`.

[149] J. F. Henninot, J. F. Blach, and M Warenghem. "Experimental study of the nonlocality of spatial optical solitons excited in nematic liquid crystal." In: *J. Opt. A Pure Appl. Opt.* 9.1 (2007), pp. 20–25. DOI: `10.1088/1464-4258/9/1/004`.

[150] R. Chang and P. Meystre. "Instabilities of counterpropagating beams in a nonlinear medium." In: *Phys. Rev. A* 44.5 (1991), pp. 3188–3200. DOI: `10.1103/PhysRevA.44.3188`.

[151] C. Rotschild, B. Alfassi, O. Cohen, and M. Segev. "Long-range interactions between optical solitons." In: *Nat. Phys.* 2.11 (2006), pp. 769–774. DOI: `10.1038/nphys445`.

[152] C. Denz et al. "Spatio-temporal dynamics of counter-propagating photorefractive self-trapped beams." In: *Photorefractive Eff. Mater. Devices*. 2005.

[153] P. Jander et al. "Dynamic instability of counterpropagating self-trapped beams in photorefractive media." In: *Proc. SPIE*. Ed. by N. Rosanov and S. Trillo. Vol. 6255. 62550A. 2006, 62550A–62550A–8. DOI: `10.1117/12.676737`.

[154] Y. Fattal, A. Rudnick, and D. M. Marom. "Soliton shedding from Airy pulses in Kerr media." In: *Opt. Express* 19.18 (2011), p. 17298. DOI: `10.1364/OE.19.017298`.

[155] A. Rudnick and D. M. Marom. "Airy-soliton interactions in Kerr media." In: *Opt. Express* 19.25 (2011), p. 25570. DOI: `10.1364/OE.19.025570`.

[156] M Sciamanna and K. A. Shore. "Physics and applications of laser diode chaos." In: *Nat. Photonics* 9.3 (2015), pp. 151–162. DOI: `10.1038/nphoton.2014.326`.

[157] M. Virte et al. “Physical random bit generation from chaotic solitary laser diode.” In: *Opt. Express* 22.14 (2014), p. 17271. DOI: `10.1364/OE.22.017271`.

[158] F. Diebel et al. “Soliton formation by decelerating interacting Airy beams.” In: *Opt. Express* 23.19 (2015), p. 24351. DOI: `10.1364/OE.23.024351`.

# COLOPHON

This document was typeset using the typographical look-and-feel `classicthesis` developed by André Miede. The style was inspired by Robert Bringhurst's seminal book on typography *"The Elements of Typographic Style"*. `classicthesis` is available for both LaTeX and LyX:

`https://bitbucket.org/amiede/classicthesis/`